University of Nottingham
Sir Peter Mansfield Imaging Centre

UNIVERSITY OF NOTTINGHAM

PHYSICS AND ASTRONOMY

SIR PETER MANSFIELD IMAGING CENTRE

Implementation of ^{23}Na MRI

Author:
Benjamin L. Prestwich, MSci

30$^{\text{th}}$ July 2021

Thesis submitted to the University of Nottingham
for the degree of Doctor of Philosophy

Abstract

Sodium magnetic resonance imaging (^{23}Na MRI) has the potential to provide insight into cellular, tissue and organ health. Proton (^{1}H) MRI is well established, but ^{23}Na MRI faces several challenges, principally due to the low inherent ^{23}Na signal from the body and the need for specialist hardware. The aim of this thesis was to lay the groundwork for carrying out ^{23}Na MRI in humans on a clinical MRI scanner, to determine quantitative ^{23}Na measures in the kidneys, muscle and skin.

Firstly, work was carried out to install the ^{23}Na RF coils to allow for the study of the ^{23}Na distribution in the leg, muscle and skin, and abdomen. This required modelling of the specific absorption rate (SAR), phantom construction, temperature testing, coupling checks, power calibration and measurement of the coil's transmit/receive switching time.

Secondly, the implementation and assessment of scanning techniques and calibration methods for the measurement of tissue sodium concentration (TSC) in the calf is described. This work includes 3D gradient recalled echo (GRE) imaging and sequence optimisation and the development of improved B_1 mapping for correction of sodium images to more accurately compute TSC. Comparisons of measures using 3D GRE and ultrashort echo time (UTE) schemes are made, and measurement of the bi-exponential ^{23}Na transverse relaxation time performed. An optimised 1 hour scan protocol for future studies is outlined.

Thirdly, ^{23}Na imaging of the abdomen, specifically of the kidney, is outlined. Results of initial scans performed *in vivo* using the dual loops coil to assess TSC in the kidney are shown. The limitations of such methods in terms of image homogeneity are described. This is followed by the assessment of a 6-channel body coil for improved homogeneity of sodium measures, and the evaluation of receive sensitivity correction.

Finally, work on proton (^{1}H) imaging using a skin coil to assess changes in skin hydration, lays the ground work for future studies combining ^{1}H measurement of skin water content with ^{23}Na imaging of the skin.

Acknowledgements

First and foremost, I would like to thank my supervisor Prof. Sue Francis who has mentored me through this PhD. Her ceaseless knowledge, infectious enthusiasm and support has made this PhD possible.

I would also like to thank Dr Matthew Clemence, Dr Paul Glover and Dr Andrew Peters for your help along the way.

I would like to thank everyone in the SPMIC, who make it such a great place to work. Alex, Andrew and Daisie for being great company for all the tea breaks, lunches and conferences. Lesley for being a friendly face every morning and solving all problems.

I would like to thank the hepatorenal team, Charlotte, Chris and Eleanor for their knowledge, support and great company.

I would also like to thank my family for their support and interest in my work, and my friends, who have made my time at Nottingham good fun. Finally, Katie for keeping me sane during the write-up/lockdown.

Contents

List of Abbreviations

ASL : Arterial Spin Labelling

AFI : Actual flip anlge

AKI : Acute kidney injury

ATN : Acute tubular necrosis

BOLD : Blood Oxygen Level Dependent

BW : Bandwidth

CKD : Chronic Kidney Disease

CMSG : Corticomedullary sodium concentration gradient

CSF : Cerebrospinal fluid

DA : Double angle

EBC : Electrolyte balancing control

FA : Flip anlge

FDTD : Finite-Difference Time-Domain

FFE : Fast field echo

FID : Free Induction Decay

FOV : Field of view

GDR : Glucose disposal rates

GFR : Glomerular filtration rate

GRASE : Gradient and spin echo

GRE : Gradient recalled echo

HD : Haemodialysis

HV : Healthy Volunteer

ICP : Inductively Coupled Plasma

IR : Inversion recovery

LDR : Leucine disposal rates

LVH : Left ventricular hypertrophy

LVM : Left ventricular mass

MN : Multi-nuclear

MRI : Magnetic resonance imaging

MRS : Magnetic resonance spectroscopy

MT : Magnetisation transfer

NMR : Nuclear magnetic resonance

NS : Non-selective

NSA : Number of signal averages

PET : Positron emission tomography

PPE : Pulse programming environment

PSF : Point spread function

RF : Radiofrequency

ROI : Region of interest

SAR : Specific absorption rate

SE : Spin-echo

SENSE : Sensitivity encoding

SEPS : Spin Echo Phase-Sensitive

SI : Signal intensity

SNR : Signal-to-noise ratio

SOS : Stack of stars

SPMIC : Sir Peter Mansfield Imaging Centre

SSE : Sum of squares error

TA : Acquisition time

TE : Echo time

TI : Inversion time

TPI : twisted projection imaging

TR : Repetition time

TSC : Tissue sodium concentration

UHF : Ultra-high field

UTE : Ultrashort echo time

List of Tables

List of Figures

Chapter 1

Introduction

1.1 Motivation

Although the potential clinical use of sodium (^{23}Na) MRI was first demonstrated in 1984 [7], it is only the recent developments in MRI technology that the significant potential of this approach for clinical imaging has started to be explored. This step change has been enabled by the establishment of higher magnetic field strength MRI scanners in healthcare, with clinical systems at 3T and MR manufacturers investment in ultra-high field (UHF) systems (7T and 9.4T), coupled with extended hardware capabilities such as access to a broadband frequency range allowing MRI with nuclei other than hydrogen (^{1}H), and high gradient strengths and slew rates that provide ultrashort echo time (UTE) pulse sequences. Furthermore, using the inbuilt body transmit proton (^{1}H) radiofrequency (RF) coil or a dual-tuned ^{1}H/^{23}Na RF coils allow the overlay of high resolution structural features obtained from ^{1}H images with ^{23}Na functionality obtained from ^{23}Na imaging.

1.1.1 The ^{23}Na Challenge

In vivo, ^{23}Na MRI is challenging when compared to ^{1}H MRI, this is primarily due to its low MR sensitivity, which is of the order of 3,000-20,000 times less than ^{1}H MRI. This is organ dependent, but for example there are approximately 35 mM ^{23}Na nuclei as compared to 80 M protons in the human brain, and of the order of 70-150 mM ^{23}Na

nuclei in the kidney. This results from the four fold lower gyromagnetic ratio (γ) of ^{23}Na compared to ^{1}H (γ of ^{23}Na is 11.26 MHz/T compared to 42.58 MHz/T), the quantum mechanical property of spin of the ^{23}Na nucleus which takes a value of 3/2 compared to 1/2 for ^{1}H, and the low natural abundance of ^{23}Na in the biological tissues. Further, the 3/2 spin results in ^{23}Na having a quadrupolar moment, meaning that the MR signal from ^{23}Na decays significantly faster than for protons, resulting in a short longitudinal (T_1) and rapid bi-exponential transverse (T_2/T_2^*) signal decay with fast (T_{2f}, 60% of signal) and slow (T_{2s}, 40% of signal) components.

1.1.2 ^{23}Na at a Cellular Level

^{23}Na is a vital electrolyte in the body and plays several roles, including maintaining the volume of blood and extracellular fluid within the human body [8]. At a cellular level there is a carefully maintained difference in the intracellular and extracellular ion concentrations, with ^{23}Na being predominantly extracellular, Figure [1.1]. ^{23}Na can cross the cell membrane through a number of channels, these include Na^+/K^+, Na^+/Ca^{2+} and Na^+/Mg^+ exchangers. The most important transporter is the Na^+/K^+-ATPase (adenosine triphosphatase), known as the sodium-potassium pump, which with the consumption of ATP moves sodium and potassium against the substantial electrochemical gradient across the cell walls. If a cell's health or integrity is compromised by any condition that effects the ion transporters there will be a change in the gradient, and with ^{23}Na MRI this gradient can potentially be monitored.

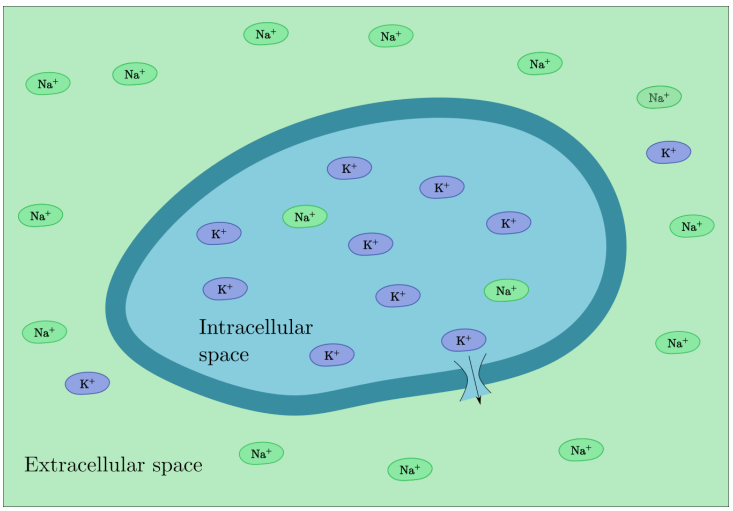

Figure 1.1: The distribution of Na^+ and K^+ inside and outside a typical cell.

In a voxel of a ^{23}Na image of for example 3 mm^3, there are roughly 6 million cells, therefore ^{23}Na MRI measures the bulk signal with contributions from both the intra- and extra-cellular space, Figure [1.2a]. Pathologies that can be studied by measuring the bulk signal include conditions that cause sodium-potassium pump breakdown allowing the high concentration of ^{23}Na in the extracellular space to move into the cells, increasing the bulk signal Figure [1.2b]. Also if cell shrinkage were to take place then although the gradient has not changed the bulk signal will increase, Figure [1.2c].

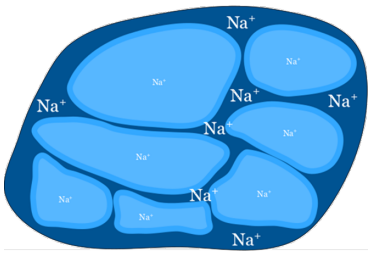

(a) Sketch of a group of cells, with low ^{23}Na concentration inside and high ^{23}Na concentration outside.

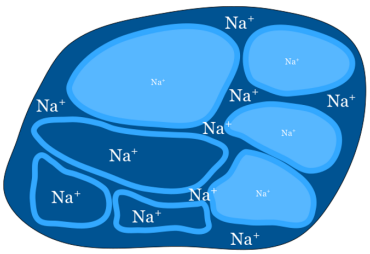

(b) If the sodium-potassium pumps were to breakdown the high concentration of ^{23}Na outside the cell will enter the cells, increasing the overall ^{23}Na signal in the voxel.

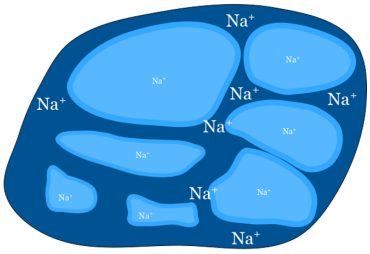

(c) If cell shrinking takes place then although the concentration inside the cells does not change the overall ^{23}Na signal would increase.

Figure 1.2: Some mechanisms that could cause a change in the measured ^{23}Na signal intensity using MRI.

Therefore ^{23}Na MRI can be used as an indicator of cell health and integrity and can monitor changes brought about by illness, such as kidney disease [9–11] and hypertension

[12], as well as brain disorders. [13–15].

1.1.3 ^{23}Na Storage

^{23}Na in the body can be thought to be in three locations: (i) osmotically active ^{23}Na in the total extracellular space implicated in the control of extracellular fluid volume and the compartmental fluid composition; (ii) the slowly exchangeable pool of ^{23}Na in the bones; (iii) ^{23}Na stored in the tissue (skin and muscle interstitium) representing water-free tissue storage. These three compartments are illustrated in Fig.[1.3].

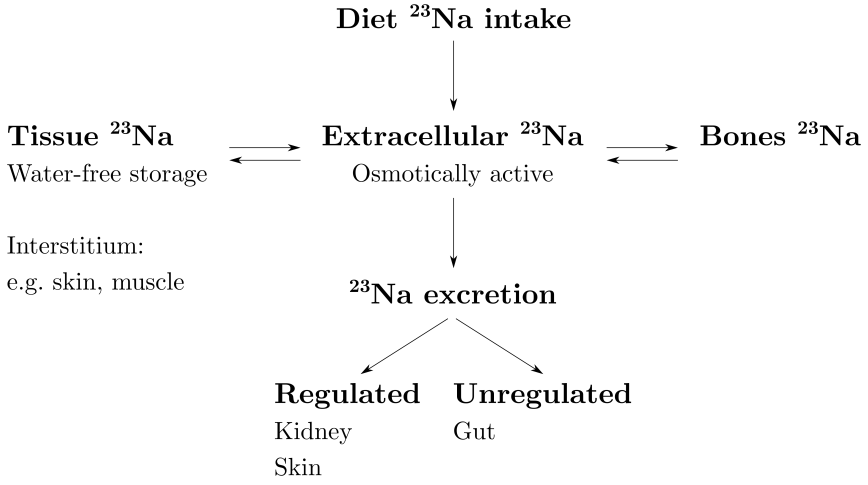

Figure 1.3: Storage of ^{23}Na in the body [4].

1.1.4 ^{23}Na and the Kidneys

One of the main tasks of the human kidneys is to maintain the homeostasis of the body's fluid and electrolyte balance, by filtration of the plasma and excretion of the end products. The regulation of extracellular ^{23}Na and water balance in the kidney is of particular importance, as this depends on an increasing ^{23}Na concentration gradient from the renal cortex to the medulla. A high ^{23}Na concentration in the medulla is crucial for the final concentration of the urine through reabsorption of water as shown in Fig.[1.4]. The ability to image the tissue sodium content (TSC) and monitor any changes in the corticomedullary sodium concentration gradient (CMSG) *in vivo* will potentially increase our

knowledge of renal physiology and allow the monitoring of changes during a variety of kidney diseases.

Patients with nephrology related diseases such as Chronic Kidney Disease (CKD) are advised to limit their ^{23}Na intake as the kidneys are less able to eliminate excess ^{23}Na and water from the body. Hypertension is also a very common complication of CKD, with inadequate treatment increasing the risks of both progressive decline in renal function and increased risk of cardiovascular disease. Acute Kidney Injury (AKI) has been associated with ^{23}Na accumulation in the extracellular space [16] resulting in oedema and hypertension.

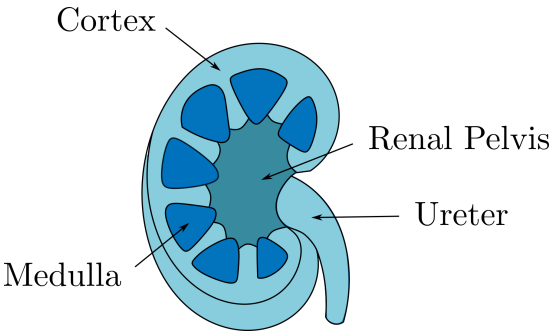

(a) The structure inside the kidney.

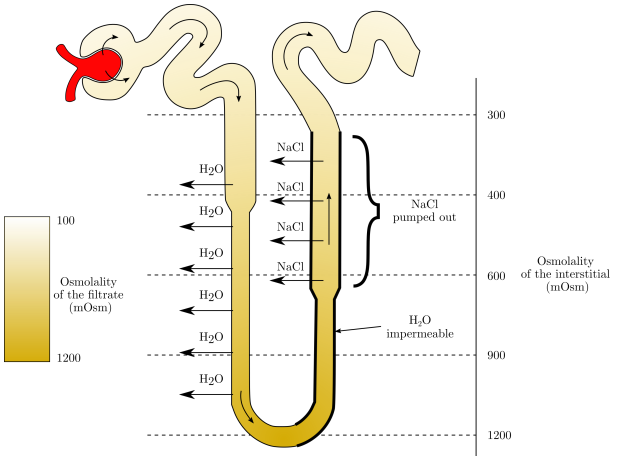

(b) The loop of Henle, shown here, is part of the kidney's nephron and is responsible for the reabsorption of ^{23}Na and water. This diagram shows the path of the filtrate through the loop of Henle. ^{23}Na is actively pumped out of the loop of Henle creating a large osmotic gradient which moves the water out of the filtrate.

Figure 1.4: Structure of the kidney and the loop of Henle.

Animal studies using micropuncture have demonstrated a steep intra-renal ^{23}Na gradient between the cortex and medulla [17–19]. Early studies applied ^{23}Na imaging to study the kidney in animal models. Maril et al. [20] showed in rats that the CMSG increased linearly from the cortex to the medulla by 31 mmol/L/mm. Further they used Furosemide, a diuretic medication, to induce a 50% reduction in the inner-medulla ^{23}Na and 25% increase in outer cortical ^{23}Na. This was followed by a study using ^{23}Na imaging to assess the effect in rat kidneys at 6 hours after induced acute tubular necrosis (ATN) [10]. Here

a 21% reduction in the CMSG was demonstrated ($P < 0.01$, $n = 7$ animals). Recently, in a preclinical pig study, and accompanying human study, Grist et al. [21] showed the quantification of the diuretic induced changes in the CMSG in pigs 20 minutes after the introduction of a Furosemide injection. In the human component, baseline ^{23}Na images were acquired in healthy volunteers with total ^{23}Na concentrations in the medulla, cortex and whole kidney shown to be of ∼135 mmol/L, 71 mmol/L and 93 mmol/L respectively. Maril and Zollner et al. [10, 22] performed ^{23}Na MR in native kidneys and showed a qualitative measure of the CMSG. Whilst Moon et al. [23] demonstrated quantitative differences in the CMSG between transplanted and native kidneys, with lower TSC in transplanted kidneys (154 ± 12 mmol/L vs 193 ± 10 mmol/L) and a reduced CMSG (8.9 ± 1.5 mmol/L/mm vs 10.5 ± 0.9 mmol/L/mm).

1.1.5 ^{23}Na Storage in Muscle and Skin

Recent evidence that ^{23}Na is stored in the skin and that interstitial electrolyte balance is achieved by renal and extra-renal mechanisms [4,24–26] has identified a need for ^{23}Na MRI to assess muscle and interstitial skin ^{23}Na *in vivo*. This is now being used in a variety of experimental conditions to evaluate the role of muscle and skin ^{23}Na in the pathogenesis of hypertension and cardiovascular disease [26]. Studies to date indicate tissue ^{23}Na levels cannot be reliably measured by sampling blood or interstitial fluid. Recent evidence from chemical analysis of tissue electrolyte and water composition has shown that body ^{23}Na content does not always readily equilibrate with water and cannot be exclusively controlled by the renal mechanisms [27]. In muscle, ^{23}Na changes have been linked to several disease states, including diabetes mellitus, hypertension, and cardiovascular risk. It has thus been suggested that the pathophysiological process of skin and muscle ^{23}Na storage is of relevance for health and disease. Using ^{23}Na imaging Kopp et al. [12, 28] have shown that ^{23}Na accumulation in the extracellular space is closely associated with essential hypertension. In their 2012 study, Kopp et al. [28] showed in an animal study in rats that ^{23}Na MRI data compared well with actual tissue ^{23}Na content by chemical analysis, and went on to show in humans that ^{23}Na content differed in patients with

hyperaldosteronism compared with healthy women and men. In their 2013 study, Kopp et al. [12] used ^{23}Na MRI to exhibit an age-dependant increase of muscle ^{23}Na without a corresponding change in water content, suggesting water free ^{23}Na storage. Skin ^{23}Na also showed an age-dependant increase but with increased water content. There was also a significant increase in the ^{23}Na storage in refractory hypertension subjects versus healthy controls, indicating a connection between ^{23}Na storage and cardiovascular morbidity.

1.1.6 ^{23}Na and Haemodialysis

Restoring salt and water homeostasis in haemodialysis (HD) patients is a key consideration. Salt and water management in dialysis patients relies on: (i) accurate assessment of fluid and ^{23}Na status, (ii) adequate removal of excess salt and water, and (iii) dietary salt restrictions. The group of Jen Titze has used ^{23}Na MRI to show that haemodialysis can mobilize tissue ^{23}Na [25,29]. They studied HD patients and age-matched healthy controls and showed that older HD patients had increased ^{23}Na and water in the skin and muscle compared to age-matched controls, therefore suggesting that ^{23}Na MRI could be a useful tool to evaluate different haemodialysis techniques, as illustrated in Fig.[1.5].

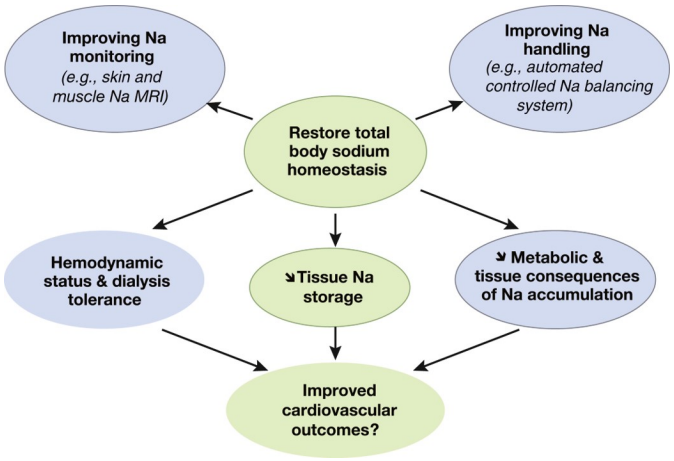

Figure 1.5: The potential role of ^{23}Na MRI in haemodialysis treatment. Taken from "Sodium and water handling during haemodialysis: new pathophysiologic insights and management approaches for improving outcomes in end-stage kidney disease" by Canaud et al. [4].

1.2 Aims and Objectives

The aim of this thesis was to lay the groundwork for carrying out ^{23}Na MRI in humans on a clinical Philips system, to determine quantitative ^{23}Na measures in the kidneys, muscle and skin. Prior to this thesis no *in vivo* ^{23}Na MRI work had been performed at the Sir Peter Mansfield Imaging Centre (SPMIC). Thus, work outlined in this thesis includes:

- Collaboration with Philips and third-party RF coil vendors to install and setup ^{23}Na RF coils to enable the *in vivo* scanning to estimate ^{23}Na distribution in the kidneys, muscle and skin.
- Safety tests and measures for the RF coils, SAR and temperature measurements.
- Implementation and assessment of scanning techniques and calibration methods for the accurate measurement of ^{23}Na concentration.

1.3 Description of the Work

Chapter 2 details the Magnetic Resonance theory related to the work carried out in this thesis. This describes the key components of Magnetic Resonance Imaging (MRI), including magnetisation, signal generation and detection, relaxation, spatial encoding and pulse sequences. It outlines RF coil design and the concepts of RF modelling for safe use of RF coils and measurement of transmit RF fields.

Chapter 3 covers the steps involved with installation of the RF coils for this thesis for the study of muscle, skin (surface coils, birdcage coils) and kidneys (dual loops and 6-channel coil body coils). It starts by providing an overview of the RF coils used in this work and their choice and development. Next the methods and results of the specific absorption rate (SAR) simulations are outlined for safe use of the RF coils. The different phantoms used throughout this project are then detailed followed by the final safety test, temperature testing. The next sections outline the steps taken when installing the coils on the scanners, including checking the compatibility between the MRI scanner's inbuilt ^{1}H body transmit (Q-Body) coil and the ^{23}Na RF coils. Finally, the assessment of the

coils power calibration and measurement of coil switching times is described.

Chapter 4 describes the setting up of imaging techniques and corrections needed to carry out ^{23}Na MRI in the leg. Initial work performed using a surface coil to image ^{23}Na in the calf muscle to monitor changes in ^{23}Na signal after exercise is described. This is followed by the optimisation of the gradient recalled echo (GRE) sequence for ^{23}Na imaging on the birdcage leg coil. The conversion of ^{23}Na image signal intensity to ^{23}Na concentration maps is covered. This includes the implementation of a phase sensitive B_1 mapping scheme to improve quantification. The UTE sequence is compared to the GRE technique and assessment of the T_2^* relaxation time is performed. The chapter concludes with an optimised protocol for future ^{23}Na imaging studies.

Chapter 5 studies ^{23}Na imaging of the kidney using the dual loops ^{23}Na coil and a 6-channel body ^{23}Na coil. Initial data is shown in healthy controls and CKD patients using the dual loops ^{23}Na coil, highlighting feasibility. This is followed by optimisation of the gradient echo sequence. Developments on the 6-channel coil for improved homogeneity of body measures is then described along with the correction of images using the receive sensitivity profile.

Chapter 6 outlines work on proton (^{1}H) imaging using a skin coil to assess changes in skin hydration, and lays the groundwork for future studies of combining ^{1}H measurement of skin water content with ^{23}Na imaging of the skin.

Finally, Chapter 7 provides a conclusion, outlining the key findings in this thesis and directions for future work.

Chapter 2

Theory

This chapter outlines the theory of the Nuclear Magnetic Resonance (NMR) signal covering the fundamental properties of spin, excitation and detection, relaxation and imaging. In particular, throughout this chapter will refer to proton (^{1}H) MRI and the inherent differences associated with performing sodium (^{23}Na) MRI. An outline of RF coils is then provided, followed by SAR modelling required before using coils *in vivo* including the Finite-Difference Time-Domain method. Finally, a description of B_1 mapping methods to measure the transmitted RF field is provided.

2.1 Nuclear Magnetic Resonance (NMR)

2.1.1 NMR Signal

Magnetic resonance Imaging (MRI) exploits nuclei with either an odd number of protons or neutrons, or both. These nuclei have an intrinsic spin angular momentum, $\boldsymbol{J}$, therefore these rotating charged nuclei have an associated magnetic moment $\boldsymbol{\mu}$ given by

$$\boldsymbol{\mu} = \gamma \boldsymbol{J} \tag{2.1}$$

where γ is the gyromagnetic ratio.

MRI is typically carried out on ^{1}H due to its high natural abundance, ^{23}Na is second to ^{1}H in having the most sensitive biologically relevant MR signal. Table [2.1] shows a selection of NMR sensitive nuclei.

Nucleus	Spin **I**	GMR γ (MHz/T)	Relative sensitivity	Abundance %
^{1}H	1/2	42.58	1.000	99.99
^{3}He	1/2	32.43	0.442	0.0001
^{13}C	1/2	10.71	0.016	1.108
^{19}F	1/2	40.06	0.833	100
^{23}Na	3/2	11.26	0.083	100
^{31}P	1/2	17.24	0.066	100
^{129}Xe	1/2	11.78	0.021	26.44

Table 2.1: NMR properties of different nuclei.

There are several inherent challenges when carrying out ^{23}Na MRI, these can be highlighted by comparing ^{23}Na to ^{1}H. It can be seen that ^{23}Na has 8% of the relative sensitivity of ^{1}H, it is also important to note that ^{23}Na is a spin 3/2 nuclei which causes a rapid biexponential decay, as covered in Section [2.1.5.3]. It is this rapid signal loss that led to the term "invisible sodium", due to the loss of signal before it could be measured [30]. The next difference between ^{23}Na and ^{1}H is that of concentration, typical ^{23}Na concentrations can be seen in Table [2.2]. Compared to the water (^{1}H) concentration in the brain of approximately 80,000 mmol/L, the ^{23}Na concentration is considerably less than ^{1}H. Combining the reduced sensitivity and concentration of ^{23}Na leads to a SNR for ^{23}Na imaging that is 3,000 - 20,000 less than for ^{1}H imaging.

Tissue	$[Na^{+}]$ (mmol/L)	^{23}Na T_1 (ms)	^{1}H T_1 (ms)	^{23}Na $T_{2,fast}$ (ms)	^{23}Na $T_{2,slow}$ (ms)	^{1}H T_2 (ms)
Brain						
WM	20-60	15-35	832	0.8-3.0	15-30	80
GM	30-70	15-35	1331	0.8-3.0	15-30	100
CSF	140-150	50-55	3817	-	55-65	-
Cartilage	250-350	15-25	1420	0.5-2.5	10-30	30
Blood	140-150	20-40	1930	2.0-3.0	12-20	275
Muscle	15-30	12-25	898	1.5-2.5	15-30	30

Table 2.2: Typical values of ^{23}Na concentration, and T_1 and T_2 of ^{23}Na and ^{1}H at 3T [1,2].

From quantum mechanics, angular momentum $\boldsymbol{J}$ is quantised and is a vector with mag-

nitude given by,

$$|\boldsymbol{J}| = \hbar\sqrt{\boldsymbol{I}(\boldsymbol{I}+1)} \tag{2.2}$$

where $\hbar$ is Planck's constant divided by 2π. $\boldsymbol{I}$ is the spin angular momentum quantum number, where for ^{1}H nuclei $\boldsymbol{I} = \frac{1}{2}$ and for ^{23}Na nuclei, $\boldsymbol{I} = \frac{3}{2}$. The direction of the $\boldsymbol{J}$ is described by the quantum number, m_I, the magnetic spin quantum number. When an external magnetic field is applied, m_I can take $2\boldsymbol{I}+1$ values given by,

$$m_I = \boldsymbol{I}, (\boldsymbol{I}-1), (\boldsymbol{I}-2), \ ..., -\boldsymbol{I}. \tag{2.3}$$

Therefore for a hydrogen nuclei where $\mathbf{I} = \frac{1}{2}$, there are two possible spin states at $m_I = \pm\frac{1}{2}$ whilst for ^{23}Na where $\mathbf{I} = \frac{3}{2}$ there are four possible spin states at $m_I = -\frac{3}{2}, -\frac{1}{2}, \ \frac{1}{2}, \ \frac{3}{2}$. The resulting energy states are represented in Fig.[2.1]. For ^{23}Na there are thus four energy levels, with three possible single quantum transitions, $\Delta m = \pm 1 \left(i.e. \frac{3}{2} \rightarrow \frac{1}{2}, \ \frac{1}{2} \rightarrow -\frac{1}{2}, \text{ and } -\frac{1}{2} \rightarrow -\frac{3}{2}\right)$. These transitions are termed single quantum coherences.

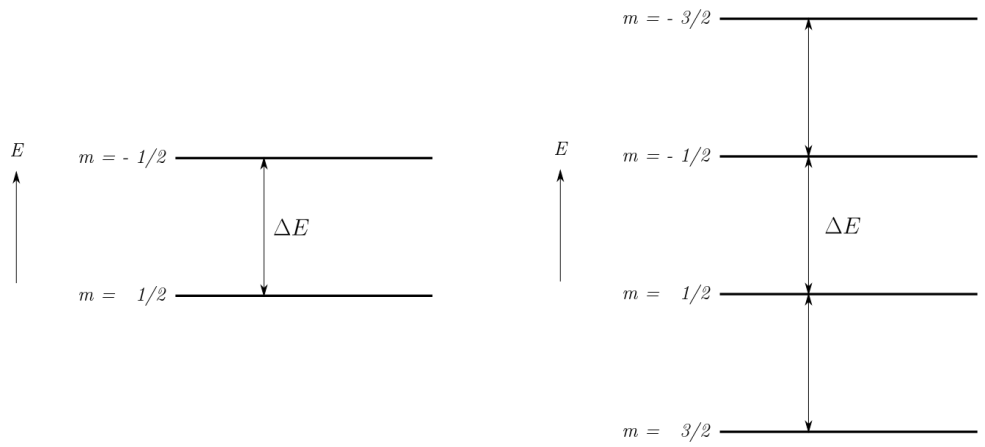

(a) Proton energy levels (b) ^{23}Na energy levels

Figure 2.1: The energy levels of proton and ^{23}Na when in an external magnetic field.

The environment in which ^{23}Na is present will affect the energy levels, as summarised in Figure [2.2]. This energy shift is caused by electric field gradients (EFG) of the ^{23}Na nuclei, and is dependant on the molecular environment and the physical state of the nuclei. If ^{23}Na forms a single crystal, described as type **a**, then there will be four discrete

energy levels and three sharp transitional peaks. If the ^{23}Na is in a powdered form with randomly orientated crystals then it is described as type **b**. Both type **a** and **b** are not found in the body, except in rare cases. Type **c** and **d** are ^{23}Na in aqueous solution, where the ions are free to move around. In type **d** ^{23}Na is in a solution with only water, where the ions are moving rapidly and the EFG interactions are averaged out, causing the spacing between energy levels to be equal which produces a single resonance peak. In type **c** the ions are in tissue where they are more restricted compared to type **d**, therefore their motion is slower, on the order of the Larmor frequency and the EFG interactions ω_Q that will cause a shift in the energy levels in the system. Within this system Multiple Quantum Coherences (MQC) are possible. The transitions have coalesced producing a single, broad, homogeneous peak, described as a bi-exponential spectrum. Both intra- and extra-cellular ^{23}Na will contribute to a type **c** spectrum.

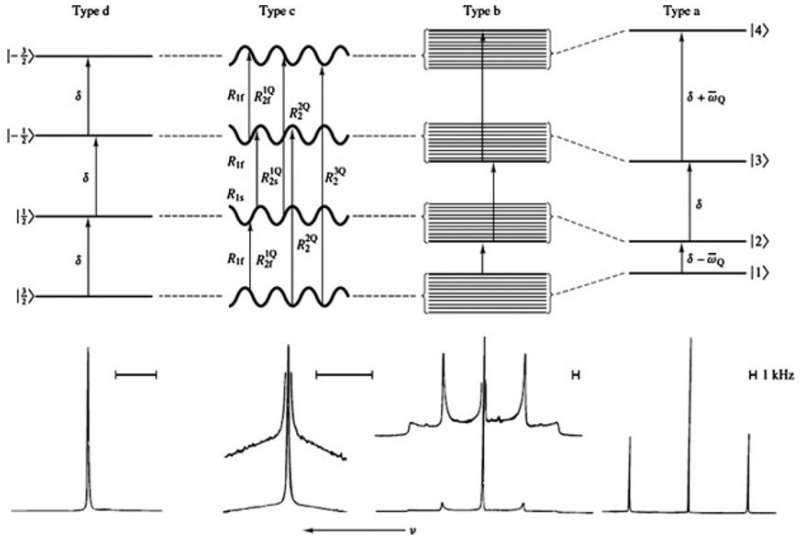

Figure 2.2: ^{23}Na energy levels as illustrated by Rooney et al. [5]

2.1.1.1 Application of an External Magnetic Field

The potential energy of a magnetic moment $\boldsymbol{\mu}$ in a magnetic field $\mathbf{B}$ is given by,

$$E = -\boldsymbol{\mu}.\mathbf{B} = -\gamma J_z B_0 \tag{2.4}$$

therefore for ^{1}H with two energy states $E_{+\frac{1}{2}} = -\gamma\hbar\frac{B_0}{2}$ and $E_{-\frac{1}{2}} = +\gamma\hbar\frac{B_0}{2}$, the energy dif-

ference between the levels will be $\Delta E = \gamma\hbar B_0 = \hbar\omega$. Applying electromagnetic radiation at frequency, ω, will cause a transition between the spin states.

So far only a single spin has been considered in a bulk ensemble, i.e in the body, there are many spins present, and the net magnetisation, $\mathbf{M}$, is the sum of all the individual magnetisations per unit volume V and is given by

$$\mathbf{M} = \frac{1}{V}\sum_i \boldsymbol{\mu_i}. \tag{2.5}$$

The spins will align with or against the applied magnetic field $\mathbf{B}$, and there must be a net population difference between these two states in order to produce a net magnetisation. The nuclei have an associated thermal energy which is large compared to the nuclei's magnetic potential energy, and the spin will tend to align with the magnetic field as represented in Fig.[2.3].

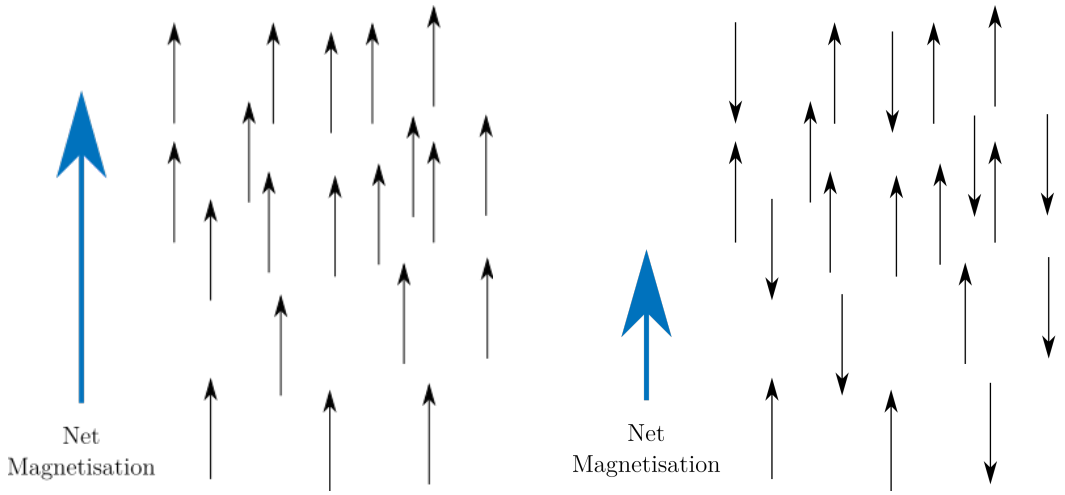

(a) An ensemble of spins at 0 K, all spins align with the applied magnetic, producing a large net magnetisation.

(b) When the spins are at body temperature, 310 K, fewer align with the external field, producing a smaller net magnetisation.

Figure 2.3: The effects of temperature on bulk magnetisation.

The population of the different energy states is given by the Boltzmann distribution,

$$\frac{N_m}{N} = e^{-\frac{E_m}{k_B T}} \Bigg/ \sum_{m=-I}^{I} e^{-\frac{E_m}{k_B T}} \tag{2.6}$$

$$= e^{\frac{m\hbar\gamma B_0}{k_B T}} \Bigg/ \sum_{m=-I}^{I} e^{\frac{m\hbar\gamma B_0}{k_B T}} \tag{2.7}$$

$$\approx \left(1 + \frac{m\hbar\gamma B_0}{k_B T}\right) \Bigg/ \sum_{m=-I}^{I} \left(1 + \frac{m\hbar\gamma B_0}{k_B T}\right) \tag{2.8}$$

$$\approx \frac{1}{2I+1}\left(1 + \frac{m\hbar\gamma B_0}{k_B T}\right) \tag{2.9}$$

where N_m is the number of spins the the mth energy state, k_B is the Boltzmann constant and T is the temperature in Kelvin and N is the total number of spins. In the body T is large and $m\hbar\gamma B_0/k_B T \ll 1$ allowing for the exponential component of Eq.[2.7] to be approximated as a first order Taylor expansion to achieve Eq.[2.8].

Eq.[2.9] can be used to calculate the population difference, n between the number of spins that align with (known as spin up $n_\uparrow$) and against (known as spin down $n_\downarrow$) the applied magnetic field. For ^{1}H with two energy states Eq.[2.9] becomes

$$n = \frac{N\hbar\gamma B_0}{2k_B T} \tag{2.10}$$

where N is the total number of nuclei. For ^{23}Na with the four energy states the population difference is

$$n = \frac{N\hbar\gamma B_0}{4k_B T}. \tag{2.11}$$

For protons at 3T and a body temperature of 310 K, the population difference is equivalent to roughly 10 ppm, small but measurable. At the same field strength and temperature for ^{23}Na the population difference would be approximately 1 ppm, but then it should also be considered that the concentration is small as outlined in Table [2.2].

When considering an ensemble of spins, they can be thought of classically with the net magnetisation lying along the axis of the external magnetic field B_0, by convention this is the z-axis.

2.1.2 Precession in a Magnetic Field

When nuclei are placed in a magnetic field, **B**, the magnetic moment experiences a torque to try to align it with the applied field. However, because of the angular momentum of the nuclei, the magnetic moment will also precess around the **B** field. The net torque and thus change in angular momentum is given by

$$\boldsymbol{\tau} = \frac{d\mathbf{J}}{dt} = \boldsymbol{\mu} \times \mathbf{B} = \mu B \sin\theta \tag{2.12}$$

and so

$$\frac{d\boldsymbol{\mu}}{dt} = \gamma \boldsymbol{\mu} \times \mathbf{B}. \tag{2.13}$$

This is describing precession where θ is the angle between the magnetic moment $\boldsymbol{\mu}$ and the applied field **B** as shown in Fig.[2.4]. Based on the geometry in Fig.[2.4] it can be shown that

$$dJ = J \sin\theta d\phi \tag{2.14}$$

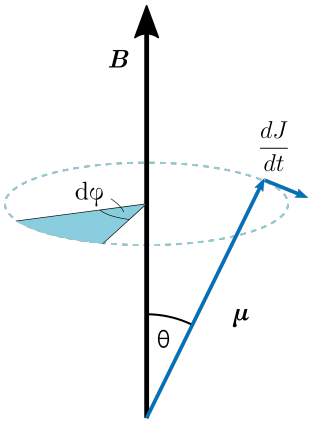

Figure 2.4: Geometry of precession.

and by defining the angular frequency of precession ω as

$$\omega = \frac{d\phi}{dt} = \frac{dJ}{dtJ\sin\theta} = \frac{\mu B \sin\theta}{J \sin\theta} \tag{2.15}$$

which from Eq.[2.1] gives the Larmor equation

$$\omega = \gamma B_0, \tag{2.16}$$

where the frequency of the precession, ω is known as the Larmor frequency. The gyromagnetic ratio for ^{1}H $\gamma = 42.57$ MHz/T and for ^{23}Na $\gamma = 11.26$ MHz/T. Therefore at the common MR field strength of 3T the Larmor frequency of ^{1}H is 128 MHz and that of ^{23}Na 34 MHz. Note for an ensemble of spins the magnetic moment can be replaced by the magnetisation vector $\mathbf{M}$ and so Eq.[2.13] can be written as

$$\frac{d\mathbf{M}}{dt} = \gamma \mathbf{M} \times \mathbf{B} \tag{2.17}$$

2.1.3 Excitation

In order to measure the net magnetisation $\mathbf{M}$, an additional external magnetic field, the B_1 field is applied perpendicular to the B_0 field. The B_1 field has two effects, it knocks the spins from alignment with the B_0 field and brings the precessing spins into phase. The B_1 field oscillates at the same frequency as the spins are precessing, the Larmor frequency. The B_1 oscillation frequency is in the range of radio frequency (128 MHz for ^{1}H and 34 MHz for ^{23}Na) and is only applied for a short period of time, therefore it is described as a radio frequency (RF) pulse. The angle through which the net magnetisation is knocked from the z-axis is known as the flip angle (FA). A 90° RF pulse will rotate the spins 90° and bring them into phase resulting in a net magnetisation in the x-y plane (Fig.[2.5]), whilst a 180° pulse will invert the spin population causing inversion of the magnetisation along the z-axis. By varying either the time the RF pulse is applied for (τ) or the magnitude of the $B_1(t)$ field, any flip angle (α) can be applied and this is described by

$$\alpha = \int_0^\tau \gamma B_1(t) dt. \tag{2.18}$$

For a constant B_1 amplitude, the flip angle α is given by

$$\alpha = \gamma B_1 \tau. \tag{2.19}$$

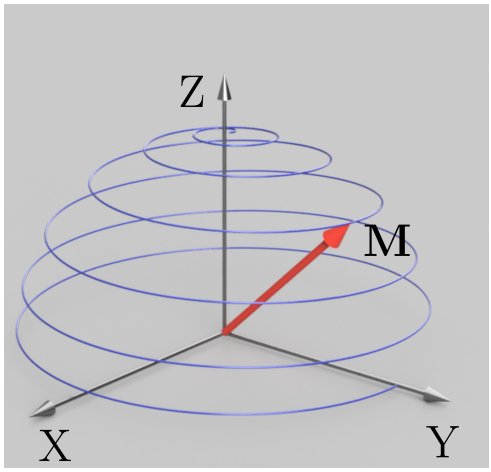

(a) The effects of a 90° RF pulse on the bulk magnetisation **M** (red arrow) as it is precesses from the z axis down into the x-y plane. This is shown in the laboratory frame. The blue spiral shows the path of the magnetisation **M** path as it continues to precess.

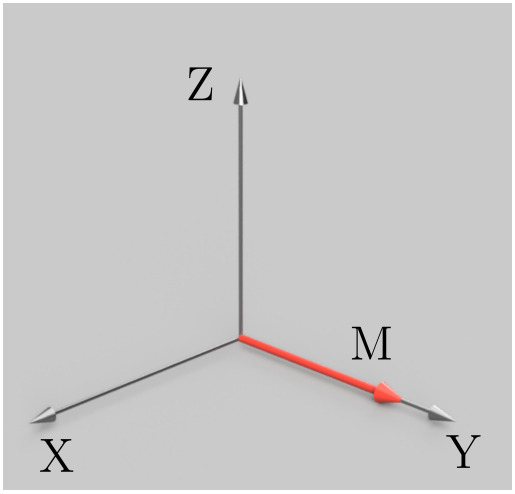

(b) The bulk magnetisation **M** immediately after a 90° RF pulse (in the x-y plane). This view is shown in the rotating frame of reference meaning the frame is rotating around the z-axis at the precessional frequency, so in this view the magnetisation is not precessesing.

Figure 2.5: The effects of an RF pulse on the bulk magnetisation shown from a) the laboratory frame and b) the rotating frame.

2.1.4 Signal Detection

Once a RF pulse has been turned off, the net magnetisation in the x-y plane will precess about the z-axis at the Larmor frequency. If a loop of wire or "coil" is placed near the precessing magnetisation, in keeping with Faraday's Law, an oscillating current will be induced in the wire. This induced current is the basis of signal detection in MRI and the simplest NMR signal is a Free Induction Decay (FID), as shown in Fig.[2.6].

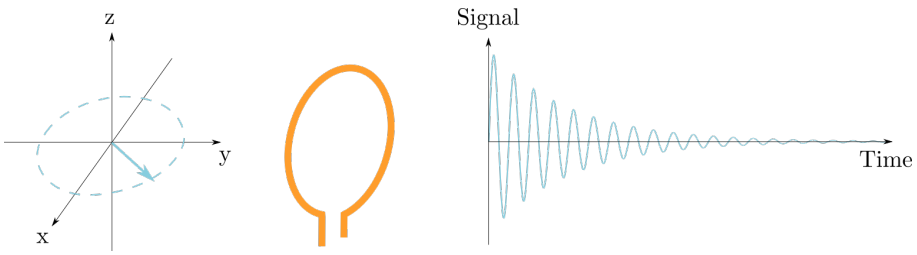

Figure 2.6: Signal detection.

The coils that apply and measure the RF fields are known as RF coils and either one RF

coil can carry out both the transmit and receive of the RF signals or two separate RF coils can be used, one to transmit and one to receive. RF coil design is covered in more detail in Section [2.3].

2.1.5 Relaxation

After the spins have been excited by an RF pulse, over time they will return to their equilibrium state, this is known as the process of relaxation. There are two components of relaxation described as the longitudinal and transverse components which are caused by differing effects. Felix Bloch deduced a set of equations that describe the behaviour of the magnetisation during and after an RF pulse, including relaxation. These are known as the Bloch equations and were principally given in the paper "Nuclear Induction" [31]. The rate of change of the magnetisation $\mathbf{M}$ is dependent on the applied magnetic field $\mathbf{B}$ and is given by

$$\frac{d\mathbf{M}}{dt} = \gamma \left|\mathbf{M} \times \mathbf{B}\right| \tag{2.20}$$

and when relaxation is included this is described by:

$$\frac{d\mathbf{M}}{dt} = \gamma \left(\mathbf{M} \times \mathbf{B}\right) - \frac{M_x\mathbf{i} + M_y\mathbf{j}}{T_2} - \frac{(M_z - M_0)\mathbf{k}}{T_1} \tag{2.21}$$

where T_1 and T_2 are the longitudinal and transverse relaxation time constants and M_x, M_y and M_z are the components of $\mathbf{M}$ in the x, y and z direction respectively.

2.1.5.1 Longitudinal Relaxation

Following an RF pulse, over time the excited spins will lose energy and return to thermal equilibrium, returning to align with the B_0 field. The excited spin's energy is transferred to the environment, the spin lattice, for this reason the longitudinal relaxation is also known as spin-lattice relaxation. Following a 90° RF pulse, the recovery of the longitudinal component of the magnetisation M_z back to its initial state M_0 is given by the solution to the Bloch equation, Eq.[2.22], which describes a saturation recovery.

$$M_z = M_0 \left(1 - e^{-\frac{t}{T_1}}\right) \tag{2.22}$$

where t is the time after the RF excitation pulse and T_1 is the longitudinal relaxation time constant. The longitudinal relaxation following a 90° RF pulse is shown in Fig.[2.7]. At a time $t = T_1$ the signal will have recovered to 63% of its initial value.

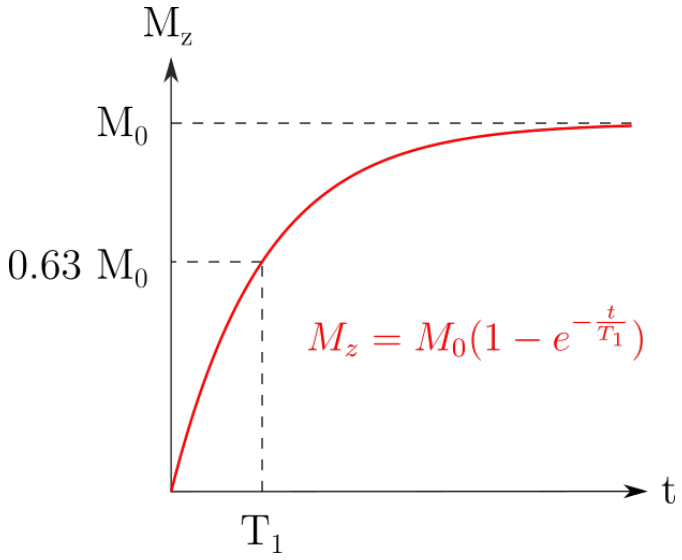

Figure 2.7: The recovery of longitudinal magnetisation following a 90° RF pulse.

Typically to measure T_1 a 180° inversion pulse is applied and the signal measured at differing inversion times (TI) are fit to an inversion recovery given by

$$M_z = M_0 \left(1 - 2e^{-\frac{t}{T_1}}\right). \tag{2.23}$$

The efficiency of energy transfer and thus the longitudinal relaxation time is dictated by the molecular motion of the lattice, leading to fluctuating magnetic fields in the local environment. If the fluctuations, characterised by the molecular tumbling rate, also known as the correlation time τ_c, are of a similar frequency to the Larmor frequency, then energy transfer via dipole-dipole interactions will be efficient, leading to a short T_1 as depicted in Fig.[2.8].

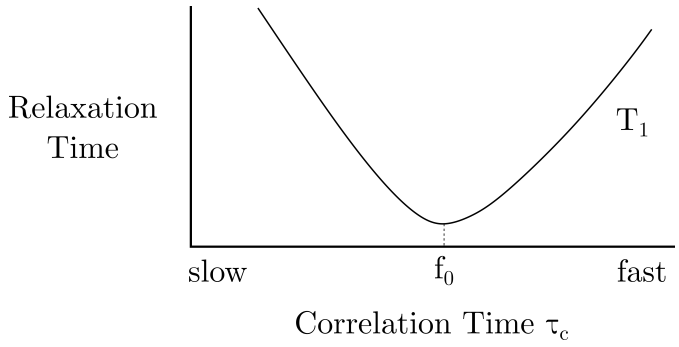

Figure 2.8: The relationship between correlation time and longitudinal relaxation time.

2.1.5.2 Transverse Relaxation

After a 90° excitation pulse, the spins will rotate from alignment with the B_0 field into the transverse plane, the spins precess about the B_0 in phase with each other, i.e. there is phase coherence. Over time this phase coherence will decrease, the most common reason is due to local magnetic field variations. The excited spins will precess around the B_0 field, at a frequency of precession governed by the Larmor equation and dependent on B_0, however individual spins will experience local deviations in the magnetic field strength. The different magnetic fields will cause the spins to precess at different frequencies to each other, and over time the spins will fall out of phase with each other and the net transverse magnetisation in the ensemble will reduce and M_{xy} will decay to zero. This evolution is shown in Fig.[2.9] and is described by transverse relaxation, with the time constant of transverse relaxation given T_2.

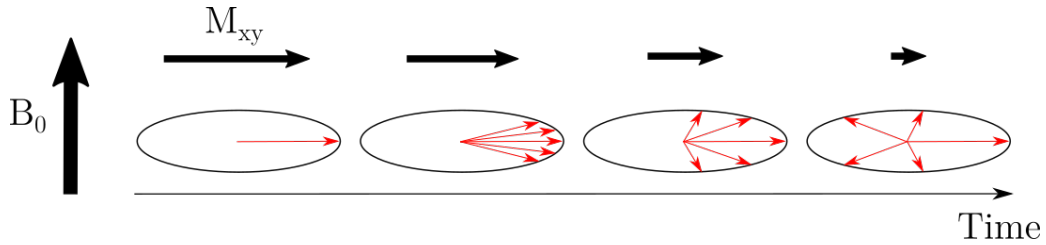

Figure 2.9: The evolution of the spins phase decoherence after a 90° RF pulse.

The transverse relaxation with time t is described as

$$M_{xy} = M_0 e^{-\frac{t}{T_2}} \tag{2.24}$$

where M_{xy} is the transverse magnetisation, M_0 is the magnetisation at $t = 0$. The rate constant for the transverse relaxation is T_2, i.e. the time it takes for the transverse magnetisation to fall to 37% $(1/e)$ of its initial value.

The relation in Eq.[2.24] is shown in Fig.[2.10].

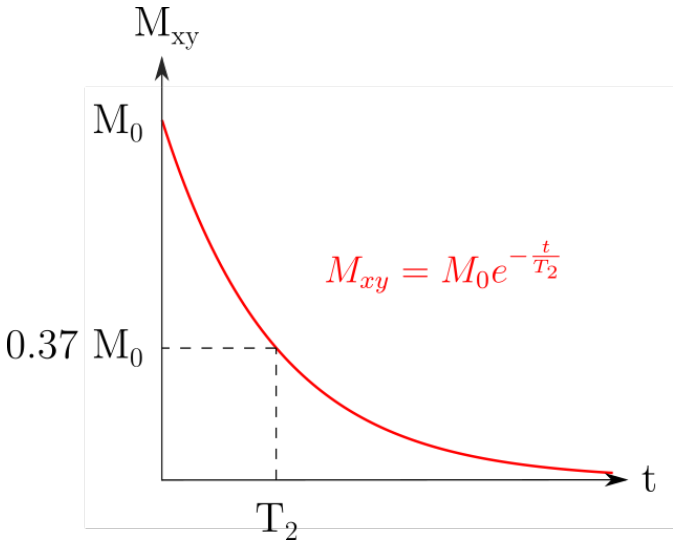

Figure 2.10: The decay of MR signal due to T_2 relaxation.

In practice, the transverse magnetisation decays faster than expected from local interactions alone, as there are inhomogeneities in the B_0 field either caused by magnet design or susceptibility effects produced by materials within the field. This additional effect is incorporated by the introduction of the parameter T_2' giving rise to a net transverse relaxation time constant T_2^*;

$$\frac{1}{T_2^*} = \frac{1}{T_2} + \frac{1}{T_2'} \tag{2.25}$$

which is the combination of the true T_2 and the additional relaxation time T_2'.

2.1.5.3 Bi-exponential decay

Unlike spin 1/2 nuclei such as hydrogen ^{1}H, spin 3/2 nuclei such as ^{23}Na have an asymmetric distribution of nucleons. This produces a non-spherical positive charge distribution which gives the nuclei an electric quadrupolar moment. The electric quadrupolar moment experiences strong interactions with surrounding electric field gradients [32]. These electric field interactions are in addition to the magnetic field interactions which cause signal

relaxation in a spin 1/2 nuclei system. The electric field interactions are stronger than the magnetic field interactions and are the main cause of relaxation in 3/2 nuclei and this causes a bi-exponential decay of both T_1 and T_2. However, the difference between the fast and slow component of the T_1 decay is close to indistinguishable, meaning that the T_1 decay is often treated as mono-exponential [33]. The bi-exponential decay of T_2 can be characterised by two components T_{2f} and T_{2s}, with the decay described by,

$$M_{xy} = M_0 \left(f_s e^{-t/T_{2s}} + f_f e^{-t/T_{2f}} \right) \tag{2.26}$$

where f_f and f_s are the fractions associated with the fast and slow component of the decay, typically 0.6 and 0.4 respectively.

Typical T_1 and T_2 relaxation values at 3T of ^{1}H and ^{23}Na in different tissues can be seen in Table [2.2]. The T_2 decay of ^{23}Na signal can be seen to occur very rapidly, this means that to achieve maximum SNR rapid image sequences have to be used, to acquire the signal before it has had chance to decay. The imaging sequences used for ^{23}Na are outlined in Section 2.2.2.

2.1.6 Quantification of Metabolite Concentrations

The Curie Law describes how the maximum measured MR signal S_0 is dependent on the number of spins N in the sample,

$$S_0 = \frac{N\gamma^2\hbar^2 I(I+1)B_0}{3kT} \tag{2.27}$$

where γ is the gyromagnetic ratio, $\hbar$ is Plank's constant, I is the nuclear angular momentum quantum number, B_0 is the applied magnetic field, k is the Boltzmann constant and T is the temperature. By considering N as a concentration C, then using Eq.[2.27] and collecting data on a calibration solution with concentration $C_{calibration}$, it is possible to estimate the concentration of a sample C_{sample} from the relationship

$$C_{sample} \approx C_{calibration} \frac{S_{0sample}}{S_{0calibration}} \frac{V_{calibration}}{V_{sample}}, \tag{2.28}$$

where $S_{0sample}$ and $S_{0calibration}$ is the measured MR signal for the sample and the calibration solution respectively. V_{sample} and $V_{calibration}$ are the corresponding volumes.
Thus the relationship in Eq.[2.28] allows the pixel intensities in a MR image to be converted to an equivalent ^{23}Na concentration if a calibration solution of known concentration is also imaged. Thus for work in this thesis, bottles with known ^{23}Na $C_{calibration}$ are imaged at the same time as the sample of interest (leg or abdomen) $S_{0sample}$. Eq.[2.28] is then used to calculate C_{sample} to provide the tissue sodium (^{23}Na) concentration (TSC). In order for Eq.[2.28] to be true, the calibration solution and the sample must be in the same B_0 and B_1 fields, or any differences in these fields must be corrected for prior to quantification. Similarly consideration needs to be taken to ensure that the calibration solutions MR properties' are the same, or are corrected for, such as their differing relaxation times T_1 and T_2. These effects are explored in Chapter 4.

2.2 MR Image Formation

2.2.1 Encoding

Once spins have been excited, they will generate a bulk signal and this then needs to be spatially located to generate an image. This is done by encoding the spins location within a sample using magnetic field gradients, these are denoted by G_x, G_y and G_z:

$$G_x = \frac{dB_z}{dx}, G_y = \frac{dB_z}{dy}, G_z = \frac{dB_z}{dz}. \tag{2.29}$$

Traditionally spatial encoding is performed by three techniques: slice selection, frequency encoding and phase encoding.

2.2.1.1 Gradients

In addition to the main magnetic field B_0 and the RF coils, there is a third source of magnetic fields inside the MR scanner, gradient coils. The gradient coils produce linearly varying magnetic fields in three perpendicular directions within the scanner. A gradient

field, G_r, produces a spatial variation in the B_0 field at a position r given by

$$B(r) = B_0 + G_r r. \tag{2.30}$$

This spatial variation in the B_0 field will produce spatial variations of the Larmor frequency in the scanner, with the accompanying Larmor equation Eq.[2.16] given by

$$\omega = \gamma \left(B_0 + G_r r \right). \tag{2.31}$$

Within the scanner there are three sets of gradient coils, G_x, G_y and G_z allowing a gradient field to be applied in any arbitrary direction. The spatial variation of the spins Larmor frequency can be used to distinguish between MR signals from different spatial positions.

2.2.1.2 Slice Selection

The first step in the spatial encoding process is slice selection. Slice selection uses an RF pulse applied at the same time as a gradient, G_z, to excite a set of spins in a two-dimensional plane or slab. Applying a gradient in a given direction will introduce a frequency variation in that direction. By applying an RF excitation pulse with a small range of frequencies, bandwidth of $\Delta\omega$, this RF pulse will only affect spins that are precessing in that frequency range. The magnitude of the gradient, G_z, and the centre frequency and bandwidth of the RF pulse can be adjusted to select the position and thickness of the excited slice, with the slice thickness being given by:

$$\Delta z = \frac{\Delta\omega}{\gamma G_z} \tag{2.32}$$

This is depicted in Fig.[2.11a]. An RF pulse with a bandwidth ($\Delta\omega$) is made by modulating the amplitude of an RF pulse of a single frequency (at the centre of the desired frequency range) with a commonly a sinc function but others functions can also be used. In Fourier space, this is equivalent to convolving a top hat function covering the desired frequency range with the central frequency. To exactly excite the required frequency range the sinc pulse envelope would have to be infinitely long, however, in practice the

sinc pulse is truncated. To achieve a narrower frequency range and therefore a thinner slice a longer sinc pulse can be used, but the long pulse will in turn increase the echo time (TE), alternatively a higher gradient G_z can be applied to excite a thinner slice.

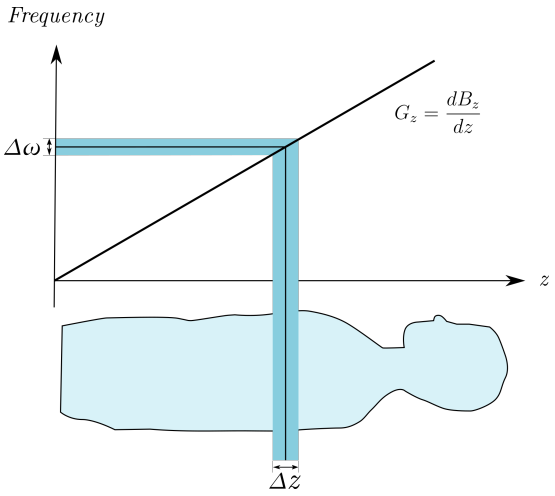

(a) Slice selection, the dark blue region is the slice (Δz) that is selected, the slice contains a range of frequencies ($\Delta\omega$) produced by the applied gradient field G.

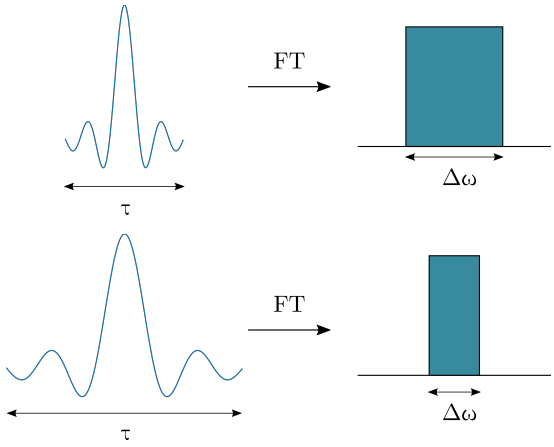

(b) The relationships between the pulse length (τ) and the range of frequency excited ($\Delta\omega$).

Figure 2.11: Slice selection.

After slice selection, only spins in a single slice of thickness Δz will have been excited by an RF pulse of centre frequency ω_0 and bandwidth $\Delta\omega$. This process can then be repeated for a different central frequency to select the adjacent slice, this process is termed multislice imaging.

Gradients can be used in a similar way as in slice selection to encode spatial information in plane using phase and frequency encoding.

2.2.1.3 Phase Encoding

Without any applied gradients and ignoring other T_2 effects following slice selection, the excited spins will precess at the same frequency, in-phase with each other. If a gradient G_y, is applied for a time τ across the spins; the spins will precess at different frequencies

$$\omega(y) = \gamma(B_0 + G_y y) \tag{2.33}$$

falling out of phase with each other, with the phase accrued being dependant on the magnitude and duration of the gradient given by

$$\phi(y) = \gamma y \int_0^{\tau} G_y(t)dt \tag{2.34}$$

This is know as phase encoding. Once the gradient is removed the spins will return to precessing at the same frequency. However, the phase difference introduced by the previously applied gradient will remain.

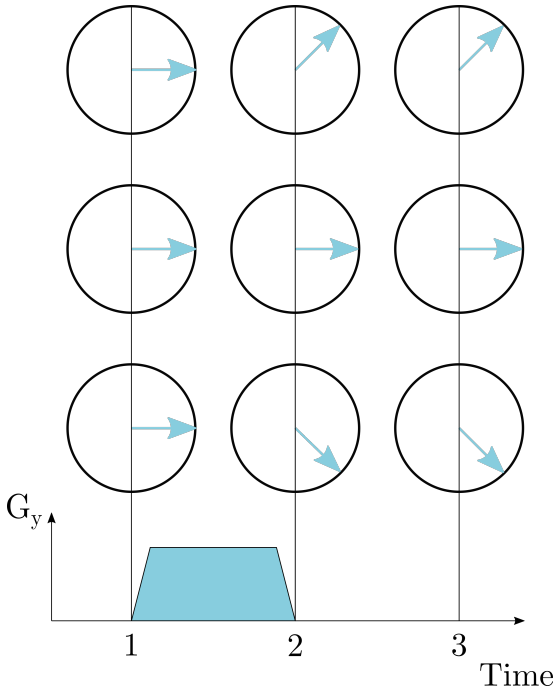

Figure 2.12: Phase encoding of spins using a gradient G_y. At time 1, with no gradient applied the spins are in phase. The gradient is applied for a time τ between 1 and 2 and acts to dephase the spins. At time 3 the phase difference remains and the spins precess at the same frequency.

Phase encoding takes place after the excitation and slice selection and before the acquisition and frequency encoding. In order to gather sufficient information about the spin's spatial location using phase encoding the acquisition is repeated, using different G_y magnitude each time.

2.2.1.4 Frequency Encoding

A gradient G_x can be applied to produce a position dependent variation of the spin frequency, hence the name frequency encoding. If the RF signal is measured (read out) while the frequency encoding gradient is applied, the acquired signal will contain a summation of all the spins precessing at different frequencies. A Fourier transform of the measured signal will separate out the individual frequencies. As this gradient is applied when the signal is being measured, it is referred to as the readout gradient.
By applying a range of different strength frequency and phase encoding gradients, enough spatial information can be collected about the received MR signals to allow an image to be formed as described below.

2.2.1.5 K-space

The MR image data is stored in a two-dimensional matrix known as k-space, values in k-space correspond to the spatial frequency of the MR image. The columns ($\mathrm{k}_x(t)$) in k-space correspond to the frequency encoding gradient direction, the rows ($\mathrm{k}_y(t)$) correspond to the phase encoding gradient direction. Due to the application of gradient fields the measured signal $S(t)$ is given by

$$S(t) = \iint m(x,y)e^{-i2\pi[k_x(t)x+k_y(t)y]}dxdy \tag{2.35}$$

where

$$k_x(t) = \frac{\gamma}{2\pi}\int_0^t G_x(\tau)d\tau \text{ and } k_y(t) = \frac{\gamma}{2\pi}\int_0^t G_y(\tau)d\tau. \tag{2.36}$$

This shows that the signal is a Fourier transform of the magnetisation ($m(x,y)$), and

$$f(x,y) = \int_{-\infty}^{\infty}\int_{-\infty}^{\infty} F(k_x,k_y)e^{-i2\pi[k_xx+k_yy]}dk_xdk_y \tag{2.37}$$

where $f(x,y)$ is the MR image and $F(k_x,k_y)$ is k-space. A 2D Fourier transform of the k-space thus produces the MR image. Different parts of k-space correspond to different spatial frequencies, for example the centre of k-space corresponds to the low spatial frequency components of the MR image, e.g. large structures and contrasts. The outer parts

of k-space corresponds to the high spatial frequency components such as edges and fine details, as demonstrated in Fig.[2.13].

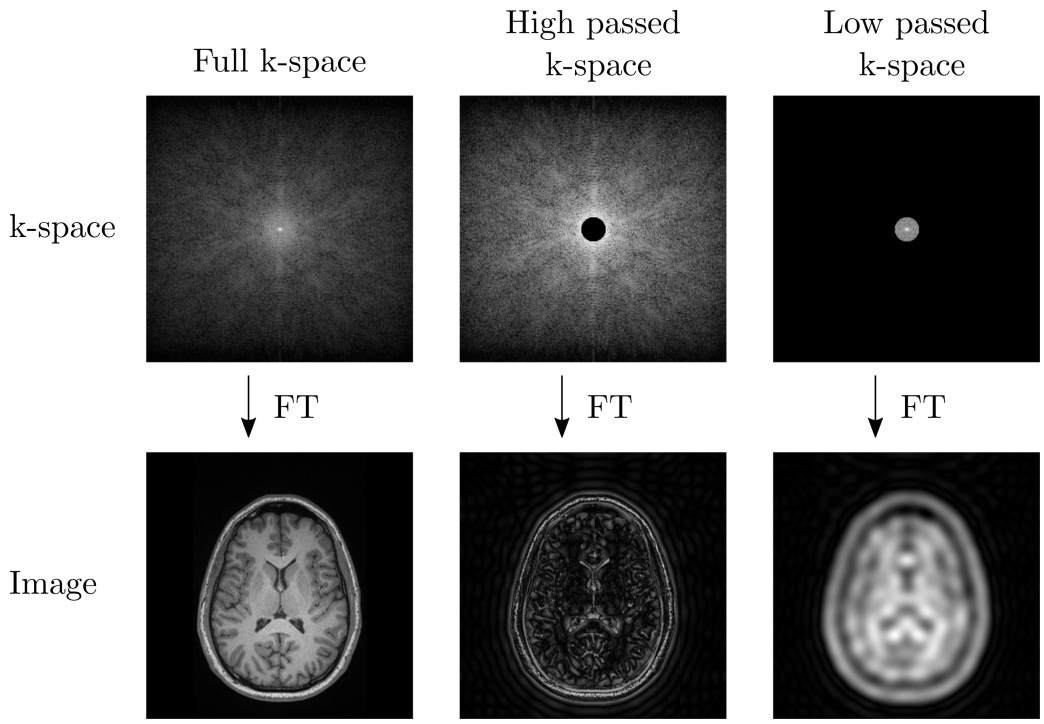

Figure 2.13: ^{1}H images of the brain showing the contributions of regions in k-space to the MR image.

2.2.2 Image Acquisition Pulse Schemes

Different image acquisition schemes use different combinations of gradients to populate k-space. Advances have improved spatial resolution resulting in shorter acquisition times with faster switching and shorter transmit-receive delays. The following section covers the sequences used within this thesis for ^{23}Na imaging, which can be separated into those which employ cartesian and non-cartesian imaging schemes, and those sequences collected for accompanying ^{1}H imaging.

2.2.2.1 Gradient Recalled Echo (GRE)

One category of techniques most suitable for collecting ^{23}Na images is that of a gradient recalled echo (GRE). A basic GRE sequence is shown in Fig.[2.14] and comprises of an RF excitation pulse and each of the spatial encoding gradient pulses ($G_{slice}, G_{phase}, G_{frequency}$).

Once the precessing spins have been excited through slice selection, applying a frequency gradient will cause the spins to fall out of phase with each other and they will dephase. If the same gradient is then applied in the opposite direction the spins will come into phase with each other forming an echo at $k_x = 0$, as demonstrated in Fig.[2.14]. The echo is sampled for both the negative and positive side of k_x. The whole process is then repeated for a range of different phase encoding gradients, typically applied at the same time as the negative frequency encoding gradient, as shown in Fig.[2.14]. This allows k-space to be filled in a cartesian fashion. To avoid transverse magnetisation coherence from previous excitation pulses, the repetition time (TR) of the GRE sequence needs to be long enough for the signal to decay to nearly zero through T_2 decay. Alternatively, typically the transverse magnetisation is disrupted by applying spoiling. Gradient spoiling is performed by applying an additional gradient before the next excitation as shown in Fig.[2.14a], or RF spoiling can be used by changing the phase of the RF pulse from TR to TR.

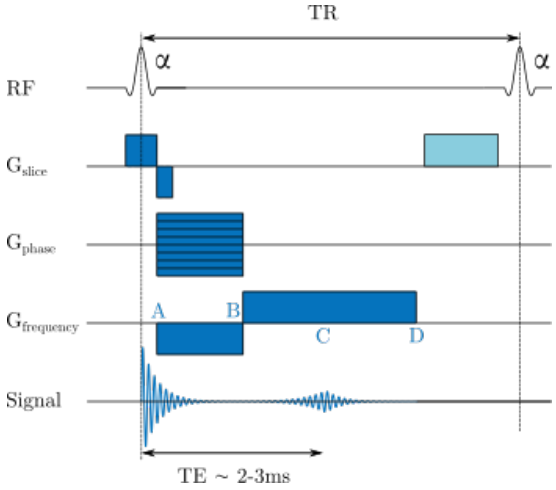

(a) A basic 2D GRE echo sequence, spoilers are often added to GRE sequence shown here as an additional gradient pulse (light blue) after the read gradient. Alternatively RF spoiling which changes the phase of the RF pulse between TR periods can be used.

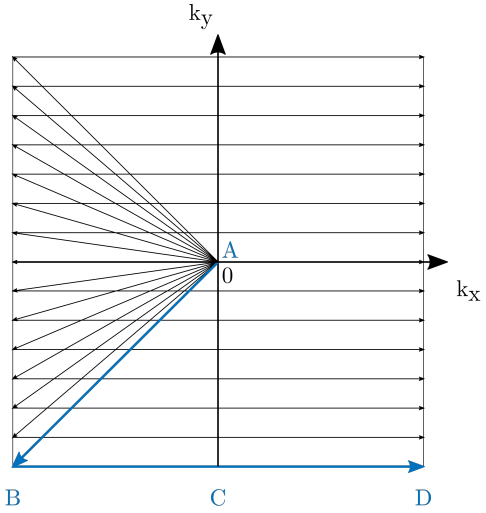

(b) The k-space sampling trajectory for a GRE acquisition.

Figure 2.14: Pulse sequence diagram and k-space sampling of a GRE acquisition.

To extend the image acquisition to acquire a volume, the 2D GRE scheme can be repeated using slice selection to excite different slices and build up a 3D volume. Alternatively, in

3D GRE an additional gradient is applied in the z-direction to produce additional phase encoding in that direction as shown in Fig.[2.15]. Slice selection can still be applied to instead excite a volume known as a slab, the additional phase encoding allows for multiple slices to be reconstructed within the slab. As the slice selection is used to excite a larger volume than a single slice, a shorter RF pulse can be used, reducing the TE. This can be taken further by not applying any slice selection and using a non-selective pulse to excite the whole volume. The sensitivity profile of the RF coil is then used to restrict the region over which signals are acquired. A 3D GRE scheme is used for ^{23}Na imaging described in Chapters 4 and 5, whilst a 2D GRE for ^{1}H imaging is used in Chapter 6.

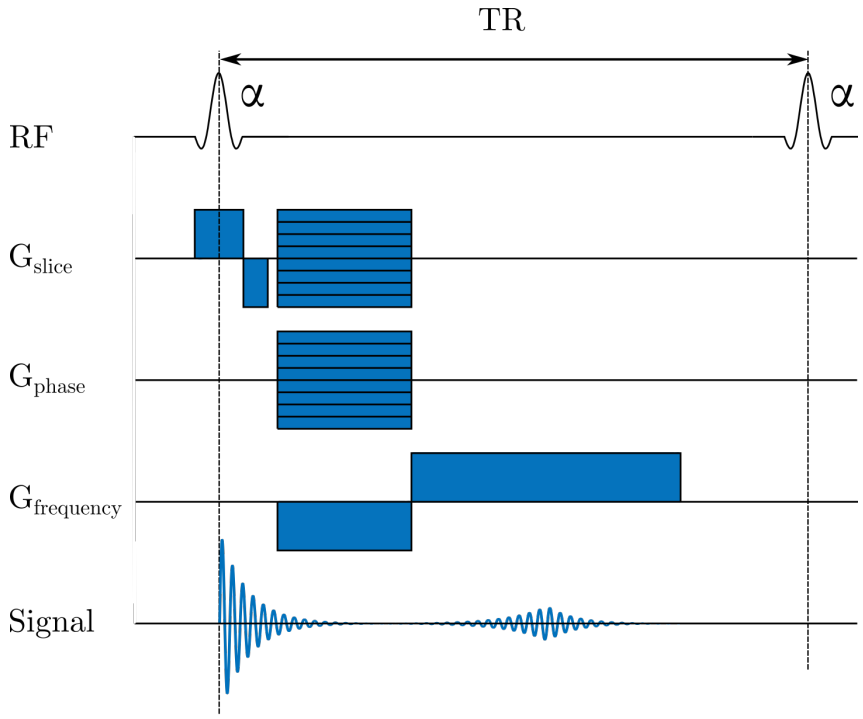

Figure 2.15: A 3D GRE imaging sequence, similar to Fig.[2.14a] but with additional phase encoding gradient in the slice select direction.

2.2.2.2 Ultra-short TE (UTE)

With the very short transverse relaxation time of ^{23}Na (see Section [2.1.5]) the image acquisition used should have the shortest echo time (TE) possible. A GRE sequence typically has a TE of 2-3 ms, limited by the time it takes to carry out the phase encoding and form the echo. To reduce the TE further the phase encoding gradient can be removed,

and the gradients in both the x and y direction are used to frequency encode the spins. Instead of producing and acquiring an echo the initial free induction decay (FID) is sampled immediately after the RF pulse, achieving TEs of < 1 ms (limited by the pulse length and hardware delays). This sequences is described as an ultra short echo time (UTE) scheme. When comparing these TEs to the T_2 values in Table [2.2] it can be seen that the UTE is most suited to capturing the shortest T_2 tissues. UTE sequences sample k-space from the centre out, the sample points are located on lines known as radial spokes. The gradients can be used to provide a number of different trajectories that the spokes can take to sample k-space. The simplest 2D trajectory is achieved by applying fixed gradients in the x and y directions to produce a straight spoke, sampling k-space from the centre out. This is then repeated at a range of spoke angles to produce a 2D star pattern. To sample 3D space, phase encoding can be applied in the z-direction and the radial stars are stacked up, as shown in Fig.[2.17a]. This technique is known as stack of stars (SOS).

The radially sampled data points can subsequently be interpolated onto a rectangular matrix and a conventional 2D Fourier transform can be used to form an image.

To achieve a true UTE sequence and shorter TEs, frequency encoding is carried out in all three directions, x, y and z, see Fig.[2.16b]. This moves the spokes in three dimensions and as is done in the Kooshball technique, where the straight spokes are arranged in spiral interleaves, the ends of the spokes form the surface of the sphere, Fig.[2.17b]. The Kooshball can produce a shorter TE than SOS as there is no phase encoding gradient. However, with both SOS and Kooshball, k-space is sampled non-uniformly and so to ensure sufficient sampling of the higher frequencies many spokes have to be collected increasing the scan time. In practice, full coverage using centre-out of an $n \times n$ image requires $n\pi$ acquisitions. A consequence of this is that there is a higher sampling density of the lower spatial frequencies than the higher spatial frequencies which leads to better SNR in the images.

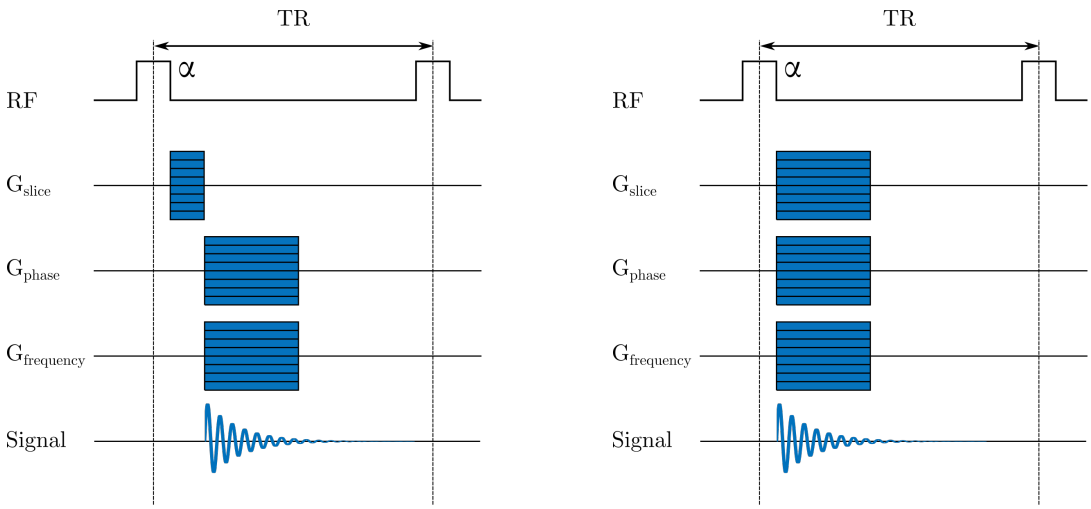

(a) UTE SOS (b) 3D koosh

Figure 2.16: Two UTE pulse sequences.

Beyond Kooshball, other sampling techniques aim to improve time efficiency by ensuring that k-space is sampled uniformly, these are namely twisted projection imaging (TPI) [34], density-adapted 3D projection reconstruction (DA-3DPR) [35] and 3D cones trajectories [36]. For example, 3D cones uses a short straight radial section to move rapidly away from the centre of k-space, the spokes then twist and move out in a spiral pattern. These spirals are projected into cones to sample 3D space, Fig.[2.17c]. These techniques are currently not routinely available on clinical platforms.

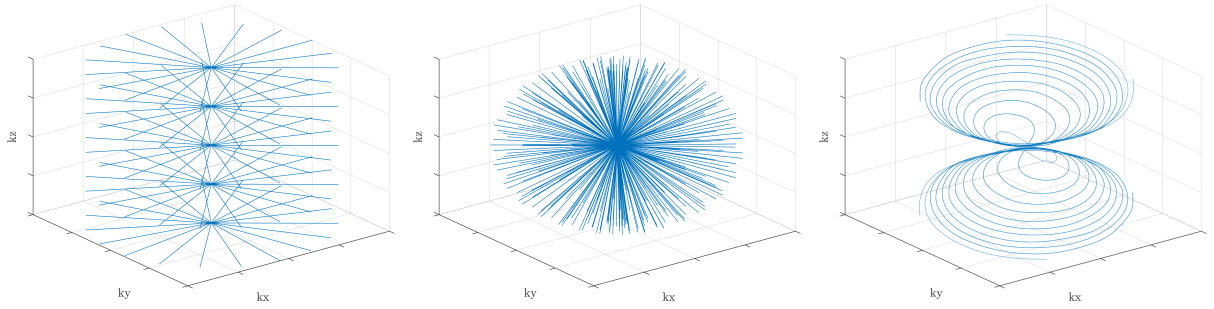

(a) Stack-Of-Stars. (b) Kooshball. (c) A single set of Cones trajectories.

Figure 2.17: Example UTE sampling trajectories.

Spatial resolution is equated differently in Cartesian and non-Cartesian imaging schemes. In Cartesian imaging the resolution of the scan is dictated by the voxel size, however in non-Cartesian imaging a voxel's signal can contribute to the neighbouring voxel's signal, as

the point spread function (PSF) of non-Carteison imaging extends beyond the boundaries of each voxel, [37]. This wider PSF is a consequence of collecting only a spherical representation of a cubic k-space, and can widen the PSF by approximately 40% [34, 38–40]. This will be discussed in Chapter 4 where 3D GRE and 3D UTE schemes are compared.

2.2.2.3 Spin Echo

Alternatively, an echo can also be formed by using an additional 180° RF pulse to generate a spin echo. After the initial 90° excitation RF pulse has tipped the spins into the transverse plane, the spins will begin to dephase, as the spins precess at different frequencies. If a 180° RF pulse is applied it will flip the spin system, changing the direction of the spins thus rephasing to generate an echo. The formation of a spin echo and a spin echo pulse sequence can be seen in Fig.[2.18]. The spin echo follows a T_2 decay unlike the GRE which follows T_2^* decay. This is due to the 180° RF pulse reversing the effects of static local field distortions, e.g. B_0 inhomogeneity.

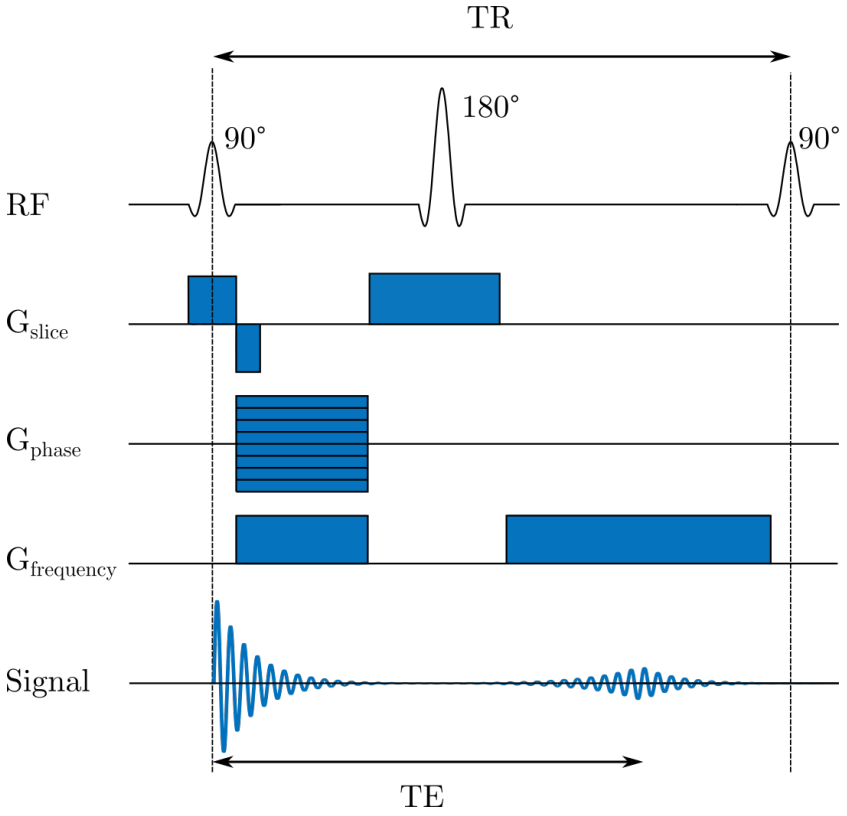

Figure 2.18: A typical SE sequence.

2.2.2.4 Multi-Echo Spin Echo

A multi echo spin echo (ME-SE) sequence is used in Chapter 6 of the thesis for ^{1}H imaging of the skin. A pulse sequence timing diagram for a ME-SE scheme is shown in Fig.[2.19]. A standard multi-echo spin echo imaging sequence follows the same structure as a spin echo, as described in Section [2.2.2.3], but has repeated 180° refocusing pulses following a single 90° excitation pulse. Thus repeated spin echoes are measured from a common excitation pulse to generate a single phase-encoding line of k-space. All phase-encoding steps are then performed with the same multi-echo acquisition, from this an image can be reconstructed at each echo time (TE). Often, a ME-SE acquisition collects the later TEs at a multiple of the first TE, as is implemented in Chapter 6, though this is not a requirement, and typically a TR of $\sim$ 2,000 ms is used.

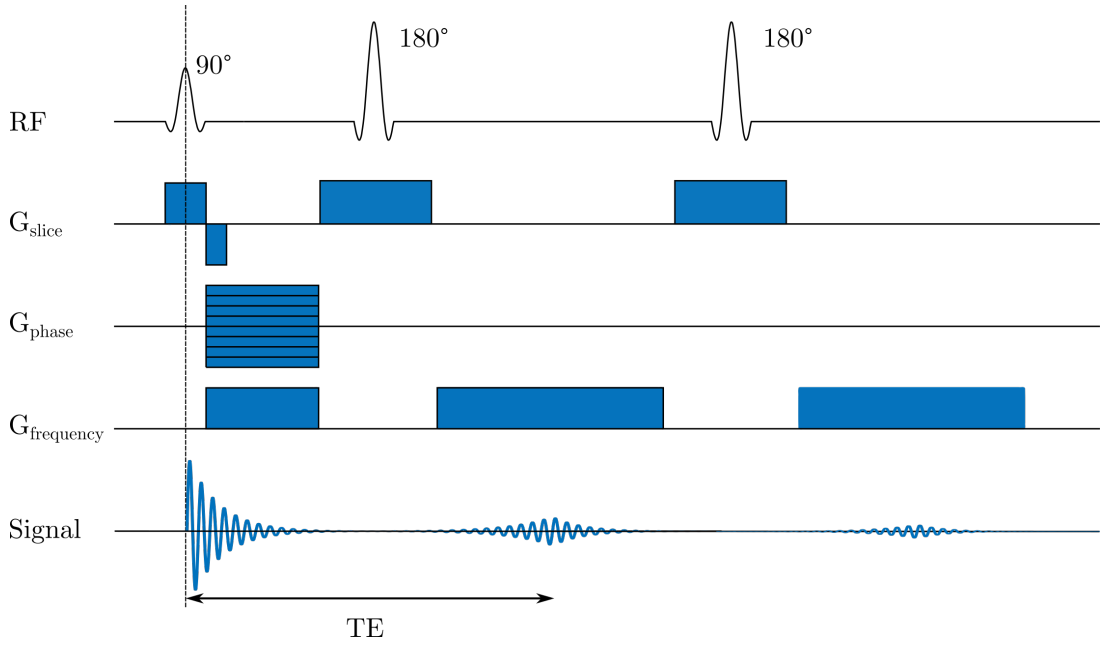

Figure 2.19: Multiple-echo spin-echo pulse sequence timing diagram illustrated here for two echoes. Multiple refocusing RF pulses are used to produce multiple echoes, each echo is detected in the presence of a constant amplitude readout gradient. Note in Chapter 6 this scheme is implemented with eight echoes.

2.2.2.5 Dixon Method

Chemical shift is the small change in resonant frequency introduced by the nuclei's molecular environment. The Dixon method [41] utilises the chemical shift difference of ^{1}H between fat and water, which is 3.5 ppm or 440 Hz at 3 Telsa. Due to this chemical shift

effect, the protons in water and fat precess at slightly different frequencies. By selecting an appropriate echo time (TE), images can be collected with the fat and water spins in-phase or out-of-phase with each other. In Chapter 4 a dual echo acquisition is used. Dixon suggested that the combination of these images can produce separate images of fat and water. The in-phase signal (S_{ip}) is a sum of the water signal (S_w) and fat signal (S_f),

$$S_{ip} = S_w + S_f \tag{2.38}$$

and the out-of-phase S_{of} is the difference

$$S_{of} = S_w - S_f. \tag{2.39}$$

by summing the in-phase and out of phase images the fat and water signal can be separated

$$S_{ip} + S_{of} = (S_w + S_f) + (S_w - S_f.) = 2S_w \tag{2.40}$$

$$S_{ip} - S_{of} = (S_w + S_f) - (S_w - S_f.) = -2S_f \tag{2.41}$$

Example images can be seen in Fig.[2.20].

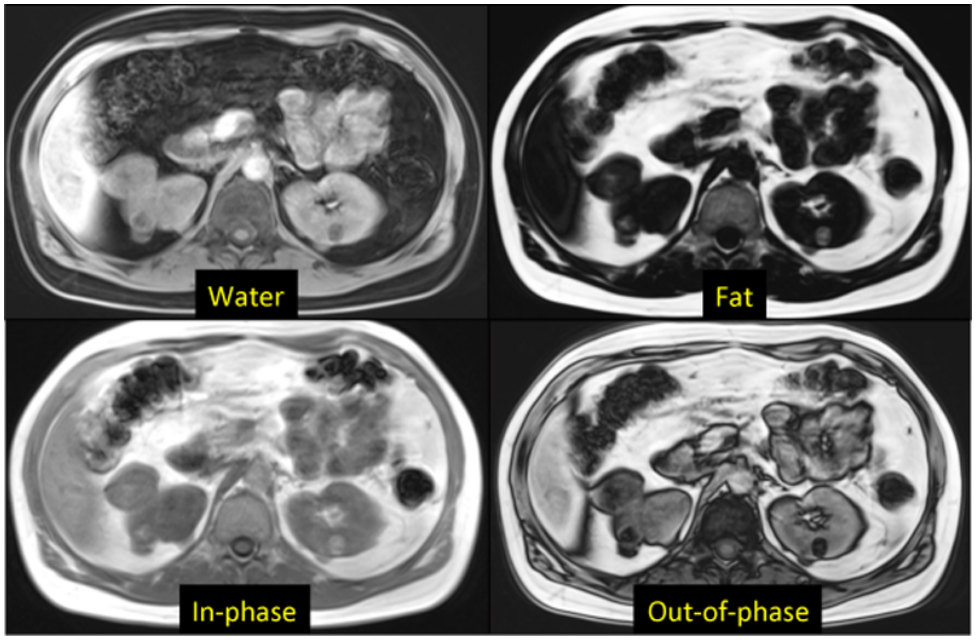

Figure 2.20: Example Dixon image showing the different image types. Source: http://mriquestions.com/dixon-method.html

More than two echo times can be used to allow for correction of B_0 inhomogeneities, the Philips system provides this as a multi-point six echo Dixon know as a mDixon scan which is used in Chapter 4.

2.3 Radiofrequency coils

At the time that work in this thesis commenced there were no RF coils available for ^{23}Na imaging, thus RF coils had to be built, and designed in collaboration with RF coil suppliers. The following sections outline the RF coil designs and the concepts of RF modelling that must be performed to ensure safety requirements are met prior to RF coil use.

2.3.1 Type of Coils

There are numerous RF coil designs, each with different features and functionality. The section below will provide an introduction to the different RF coil types, specifically focusing on those types used in this thesis.

In MRI, RF coils provide two functions: firstly, that of excitation to produce a B_1 field to flip the spins into the transverse plane, secondly, detection, to pick up the RF fields produced by the precessing spins. These two functions can be done separately by two sets of coils, a transmit coil (Tx) and a receive coil (Rx). Alternatively, one RF coil can both transmit and receive the RF signal, this is termed a transmit-receive coil (TxRx). The principle of reciprocity states that the field profiles for a coil are the same for both the transmit and receive fields.

2.3.1.1 Surface Coils

The simplest RF coil is a loop of wire placed next to the region that is to be imaged. The loop will produce an inhomogeneous B_1 field, with the maximum at the centre of the coil which rapidly decreases with distance away from the coil. This is the origin of the name surface coil; the coil must be placed as close as possible to the region being imaged to

maximise the signal.

The B_1-sensitive region of a surface coil is said to be approximately a hemisphere equal to the radius the coil. The radius of the coil can be selected depending on the anatomical region of interest. The larger the coil the larger the area the B_1 field will cover, although a larger coil will need more power to achieve the required flip angle when the coil is transmitting. When receiving a larger coil will also receive more noise [42].

To increase the limited field of view produced by a single loop surface coil and maximise the high SNR associated with a small surface coil, multiple loops can be used together to produce a phased array coil. This is enabled by incorporating techniques to decouple the individual coils' mutual inductances and thus reduce crosstalk between the loops. Phased array coils can provide a receive coil with a high SNR covering a large field of view.

2.3.1.2 Volume Coils

Volume coils are used to achieve a homogeneous B_1 field. The most common volume coil design is that of the birdcage coil [43]. The 3T Philips MRI scanners have a ^{1}H birdcage coil built into the bore of the scanner. Surface and volume coils are often used in conjunction with each other; with the volume coils providing a homogeneous transmit field whilst a surface coil is placed close to the imaging region to receive the MR signals. When using a transmit-receive coil, a transmit/receive (T/R) switch is used to ensure that the high currents used when transmitting RF do not damage the sensitive receive equipment.

2.3.2 The LCR circuit

RF coils come in a wide range of designs each tailored for specific use and anatomical region, but all coils rely on one common principal of resonance. A resonant circuit consists of a inductance component, L, capacitance component, C, and resistive component, R, see Fig.[2.21].

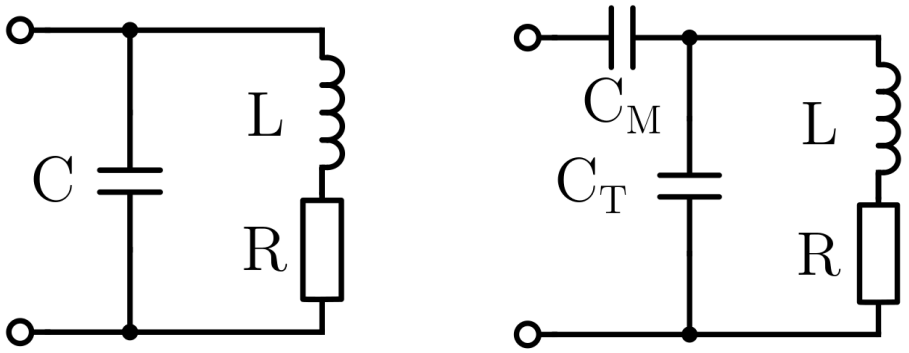

(a) The parallel LCR circuit, the capacitor (C) is in parallel with in the inductor (L) and the resistor (R)

(b) The LCR circuit including a matching capacitor (C_M) in addition to the tuning capacitor (C_T)

Figure 2.21: The LCR circuit.

The inductance is produced in the loop of wire in which the emf is induced in, the resistance in the circuit comes from the inherent resistance in the wires and the components. The capacitance is introduced by adding a capacitor to the circuit. The electrical reactance of the inductor is $X_L = i\omega L$, where ω is the angular frequency of the current and L is inductance. The electrical reactance of the capacitor is $X_c = i/\omega C$ where C is the capacitance. At the frequency at which the reactances compensate each other, a sharp frequency response is produced, this is the circuit's resonance frequency ω_0 and is given by

$$\omega_0 = \frac{1}{\sqrt{LC}} \tag{2.42}$$

By careful selection of the size of the capacitor or amount of inductance used in the circuit, the coil can be tuned to resonate at the Larmor frequency of the nuclei of interest.

In order to both transmit and receive signals, the coil has to be connected to the MRI scanner. Both the amplifiers and the co-axial cables connected to the scanner will have a characteristic impedance of 50Ω. In order for efficient transfer of the signals to and from the coil, the impedance of the coil must also be as close as possible to 50Ω. This can be achieved by adding an additional capacitor in series with the input, this is described as a matching capacitor and is designed to match the impedance of the coil to that of the rest of the system, Fig.[2.21b].

When a coil is placed on the human body, mutual inductance takes place been the coil and the body. This changes the total inductance of coil and can adjust both the tuning and matching of coil, and so must be taken into account when designing the coil. The amount of loading the coil experiences depends on the anatomical region being imaged and can be approximated by using a phantom, as detailed in Chapter 3 Section [3.3].
The tuning and matching of a coil can be evaluated by measuring the reflection coefficient. This is done by applying an RF signal to the coil and measuring the amount of signal reflected. When the impedance of the coil matches the impedance of the load the reflected signal is minimised. By measuring the reflected signal across a range of applied signal frequencies, the coil's resonant frequency can be ascertained. An example of a measured reflection coefficient can be seen in Fig.[2.22].

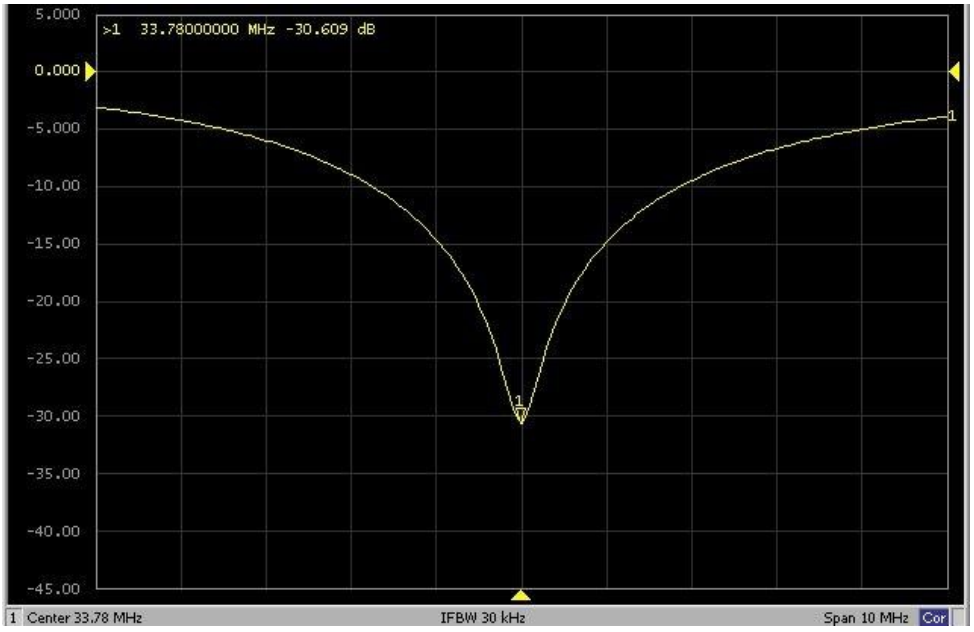

Figure 2.22: Example measurement of the reflection coefficient, the results are displayed on a log scale. The curve here shows that the coil is tuned and matched at 33.78 MHz for ^{23}Na imaging.

2.3.3 Specific Absorption Rate (SAR)

The oscillating B_1 fields can deliver enough power in the body to cause a temperature change in the tissue. The amount and distribution of the power delivered into the body must be carefully monitored to ensure no damage to the subject is caused. The main

mechanism that produces the heating effect is Ohmic heating, which arises due to the electrical conductivity of the tissue. The RF fields induce electrical currents in the tissue, and the energy from the induced currents is transformed into heat [44]. The amount of energy deposited into the tissue is quantified as the specific absorption rate (SAR), which is the rate at which power is deposited into the tissue per mass of tissue, given in W/Kg. At any one point in tissue, the SAR depends on the electric field component, **E** of the RF field, and is given by

$$SAR = \frac{\sigma \left|\mathbf{E}\right|^2}{\rho} \tag{2.43}$$

where σ and ρ are the conductivity and density of the tissue respectively. As there are numerous types of tissue in the body, each with different conductivity and density, assessing the SAR is a non-trivial task and requires computational simulation. There are limits on the SAR that a human body can be safely exposed to, these are outlined by the International Electrotechnical Commission in the document IEC 60601-2-33 [3], shown in Table [2.3]. The local SAR is defined as an average SAR over any 10g of tissue.

	Average SAR (W/kg)			Local SAR (W/kg)		
Operating Mode	**Whole Body**	**Partial Body**	**Head**	**Head**	**Trunk**	**Extremities**
Normal	2	2 - 10	3.2	10 (c)	10	20
First Level Controlled	4	4 - 10	3.2	10 (c)	10	20
Second Level Controlled	>4	>(4 - 10)	>3.2	>10 (c)	>10	>20
Short term SAR	The SAR limit over any 10s period shall not exceed three times the stated values					

Table 2.3: SAR body limits given by IEC 60601-2-33 [3].

During an MRI sequence there will be several RF pulses applied to the body. Each of these pulses will contribute to the SAR in the body, the extent that they increase the SAR depends on the RF pulse's properties e.g. magnitude and duration in addition to the sequences' requirements e.g. TR. Therefore, the SAR needs to be calculated on a sequence by sequence basis, this is done by the MRI scanners software before each sequence is run to determine the sequence specific SAR to ensure no limits are exceeded. The software bases these calculations on a SAR scale, a ratio of peak SAR to $(B_1^+)^2$ for each coil the scanner uses. This scale is derived from computational modelling, the technique is

explained below and the method is covered in more detail in Section [3.2].

2.3.4 Finite-Difference Time-Domain Simulations

In this thesis, the Finite-Difference Time-Domain (FDTD) method is used to solve the pair of time-dependent Maxwell's "curl" Equations in order to calculate the RF electromagnetic field associated with each of the coils to collect ^{23}Na images of the human leg and abdomen (see Chapter 3).

In order to estimate the SAR scale for a coil, the EM fields produced by the coil must be modelled. This can be done using a Finite-Difference Time-Domain (FDTD) method [45]. In this, the simulation space is divided into a cartesian rectangular grid where each cell represents a material within the simulation space. The E fields are located at the edges of the cells and the B field on the cell's faces. Each cell shares its edges with its neighbouring cell therefore each cell is assigned three E fields at three edges and the remaining nine edges are owned by its neighbouring cells. The faces adjacent to the three E fields are assigned as the cells B fields. This arrangement is known as the Yee Cell [46], as shown in Fig.[2.23a].

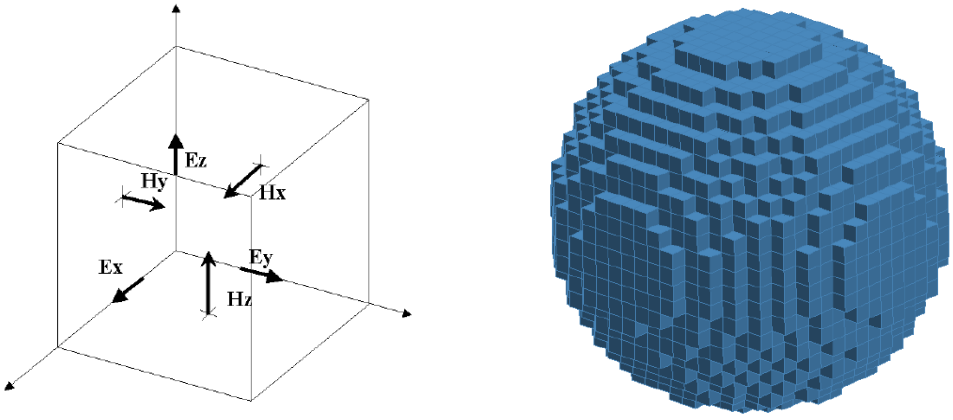

(a) A single YEE cell.

(b) Gridded ball showing hope the simulation space is divided in to Yee cells.

Figure 2.23: The YEE cell.

The FDTD simulation involves solving Maxwell's curl equations in the time domain for

each cell.

$$\nabla \times \mathbf{E} = -\mu \frac{\partial \mathbf{H}}{\partial t} \tag{2.44}$$

$$\nabla \times \mathbf{H} = \varepsilon \frac{\partial \mathbf{E}}{\partial t} + \sigma \mathbf{E} + \mathbf{J} \tag{2.45}$$

where **E** is the electric field strength vector, **H** is the magnetic field strength vector, **J** electric current density.μ, ε and σ are the permeability, permittivity and conductivity of the medium respectively. Each cell can have different electromagnetic properties to represent different materials such as conductors or dielectrics. The simulations solve the Maxwell's equations for E and H fields for every cell in the simulation. At each time point solving either the E field followed by the H field at the next time point, repeating in this fashion until a steady state is achieved.

2.4 B_1 Mapping Methods

To estimate the delivery of RF into tissues, B_1 mapping methods are required. This is further needed for ^{23}Na imaging to allow correction of the ^{23}Na images for quantitative evaluation of tissue sodium concentration (TSC) (see Section [2.1.6]).

There are two general categories of B_1 mapping: magnitude based and phased based measures. Magnitude based methods estimate the B_1 map from the magnitude image. Common magnitude based methods are the Double Angle (DA) method introduced by Insko and Bolinger in 1993 [47] and the Actual Flip Angle (AFI) method introduced by Yarnykh in 2007 [48]. In this thesis, the DA method is used.

In contrast, phase B_1 mapping uses the phase of the image, and this include methods such as the Spin Echo Phase-Sensitive (SEPS) method by Oh published in 1991 [49], and the Phase-Sensitive method in 2008 introduced by Morrell et al. [50], the latter is used in this thesis.

2.4.1 Gradient Recalled Echo Double Angle (DA) B_1 mapping

The double angle B_1 mapping method is a magnitude mapping method which measures the B_1 by comparing the ratio of two gradient recalled echo (GRE) images [47]. The first image is collected with a nominal flip angle α with the signal magnitude being given by

$$S_1 = A\sin(\alpha). \tag{2.46}$$

The second image is acquired with a nominal flip angle of 2α

$$S_2 = A\sin(2\alpha) = 2A\cos(\alpha)sin(\alpha) \tag{2.47}$$

and by comparing the signal intensity of the two images the flip angle estimate is given by:

$$\alpha = \cos^{-1}\left(\frac{S_2}{2S_1}\right). \tag{2.48}$$

Eq.[2.48] assumes that the TR is long enough for the magnetisation to fully recover (5·TR). If T_1 effects are not eliminated by a long TR then a mean bias will be introduced into the B_1 estimate. The pulse sequence used to collect this is shown in Fig.[2.24].

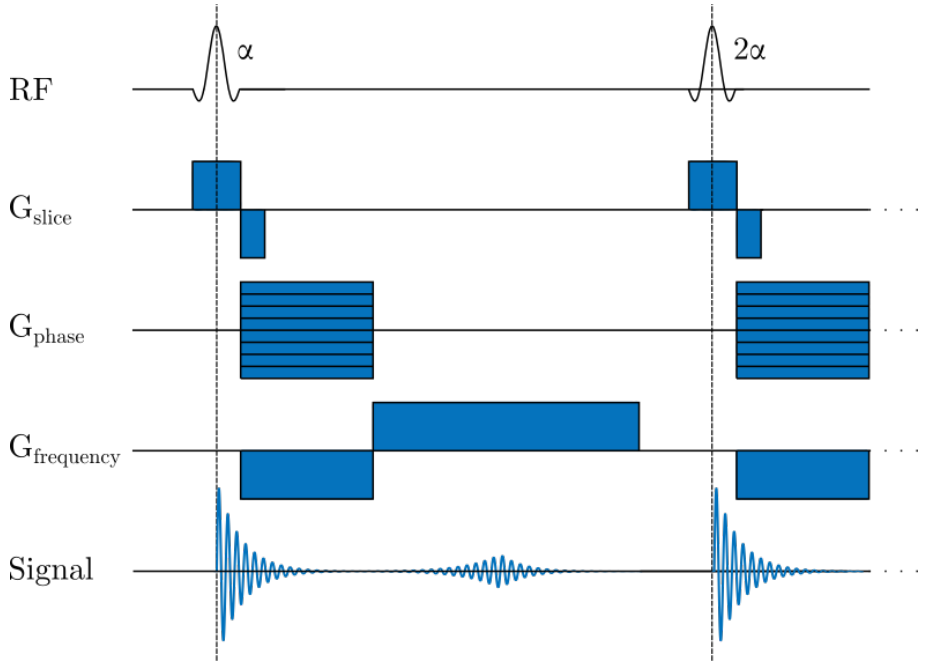

Figure 2.24: Double angle pulse sequence.

2.4.2 Phase-sensitive B_1 mapping

It has been shown that for ^{23}Na MRI, the accuracy of the double angle method suffers due to the low SNR of ^{23}Na imaging. Phase-sensitive technique B_1 mapping originally described by Morrell [50] has been shown to be more suitable for ^{23}Na MRI and provide accurate flip angle estimation over a wide range of flip angles at low SNR [51, 52]. The phase sensitive B_1 mapping method consists of a nonselective RF pulse about the x-axis with a flip angle 2α, immediately followed by an RF pulse about the y-axis with a flip angle α (composite RF pulse). In the original work $\alpha = 90°$ and the trajectory of the magnetisation can be seen in Fig.[2.25b]. The phase of the image produced will be dependent on the flip angle of the first pulse, and it is this dependency that allows for deviations in the B_1 fields to be measured. Measurement of phase allows estimate of flip angle as other sources of phase are removed by taking the phase difference of two acquisitions, one with $2\alpha_y$ and one with the pulse sign reversed.

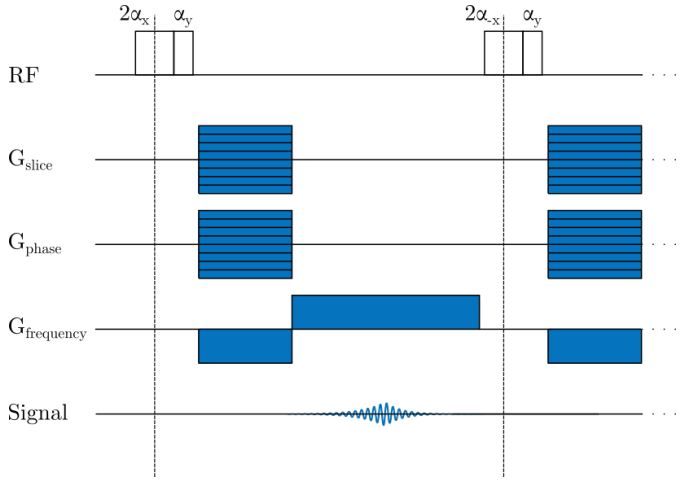

(a) Pulse sequence diagram for GRE phase-sensitive B_1 mapping.

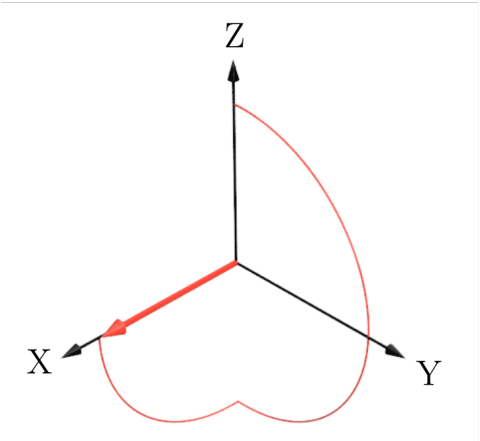

(b) The trajectory of the magnetisation during the phase-sensitive B_1 mapping method for $\alpha = 90°$.

Figure 2.25: Phase-sensitive sequence and magnetisation trajectory.

Assuming no relaxation effects and B_0 homogeneity, with an initial magnetisation of $M_0\hat{z}$,

following the two RF pulses the magnetisation is described by

$$M_x = -M_0 \sin\alpha \cos 2\alpha \tag{2.49}$$

$$M_y = M_0 \sin 2\alpha \tag{2.50}$$

$$M_z = M_0 \cos\alpha \cos 2\alpha \tag{2.51}$$

$$M_{xy} = M_x + iM_y \tag{2.52}$$

where M_{xy} is the transverse component of the magnetisation and a plot of M_{xy} is shown in Fig.[2.26a].

Equations [2.52] are only valid when there are no B_0 inhomogeneity effects. When B_0 inhomogeneities are present the first pulse will have a flip angle $2\sqrt{\alpha^2 + \Delta\omega^2\tau^2}$ about the vector $[2\alpha, 0, 2\Delta\omega\tau]$ where $\Delta\omega$ is the frequency offset due to the B_0 inhomogeneity and τ is the time between the centre of the 2α and α pulse (see Fig.[2.25a] for the pulse sequence). The second pulse will have a flip angle $\sqrt{\alpha^2 + \Delta\omega^2\tau^2}$ about the vector $[0, \alpha, \Delta\omega\tau]$. To remove the effects of the B_0 inhomogeneity a second image can be acquired using the same sequence but with a negative initial 2α pulse. The magnetisation equations then become

$$M_x = \pm\frac{M_0\alpha\Delta\omega\tau}{\beta^2}\left(4\sin^2\beta\cos\beta\right) - \frac{M_0\alpha\sin\beta}{\beta^3}\left(\alpha^2\cos 2\beta + \Delta\omega^2\tau^2\right) \tag{2.53}$$

$$M_y = \pm\frac{M_0 2\alpha\sin\beta}{\beta^3}\left(\Delta\omega^2\tau^2\cos 2\beta + \alpha^2\cos\beta\right) + \frac{M_0\alpha\Delta\omega\tau}{\beta^4}(1-\cos\beta)\left(\alpha^2\cos 2\beta + \Delta\omega^2\tau^2\right) \tag{2.54}$$

$$M_z = \pm\frac{2M_0\alpha^2\Delta\omega\tau\sin\beta}{\beta^3}(\cos\beta - \cos 2\beta) + \frac{M_0\alpha^2\cos 2\beta + \Delta\omega^2\tau^2}{\beta^4}\left(\alpha^2\cos\beta + \Delta\omega^2\tau^2\right) \tag{2.55}$$

where $\beta = \sqrt{\alpha^2 + \Delta\omega^2\tau^2}$, and the $\pm$ in Eqs. (2.53) to (2.55) represent the two images. The effects on the magnetisation of B_0 inhomogeneity and positive and negative the initial 2α pulse can be seen in Fig.[2.26].

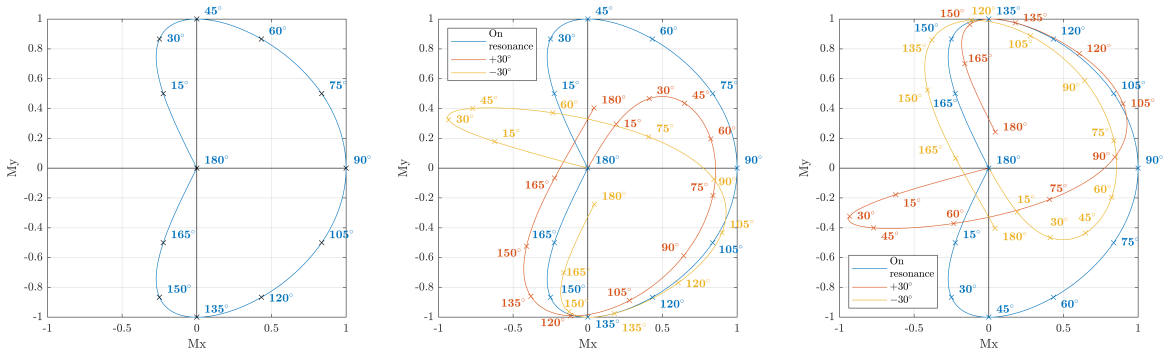

(a) Without perturbations.

(b) With B_0 inhomogeneity present of $\pm 30°$ angle of precession ($\Delta\omega\tau$).

(c) With B_0 inhomogeneity present of $\pm 30°$ angle of precession ($\Delta\omega\tau$) but with a negative initial 2α pulse.

Figure 2.26: The theoretical trajectory of the magnetisation for a given α during the phase-sensitive B_1 mapping method.

By considering the phase of the magnetisation and the difference in phase between the two images the flip angle α can be calculated. The phase difference without B_0 inhomogeneity derived from Eq. (2.52) is given by

$$\Delta\theta = 2\tan^{-1}\left(\frac{2\cos\alpha}{\cos 2\alpha}\right) \tag{2.56}$$

However when considering the B_0 inhomogeneity the relationship between α and the phase difference becomes more complicated and is shown in the plot Fig.[2.27].

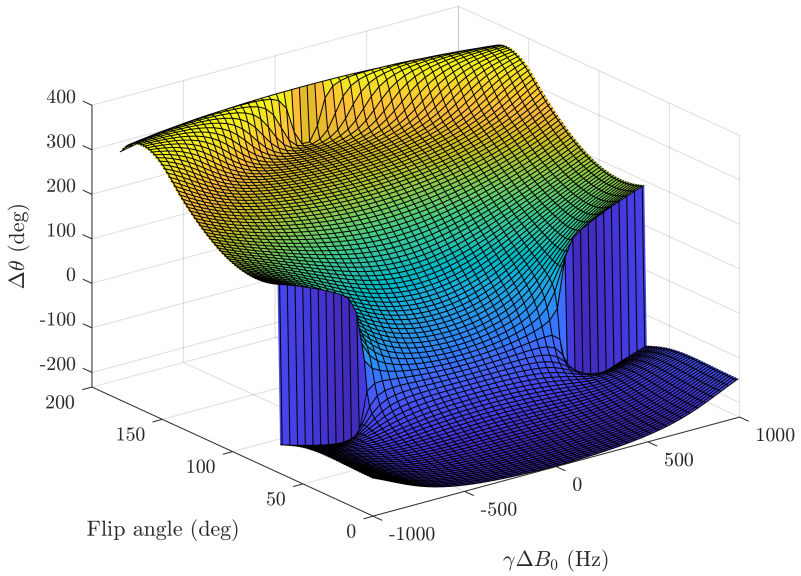

Figure 2.27: The relationship between phase difference ($\Delta\theta$) on flip angle and B_0 inhomogeneity (ΔB_0).

2.5 Conclusion

This chapter has provided an overview of the MR theory relevant to ^{23}Na imaging developments in this thesis. An outline of NMR signal and relaxation time effects, and the spatial encoding of ^{23}Na signal is provided. Finally an introduction to RF coil developments and SAR modelling is given, followed by methods used for B_1 mapping to provide a basis of understanding for the following experimental chapters.

Chapter 3

^{23}Na RF Coil Setup, SAR Distributions and Calibrations

This chapter describes the RF coil designs for the applications outlined in Chapters 4-6 of this thesis, to study sodium distribution in the leg, muscle and skin, and abdomen. Here the RF coil designs are outlined and the Finite-Difference Time-Domain (FDTD) method is used to compute the RF electromagnetic fields from each coil, to predict the SAR distribution within a model of the human leg and abdomen. Phantoms for calibration are outlined together with resultant temperature testing, proton decoupling power calibration and switch time assessment prior to use *in vivo*.

At the time of commencing this PhD through to the point of submission of this thesis, there were no ^{23}Na coils produced by our MR scanner vendor, Philips. Therefore, to perform ^{23}Na imaging within this PhD required the purchase of third-party coils or development of homebuilt coils. The RF coils used within this thesis are divided into three groups depending on their intended imaging region: leg, body and skin. In order to use the third-party RF coils on the 3T MR Philips scanners, certain criteria had to be met and this chapter provides an outline of the steps that were performed to enable use of the ^{23}Na RF coils, including how the coils are interfaced with the Philips 3T Achieva and Ingenia MR scanners, to ensure that they were both suitable and safe to use with the

scanner hardware and met the required safety testing to scan human subjects.

3.1 RF Coils Overview

This section provides an overview of the design of each of the ^{23}Na RF coils developed and used within this thesis. All the RF coils detailed below, apart from the skin coil, are single resonant coils to collect ^{23}Na data. The full potential of ^{23}Na imaging is realised from the combination of a ^{23}Na image with an underlying structural and/or functional ^{1}H MRI measure. This means that during a scan session both ^{23}Na and ^{1}H images should be collected in the same space without moving the subject. In this work, the ^{1}H body coil built into the 3T Achieva/Ingenia scanner (described as the Q-Body coil) is used to collect the ^{1}H images of the leg and abdomen. For standard ^{1}H imaging on the 3T Achieva/Ingenia, the Q-Body coil is commonly used as a transmit coil in conjunction with localised ^{1}H receive only coils. Whereas, in the work performed in this thesis, the Q-Body coil is used to both transmit and receive ^{1}H signals. As each of the RF ^{23}Na coils are physically placed inside the Q-Body coil, when the Q-Body coil transmits the ^{1}H RF pulses, the ^{23}Na RF coils must be designed such that there is minimal coupling with the Q-Body coil to avoid damaging either coil. Therefore, all the ^{23}Na RF coils detailed below, apart from the skin coil are compatible with transmit/receive on the Q-Body RF coil. Verifying this decoupling between the ^{1}H Q-Body and the ^{23}Na RF coils is one of the first tests that must be carried out with any RF coil, and is described in detail in Section [3.5].

3.1.1 Overview of ^{23}Na RF Coils for Leg Imaging

3.1.1.1 ^{23}Na 13cm Loop Coil

The first ^{23}Na coil acquired was a 13cm square loop coil from Clinical MR Solutions (Brookfield, Wisconsin, USA), as shown in Figure 3.1a, this is a single channel ^{23}Na Tx/Rx coil. It was used in the first stages of the ^{23}Na project to collect pilot data and test the systems, along with the additional 8cm and 15cm loop coils (see Appendix [A.1]).

The dimensions of the 13cm loop coil meant that it had a B_1 field profile that was well suited to imaging the calf muscles. To do this in a patient friendly manner, a support was designed to hold this RF coil such that the leg could be placed above the imaging coil, this can be seen in Fig.[3.1]. Also contained within the support are a series of reference bottles containing solutions of 10, 20, 30, 40, and 50 mmol/L of NaCl, positioned to allow for the concentrations of tissue ^{23}Na to be calculated. The coil and support were used for the first study of the leg, outlined in Section [4.2]. The advantage of this simple loop coil is that it can be used to image any region of the body, for example not only the calf muscles but also the upper leg muscles [53]. However, due to its simple loop nature it has a spatially inhomogeneous field that decreases rapidly with the distance from the coil.

(a) 13cm ^{23}Na coil without the case.

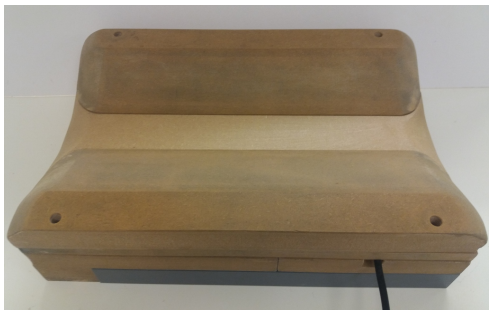

(b) Wooden support for the 13cm leg coil which sits inside this base, designed to fit underneath the calf.

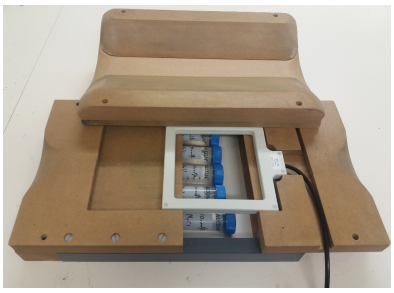

(c) Inside the support there is the 13cm coil and 5 bottles containing reference solutions of 10, 20, 30, 40, 50 mmol/L of NaCl.

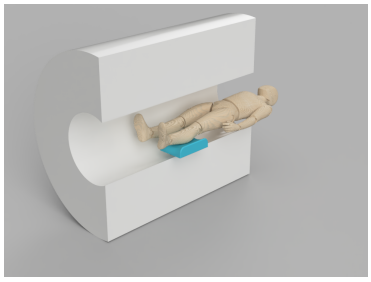

(d) Position of coil in the scanner shown in blue under the calf.

Figure 3.1: 13cm ^{23}Na leg coil, support and reference bottles.

3.1.1.2 ^{23}Na Birdcage Leg Coil

In order to image ^{23}Na in the muscle and skin of the calf a ^{23}Na quadrature leg birdcage (volume) coil was purchased from PulseTeq Ltd (Chobham, UK), Fig.[3.2]. The leg coil is a single channel T/R birdcage coil. It has an inner diameter of 170 mm and length of 260 mm, with the top half of the RF coil being removable to allow for the positioning of a scan subject's leg. The birdcage coil provides complete coverage of the calf with a more uniform transmit field (B_1^+) and coil sensitivity pattern (B_1^-) than the 13 cm loop coil whose coil sensitivity decreases rapidly with distance from the coil.

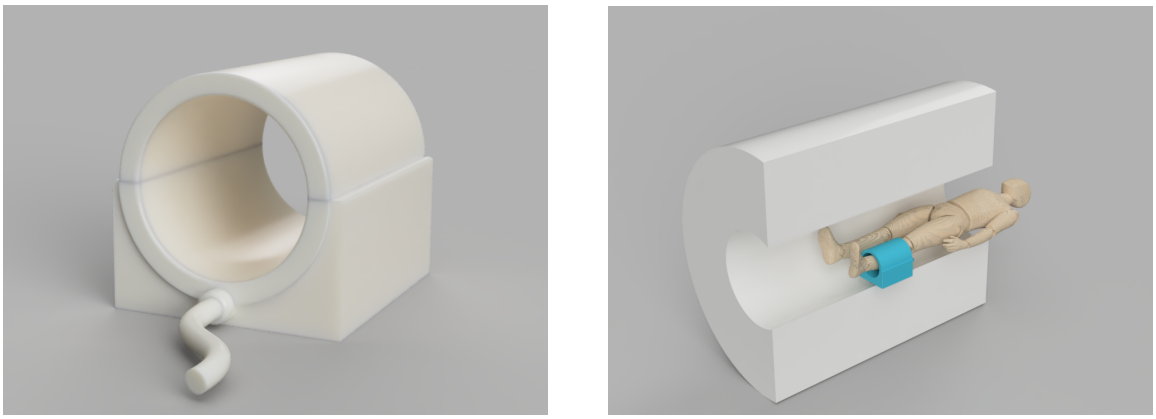

(a) The ^{23}Na birdcage leg coil of inner diameter 170 mm and length 260 mm.

(b) Birdcage leg coil in position in the scanner.

Figure 3.2: Birdcage ^{23}Na leg coil.

3.1.2 Overview of Coils for Skin Measurements

A number of studies have used ^{23}Na MRI to assess ^{23}Na stored in the skin [12, 29, 54–56]. These studies have generally used a volume coil, such as that described in Section [3.1.1.2], to measure the ^{23}Na distribution throughout the calf muscle and skin. However, using this method requires long acquisition times of 30 minutes for a spatial resolution of the order of 3×3×30 mm^3 which is suboptimal to accurately resolve the thickness of the dermal layer (1-2 mm). Therefore, here the use of a different RF coil and technique to image the skin was explored, for which I built a dual tuned ^{1}H/^{23}Na RF coil. The coil was designed to have a ^{1}H element consisting of a 55 mm diameter loop and a 30 mm ^{23}Na loop element inset inside the ^{1}H coil, see Fig.[3.3a]. The ^{1}H coil was designed to obtain ^{1}H

images, its small diameter producing large SNR enabling high resolution images to allow for the dermal thickness to be accurately resolved. The proton images that informed the loop sizes are detailed in Chapter 6. The ^{23}Na loop is designed to acquire ^{23}Na magnetic resonance spectroscopy (MRS) from the skin layer. ^{23}Na is present in the skin and muscle, but not in fat, therefore the size of the ^{23}Na loop was designed so that the sensitivity of the coil only included the dermal layer and not the muscle, see Fig.[3.3c]. Positioned below the coil is a reference sample of known ^{23}Na concentration containing a shift reagent to produce a separate spectroscopy peak, an example schematic of the resultant predicted signal is shown in Fig.[3.3d]. Using the ratio between the reference peak of known ^{23}Na concentration and the skin peak this method would allow for the skin ^{23}Na concentration to be measured. The ^{1}H image allows for the measurement of the thickness of the contributing dermal layer.

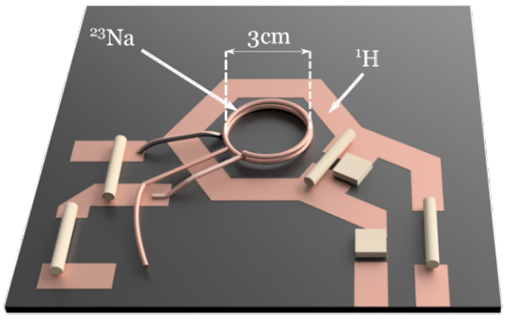

(a) Model of the skin coil. The smaller copper wire loop is the ^{23}Na element and the larger loop made from copper tape is the ^{1}H element.

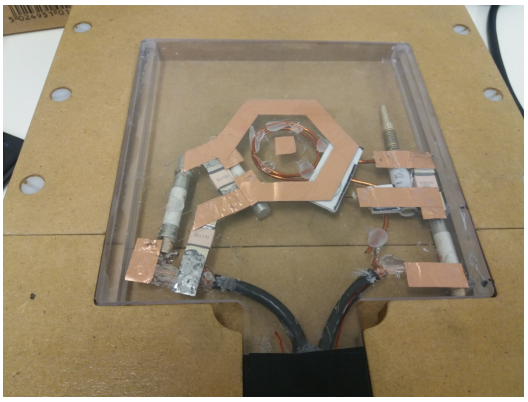

(b) Photo of the skin coil sitting in its base.

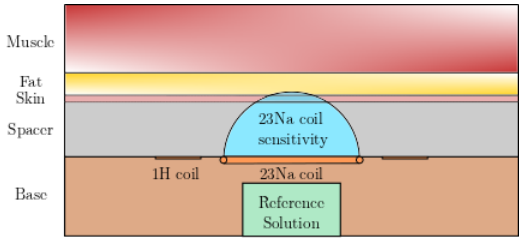

(c) Diagram showing how the penetration depth is designed to only reach the skin and a small amount of fat but not the muscle.

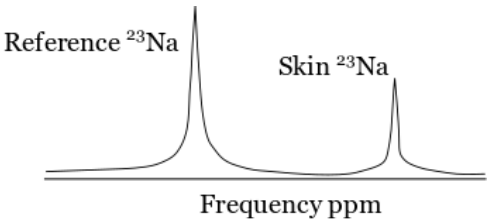

(d) A sketch of the expected spectroscopy signal obtained with the ^{23}Na skin coil.

Figure 3.3: The dual tuned ^{1}H/^{23}Na skin coil.

3.1.3 Overview of ^{23}Na RF Coils for Body Imaging

3.1.3.1 20cm Dual Loops ^{23}Na Coil

For imaging the abdomen, and specifically the kidneys, a single channel T/R ^{23}Na coil produced by PulseTeq Ltd (Chobham, UK) was purchased, see Fig.[3.4]. The 20cm loops sit either side of the abdomen and act as a Helmholtz pair. The coil was designed to produce a uniform B_1 region between the two loops with a high transmit efficiency.

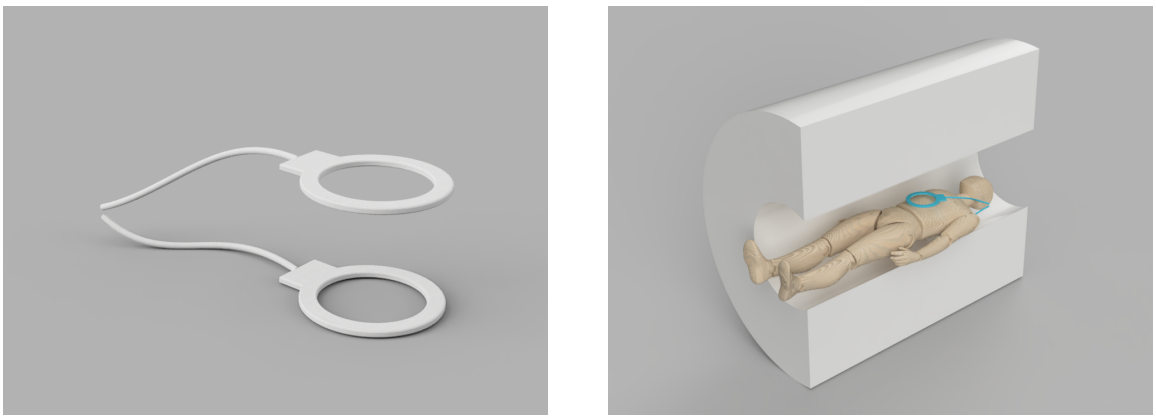

(a) Dual 20cm Loop ^{23}Na Coils.

(b) Dual Loops in position in the scanner positioned above and below the subject.

Figure 3.4: Dual loops ^{23}Na body coil.

3.1.3.2 6-Channel ^{23}Na QTAR body coil

To provide a more homogeneous field in the abdomen, as an alternative to the loops coil for ^{23}Na imaging of the kidney, working with Clinical MR Solutions(Brookfield, Wisconsin, USA) a bespoke 6-channel coil was developed. The 6-channel body coil is a flexible wraparound jacket, enabling it to fit around a range of body sizes. The coil consists of two layers, the outer layer contains a quadrature transmit coil (QTx), designed to provide a uniform B_1 transmit field. The inner layer comprises six receive loop elements. The coil design can be seen in Fig.[3.5] and comprises six 15 cm $\times$ 22 cm loops.

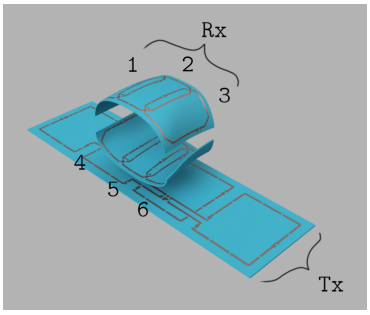

(a) The positions of the transmit and receive arrays in the coil's metal track is shown through the fabric case. The individual receive channels are labelled 1-6, each is a 15 cm × 22cm loop.

(b) The coil closed in the scan position.

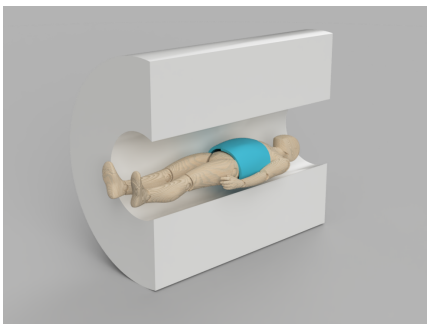

(c) Model of the 6-channel coil positioned in the scanner.

Figure 3.5: 6-Channel ^{23}Na body coil.

This coil was developed closely with Clinical MR Solutions to ensure the optimum elements sizes were used, this is detailed in Appendix [A.1].

The coil did not come with SAR evaluations therefore SAR simulations had to be performed prior to its use, these are detailed in Section [3.2.6]. The dual loops and 6-channel coil are compared in Section [5.4].

3.2 SAR Simulations

The ^{23}Na RF coils were simulated using the software XFDTD (Remcom, Inc.; State College, PA;USA), a three-dimensional full-wave electromagnetic solver based on the Finite-Difference Time-Domain method (Section [2.3.3]). The simulations were carried out on a human model to provide estimates of the maximum SAR produced in the body. This was done to ensure that when the coil is used *in-vivo*, the energy deposition remained within the SAR limits, and no damage was done to the subject as a result of heating. This SAR control depends on a reliable means of accurately predicting the distribution of electric fields and the tissue distributions from the coil and subject models.

3.2.1 Body Model

To assess the interaction between the EM fields on the body, a human body model is used in the simulations. The model provided with the XFDTD software is the Adult Reference Computational Phantom defined in the International Commission on Radiological Protection(ICRP) [57].

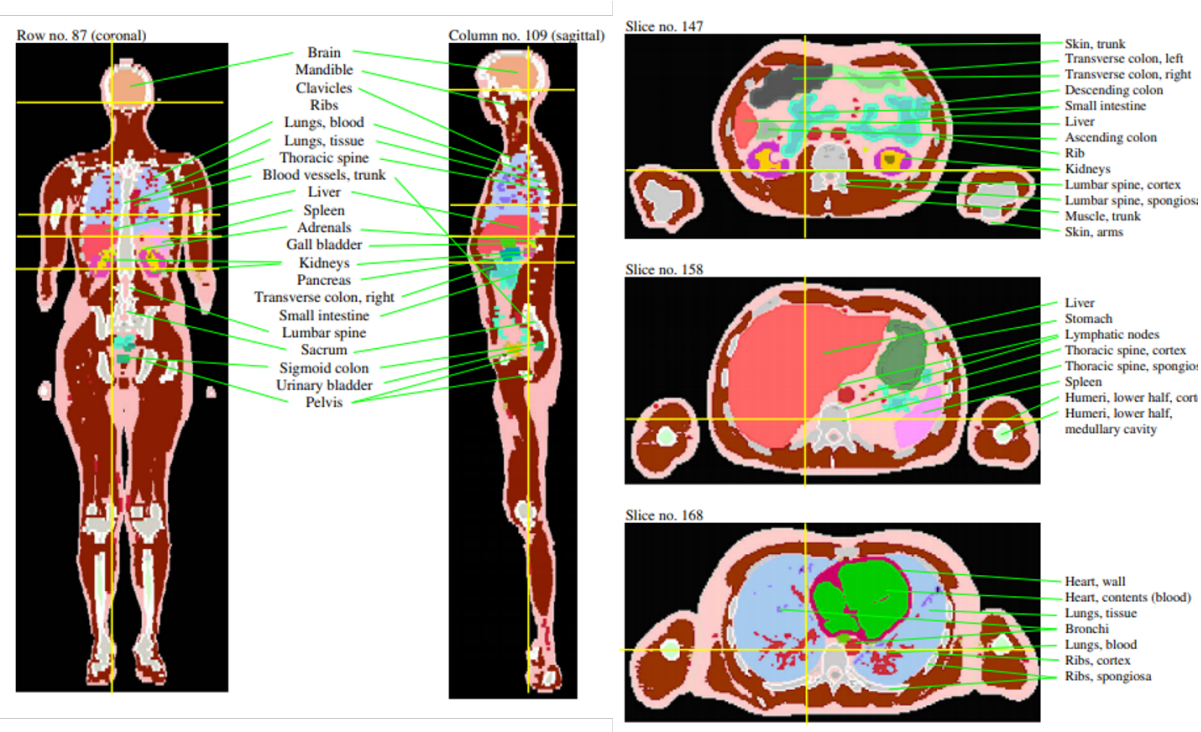

Figure 3.6: ICRP body model with the different tissues contained in the model labelled [6].

3.2.2 Simulation Setup Steps

The XFDTD software uses feature based modelling, in which geometric objects are created in the simulation space comprising of a model of the coil and the human body. The simulation space is built up with the following aspects:

- The physical components of the coil, such as the copper track and coil case.
- The materials within the model are assigned physical properties such as their electrical and magnetic properties Fig.[3.7a].
- The electronic components are added, such as capacitors and inductors for tuning and matching.

- To assess the interaction of the EM fields, the ICRP body model is included in the simulations. For example part of the leg component can be seen in Fig.[3.7c] for modelling the calf.
- The location of the coil feed Fig.[3.7b] and the associated waveform being applied to it.
- A sensor object can be defined to measure any EM fields of interest e.g E and B fields.

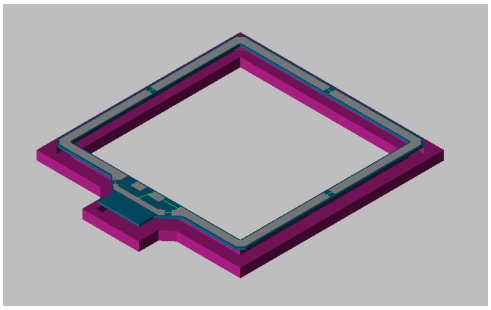

(a) The model of the inside of the 13cm coil, showing the silver conductive track.

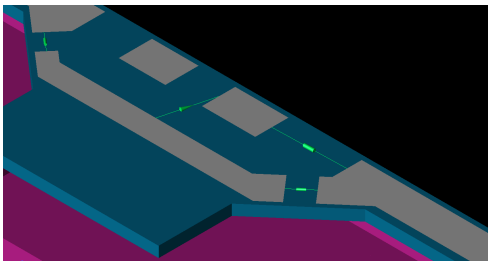

(b) The green symbols represent the electronic components of the coil e.g capacitors, inductors and feeds.

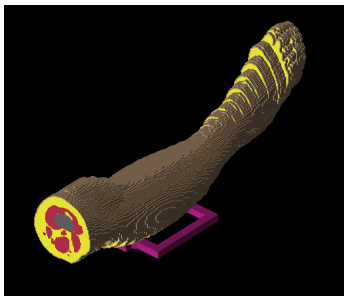

(c) The model of the 13cm coil and the leg model. The different colours in the leg denote different tissue types: Red - muscle , yellow - fat, grey - bone, beige - skin.

Figure 3.7: The SAR simulations illustrated for the ^{23}Na 13cm loop coil applied to the calf.

Once the simulation model had been built up, the first stage of the simulation was to perform validation measures in order to check that the model accurately represented the real world case. This was initially done by measuring the tuning of the simulated coil to check that the simulated coil resonance frequency matched that of the actual coil. If this

was the case it indicated that the simulation coil was an accurate representation. This was performed in a similar fashion as done on the bench-top with a real coil, by applying a range of frequencies and measuring the reflected power. The frequency at which the minimum power was reflected is the resonant frequency of the RF coil.

Once the expected resonant frequency was achieved, the next stage of the simulation was to supply a resonant RF signal to the coil and the software calculated the coil's generated EM fields. Checking that the EM fields appear as expected and comparing the modelled B_1 to measured B_1 provide the second validation step. The XFTDT software calculates the SAR for each cell of tissue in the body model and calculates a 10g average of the SAR. The EM fields and SAR are scaled for a 1W input power. For pulse sequence safety calculations, the Philips MRI scanner software requires the SAR per B_1 given as W/kg/μT^2 for each coil, therefore the maximum 10g-average SAR value from the simulation was divided by the B_1 produced in the simulation in a defined ROI (dependent on the coil and body region). The results of the simulations were displayed using Matlab (The MathWorks Inc, USA).

3.2.3 ^{23}Na 13cm Loop Coil Simulation Results

The 13cm ^{23}Na loop coil with a low geometrical complexity, few electronic components and small anatomical region meant that its simulation was straight forward to setup and had a low computational demand. The chosen imaging region for this coil was the calf therefore the simulation was carried out on the leg from above the knee down to the foot. The results of this simulation can be seen in Fig.[3.8].

As expected the maximum E-field was found to be above the capacitors (Fig.[3.8b]) which equated to the maximum SAR in the leg of 1.93 W/kg with 1 W input power. For the reference B_1 value an ROI was placed above the centre of the loop, at a height above the coil equal to its radius. The B_1 in this ROI was 4.1 μT for 1W input power. This provides a coil SAR scale (SAR/B_1^2) of 0.16 W/kg/μT^2.

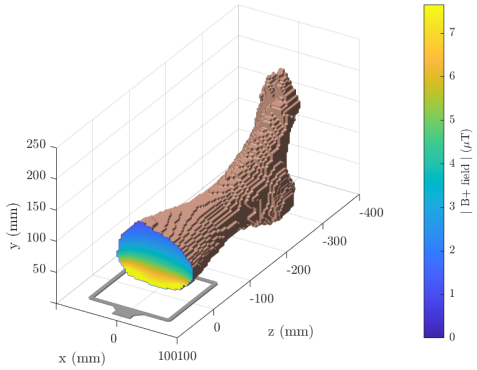

(a) Rotating B_1^+ field within the leg model.

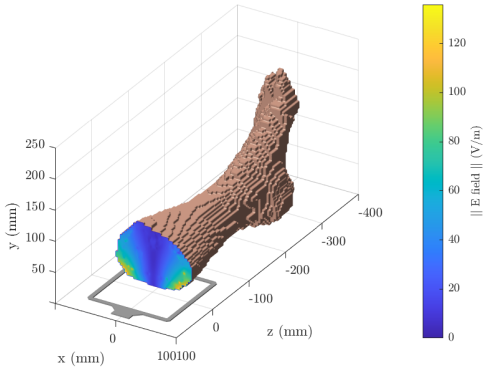

(b) The E-field within the leg model.

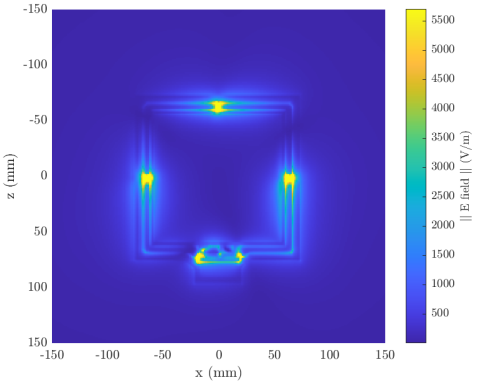

(c) E-field in the x-z plane located on the top of the coil case.

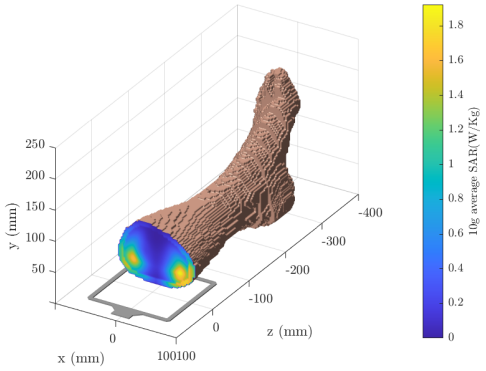

(d) 10g-average SAR, the slice shown is where the maximum was found.

Figure 3.8: Results from the SAR simulations for the 13cm ^{23}Na loop coil. The simulations were carried out on the lower leg with the coil placed under the calf muscle and the results here are shown at the location of the maximum SAR. The results are generated with an input power of 1W.

3.2.4 ^{1}H/^{23}Na Skin Coil Simulation Results

The simulations for the skin coil were similar to those of the 13cm loop coil, except performed for two coil elements tuned to ^{23}Na and ^{1}H. The two coil elements were treated as two independent coils and thus required separate SAR scales to be calculated. The simulated coil was placed under a model calf. The model was run from the knee to the ankle. The results for the ^{23}Na and ^{1}H elements can be seen in Fig.[3.9] and Fig.[3.10] respectively.

The maximum E-field in the leg for the ^{23}Na element was above the tuning capacitors (Fig.[3.9c]) and produced a maximum SAR of 0.30 W/kg with 1 W input power. For the reference B_1 value an ROI was placed above the centre of the loop, at a height above the

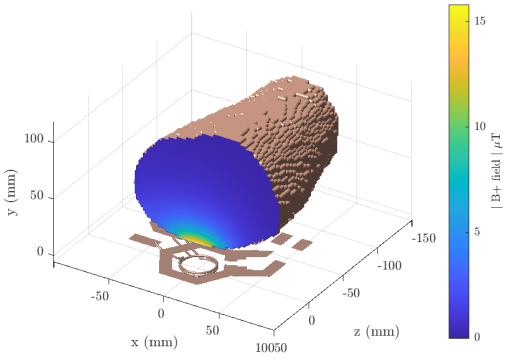

(a) Rotating B_1^+ field within the leg model shown here about the centre of the ^{23}Na loop.

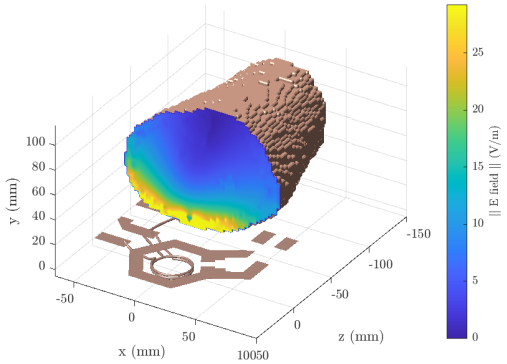

(b) The E-field within the leg model shown at the location of the maximum SAR.

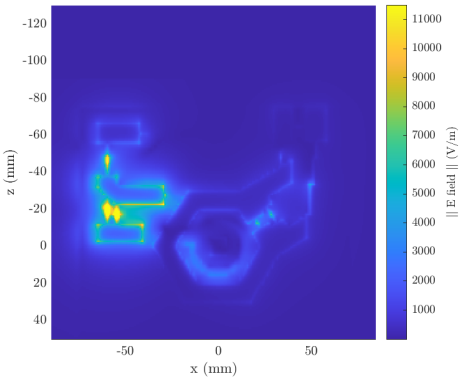

(c) E-field in the x-z plane located on the top of the coil case.

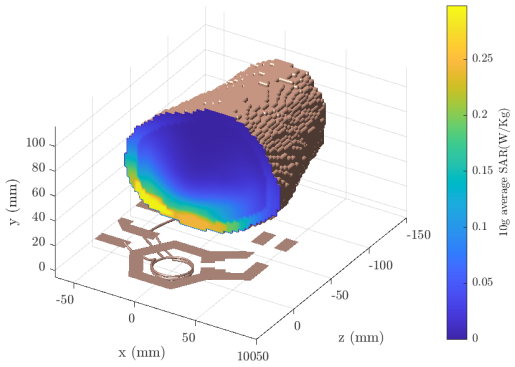

(d) 10g-average SAR, the slice shown here is where the maximum was found.

Figure 3.9: Results from the SAR simulations for the ^{23}Na element of the skin coil. The simulations were carried out on the lower leg and are generated with an input power of 1W.

coil equal to its radius, the B_1 in this ROI was 16 μT for 1 W input power. This provides a coil SAR scale (SAR/B_1^2) of 1.2×10^{-3} W/kg/μT^2.

The maximum E-field in the leg for the ^{1}H element was above the tuning capacitors (Fig.[3.10c]) and produced a maximum SAR of 2.53 W/kg with 1W input power. For the reference B_1 value, an ROI was placed above the centre of the loop, at a height above the coil equal to its radius, the B_1 in this ROI was 6 μT for 1 W input power. This provided a coil SAR scale (SAR/B_1^2) of 140×10^{-3} W/kg/μT^2.

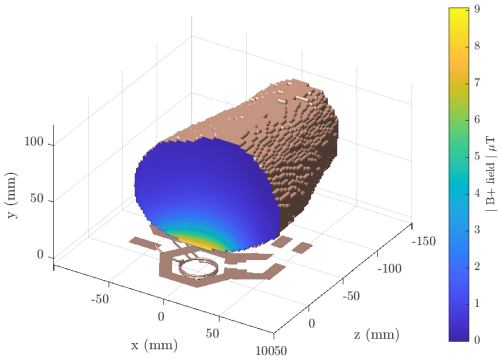

(a) Rotating B_1^+ field within the leg model, shown here about the centre of the ^{1}H loop.

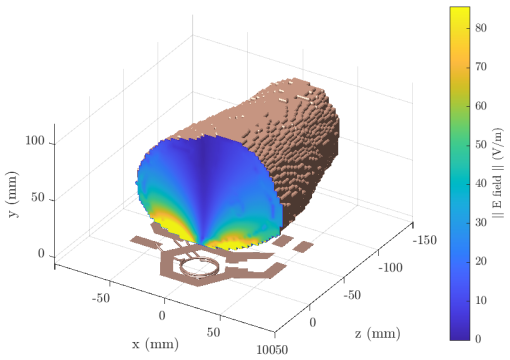

(b) The E-field within the leg model, shown at the location of the maximum SAR.

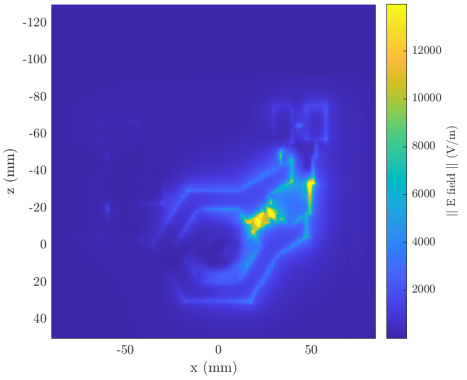

(c) E field in the xz plane located on the top of the coil case.

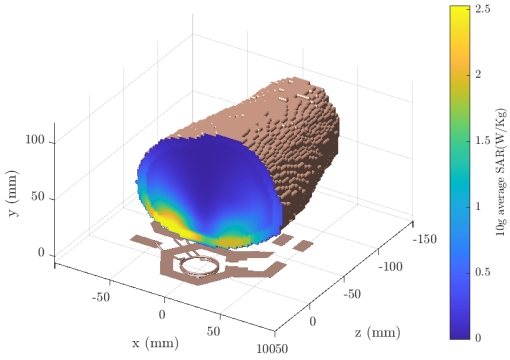

(d) 10g-average SAR, the slice shown here is where the maximum was found.

Figure 3.10: Results from the SAR simulations for the ^{1}H element of the skin coil. The simulations were carried out on the lower leg and are generated with an input power of 1W.

3.2.5 Dual Loops ^{23}Na Body Coil and Birdcage ^{23}Na Leg Coil Simulations Results

SAR simulations for the the dual loops ^{23}Na body coil and the birdcage ^{23}Na leg coil were carried out by PulseTeq and the SAR values required in the scanner software were provided when the coil was purchased. The SAR value for the loops coil was a SAR/B_1^2 of 350×10^{-3} W/kg/μT^2 and the leg coil SAR/B_1^2 of 200×10^{-3} W/kg/μT^2.

3.2.6 6-Channel ^{23}Na Body Coil Simulations Results

The increased complexity of the 6-channel coil presented a greater challenge when carrying out the SAR simulations. The main difficulties were caused by the curved coil track and

careful inspection was required to ensure the gridding algorithm accurately represented the difficult geometry. Additionally, the large number of electronic components increased the risk of the gridding algorithm misrepresenting one of these components. The 6-channel coil differs to the two previous simulations as it is formed from separate transmit and receive elements with pin diodes to selectively tune either the transmit or receive elements of the coil. The tuning of all elements was checked as part of the coil validation for both transmit and receive modes. The rest of the simulations were carried out with the transmit element applying the RF with the receive element actively detuned. The simulation was carried out with the coil wrapped around the body model and the SAR measured from the neck to hips including the arms.

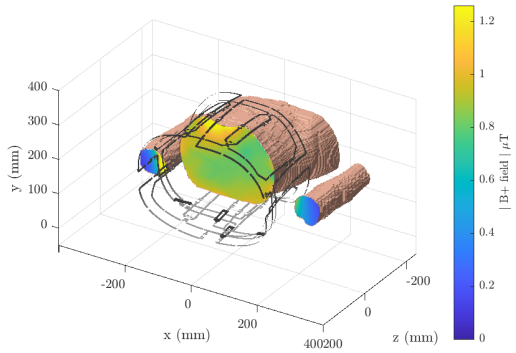

(a) Rotating B_1^+ field within the body model, shown here about the centre of the coil.

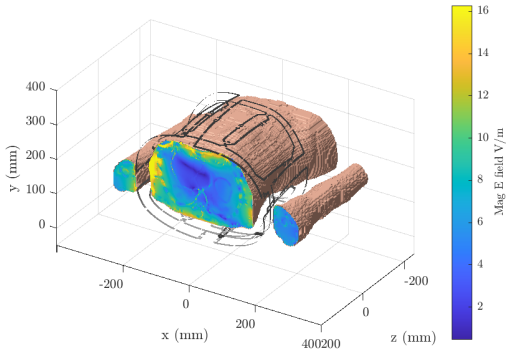

(b) The E-field within the body model, shown at the location of the maximum SAR.

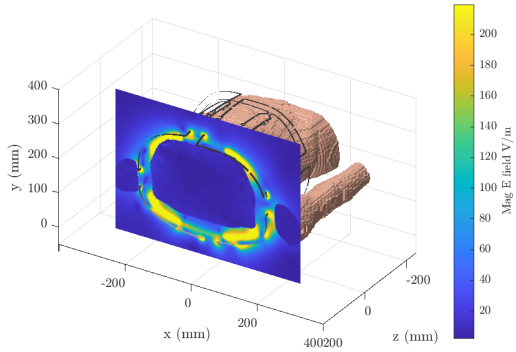

(c) The E-fields outside the body model shown at the location of the maximum SAR.

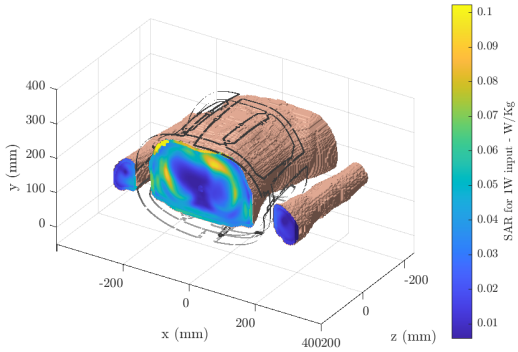

(d) 10g average SAR, the slice shown is at the location of the maximum 10g average SAR.

Figure 3.11: Results from the SAR simulations for the 6-channel ^{23}Na body coil. The simulations were carried out with an input power of 1W.

The maximum E-field in the body for the 6-channel coil was above one of the tuning capacitors of one of the receive elements (Fig.[3.11d]) and produced a maximum SAR of 0.60 W/kg with 1W input power. For the reference B_1 an ROI was assigned in the centre of the coil, the B_1 in the ROI was 0.84 μT for 1 W input power. This provides a coil SAR scale (SAR/B_1^2) of 0.85 W/kg/μT^2.

3.3 Phantoms

Phantoms are used throughout medical imaging to mimic the human body, and in this thesis for the development of ^{23}Na imaging these have been used extensively to test the RF coils and validate ^{23}Na MR imaging techniques. Phantoms are a container holding a solution, the composition of the solution is chosen to make some of the physical properties of the phantom match that of the human body. In this thesis, a number of phantoms have been made for different uses depending on the intended image region and measurements that were being carried out in the phantom.

3.3.1 Phantoms Recipe

The composition of the phantoms were based on the work by Q.Duan et al. [58,59]. Water is the main component with NaCl used to control the conductivity and sucrose used to control the permittivity. The work carried out by Q.Duan et al. focused on building phantoms for ^{1}H MRI. The principles are the same for a ^{23}Na phantom except that the NaCl concentration in their phantom was considerably higher than would be found in the body, therefore in the ^{23}Na phantoms some of the NaCl was substituted with KCl. This phantom recipe was used because the chemicals are non-toxic, inexpensive and readily available. The making of the phantom solution was easily scaled up allowing large batches to be made to fill the body phantom. When the phantoms were used for temperature measurement, the thermal diffusivity of the phantom solution was reduced by adding agar to produce a rigid gel.

3.3.2 Power Calibration Phantoms

The MR sequence used to calibrate the power requirements of a RF coil (detailed in Section [3.6]) is not localised, therefore the signal measured by the MRI scanner will be the net signal with contributions from the entire phantom within the coil. This is unfavourable for power calibration for two reasons:

1. B_1 transmit inhomogeneities within the coil will expose spins across the phantom to differing B_1 and therefore a range of flip angles.

2. The receive sensitivity of the RF coil will also affect the signal intensity across the phantom, typically having greater sensitivity at the coil surface.

The signal measured from the calibration method will be a combination of these two effects throughout the phantom. To ensure that the ^{23}Na RF coil drive scales were correctly calibrated to produce the required flip angles in the area of interest (e.g. the kidneys), carefully designed reference phantoms were used for each ^{23}Na RF coil. The reference phantoms were made of two compartments: a 150 mmol/L KCl solution to provide the correct loading for the coil and 100 mmol/L NaCl solution to provide ^{23}Na signal as reference for the power optimisations.

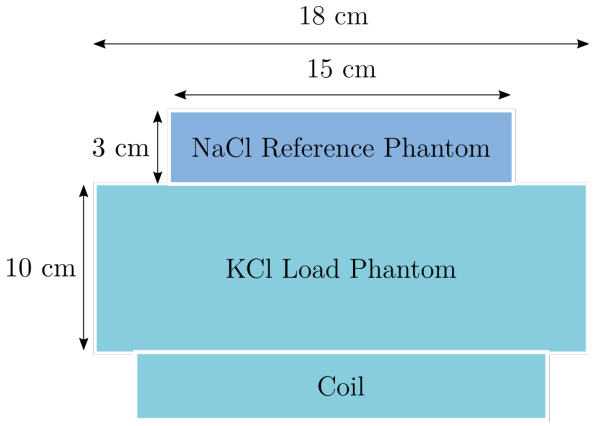

(a) The phantom setup for the power calibration for the 13cm ^{23}Na coil.

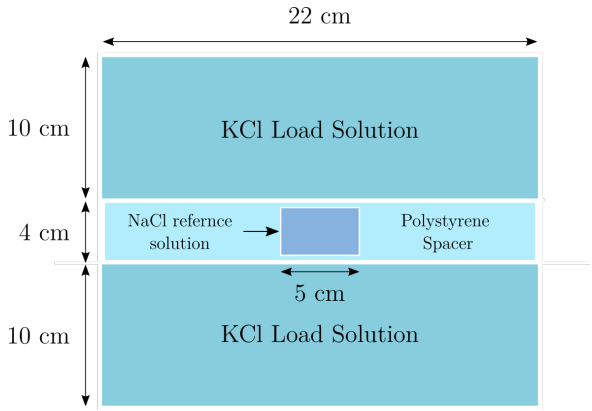

(b) This phantom setup was used for both the 6-channel ^{23}Na coil and the dual loops ^{23}Na coil.

Figure 3.12: Phantoms used for the power calibrations.

3.3.3 Leg Phantom

Two phantoms were used for sequence development with the leg coils. Both consisted of a 2L Nalgene bottle with a diameter of 200 mm and height of 245 mm. The phantoms, compositions were based on the Q.Duan et al. recipe [58, 59] and details are provided in Table 3.13a. The two phantoms were made with different ^{23}Na concentrations. One phantom had a NaCl concentration of 30 mmol/L, which represents a realistic ^{23}Na concentration found in muscles [1]. The second had a NaCl concentration of 50 mmol/L to provide a greater SNR to allow for shorter scans when carrying out sequence development work.

Ingredients	Leg Phantom 30 mmol/L NaCl	Leg Phantom 50 mmol/L NaCl
Water (L)	2	2
NaCl (g)	3.51	5.84
KCl (g)	59.3	57.0
Sucrose (g)	1770	1770
Agar (g)	30	30

(a) Components of the ^{23}Na leg phantoms.

(b) Photo of one of the leg phantoms.

Figure 3.13: The ^{23}Na leg phantoms.

3.3.4 Body Phantom

The body phantom was made from the same recipe as the leg phantoms but with a NaCl concentration of 100 mmol/L, a typical ^{23}Na concentration in the kidney [21, 23, 60], the absence of agar is explained below (Section [3.3.5.2]). The phantom had a capacity of 10 L and was 300 mm × 230 mm × 200 mm. The composition of the body phantom is given in Table 3.14a.

Ingredients	Body Phantom
Water (L)	10
NaCl (g)	58
KCl (g)	285
Sucrose (g)	8840
Agar (g)	0

(a) Components of the ^{23}Na body phantom.

(b) Photo of the body phantom.

Figure 3.14: ^{23}Na body phantom.

3.3.5 Temperature Measurement Phantoms

In order to measure local temperature changes for the SAR temperature measurements (Section [3.4]) temperature measurement phantoms were made in line with ASTM [61] and NEMA [62] standards.

3.3.5.1 Temperature Measurement Leg Phantom

A temperature measurement leg phantom was made from agar sealed in polythene pouches. A polythene sleeve was cut to the same length as a typical lower leg, it was then filled with the phantom solution and the ends of the polythene tube were then heat-sealed. The phantom is shown in Fig.[3.15a]. Fibre-optic temperature probes could then be inserted through the polythene, see Section [3.4].

3.3.5.2 Temperature measurement body phantom

For the larger body phantom, agar was not included in the phantom solution as heating large quantities of agar was not possible. Therefore, to allow for temperature measurements, agar in polythene pouches wwas positioned on the outside of the phantom. The body phantom can be seen in Fig.[3.15b]

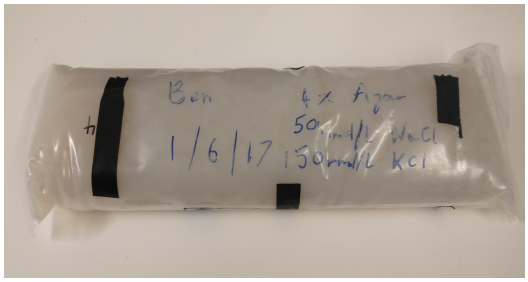

(a) Temperature measurement leg phantom consisting of a polythene sleeve containing agar.

(b) The body phantom with the agar bags in position

Figure 3.15: Procedure for temperature measurements on the phantoms.

3.3.6 Reference Bottles

In order to produce quantitative maps of ^{23}Na concentration a conversion from an image pixel intensity to ^{23}Na concentration is required. This can be done using a series of reference bottles of known ^{23}Na concentration which are positioned in the FOV of the ^{23}Na image from which an ROI of signal intensity is measured. Linear regression is then used to characterise the relationship between the ROI signal intensities inside the bottles and their know concentration. Once this relationship has been characterised the ^{23}Na MR images can be converted to tissue sodium concentration (TSC) maps. In this work, the composition of the reference bottles are the same as the leg phantoms described in Fig.[3.13a], and had concentrations of 20, 30, 40 and 50 mmol/L NaCl.

The reference bottles need to be as close as possible to the imaging region and inside the RF coil sensitivity region, thus the location of the reference bottles was different for each coil. For the ^{23}Na birdcage leg coil the reference bottles were built into a holder positioned beneath the leg between the calf and birdcage coil's inner bore, as shown in Fig.[3.16].

For the 13cm loop coil, 6-channel body coil and the dual loops coil, Falcon 50 mL conical centrifuge tubes were used as reference bottles, for the 13cm ^{23}Na coil the bottles are shown in Fig.[3.1c] below the coil. For the dual loops coil, the reference bottles were positioned underneath the subject, for the 6-channel coil the reference bottle were placed next to the body within the coil.

Figure 3.16: The four reference bottles of 20, 30, 40 and 50 mmol/L NaCl inside the ^{23}Na birdcage leg coil.

3.3.6.1 Inductively Coupled Plasma (ICP) Spectroscopy Measurement

Accurate concentrations in the reference bottles is needed in order to provide accurate calibrations. To verify the concentration, Inductively Coupled Plasma (ICP) mass spectrometry was carried out on the reference solutions, the results from one set of bottles is provided in Table 3.1.

Nominal NaCl Concentration (mmol/L)	ICP Measured NaCl Concentration (mean ± SD mmol/L)
20	20.6 ± 0.3
30	32.6 ± 0.6
40	42.6 ± 0.6
50	54.2 ± 1.0

Table 3.1: The concentration of the reference bottles, comparing the ICP measured concentrations to the nominal concentrations.

3.4 Temperature Tests

To validate the results and the limits obtained by SAR modelling, the final safety validation each RF coil had to undergo before being signed off for use was a temperature test performed on the temperature measurement phantoms Section [3.3.5].

To measure the temperature in the phantom, a 4-channel fibre optic thermometry sys-

tem from Luxtron (Santa Clara, California, USA) was used. The thermometry system provided temperature measurements from within the bore of the MR scanner allowing measures to be taken during MR data collection with different pulse sequences. Temperature testing was performed for each of the RF coils which were provided by MR clinical solutions or constructed in-house, specifically the ^{23}Na 13cm loop coil, 6-channel body coil and skin coil. The general methodology followed was the same for each RF coil. Depending on the intended imaging region, the temperature measurements were either carried out on the leg or body phantom, as detailed in Section [3.3.5]. The tip of the probes were placed at regions considered to be the most likely areas for heating to occur, these were locations where the electric field was predicted to be maximum by the simulations, see Section [3.2]. Four probes were available, thus three probes were placed at the high-risk areas whilst the fourth probe was placed far from the RF coil but still in agar, this allowed monitoring of any ambient temperature change not caused by heating from the RF coil. The fibre optic probes are flexible and were inserted through the plastic phantom case and approximately 5 mm into the agar. The phantom was then positioned in the isocentre of the scanner bore at the same position as a subject's leg or abdomen would be. The thermometry system sampled measures at 1 Hz. Five minutes of temperature data was collected before any pulse sequence commenced in order to collect a baseline temperature measurement. A high SAR gradient recalled echo (GRE) acquisition (echo time, TE = 2.07 ms; repetition time, TR = 100 ms; flip angle, FA = 90°; 128 averages, resolution: 3 × 3 × 30 mm^3) was then carried out on the phantom and throughout the scan the temperature was recorded. To evaluate any temperature change, the ambient temperature change recorded by the reference probe was subtracted from each of the remaining three probes' temperature readings. The results and additional methodology specific to each of the RF coils are provided in the following sections.

3.4.1 13cm Loop Coil Temperature Measurements

For the 13cm ^{23}Na leg coil, the leg phantom Fig.[3.15a] was used for all temperature assessments. The 13cm ^{23}Na coil was held in the coil holder shown in Fig.[3.1c] and one

temperature probe was placed above the components where the feed entered and the other two probes were placed above the capacitors, opposite each other as shown in Fig.[3.17a]. The GRE sequence was carried out for an acquisition time, TA of 10 minutes. The results of the temperature recording from each probe (with reference temperature subtracted) are shown in Fig.[3.17]. The maximum temperature change over the scan duration was 0.17 ± 0.08 ° C, well below the maximum allowed temperature increase of 1° C.

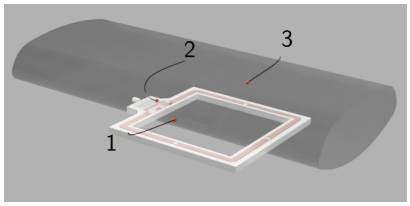

(a) Temperature probe locations in the leg phantom for the 13cm ^{23}Na coil.

Position	Temperature change (mean ± SD °C)
1	0.17 ± 0.08
2	0.09 ± 0.08
3	0.16 ± 0.09

(b) Temperature change over a 10 minute GRE scan.

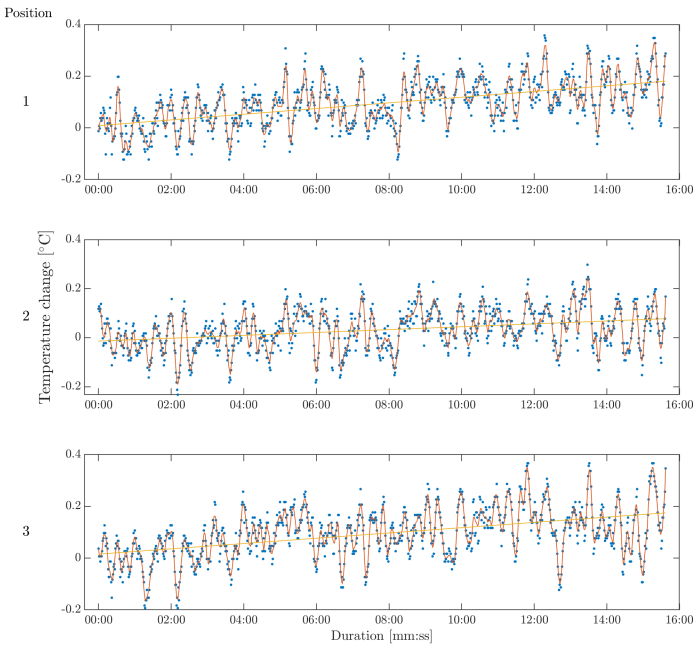

(c) Temperature measures in each of the test probes relative to the reference probe over a 10 minute GRE scans.

Figure 3.17: Temperature measurements for the 13cm ^{23}Na loop coil.

3.4.2 Skin Coil Temperature Measurements

For the skin coil, the leg phantom Fig.[3.15a] was used, and the skin coil was held in the same coil holder as the 13cm coil Fig.[3.1c]. One temperature probe was placed above the tuning components of both elements, and the third at the centre of the loop elements, see Fig.[3.18a]. An GRE acquisition (resolution: 3× 3× 30 mm^3; echo time, TE = 2.07 ms; repetition time, TR = 100 ms; flip angle, FA = 90°; 128 averages, acquisition time, TA = 8:20minutes) was carried out separately for both the ^{23}Na and the ^{1}H element. The results are shown in Fig.[3.18] for each of the probes with the reference temperature

subtracted. The maximum temperature change over the scan was $0.06 \pm 0.06°$ C, well below the maximum allowed temperature increase of 1° C.

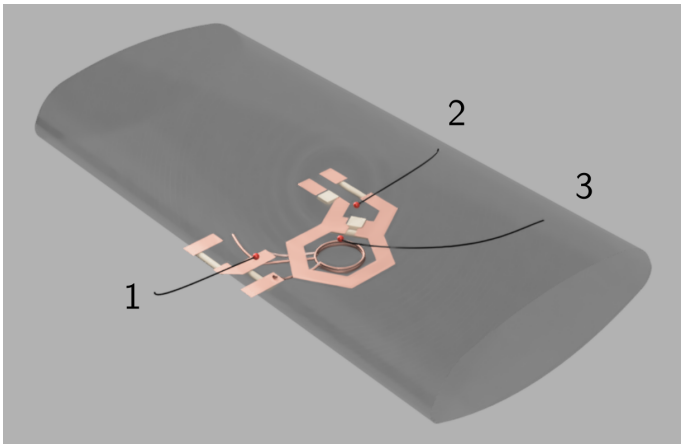

(a) The temperature probe locations in the leg phantom.

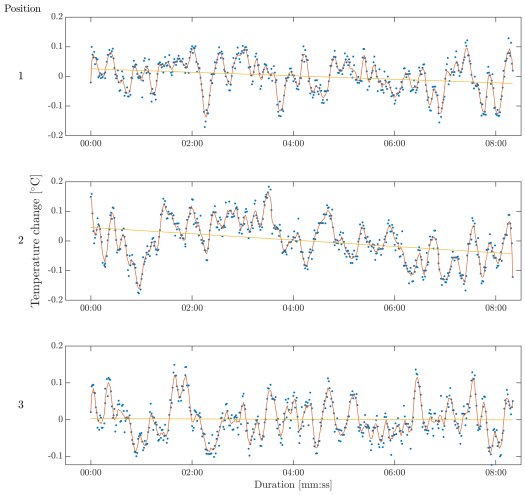

(b) Temperature measures when using ^{23}Na element, each relative to the reference probe.

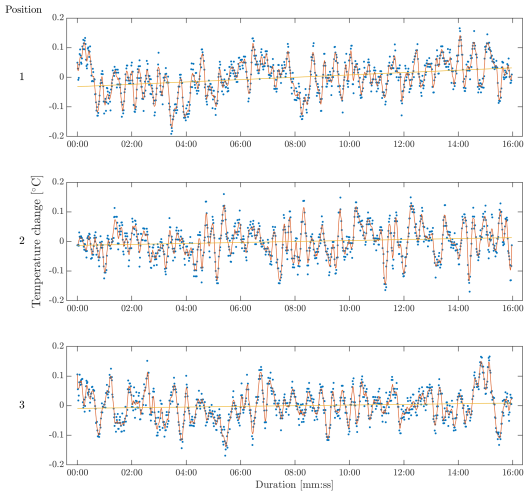

(c) Temperature measures when using ^{1}H element, each relative to the reference probe.

Figure 3.18: Temperature Measurements for the skin coil.

Position	Temperature change (mean ± SD °C)	
	^{23}Na	^{1}H
1	-0.05 ± 0.06	0.06 ± 0.06
2	-0.09 ± 0.02	0.03 ± 0.06
3	0.00 ± 0.07	0.02 ± 0.06

Table 3.2: Temperature Measurements for the skin RF coil.

3.4.3 6-Channel ^{23}Na Body Coil Temperature Measurements

Due to the size of the 6-channel coil (Fig.[3.5]), the temperature measurements were collected with the probe in six positions, with measurements taken in two sets, using the three available temperature probes. The body phantom was used, as shown in Fig.[3.15b], with the three agar sections moved between the two sets of temperature measurements to allow for the measurement of the temperature at the locations shown in Fig.[3.19a]. The results are shown in Fig.[3.19] for the six locations. The maximum temperature change over the scan was 0.20 ± 0.05 ° C, well below the maximum allowed temperature increase of 1 ° C.

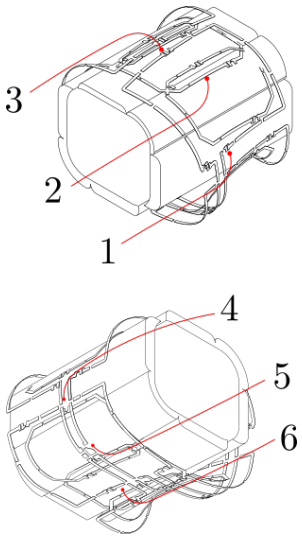

(a) Position of temperature probes for the 6-channel coil. The top image shows the positions used in the first set of temperature measurements.The bottom image shows the positions used in the second set of temperature measurements

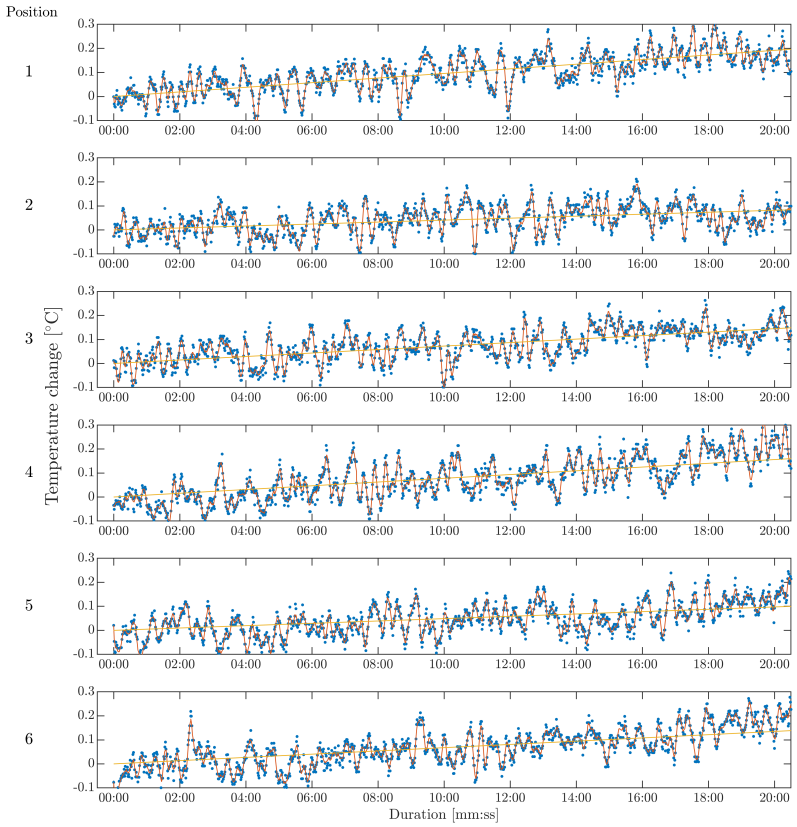

(b) Six temperature measures with each relative to the reference probe

Figure 3.19: Temperature Measurements for the 6-channel ^{23}Na coil.

Position	Temperature change (mean ± SD °C)
1	0.20 ± 0.05
2	0.08 ± 0.05
3	0.15 ± 0.05
4	0.18 ± 0.06
5	0.11 ± 0.05
6	0.15 ± 0.05

Table 3.3: 6-Channel maximum temperature change.

3.5 Proton Decoupling Tests

As outlined in Section [3.1], the ^{23}Na coils are designed to be compatible with the scanners' inbuilt ^{1}H Q-Body coil. When one RF coil is brought close to another RF coil there is a possibility that they will interact with each other, this is known as coupling. The coupling between two coils can have several effects:

- The inductive coupling can shift the resonance of both coils, moving it further away from the Larmor frequency, therefore reducing their RF efficiency.
- If there is coupling between the two coils, when one coil is transmitting RF this can induce currents in the second coil. If the high-power transmitted RF couples to a receive component of a coil, then it could produce a large enough induced current to cause damage to the sensitive receiver circuitry such as the preamps.
- The coupling can distort the B_1 fields within the RF coils.

A series of measures were carried out to ensure there was no significant coupling between the ^{1}H Q-Body coil and any third party or home built coil used.

3.5.1 Q-Body Tuning

The Philips MR scanner performs several measures and calibration steps before running any scan. Some of these prescan measures are run using the Q-Body coil and can be used to check for coil coupling. One of the prescans performs a power calibration of the Q-Body coil to measure how much power is needed to achieve a required flip angle. This power calibration determines a power scale used to set the power output of the RF amplifier, see Section [3.6] for more detail. The power calibration is carried out by applying two RF pulses, to generate a spin echo (SE) and a stimulated echo (STE), the ratio of the signals produced by the SE and STE provides an effective flip angle, at the centre of the imaging region for a given RF power. If the measured flip angle is too small or too large the RF power is adjusted and the flip angle is measured again. This is repeated until the target flip angle is reached and the scanner will use the final RF power scale as the basis for the subsequent scans. Ordinarily, this power calibration is to allow for a range of coil loading introduced by the variability of the subject size or positioning in the scanner. However, by monitoring how the RF power scale changes when an RF coil is placed inside the bore of the MR scanner, it is possible to check for coil coupling. Philips recommend a maximum difference of 5 % in the Q-Body RF power scale with and without the ^{23}Na coil present. This was confirmed for all the ^{23}Na coils.

3.5.2 Image Uniformity

In addition, to assessing a change in the loading of the Q-Body coil, the effects of localised coupling can be determined by acquiring ^{1}H images using the Q-Body coil. By collecting a ^{1}H GRE sequence (resolution: 1.7× 1.7× 5 mm^3, TE = 3.5 ms; repetition time, TR = 30 ms, FA=30°) of a uniform phantom, coupling effects will show as a signal drop out in the acquired images.

Initially, coupling between the PulseTeq ^{23}Na birdcage leg coil and the Q-Body coil was observed. Working with PulseTeq and by studying the image uniformity helped to identify the cause. For example, a signal dropout in a small region showed localised coupling as shown in Fig.[3.20a] which, in this case was due to coupling to one rung of the birdcage

coil in the ^{23}Na leg coil.

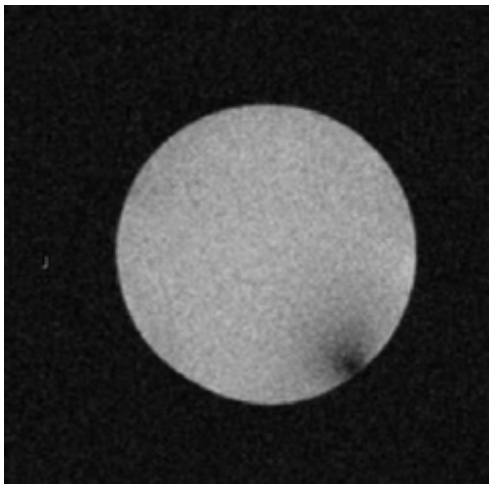

(a) Signal dropout which indicated coupling between the Q-Body coil and the ^{23}Na birdcage leg coil. The size and location suggested coupling to one of the rungs of the birdcage coil.

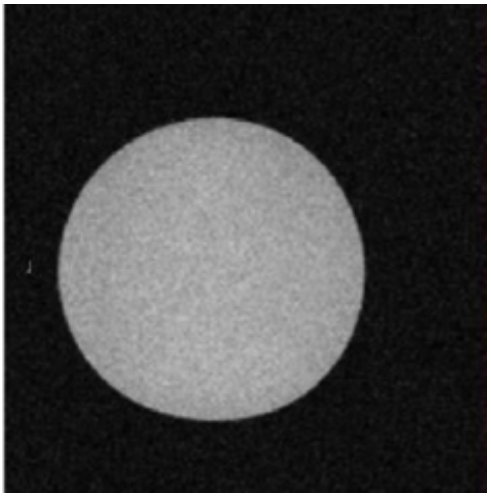

(b) The same image after the coupling was removed.

Figure 3.20: Coronal slice through a uniform phantom collected using the ^{1}H Q-Body coil.

Alternatively, the effect of coupling can produce more global effects, as was seen in Fig.[3.21], where in this case coupling caused a large drop in ^{1}H signal intensity inside the ^{23}Na birdcage coil.

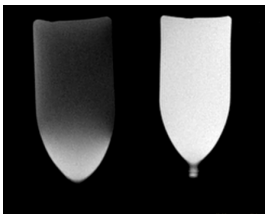

(a) Coronal ^{1}H image with coupling present.

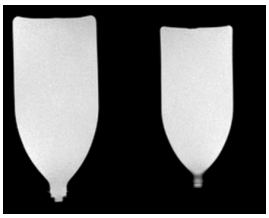

(b) Coronal ^{1}H image with the ^{23}Na coil fixed and no coupling present.

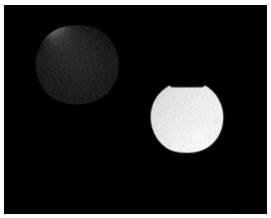

(c) Axial ^{1}H image with coupling present.

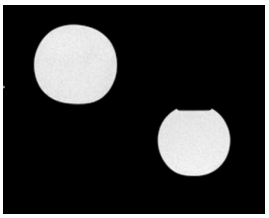

(d) Axial ^{1}H image with the ^{23}Na coil fixed and no coupling present.

Figure 3.21: ^{1}H scans acquired using Q-Body coil showing the effects of coupling between the Q-Body coil and the ^{23}Na birdcage coil. The left-hand bottle in each image is in the ^{23}Na birdcage coil.

The work needed to reduce the coupling effects between the Q-Body coil and the ^{23}Na birdcage coil took a number of months to resolve. However, this was essential to reduce the coupling to a minimum to allow high resolution ^{1}H images to be acquired alongside

^{23}Na images.

3.6 Power Calibration

Each RF coil used in the MR scanner has its own RF characteristics, including its B_1 transmit efficiency; how much B_1 is generated by the coil for a given power, and the maximum power that can be applied to the coil before damaging components. The MR scanner software uses these properties to calculate the power to output from the RF amplifier to achieve the required RF pulses. The peak power of an RF pulse is dependent on the B_1 and is given by

$$PeakPower = 5kW \cdot (drive\ scale)^2 \cdot \left(\frac{B_1}{B_1 ref}\right)^2 \tag{3.1}$$

where 5 kW is the maximum power of the amplifier. The drive scale is a dimensionless scaling factor and is unique to each coil and is obtained by calibration. B_{1ref} is set in the initial calibration and used as a reference for following power calculations. The software also allows a value of maximum B_1 (B_{1max}) to be set, which limits the maximum peak power that can be applied to the RF coil in order to protect the electronic components within the coil.

3.6.1 Power Calibration Method

To calibrate the drive scale for each ^{23}Na RF coil, the power calibration phantom (Section [3.3.2]) was scanned using a single voxel spectroscopy sequence. This sequence comprised of a non-selective pulse and acquire using a hard RF pulse to obtain one FID. A series of 21 scans were carried out, the first scan had a nominal flip angle of 10° and the flip angle increased in steps of 10° for the complete series. The scanner software calculates the length and magnitude of the required RF pulses to generate the range of flip angles used in the series. The largest flip angle, in this case 220°, will have the maximum B_1 permitted by the coil (B_{1max}). The corresponding pulse length needed for this 220° pulse is then used for all the other pulses in the series and the B_1 reduced in order to achieve

the required flip angles.

The peaks of the acquired signal will follow a sinusoidal shape. With a correctly set drive scale the maximum acquired signal will be observed at a 90° pulse and a minimum acquired signal at 0° and 180°, as seen in Fig.[3.22a]. However, if the drive scale is not properly calibrated the nominal flip angle set in the exam card will not be the actual flip angle the spins experience. This is shown in Fig.[3.22b] where calibration was not correct and the maximum signal did not correspond to the nominal 90° pulse.

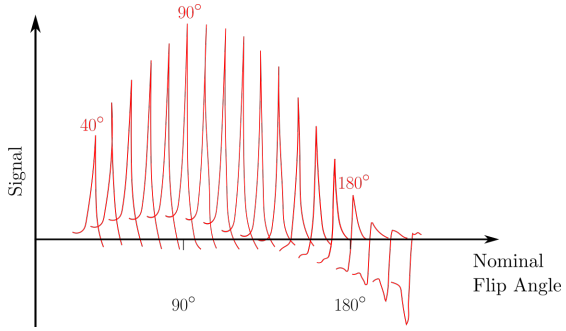

(a) With correct drive scale, the maximum signal occurs when the scanner applies a nominal flip angle of 90°.

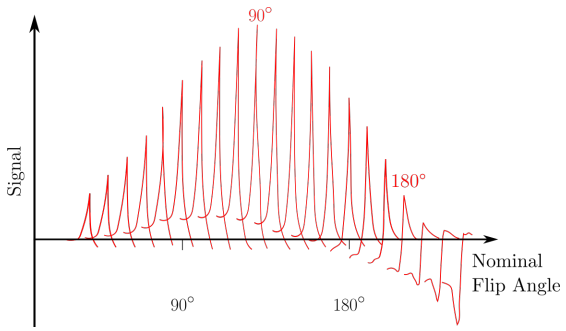

(b) A flip angle series where the drive scale is too low, the maximum signal occurs when the scanner applies a nominal flip angle of over 90°.

Figure 3.22: Results of a flip angle series calibration scan used to ascertain the correct drive scale.

There are a couple of potential sources of error using this method. If the B_1 field of the coil is not homogeneous, then the measured signal will be a result of a range of applied B_1 magnitudes. The effects of this can be reduced by using a phantom with a small volume of ^{23}Na solution to provide the signal, such as the ones covered in Section [3.3.2]. Additionally, a sufficiently long TR is needed to ensure no T_1 effects are present.

3.7 Transmit/Receive Switching Time

The ^{23}Na RF coils have two modes: transmit and receive. During a pulse sequence the scanner will use the RF coil to apply an RF pulse, it will then change modes from transmit to receive and acquire the RF signal produced. The mode switching is not instant; the time it takes to switch is known as a switching delay. As the coil is switching from transmit to receive mode, the coil will not receive RF signals until the switching is complete. The

switching delay is typically in the order of 100μs which, in a standard spin or gradient echo sequence is encompassed in the time taken for an echo to be generated, the TE. However, with UTE imaging where the FID is sampled immediately after the excitation pulse (Section [2.2.2]) the acquisition could begin before the RF system has completed switching, leading to artefacts. This is an important consideration for ^{23}Na imaging, as due to the short relaxation times of ^{23}Na, short echo time UTE acquisitions are optimal. To prevent this from happening the scanner software uses a delay known as a tune delay which is the time for which the software will ignore any sampling after the end of a transmit pulse. The switching delay of each of the ^{23}Na coils had to be measured to verify that the tune delay was suitable.

To measure the switching delay a spectroscopy sequence was performed on the associated ^{23}Na phantom for each ^{23}Na RF coil. The sequence used to assess this was a non-selective; pulse and acquire which used a hard RF pulse to obtain an FID. This was performed for all coils and is shown in Table [3.4].

Coil	Approximate switching delay (ms)
13cm Loop	0.19
Birdcage Leg	0.13
Dual Loops	0.14
6-channel	0.51

Table 3.4: Approximate switching delay for the ^{23}Na RF coils.

An example measurement for the ^{23}Na birdcage leg coil can be seen in Fig.[3.23] at the beginning of the FID the effects of coil switching can be seen. Fig.[3.24] shows the results for the 6-channel body coil. The 6-channel coil has larger delay of approximately 0.6 ms due to its increased size and complexity.

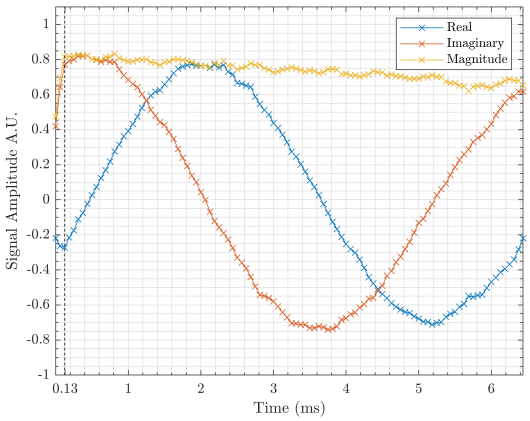

Figure 3.23: ^{23}Na FID from the birdcage leg ^{23}Na coil. The period up to the dashed line shows unexpected behaviour of the signal, which was designated as the switching time of the coil.This can be seen to be 0.13 ms.

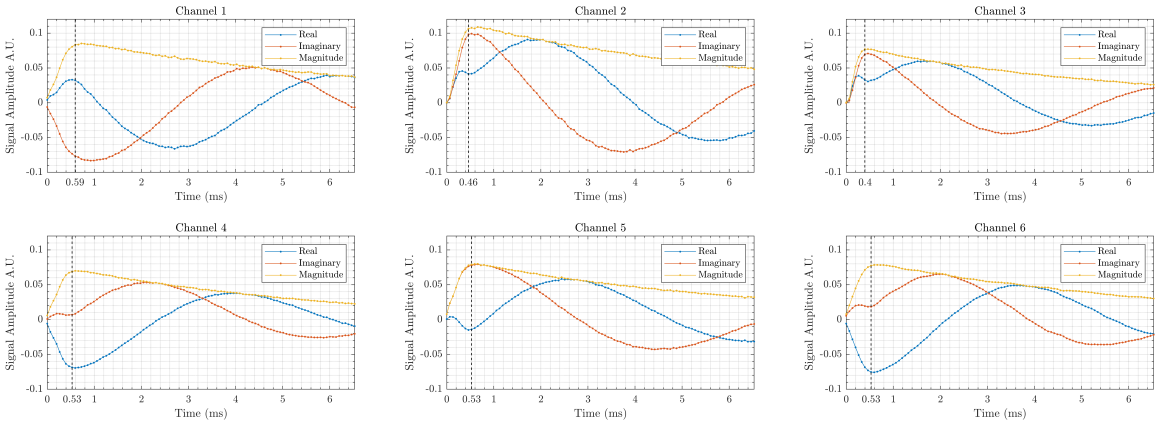

Figure 3.24: ^{23}Na FID from the six channels of the 6-channel ^{23}Na body coil. The period up to the dashed line shows the unexpected behaviour of the signal, which was designated as the switching time of the coil. This can be seen to be approximately 0.5 ms.

3.8 The Philips 3T Achieva and 3T Ingenia

The Sir Peter Mansfield Imaging Centre (SPMIC), where this work was carried out has a 3T Philips Achieva and a new configuration 3T Philips Ingenia MRI scanner installed in 2018 which is on the digital release. When work for this PhD commenced multi-nuclear (MN) imaging was not supported on the Ingenia platform therefore the initial work took place on the Achieva scanner. The skin coil used the Achieva's inbuilt research coil interface for pre-amplifying and TR switching. This was performed prior to August 2019. In 2019, MN became available through a research agreement facilitating transition of the ^{23}Na work to the Ingenia.

3.8.1 3T Achieva

The receive hardware on the Achieva has a limited number of ^{23}Na receive channels, four as standard. To increase the number of channels to enable the use of the 6-channel coil, the receive hardware configuration had to be modified. As a non-standard procedure, I worked with Philips to implement and troubleshoot this configuration. The final scan setup required reconfiguration of the receive hardware, namely swapping a phosphorus (^{31}P) receiver board to a ^{23}Na one and rerouting the receive cables to the correct boards. This had to be done before and after every scan session adding 20 mins to each scan session.

3.8.2 3T Ingenia

Part way through this PhD, in August 2019, the Ingenia was upgraded, to enable it to carry out MN scanning and so the ^{23}Na work was moved across to the Ingenia. The Ingenia provided a number of benefits. The scanner bore on the Ingenia is wider, 70 cm compared to 60 cm in the Achieva, in future this will increase the size of the patient recruitment pool as obesity is associated with kidney related diseases [63]. The wider bore also improves the volunteers' experience during the scan. The Ingenia also has improved RF performance, the ^{1}H RF coil architecture is fully digital which is expected to increase SNR of the Q-Body RF coil measures that will be carried out. The MN coil architecture on the Ingenia remains non-digital meaning that the ^{23}Na coils were still compatible. The MN RF receiver has been moved from an external control room to on-top of the magnet, this has reduced the length of cables from the coil thereby reducing signal losses. Finally, the Ingenia can receive six ^{23}Na channels without reconfiguration being necessary, reducing the length of the scan sessions. A downside to switching to the Ingenia is that it no longer contains the interface for home-built coils. For research coils to be used with the scanner, they need their own pre-amplifier and TR switch, therefore it is not possible to use the skin coil with the Ingenia.

3.9 Conclusion

This chapter has provided an overview of the RF coils used in this work and the required modelling of the specific absorption rate (SAR), phantom construction, temperature testing, coupling checks, power calibration and measurement of the tune delay.

Chapter 4

Optimisation of ^{23}Na Image Acquisition Schemes in the Human Calf Muscle

---

This chapter explores ^{23}Na image acquisitions for applications in the human calf muscle. An initial pilot study using a surface coil to assess the change in ^{23}Na signal intensity in response to anaerobic exercise is first outlined. The optimisation of the gradient recalled echo (GRE) scheme on the PulseTeq birdcage leg coil is then presented. Methods of B_1 mapping are evaluated to allow correction of the ^{23}Na signal intensities to compute tissue sodium concentration (TSC). To assess whether the SNR of ^{23}Na imaging can be further improved, an ultrashort TE (UTE) scheme is implemented to minimize the effects of T_2^* relaxations, as ∼60 % of the ^{23}Na signal fraction has a fast decay time constant of 0.5-5 ms. This is followed by UTE T_2^* mapping to measure the short and fast relaxation time components. The chapter concludes with a recommended protocol for future ^{23}Na imaging studies of the human calf muscle.

4.1 Introduction

Recent studies have demonstrated that ^{23}Na MRI of the lower leg muscle can be a useful imaging modality for the detection of ^{23}Na content and changes in response to exercise or as a result of disease. The majority of clinical studies to date have been performed by the group of Jens Titze and colleagues [12, 25, 29, 64–66], using a single slice 2D GRE scheme without B_1 mapping correction. They have showed that ^{23}Na concentration increases or decreases in the body may be induced by diseases, such as diabetes mellitus, chronic kidney disease (CKD), hypertension, and acute heart failure, with ^{23}Na concentration alterations in the calf muscle being closely related to developed pathologies.

4.1.1 Effect of Exercise on ^{23}Na Measures

^{23}Na MR imaging has been used to monitor changes in ^{23}Na in the leg muscle after exercise. An early study by Bansal et al. [67] in 2000 imaged the leg in a ^{23}Na head coil to measure an increase in ^{23}Na image intensity of 34 $\pm$ 7 % in the calf muscle following ankle flexion-extension exercise, which then reduced to baseline with a half-life of 30 $\pm$ 6 minutes. However, the same change was not seen in the calculated ^{23}Na concentration. They attributed this to an increase of the long T_2 relaxation component of the muscle, thus the change in ^{23}Na signal intensity was proposed to be due to a change in the macromolecules interaction increasing T_2 instead of ^{23}Na tissue concentration. Similar measurements were made by Constantinides et al. [68] using a ^{23}Na suface coil where the change in ^{23}Na signal intensity was measured in the lower leg of two healthy subjects after exercise. An increase of 16 % and 22 % in the mean ^{23}Na signal intensity was observed immediately after exercise. They also performed the same measures in two subjects with myotonic dystrophy, for whom the signal intensity in the dystrophic muscles increased by a greater extent at 47 % and 70 %. The cause of the increased change in ^{23}Na signal was suggested to be due to a change in the Na^+-K^+ pump activity. Hammon et al. [65] measured the change in ^{23}Na concentration in the lower leg during aerobic and anaerobic exercise. They observed a significant increase in the ^{23}Na concentration in all muscle compartments in the leg except the gastrocnemius during anaerobic exercise. The

mean ^{23}Na concentration in the triceps surae and the whole leg increased by 9 % (3.1 ± 2.1 mmol/kg, P = 0.16) and 6.5 % (2.2 ± 1.3 mmol/kg, P < 0.01) respectively. In contrast, a significant change was measured during aerobic exercise only in the soleus muscle which increased by 4.5 % (1.6 ± 1.5 mmol/kg , P = 0.046). Chang et al. [69] assessed whether diabetes affected the exercise induced change in measured ^{23}Na signal intensity. In healthy subjects they measured an increase in signal intensity of 8-13 % (P < 0.03) in the soleus and gastrocnemius muscles, the half-life of the return to baseline was 22 minutes. In diabetic patients, the ^{23}Na signal intensity increased by 10 - 11 % (P < 0.04) with a return half-life of 27-37 minutes. The possible cause for the longer recovery time in diabetic patients was suggested to be due to the reduced activity of the Na^+-K^+ pumps associated with insulin resistance. These studies have shown that ^{23}Na MRI can provide insights into the cellular response to exercise and how disease effects the response to exercise in the calf muscles.

4.1.2 Changes in ^{23}Na Content in Diabetes Mellitus

In addition to Chang's work described above [69], Kannenkeril et al. [70] used ^{23}Na MRI to study differences in tissue sodium concentration (TSC) in the calf at baseline in patients with diabetes. They studied the ^{23}Na concentration in the muscle and skin in two groups of patients, one with Type-2 diabetes and the other with hypertension. The group with Type-2 diabetes had significantly greater ^{23}Na concentration in the muscle of 20.6 ± 3.5 mmol/L compared to hypertension at 16 ± 2.5 mmol/L, P < 0.001. Similarly greater ^{23}Na concentration was seen in the skin of diabetes patients at 24.5 ± 7.2 mmol/L compared to hypertension at 20.6 ± 5.7 mmol/L, P = 0.01. When adjusting for confounding factors (age, BMI, gender, blood pressure, glomerular filtration rate), the difference was still significant. The authors highlight the known risk of increased ^{23}Na on organ damage, and that therapies should be used to reduce the ^{23}Na content in the bodies of patients with diabetes.

4.1.3 Changes in ^{23}Na Content in Hypertension

^{23}Na MRI in the calf muscle has been used to assess the increase in body ^{23}Na content due to high blood pressure. Kopp *et al.* [28] used a birdcage coil and collected 2D GRE data (in absence of B_1 mapping) at $3 \times 3 \times 30$ mm^3, TE 2.07 ms and showed a 29 % increase in muscle ^{23}Na content in patients with hypertension compared to healthy subjects. The ^{23}Na concentration in muscle was found to increase significantly with age in men (from $\sim$ 12 mmol/L at 20 - 30 years to $\sim$ 22 mmol/L at 60 years, reaching $\sim$ 30 mmol/L at 80 years) but not women ($\sim$ 15 mmol/L at 20 - 30 years and $\sim$ 18 mmol/L at 60 years). ^{23}Na concentration in the skin was also shown to increase with age in men ($\sim$ 12 mmol/L at 20 - 30 years and 25 mmol/L at 60 years reaching 35 mmol/L at 80 years) as well as in women ($\sim$ 12 mmol/L at 20 - 30 years and 20 mmol/L at 60 years). When corrected for age, compared with age-matched normotensive controls, it was found that women with refractory hypertension had increased stored ^{23}Na in the skin (17 ± 3 mmol/L control, 23 ± 3 mmol/L HTN) and men with refractory hypertension had increased ^{23}Na in muscle (18 ± 2 mmol/L control, 24 ± 3 mmol/L HTN). Ott *et al.* [71] used the same ^{23}Na imaging sequence as Kopp et al. [28] to monitor the ^{23}Na concentration in tissue in response to renal denervation to reduce blood pressure in patients with treatment-resistant hypertension. They measured tissue ^{23}Na concentration in the calf after denervation, but found no change when compared to baseline, suggesting that the reduction in blood pressure attributed to denervation is not linked to tissue ^{23}Na concentration.

4.1.4 Changes in ^{23}Na Content in Renal Disease

Chronic kidney disease (CKD) results in ^{23}Na retention and is linked with an increased risk of cardiovascular events, in part due to the high prevalence of left ventricular hypertrophy (LVH) in CKD. The pathogenesis of LVH in CKD is not fully understood and associations with dietary ^{23}Na intake have been inconsistent. A recent study by Schneider et al. [55] perfomred 2D GRE ^{23}Na MRI (again a matched sequence to that used in Kopp et al. [28]). They found that in patients with CKD, high skin ^{23}Na content was associated with greater age, male sex, higher body mass index, higher 24 hour systolic blood pressure and

number of antihypertensives, urine albumin excretion, diabetes and cardiovascular disease. Furthermore, skin ^{23}Na content in the calf correlated significantly with left ventricular mass (LVM) assessed using ^{1}H cardiac MRI ($r = 0.56$, $P < 0.001$), with skin ^{23}Na content from 10 - 50 mmol/L for LVM of 7 to 20 g. In a multivariable linear regression analysis, skin ^{23}Na content was a strong determinant of LVM, independent of 24 hour systolic blood pressure and total body hydration.

Acute kidney injury (AKI) is frequently associated with the accumulation of extracellular ^{23}Na and water but it has not previously been possible to quantitate this accurately. In recent work, Hammon et al. [56] (again using the ^{23}Na MRI protocol of Kopp et al. [28]) assessed skin and muscle ^{23}Na MRI in seven patients with AKI, peripheral oedema and weight gain. Before dialysis, patients with AKI evidenced higher calf muscle and skin ^{23}Na concentration than age matched controls (muscle: control = 16.6 ± 21 mmol/L, AKI patient = 31.7 ± 10.2 mmol/L, skin: control = 17.9 ± 3.2 mmol/L, AKI patient = 42.8 ± 11.8 mmol/L), but there was no reduction in skin and muscle ^{23}Na or water content after four to five cycles of haemodialysis, despite this achieving a mean total ultrafiltration volume of 8.36 litres. These observations are in contrast to those in patients receiving chronic haemodialysis (see below) and others with heart failure. Limitations of this study included the small number of participants and variation in the haemodialysis delivered. The failure to reduce tissue ^{23}Na with acute haemodialysis in the setting of AKI may be due to a more severe ^{23}Na accumulation in this setting and the unstable condition of patients leading to inconsistent ^{23}Na accumulation and mobilisation. The importance of this study was that it demonstrated the feasibility of monitoring calf muscle tissue sodium with ^{23}Na MRI in the context of AKI. Larger more detailed studies with standardised dialysis interventions are required to explore this topic further.

^{23}Na MRI has been used to study the removal of ^{23}Na from the skin and muscle during haemodialysis (HD) [29], (again with a 2D GRE imaging scheme) collecting ^{23}Na images of the calf before and after dialysis treatment. Skin and muscle ^{23}Na concentration increased with age in the HD patients, and also control subjects. Younger HD patients (<60 yrs) had similar skin and muscle ^{23}Na concentration as healthy controls before HD, after

HD the ^{23}Na levels in muscle decreased ($P < 0.01$) and also tended to decrease in the skin ($P = 0.1$). Before HD, older patients ($\geq$60 yrs) had a higher TSC than controls, whilst post-dialysis a reduction in TSC was found such that the ^{23}Na concentration post-haemodialysis was similar to controls in both skin ($P = 0.37$) and muscle ($P = 0.62$). In addition, this study compared skin and muscle ^{23}Na MRI measures to the ^{23}Na eliminated by the dialyser, however no correlation was found between ^{23}Na removal from plasma and the skin/muscle ^{23}Na reduction measured by MRI. This study therefore showed that tissue stores of ^{23}Na can be mobilised during HD. Across both skin and muscle the drop in ^{23}Na was of the order of 10 mmol/L after dialysis, but this secondary clearance of ^{23}Na from tissues was shown to be less predictable than clearance from the plasma.

Further evidence of potential adverse effects of tissue ^{23}Na accumulation was provided in a study by Deger at al. [54], which used ^{23}Na MRI to assess the mechanisms by which insulin resistance occurs in patients on maintenance haemodialysis compared to controls. All subjects underwent hyperinsulinemic-euglycemic-euaminoacidemic clamp studies to measure disposal rates of glucose (GDR) and leucine (LDR) as well as ^{23}Na MRI of the calf to assess the skin and muscle ^{23}Na concentration. GDR and LDR levels were lower in HD patients compared to healthy controls, whereas the muscle ^{23}Na concentration was higher in HD patients. An inverse linear relationship was found between TSC in the muscle and both GDR and LDR in HD patients, a trend not found in the healthy controls. There were no significant differences in skin ^{23}Na between dialysis patients and controls. This study hence concluded that excessive muscle ^{23}Na may contribute to the development of insulin resistance in patients with end stage renal disease on haemodialysis.

4.1.5 Aims

This chapter describes a pilot study to explore ^{23}Na signal intensity changes due to exercise. This is followed by a series of studies which aim to optimise methods of assessment of ^{23}Na concentration in the calf muscle and skin including optimisation of a 3D GRE scheme, B_1 correction methods and estimation of T_2^* relaxation time. This ultimately aims to develop a comprehensive ^{23}Na MRI protocol for imaging the calf to be applied in

future studies of clinical populations.

4.2 Studying the Effects of Exercise on Muscle ^{23}Na Signal Intensity Using a Surface Coil

This work was presented at the Joint Annual Meeting ISMRM-ESMRMB 2018, Paris Expo Porte de Versailles, Paris, France. As described in Section [4.1.1], ^{23}Na imaging has been used to show an increase in the ^{23}Na signal intensity in the calf muscle after exercise [67, 68]. Exercise causes a change in the exchange of metabolites and water between the intra-cellular and extra-cellular spaces. This work investigated ^{23}Na changes in response to exercising the calf inside the MR scanner. Here, the 13cm ^{23}Na RF coil described in Section [3.1.1.1] was used along with a dual echo 3D UTE scheme to compare the effects of exercise on the ^{23}Na of short and long components.

4.2.1 Method

Scanning was performed on a 3T Philips Achieva scanner using the 13 cm ^{23}Na coil housed in the coil support described in Section [3.1.1.1] Fig.[3.1], this was placed under the calf muscle for optimal imaging directly following exercise in the MRI scanner using a Trispect pedal system (Ergospect, GmbH, Austria) shown in Fig.[4.1a]. The Trispect is designed to stress-test the calf muscle undergoing planter flexion. A 3D radial FID readout with dual TE using a non-selective RF block pulse for excitation was optimised for imaging the flexor muscles in the exercise protocol. Dual echo time UTE data was collected at TE_1/TE_2 = 0.24/2.9 ms (resolution: 3 × 3 × 30 mm^3, 10 axial slices, FOV: 192×192 mm^2, TR: 100 ms, FA: 90°, NSA: 30, TA: 6:34 mins). Two subjects (2M; 22-23yrs) performed a high intensity anaerobic exercise protocol while supine on the scanner bed and were instructed to exercise to fatigue. Immediately following this, the 3D ^{23}Na UTE scans were serially collected every 6:34 minutes to image the return to baseline of the ^{23}Na signal following exercise. Following these ^{23}Na scans, a high resolution ^{1}H mDixon scan was acquired in the same space to allow for accurate muscle region segmentation

(resolution: 1×1×6 mm^3, 50 axial slices, FOV: 192×192 mm^2, TE_1 = 1.3 ms, ΔTE = 1.0 ms, FA = 3°, 6 echoes, TA: 2:16 mins). The scan protocol is outlined in Fig.[4.1b], with the total scan duration being 53 minutes.

(a) Trispect pedal system, Ergospect, GmbH, Austria, with the 13 cm coil base shown in blue under the calf. See Chapter 3, Fig.[3.1].

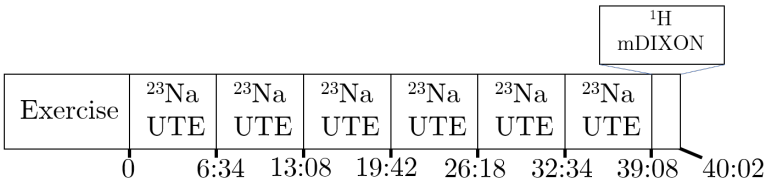

(b) Sequence of scans that made up the exercise protocol.

Figure 4.1: Scan protocol for exercise study.

The soleus and medial gastrocnemius muscle groups were manually segmented from the ^{1}H mDixon in-phase image to create masks of the two muscles. The masks were then applied to the ^{23}Na data and the mean ^{23}Na signal intensity within the muscles was calculated for each echo and the two echo images when summed together (combined TE).

4.2.2 Results

Fig.[4.2] shows an example data set along with segmentation of the soleus and gastrocnemius muscles from the ^{1}H mDixon scan and the corresponding ^{23}Na UTE image. One of the ^{23}Na data-sets can be seen in Fig.[4.3] showing the short TE, long TE and combined TE image. Note that due to the use of a surface coil the ^{23}Na signal intensity drops with distance from the coil, limiting the study only to the soleus and medial gastrocnemius muscles which lie close to the coil.

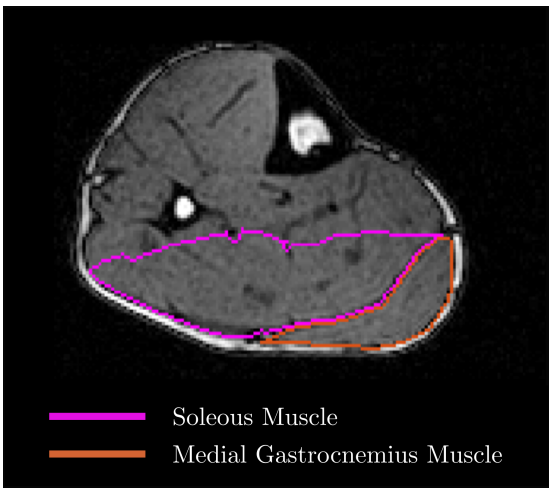

(a) mDixon ^{1}H image showing the soleous and medial gastrocnemius manually segmented.

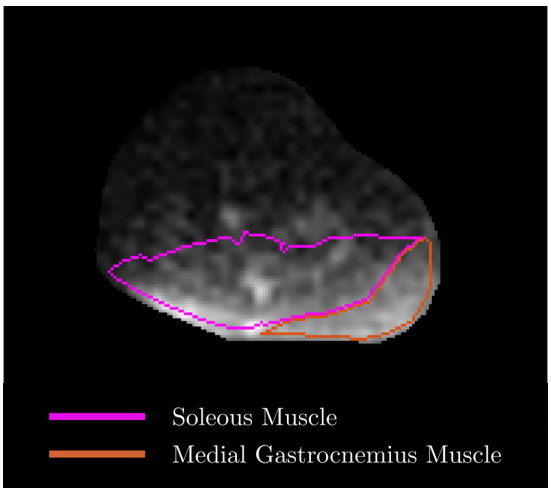

(b) Example short TE (0.24 ms) ^{23}Na UTE image of the calf acquired using the 13 cm surface coil, with the two muscle groups outlined.

Figure 4.2: ^{1}H and ^{23}Na image of the calf with two muscle groups outlined.

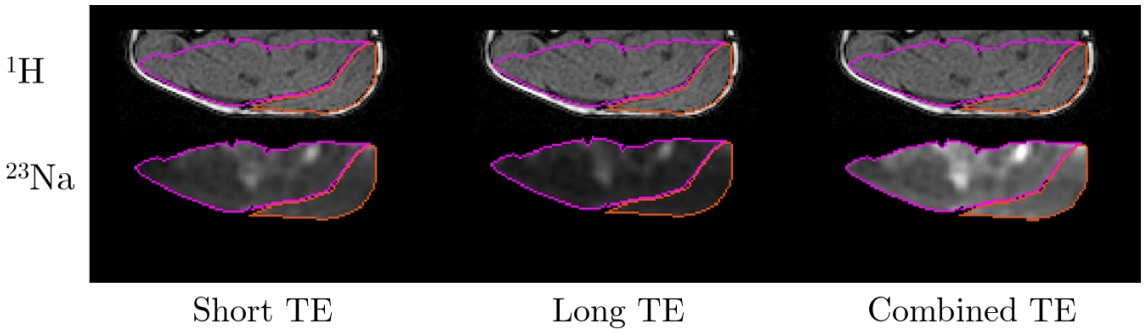

Figure 4.3: ^{23}Na images shown for the short TE (0.24 ms), long TE (2.9 ms) and combination of echoes together with the ^{1}H images and ROIs of muscle groups using to interrogate serially the ^{23}Na signal following exercise cessation.

Fig.[4.4] shows the ^{23}Na signal intensity changes immediately following exercise cessation. The short TE images showed a reduction in ^{23}Na signal intensity in the medial gastrocnemius muscle of -19 $\pm$ 5 % (P = 0.007) and in the solues muscle of -2 $\pm$4 % (P = 0.2) following exercise cessation. The long TE images showed a reduction in the ^{23}Na signal intensity of the medial gastrocnemius muscle of -25 $\pm$ 8 % (P = 0.007) and in the soleus muscle of -13 $\pm$ 6 % (P = 0.006). The combined image, the sum of signal intensities from the long and short TE images, showed a reduction in the medial gastrocnemius muscle of -21 $\pm$ 6 %(P = 0.008) and in the soleus muscle by -5 $\pm$ 6 % (P = 0.007) immediately post-exercise to baseline.

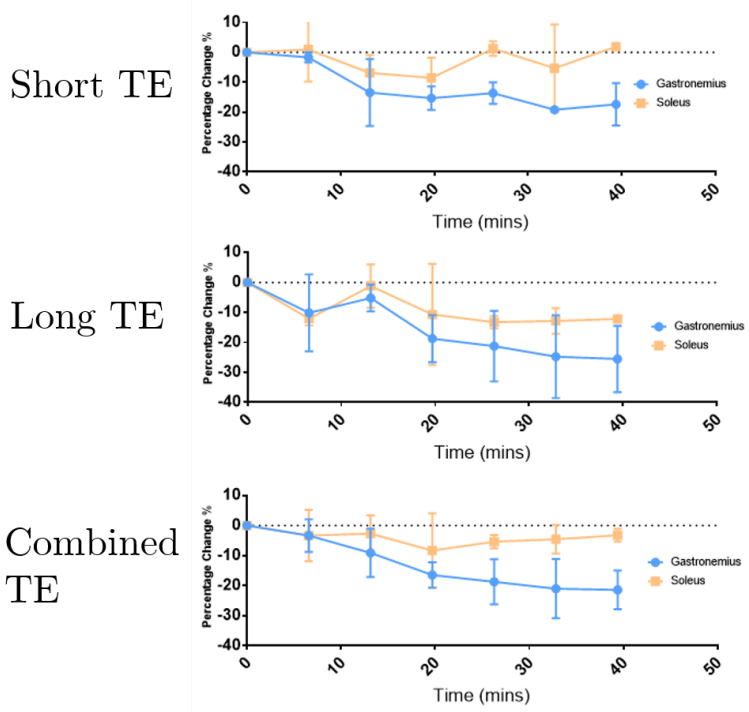

Figure 4.4: Percentage change in ^{23}Na signal intensity in the medial gastrocnemius and solues muscle after anaerobic exercise. Data shown for the short TE (0.24 ms), long TE (2.9 ms) and combined TE.

4.2.3 Discussion

The work demonstrates that at 3T it is possible to monitor the return of ^{23}Na signal intensity to baseline following anaerobic exercise in the medial gastrocnemius muscle and soleus muscles. The magnitude and half-life of the change of ∼30 mins, was in agreement with previous studies [65, 69]. The reduced variance in the ^{23}Na signal intensity measures at short TE compared to the long TE highlights the benefits of using a UTE sequence to capture the fast components of the bi-exponentially decaying T_2^* signal. The possible cause of the ^{23}Na intensity change could be intracellular Na^+ accumulation caused by depletion of the Na^+/K^+-ATPase of activated muscle cells or increased perfusion of the activated muscles after exercise [65].

The 13cm surface coil allows the flexibility to perform exercise using the Trispect immediately prior to imaging as the leg is not constrained by a coil (as can be the case for cylindrical birdcage coils) as it is placed below the calf. The surface coil does have the advantage that it can also be used to study the upper leg as has been performed by

Milani et al. [53]. However, the images demonstrate that the use of the 13cm surface coil is limiting in terms of coverage. Here only ^{23}Na signal intensity change is evaluated, no attempt has been made to quantify the ^{23}Na change using the reference bottles beneath the coil due to the need to B_1 correct the data. This requires the implementation of B_1 mapping. But this work highlights that in future, leg studies would benefit from a ^{23}Na birdcage RF coil that could provide full coverage across the entire calf to assess all muscles and allow an improvement in quantification of ^{23}Na concentration over a surface coil.
The following section outlines work performed using a ^{23}Na PulseTeq birdcage coil to determine the optimal methods for quantification of ^{23}Na concentration across the whole calf muscle.

4.3 Gradient Recalled Echo (GRE) Optimisation for ^{23}Na Imaging Using a Birdcage Coil

^{23}Na in tissue has a bi-exponential relaxation (as outlined in Section [2.1.5.3]) with rapid loss of signal, thus imaging at short echo times is required. Importantly, the short T_1 relaxation time can facilitate a short TR and fast averaging which can potentially compensate for the low intrinsic SNR of ^{23}Na imaging. For a gradient recalled echo (GRE) sequence, also termed a fast field echo (FFE) by Philips and described in Section [2.2.2], there are a number of sequence parameters which must be selected in order to produce the optimal ^{23}Na images. The low intrinsic SNR of ^{23}Na MRI means the sequence needs to be optimised to maximise the ^{23}Na signal. The GRE signal (S), is primarily dependent on flip angle, repetition time and echo time and is given by

$$S \propto \frac{\sin\alpha \cdot \left(1 - e^{-TR/T_1}\right)}{1 - \cos\alpha \cdot e^{-TR/T_1}} \cdot e^{-TE/T_2{}^\star} \tag{4.1}$$

where α is the flip angle, TR is the repetition time, T_1 is the longitudinal relaxation time, and $T_2{}^\star$ is the transverse relaxation time. For a given TR and T_1, the maximum signal is

obtained at the Ernst angle α_{Ernst} given by

$$\alpha_{Ernst} = \cos^{-1}\left(e^{-TR/T_1}\right). \tag{4.2}$$

Where if $TR >> T_1$ then the optimal flip angle is 90°.

The relationship in Equation [4.1] is represented in Fig.[4.5]. The maximum signal can be

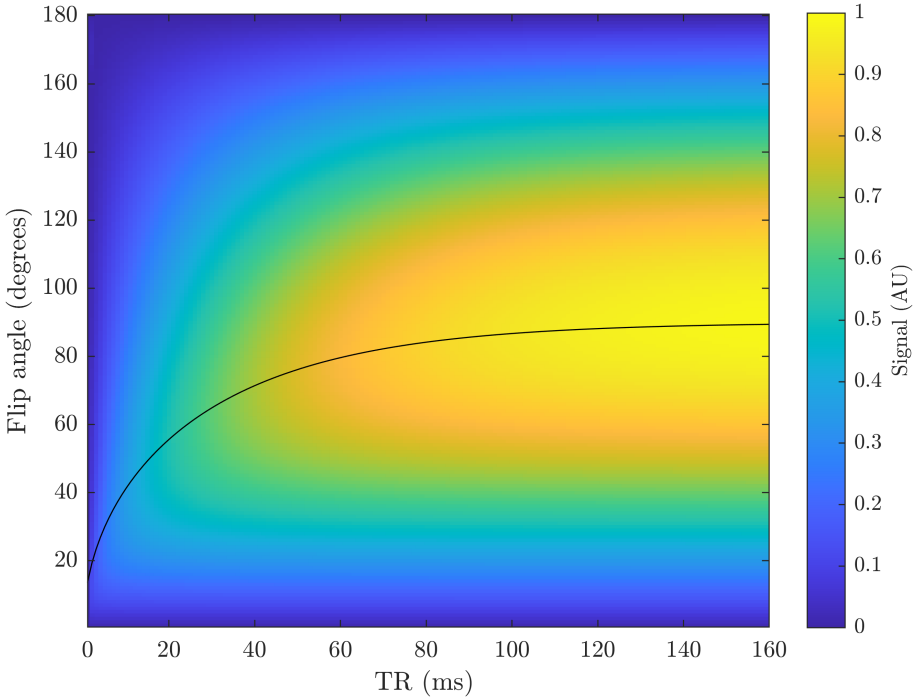

Figure 4.5: The dependence of signal intensity on TR and flip angle as given by Equation [4.1] for a T_1 relaxation time of 35 ms. The Ernst angle for a given TR is shown by the black line.

seen to occur when the TR is long enough to allow the longitudinal magnetisation to fully recover, approximately $5 \times T_1$. However, a longer TR increases the total acquisition (TA) of the scan. By collecting data at a shorter TR, the available time can instead be used to repeat acquisitions and collect a number of signal averages (NSA) which will increase the SNR by the square root of the number of acquisitions, $\sqrt{N_{acq}}$. Further, there can be several limitations that dictate the possible values that sequence parameters can take, these are mainly imposed by the scanner and RF coil hardware, such as the maximum average RF power and the maximum B_1 delivered by the RF coil and maximum flip angle

and minimum TR. The average RF power is given by

$$P_{avg} \propto \alpha TR^{-1}. \tag{4.3}$$

with the flip angle given by

$$\alpha \propto B_1 \tau \tag{4.4}$$

where B_1 is the amplitude of the RF pulse and τ is its duration. Increasing τ will increase the time between excitation and acquisition increasing TE. Due to the bi-exponential of T_2 decay of ^{23}Na, for ^{23}Na imaging the acquisition must be collected as soon as possible after the excitation, with the maximum B_1 limited by the RF coil.

Here a 3D GRE sequence is assessed to optimise the readout for ^{23}Na imaging for use at 3T with the PulseTeq birdcage coil outlined in Section [3.1.1.2]. The use of a fully relaxed sequence with a repetition time (TR) of 100 ms is compared to a spoiled steady state sequence of varying shorted TR values which facilitate increased number of signal averages within a constant scan duration.

4.3.1 Methods

This section outlines the optimisation of GRE for the ^{23}Na birdcage leg coil on the 3T Ingenia. In order to ascertain the optimum sequence parameters a series of 3D GRE scans (resolution 10 × 10 × 30 mm^3, FOV 180 × 200 × 300 mm^3, 10 slices, BW 490 Hz) were collected on the 50 mmol/L bottle leg ^{23}Na phantom. The series consisted of six 3D GRE scans each with a different TR and the corresponding Ernst angle. The maximum achievable B_1 was 30 μT. The scans position in the plot of theoretical intensity are shown in Fig.[4.6a] alongside the scan's pulse sequence parameters in Fig.[4.6b].

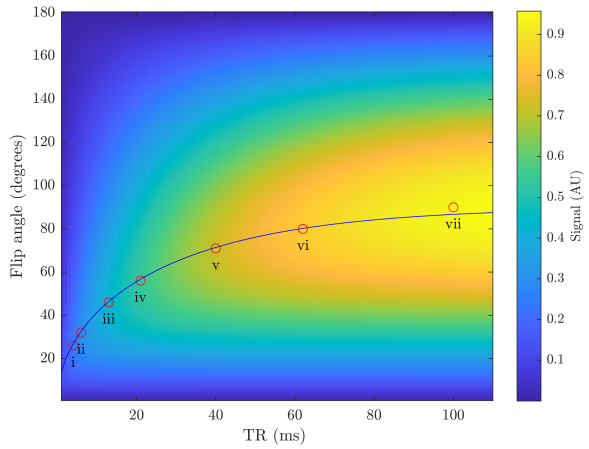

(a) The dependence of signal intensity on TR and flip angle for a T_1 of 35 ms. Each of the 3D GRE scans are shown by the red circles and the Ernst angle for a given TR is shown by the black line.

Scan	TR (ms)	Flip angle (Deg)	TE (ms)	B_1 (μT)	TA (s)
i	4	26	1.09	7.5	0.51
ii	6	32	1.06	10	0.76
iii	13	46	1.05	15	1.65
iv	21	56	1.01	20	2.67
v	40	71	0.96	30	5.05
vi	62	80	1.01	30	7.87
vii	100	90	1.05	30	12.7

(b) The key sequence parameters of TR, flip angle and TE, maximum B_1 amplitude and acquisition time (TA) for each 3D GRE acquisition.

Figure 4.6: Scan parameters for the optimisation of the 3D GRE scheme on the PulseTeq ^{23}Na birdcage coil.

The parameters in Table [4.1] were then used to collect each scan sequence in the same acquisition time. The acquisitions with the shorter TRs allowed more averages per unit time. This was tested in the leg phantom and *in vivo* (27 yrs male, University of Nottingham ethics 'Sodium MRI in the skin, muscle and kidneys' see Appendix [B.2]) using the same 3D GRE 10 × 10 × 30 mm^3 scan series with a calf positioned in the birdcage coil. Isotropic voxels with large slice thickness were used because in the calf very thick slices do not produce partial voluming because of the linear geometry of the leg.

Scan	TR (ms)	Flip angle (Deg)	TE (ms)	B_1 (μT)	NSA	TA (s)
i	4	26	1.09	7.5	195	94
ii	6	32	1.06	10	130	94
iii	13	46	1.05	15	60	94
iv	21	56	1.01	20	37	94
v	40	71	0.96	30	19	92
vi	62	80	1.02	30	12	90
vii	100	90	1.05	30	8	92

Table 4.1: Scan parameters for the scan series shown in Fig.[4.6b] where the number of signal averages (NSA) were varied so that all the scans had approximately the same total acquisition (TA) of 94 s.

For each image, the image SNR was computed from an ROI in the image (S_{image}) divided by the standard deviation of an ROI in the background noise ($\sigma_{background}$),

$$Image\ SNR = \frac{S_{image}}{\sigma_{background}}. \tag{4.5}$$

4.3.2 Results

A set of example ^{23}Na images from the central slice of the 50 mmol/L leg phantom obtained with a single average can be seen in Fig.[4.7a]. For each image the mean image SNR in the leg phantom was calculated and plot against the TR used for each acquisition as shown in Fig.[4.7b].

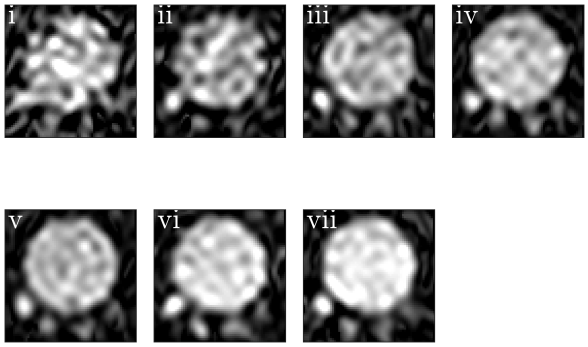

(a) ^{23}Na 3D GRE 10 × 10 × 30 mm^3 optimisation scans in the leg phantom. Each image was acquired using the scan parameters given in Fig.[4.6].

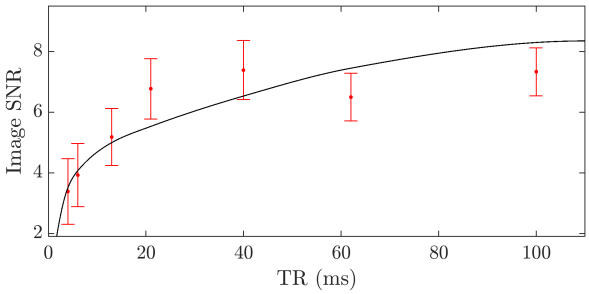

(b) Image SNR in the leg phantom for a single acquisition. The predicted SNR is shown by the black line.

Figure 4.7: Single acquisition ^{23}Na images and corresponding image SNR.

The measured image SNR in Fig.[4.7b] followed the theortical prediction in Fig.[4.6a], with the largest image SNR at the longest TR. The longer TRs allowed a higher maximum B_1 and shorter TE, but the reduction in TE is only minimal and was not expected to have a large effect on the measured image SNR, as shown in Fig.[4.7b]. However, the longer TR resulted in a longer acquisition scan time (TA) for a scan. Fig.[4.8] assesses the benefits of using a shorter TR, with scans performed varying the NSA for a given TR so that each scan was collected in the same total acquisition (TA) of 94 s. The images in Fig.[4.8a] show that enhanced image SNR per unit time is obtained when using a short TR and collecting many averages, with the mean image SNR per unit time shown in Fig.[4.8b].

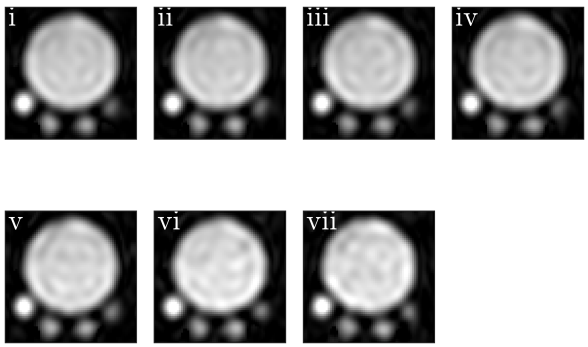

(a) ^{23}Na 3D GRE 10 × 10× 30 mm^3 optimisation scans. Each image acquired using the scan parameters in Fig.[4.1].

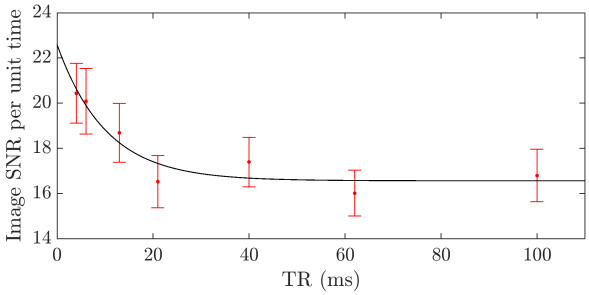

(b) Image SNR in the leg phantom shown in (a).

Figure 4.8: Example central slice images and image SNR per unit time for scans of varying TR collected in the same total acquisition time (TA) as outlined in Table [4.1].

Images of the calf for the scan parameters outlined in Table [4.1] can be seen in Fig.[4.9a], as expected the ^{23}Na concentration was lower in the body than in the 50 mmol/L leg phantom. The image SNR per unit time of the leg for a TA of 94 s is plot in Fig.[4.10a]. The same relationship between the scans collected at a given TR and image SNR per unit time was seen *in vivo* as in the leg phantom, with many acquisitions at a short TR producing a greater image SNR per unit time. Fig.[4.9b] shows all ten slices acquired in the scans, note the variation in ^{23}Na signal intensity across slices, due to the variation in B_1 field along the length of the leg coil, correction of this effect is described later in Section [4.5].

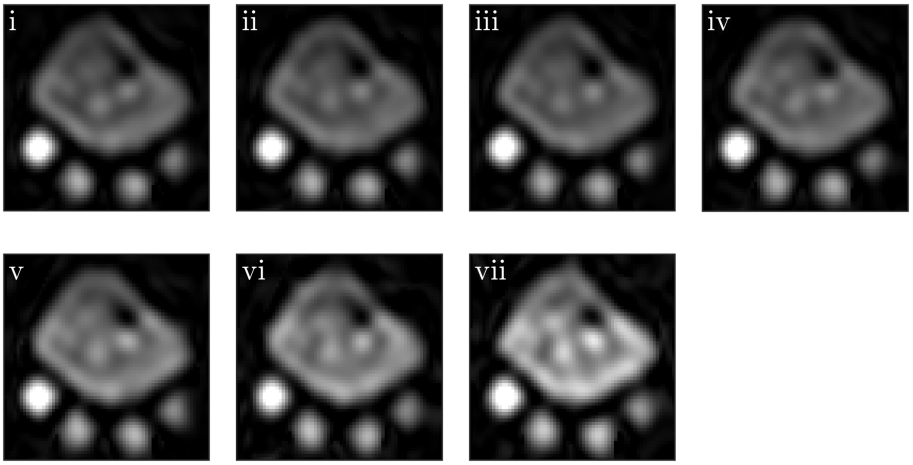

(a) ^{23}Na 3D GRE $10 \times 10 \times 30$ mm^3 optimisation scans carried out *in vivo* on the calf muscle using the ^{23}Na birdcage leg coil. Each image was acquired using the scan parameters in Table [4.1]. Four reference bottles of 20, 30, 40 and 50 mmol/L NaCl can be seen under the leg.

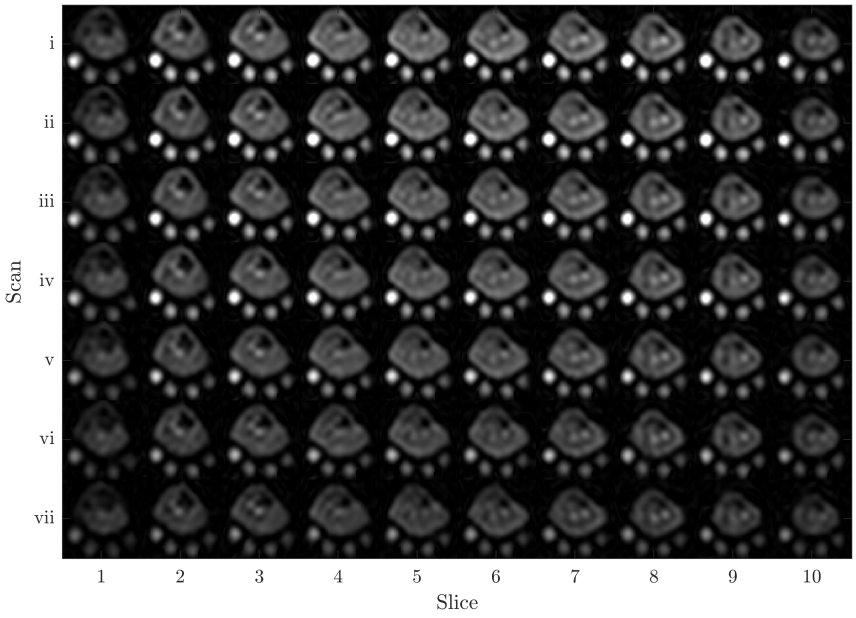

(b) Ten slices acquired in the scans showing the variation in ^{23}Na signal intensity over the slices. Note the full coverage of the muscle as compared to the surface coil in Section [4.2].

Figure 4.9: Example *in vivo* calf muscle images collected at varying TR in the same total acquisition time as outlined in Table [4.1].

Fig.[4.10b] shows the image SNR per unit time in the four reference bottles, confirming the same pattern as was seen in the leg. The ratio between the signal in the 50 mmol/L reference bottle and the leg can be seen in Fig.[4.10c]. The increased ratio at longer TR suggests a T_1 dependency due to a difference in T_1 of tissue and the reference bottles. The use of a short TR improves the image SNR per unit time but will result in some relaxation weighting. Without T_1 consideration this will effect the ^{23}Na quantification,

which is dependent on the ratio of the ^{23}Na signal intensities in the leg to the reference bottles. A similar pattern of ratio dependence is seen for all reference bottles due to their matched T_1.

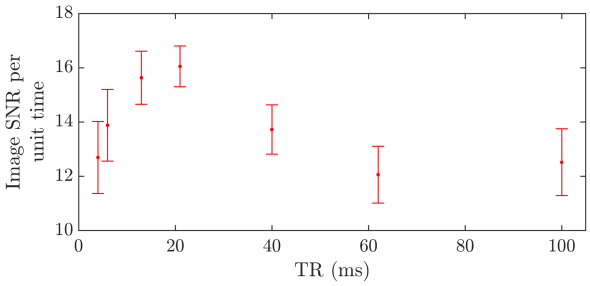

(a) Image SNR per unit time within the calf muscle.

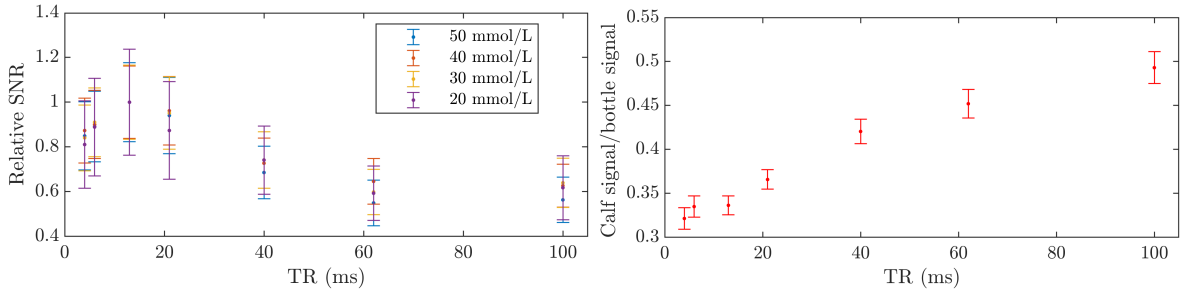

(b) Mean signal in the three reference bottles.

(c) Ratio of ^{23}Na signal intensity in the calf muscle as compared to the 50 mmol/L NaCl reference bottle.

Figure 4.10: Image SNR in the calf muscle, and relation of ^{23}Na signals in muscle to the reference bottles as a function of TR, illustrating longitudinal relaxation weighting.

The reduced SNR for scans i and ii suggests that these scans are not at the Ersnt angle, this is confirmed in Fig.[4.11] which is a simulation of the expected SNR for a range of TRs for different values of T_1.

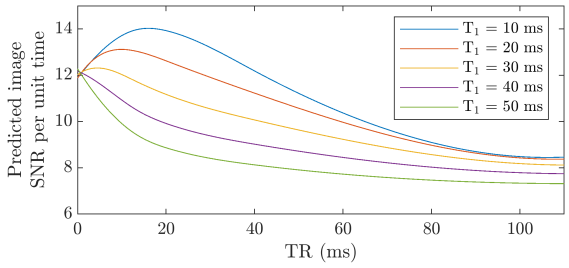

Figure 4.11: The predicted effects of the T_1 on the the image SNR.

4.3.3 Discussion

This section has demonstrated that to achieve the maximum image SNR per unit time a short TR should be used to collect many averages, this is achieved by keeping the B_1 amplitude low to allow the scan to remain under the average power limit. Here these steps were performed for the PulseTeq birdcage leg and similar methods are discussed for the ^{23}Na body RF coils in Chapter 5. However, shortening the TR to increase image SNR per unit time will result in a T_1 dependency of the GRE sequence which has to be corrected for accurate ^{23}Na quantification, this is addressed in Section [4.6].

4.4 Tissue Sodium Concentration (TSC) Calibration

In order to convert the ^{23}Na signal intensity images into maps of tissue sodium concentration (TSC) a series of reference bottle phantoms of known ^{23}Na concentration must be used to calibrate the ^{23}Na signal intensity images. These reference bottles are placed in the field-of-view of the ^{23}Na scan, as can be seen in Fig.[4.9] for the ^{23}Na birdcage leg coil.

4.4.1 Method

In Section [4.3] GRE optimisations were carried out using an in-plane resolution of $5 \times 5 \times 30\text{mm}^3$, the coarse in-plane resolution of the GRE optimisation allowed for short scan times necessary for multiple scans to be collected in a single scan session. To produce more detailed TSC maps a higher in-plane resolution is preferred, so here the data are collected at a resolution of $3 \times 3 \times$ 30 mm^3. Since the smaller voxel size reduced the image SNR, the number of scan averages was increased so that the scan time increased from 90 s to 8 mins. To assess the calibration method, four subjects (25-31yrs, 3M:1F) were scanned using a ^{23}Na GRE sequence (resolution: $3 \times 3 \times 30$ mm^3, TA: 8 mins, TR: 9 ms, TE: 1 ms, FA: 40°, BW: 490 Hz, NSA: 186).

To reduce the effect of B_1 inhomogeneity on the concentration calibration, a B_1 correction was applied to the ^{23}Na intensity images. A double angle B_1 map was collected (resolution:

$5 \times 5 \times 30$ mm^3, TA: 5.5 mins, TR: 211 ms, TE: 4.4 ms, FA: 60°), a B_1 mapping scheme which is available on the Philips system as a commercial product, the theory of this is covered in Section [2.4.1]. B_1 correction was performed on the ^{23}Na images by scaling the ^{23}Na signal intensity image by the measured B_1 map. An ROI was drawn around each bottle. The mean pixel values within each bottle ROI was calculated and a linear regression was then applied from the signal intensity to the bottles concentrations.

4.4.2 Results

Fig.[4.12] shows one example ^{23}Na with the reference bottles outlined and the accompanying double angle B_1 map.

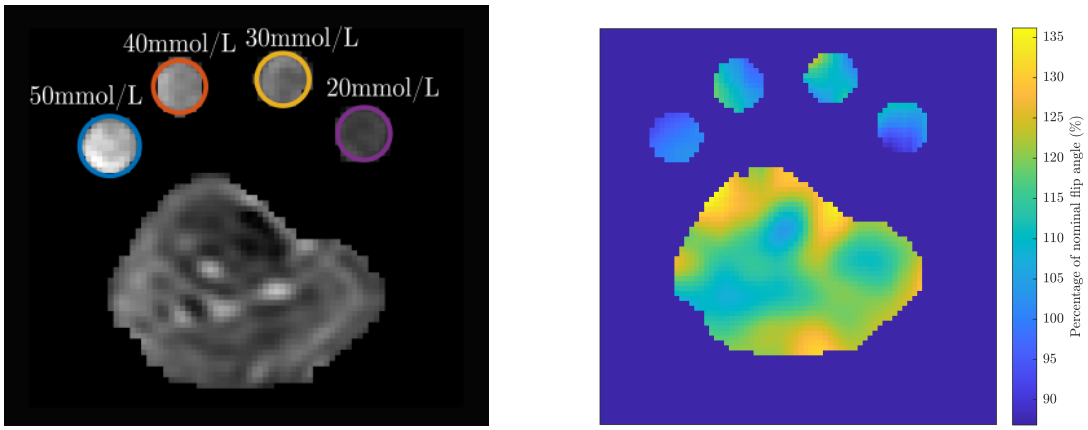

(a) ^{23}Na image of the central slice of 3D GRE *in vivo* Showing the reference bottles placed above the leg and their known concentration of NaCl.

(b) Double angle B_1 map.

Figure 4.12: A single slice of the 3D GRE ^{23}Na data and accompanying B_1 map collected using the ^{23}Na birdcage leg coil.

The linear regression of the signal in the reference bottles can be seen in Fig.[4.13], both for the uncorrected ^{23}Na signals and the signals following B_1 correction. The improvement in the regression following B_1 corrections is clearly shown in Fig.[4.13b].

Having performed the regression, this was then used to convert the pixel intensities of the ^{23}Na images into ^{23}Na concentration, as shown in Fig.[4.14]. Fig.[4.15] shows histograms of the concentration in the leg for the four subjects, note the higher ^{23}Na concentrations in the blood in vessels at > 55 mmol/L.

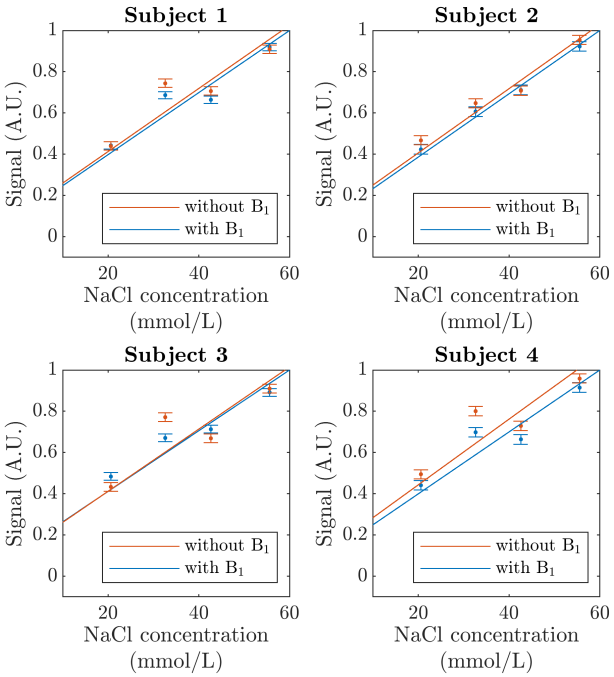

(a) The linear regression of the reference bottles in the individual subjects without and with double angle B_1 correction.

Subject	Rsquare	
	Without B_1 correction	With B_1 correction
1	0.917	0.941
2	0.973	0.992
3	0.880	0.946
4	0.891	0.933
Mean±SD	0.92±0.04	0.95±0.03

(b) Regression of reference bottles across subjects without and with double angle B_1 correction.

Figure 4.13: Linear regression of the mean pixel intensities in the reference bottles with ^{23}Na concentration without and with B_1 correction.

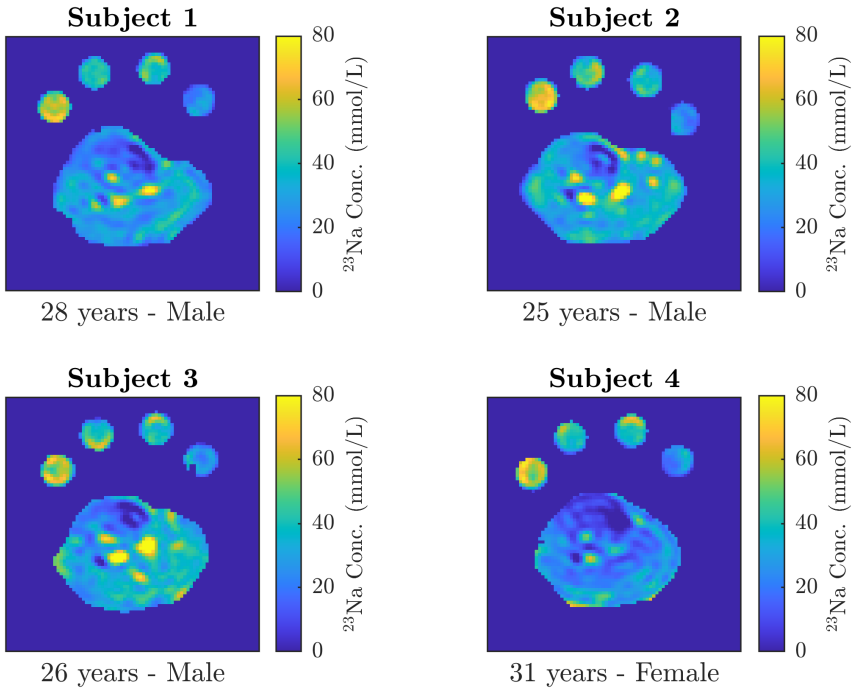

Figure 4.14: Tissue sodium concentration (TSC) maps of the four subjects after B_1 correction using double angle B_1 mapping.

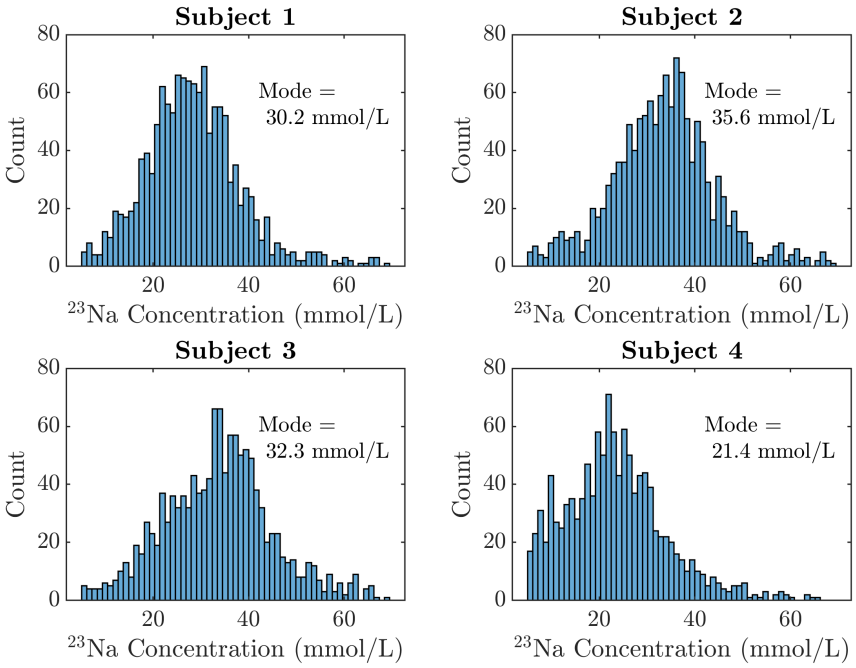

Figure 4.15: Histogram of ^{23}Na concentration in the calf muscle in Fig.[4.14].

4.4.3 Discussion

This work has used the reference bottles to produce TSC maps, following correction for B_1 inhomogeneities. After B_1 correction the fit to the linear regression for Subject 2 was excellent (0.992). However, for Subjects 1, 3 and 4 this regression was lower at 0.933 - 0.946. This can be seen to arise predominately from the outlier signal of the 30 mmol/L reference bottle giving a deviation from the fit (Fig.[4.13a]). The inaccuracy of the reference bottle signals is also apparent from the TSC maps in Fig.[4.14] from the heterogeneity across the bottles. This is likely caused by the inaccuracy in the B_1 mapping in the reference bottles. The bottles sit at the edge of the coil where the B_1 field is expected to be the most in-homogeneous from the rungs of the birdcage coil. Despite being widely used, previous work has suggested that the double angle B_1 method is not the optimal B_1 mapping scheme for ^{23}Na imaging [51,52]. The alternative phase-sensitive B_1 mapping (Section [2.4.2]) is thus implemented in the following section.

4.5 Optimisation of B_1 Mapping for B_1 Correction of ^{23}Na Images

4.5.1 Phase-sensitive B_1 Mapping Method

The phase-sensitive B_1 mapping technique was described in Section [2.4.2]. This is not a commercial sequence available on the Philips scanner software platform and so I had to implement this in the Philips Pulse Programming Environment (PPE).

The pulse sequence is shown in Fig.[4.16a]. The excitation pulse consists of two composite components, the first with a flip angle of 2α and the second with a flip angle of α. The B_1 magnitude of the two components is matched and the duration of the first 2α pulse is twice that of the second α pulse. The sequence is comprised of two mixes, the first with a positive initial RF pulse (α_0) and the second with a negative initial RF pulse ($2\alpha_{180}$).

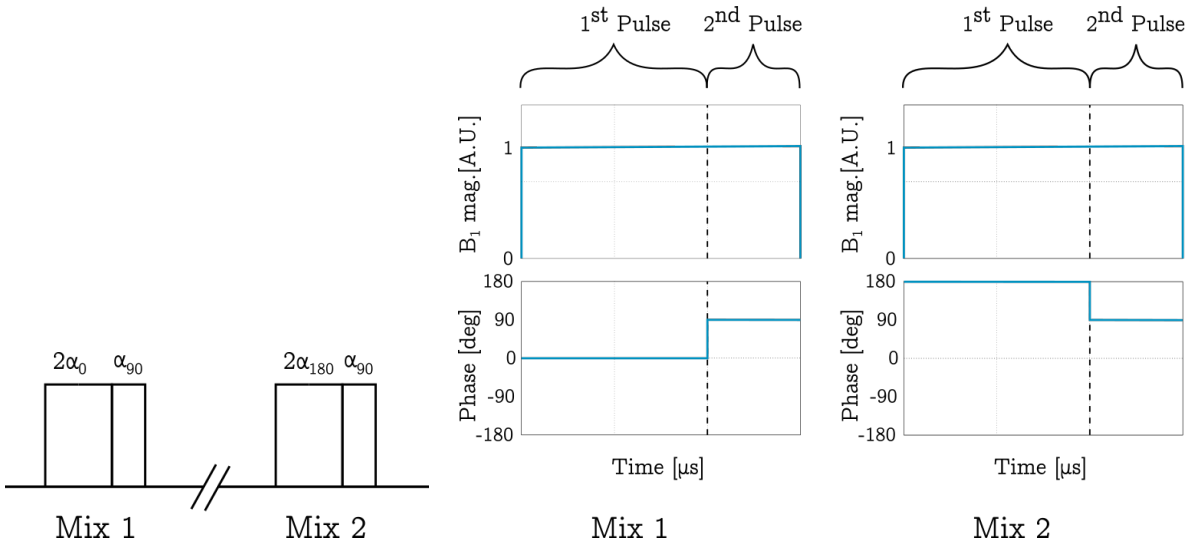

(a) Overview of the composite excitation pulses showing the flip angle 2α or α and the subscript refers to the phase of each pulse.

(b) A detailed look at the pulses showing the relative timing, magnitude and phase associated with each component.

Figure 4.16: The excitation pulses used in the phase-sensitive B_1 mapping technique.

4.5.1.1 Method

In order to test the implementation of the phase-sensitive B_1 mapping technique a series of measures were carried out using the ^{23}Na PulseTeq leg coil. The first test was to replicate

the theoretical plots shown in Chapter 2 Fig.[2.26]. A series of scans (Resolution: $5\times5\times30$ mm^3, TA: 3 mins, TE: 4.6 ms, NSA: 9, TR: 375 ms) were carried out on the 50 mmol/L leg phantom (detailed in Chapter 3 Section [3.3.5.1]), each three minutes in duration and in each scan α was increased in steps of 10° from 25° to 155°. A circular ROI with a radius 30 mm was placed in the centre of the phantom and the mean intensity values inside the ROI of the real and imaginary images was calculated.

B_0 maps were collected to assess the degree of B_0 field inhomogeneity to determine whether this would influence the phase-sensitive B_1 mapping method. B_0 maps were collected using both the ^{23}Na birdcage leg coil and the ^{1}H Q-Body coil. B_0 maps were produced using a dual GRE scan, with images collected at two echo times with the echo spacing ΔTE of 2 ms, the difference in the phase ($\Delta\phi$) of the two images is compared to calculate the B_0 map, from

$$\Delta f = \frac{\Delta\phi}{2\pi\Delta TE} \tag{4.6}$$

where the B_0 map is displayed in frequency shift Δf in Hz. B_0 maps were collected with the following parameters for ^{1}H: Resolution: $2.5 \times 2.5 \times 12$ mm^3, slices: 20, NSA: 2, TE: 3.1 ms, FA: 30°, TR: 17 ms, TA: 69 s, with the reconstruction matrix matched to the ^{23}Na images and ^{23}Na: Resolution: $3 \times 3 \times 20$ mm^3, slices: 2, NSA: 50, TE: 1 ms, FA: 60°, TR: 30 ms, TA: 153 s.

4.5.1.2 Results

Fig.[4.17] shows the resulting phase images and the calculated phase difference image. The B_1 map was converted from the phase difference image using a look-up table of Eq.[2.56] as outlined in Section [2.4.2], this was performed offline in Matlab (The MathWorks Inc, Natick, MA, USA).

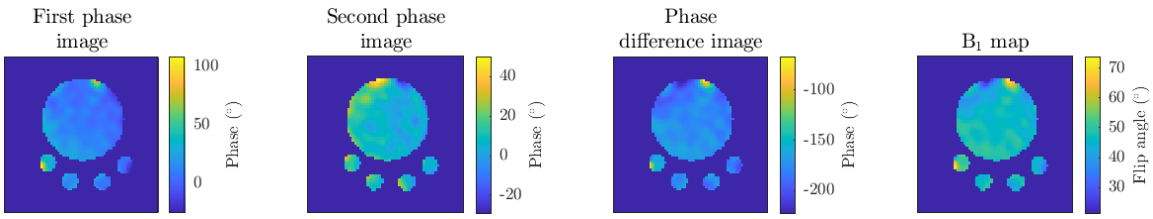

Figure 4.17: The two phase images used to generated the phase difference image and the resultant B_1 map.

Values of the real and imaginary signal across the range of α values are shown in Fig.[4.18] for mix 1 and mix 2.

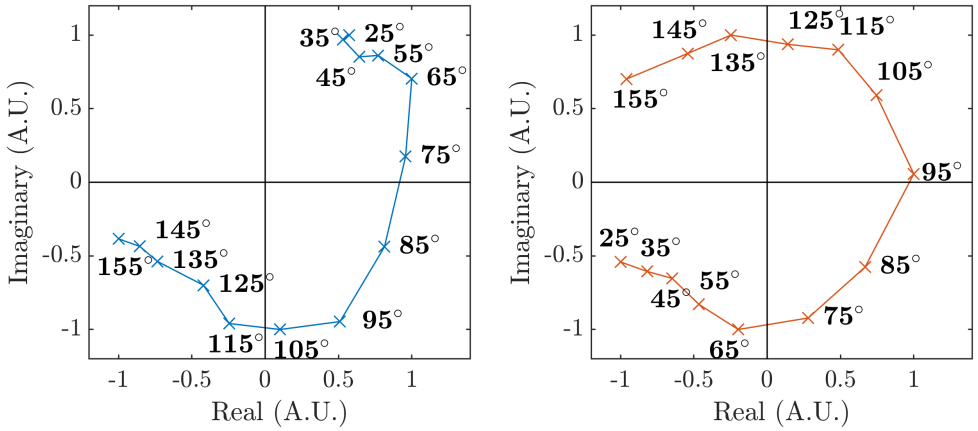

Figure 4.18: The trajectory of the magnetisation after mix 1 and mix 2 for a range of nominal flip angles, in the presence of a -40 Hz B_0 frequency offset.

The results shown in Fig.[4.18] can be seen to follow those of theory shown in Chapter 2 Fig.[2.26], except at low ($\lesssim$55°) and high ($\gtrsim$125°) flip angles which had low SNR. Taking the difference between the images from the two mixes, the measured phase difference compared to the predicted phase difference can be plot for the range of flip angles α as shown in Fig.[4.19]. Note, here the behaviour of the phase-sensitive method is shown for a range of α but in practice a B_1 map is collected for one value of α which falls within the linear range.

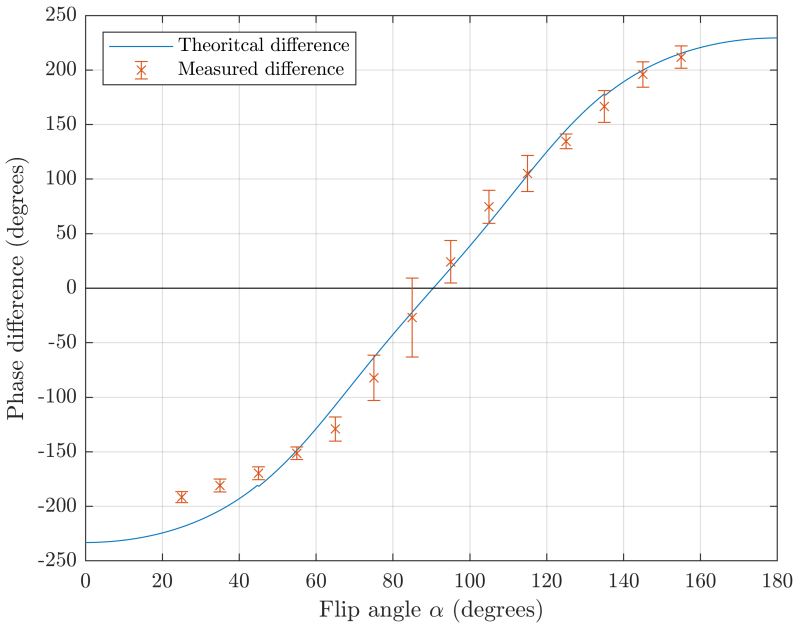

Figure 4.19: The measured compared to the theoretical phase difference for a given nominal flip angle α, as measured in the 50 mmol/L leg phantom.

Example ^{1}H and ^{23}Na B_0 maps can be seen in Fig.[4.20]. There is broad agreement between the two B_0 maps collected using ^{1}H and ^{23}Na. However, the far superior SNR for ^{1}H allowed a higher resolution acquisition and shorter acquisition time B_0 map. The phase-sensitive method is insensitive to B_0 inhomogeneity in the range of $\pm$200 Hz [72], as measured here. Importantly, the B_0 field is also far from the discontinuity seen at $\pm$500 Hz, shown in the theoretical plots in Chapter 2 Fig.[2.27].

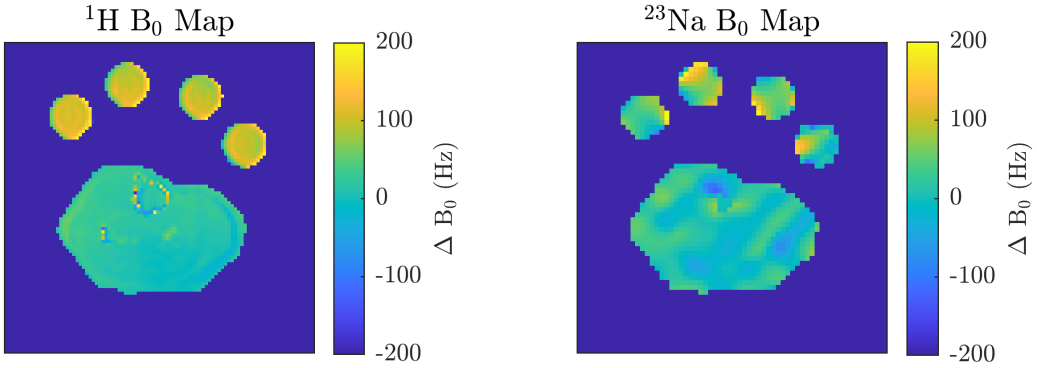

Figure 4.20: Example B_0 map collected from the leg phantom inside the ^{23}Na birdcage coil, collected using the ^{23}Na birdcage leg coil and the ^{1}H Q-Body coil.

4.5.2 Comparison of Double Angle and Phase-sensitive B_1 Mapping Techniques

4.5.2.1 Methods

To assess the benefits of the phase-sensitive B_1 mapping method, this was compared to the double angle magnitude B_1 mapping method. Scans were carried out using the PulseTeq leg coil on the 50 mmol/L leg bottle phantom (Chapter 3 Section [3.3.3]) and the accompanying reference bottles of known NaCl concentrations of 20, 30, 40 and 50 mmol/L. The double angle imaging sequence, reconstruction and B_1 map calculation is provided as part of the Philips scanning software on the 3T Ingenia scanner. For comparison both B_1 mapping methods were collected in the same total acquisition time. The scan parameters were: Double angle method: Resolution: $5\times5\times30$ mm^3, TE: 4.5 ms, first FA: 60°, TR: 240 ms, NSA: 10, TA: 7.8 mins; Phase-sensitive method: Resolution: $5\times5\times30$ mm^3, TE: 2.1 ms, first FA: 60°, TR: 210 ms, NSA: 12, TA: 7.8 mins. The B_1 maps from each technique was used to correct a GRE ^{23}Na image (resolution: $3\times3\times30$ mm^3, TA: 5 mins, TR: 6 ms, TE: 1.57 ms, FA: 32°, NSA: 183). Matched data was also collected *in vivo*.

4.5.2.2 Results

The magnitude images produced by double angle and phase-sensitive B_1 mapping sequences collected on the leg phantom are shown in Fig.[4.21]. They demonstrate that even at coarse in-plane resolution of $5\times5\times30$ mm^3 the image SNR of the magnitude images is low. The low SNR has been shown to limit the accuracy of magnitude B_1 mapping methods [51], such as the double angle method.

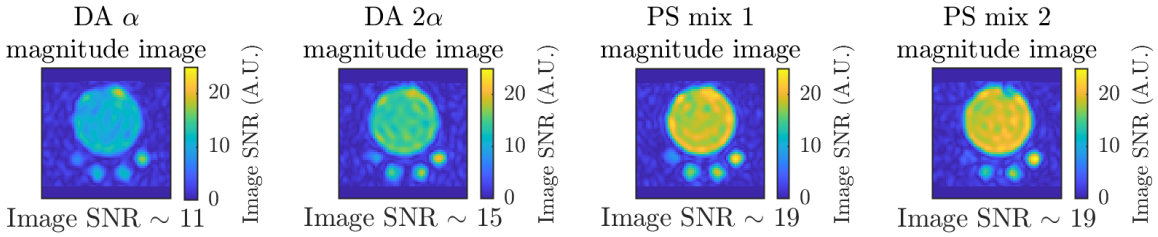

Figure 4.21: Comparison of the image SNR in the magnitude images of the double angle and phase-sensitive B_1 methods.

The results of correction using the double angle and phase-sensitive B_1 mapping is shown in Fig.[4.22]. Calibration of the ^{23}Na GRE image of the leg phantom using the reference bottles (see section Section [4.4]) was carried out using each B_1 mapping methods to produce ^{23}Na concentration maps as shown in Fig.[4.22].

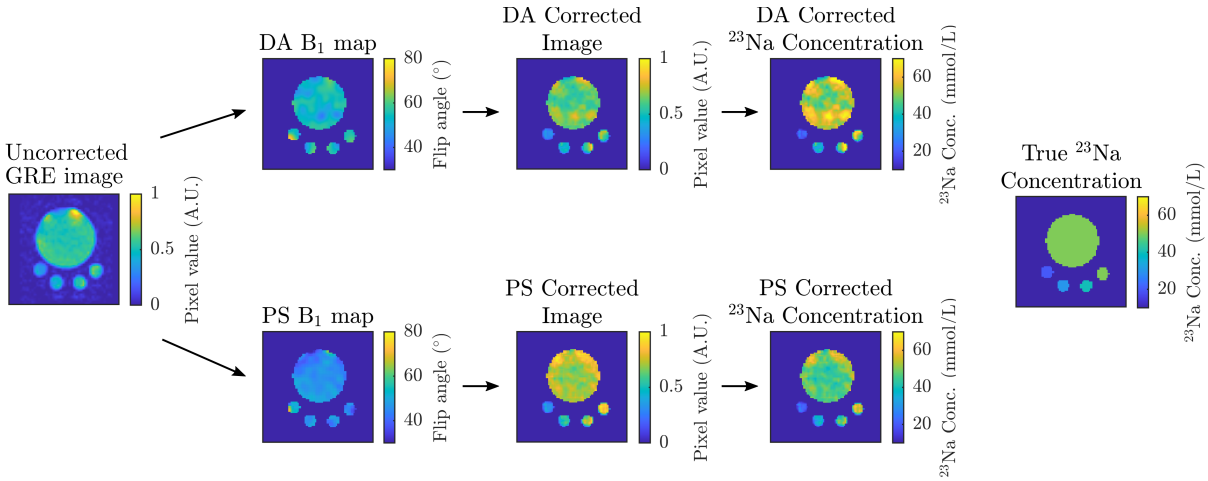

Figure 4.22: Comparison of double angle and phase-sensitivity B_1 mapping methods, (shown a nominal FA of 60°). The uncorrected GRE ^{23}Na image undergoes B_1 correction before the image is converted to ^{23}Na concentration using the reference bottles. The true ^{23}Na concentrations are shown in the right hand image

In Fig.[4.22] the uncorrected GRE image shows both high and low signal regions at the top of the 50 mmol/L leg bottle phantom, next to the edge of the RF coil. This pattern is present in the B_1 maps produced by both methods and is due to the nature of the B_1 field produced by the birdcage RF coil, with the B_1 field becoming non-uniform close to the rungs of the birdcage. A similar effect can be seen in the reference bottles which sit next to the inner edge of the RF coil, in the uncorrected GRE image the four concentrations of NaCl (20, 30, 40 and 50 mmol/L) should produce a clear difference in ^{23}Na signal intensity, however this is not seen. The variance in the B_1 field across the reference bottles accounts for the unexpected reference bottle signal intensities in the uncorrected GRE image. The accuracy of the B_1 correction of ^{23}Na signal effected the accuracy of the linear regression of the reference bottles and the conversion of the signal intensity in the leg bottle phantom to ^{23}Na concentration. For the double angle method, the linear regression R^2 of the reference bottles was 0.81 and for the phase-sensitive method the R^2 was 0.98, example regressions can be seen in Fig.[4.23].

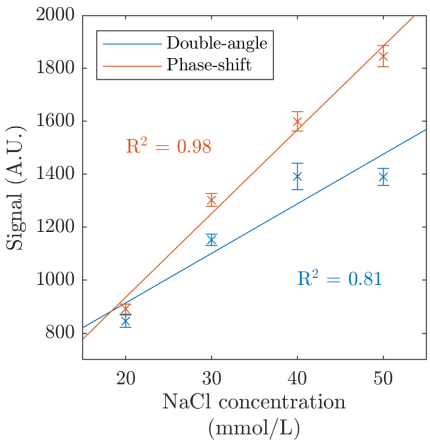

Figure 4.23: The linear regression of the reference bottles for ^{23}Na images B_1 corrected using the double angle and phase-sensitive methods.

The mean ^{23}Na concentration in the leg phantom and reference bottles calculated from the B_1 corrected ^{23}Na concentration maps is provided in Table [4.2]. The ^{23}Na concentrations in the reference bottles can be compared to the measured reference bottle concentrations obtained using ICP. Fig.[4.24] shows histograms of the ^{23}Na concentration inside the leg phantom, this can bee seen to be sharper for the phase-sensitive correction method (FWHM of 7.9 mmol/L) compared to the double angle method (FWHM of 16.0 mmol/L), with outliers produced by the noise in the B_1 map.

	^{23}Na Concentration mean ± SD (mmol/L)		
Method / Region	Double angle B_1 map corrected	Phase-sensitive B_1 map corrected	IPC measured
50 mmol/L phantom	54.7±6.7	47.7±4.4	—
20 mmol/L bottle	16.4±7.8	18.6±5.5	20.6±0.3
30 mmol/L bottle	32.9±9.0	31.6±7.0	32.6±0.6
40 mmol/L bottle	45.0±19.7	41.0±10.8	42.6±0.6
50 mmol/L bottle	45.7±15.9	49.0±11.8	54.3±1.0

Table 4.2: Comparison of the measured ^{23}Na concentration in the leg phantom and reference bottles after correction with the double angle and phase-sensitive B_1 mapping methods. Additionally the ^{23}Na concentrations in the reference bottle measured by ICP are shown.

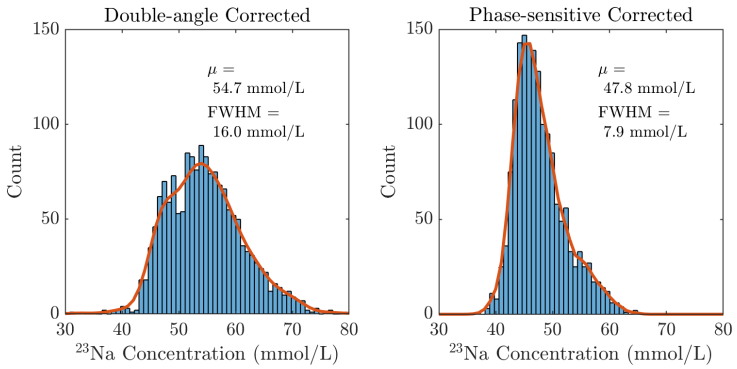

Figure 4.24: Histogram of the ^{23}Na concentrations in the 50 mmol/L leg phantom bottle after B_1 correction using the double angle and phase-sensitive methods, with FWHM of each computed.

Results of *in vivo* calf data is shown in Fig.[4.25]. The uncorrected GRE images had an image SNR of 21 ± 6. For the subject's comfort the reference bottles were placed on top of the leg and a foam mat was placed beneath the calf to increase the spacing between the coil and leg. In both B_1 maps the inhomogeneous B_1 field near the rungs of the birdcage coil can be seen, with this being detected to a greater extent in the phase-sensitive B_1 method. For this data, the R^2 of the reference bottles was 0.80 for the double angle method and 0.99 for the phase-sensitive method.

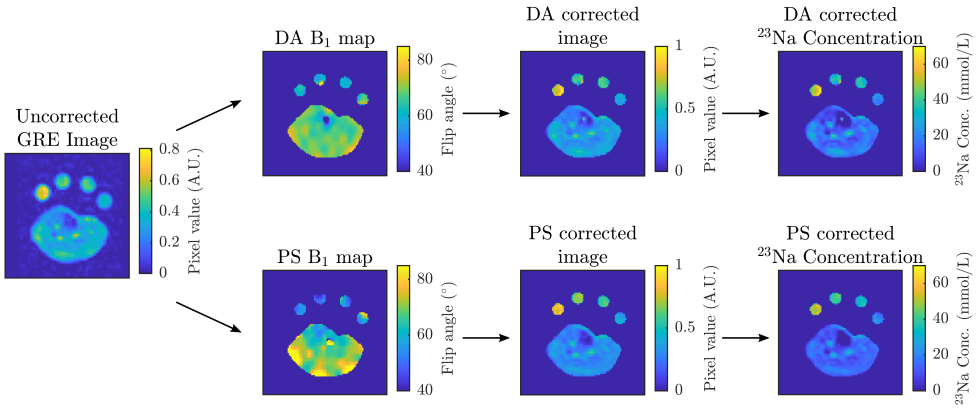

Figure 4.25: Comparison of double angle and phase-sensitive B_1 mapping applied *in vivo* to generate ^{23}Na concentration maps of the calf.

Table [4.3] provides the ^{23}Na concentrations in the reference bottles, again highlighting the greater accuracy of the phase-sensitive B_1 corrected measures.

	^{23}Na Concentration		
	mean ± SD (mmol/L)		
Region \ Method	Double angle B_1 map corrected	Phase-sensitive B_1 map corrected	IPC measured
20 mmol/L bottle	19.8±3.5	19.3±4.0	20.6±0.3
30 mmol/L bottle	33.7±5.3	31.6±4.5	32.6±0.6
40 mmol/L bottle	33.0±8.0	39.0±5.1	42.6±0.6
50 mmol/L bottle	53.4±7.9	50.2±4.2	54.3±1.0
Calf muscle	14.7±8.0	12.9±6.1	—
	median ± SD (mmol/L)		
Calf muscle	15.1±8.0	13.4±6.1	—

Table 4.3: Comparison of the measured ^{23}Na concentration reference bottles and *in vivo* after correction with the double angle and phase-sensitive B_1 mapping methods. Additionally the ^{23}Na concentrations in the reference bottle measured by ICP are shown.

Fig.[4.26] shows the histogram of ^{23}Na concentration maps of the calf for the double angle and phase-sensitive corrected maps shown in Fig.[4.25].

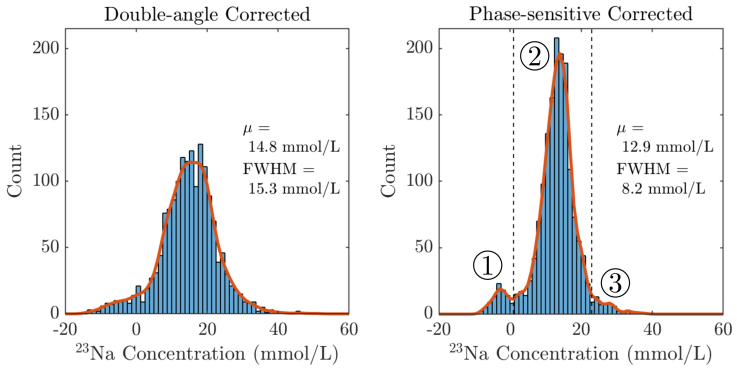

Figure 4.26: Histogram of the ^{23}Na concentration in the calf muscle following B_1 correction using the double angle and phase-sensitive B_1 mapping methods. The corresponding ^{23}Na maps can be seen in Fig.[4.25]. The three sections in the phase-sensitive histogram can be attributed to three different regions within the calf: (1) bone, (2) tissue and (3) vessels, the corresponding concentration maps for these three regions can be seen in Fig.[4.27].

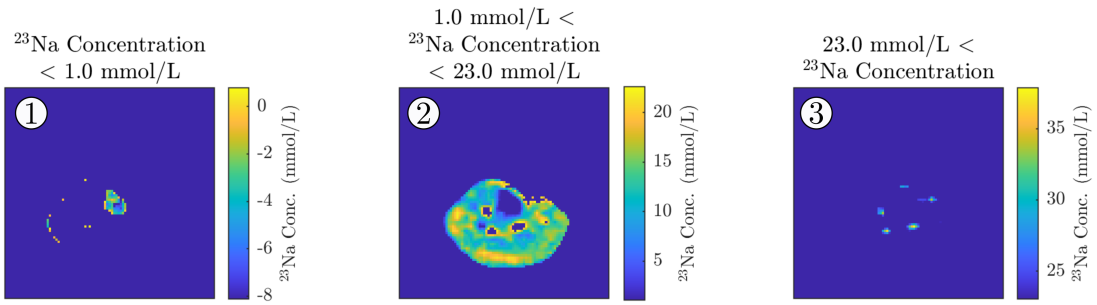

Figure 4.27: ^{23}Na concentrations in three regions within the calf: (1) bone, (2) tissue and (3) vessels, separated out using the histogram in Fig.[4.26].

Similar to the leg phantom measurements, the distribution of ^{23}Na concentrations computed using the double angle B_1 method was greater than for the phase-sensitive B_1 method, as demonstrated by a FWHM of 15.3 mmol/L compared to 8.2 mmol/L. It should be noted that the tail of low concentration, including negative values, are attributed to regions of bone where there is very low ^{23}Na signal, and the conversion to TSC produces these nonsensical values. Voxels with high ^{23}Na concentrations ($>$ 50 mmol/L) can be attributed to the vessels. This is illustrated by segmentation of ^{23}Na concentrations shown in Fig.[4.27].

4.5.3 Assessing Multislice Measures

^{23}Na leg imaging is commonly carried out on a single axial slice collected with a 2D GRE [28, 66, 67, 73]. ^{23}Na concentration images shown to this point have been those of the central slice of the 3D GRE volume. Birdcage coils should exhibit a uniform region in the centre of the coil, for studies it is important to know the size of this region to inform future scan planning and determine the reliability of multislice axial measurements.

4.5.3.1 Methods

The extent of the uniform region in the z-direction was assessed by collecting a sagittal phase-sensitive B_1 map (Resolution: $3 \times 3 \times 30$ mm^3, TA: 5 mins, TE: 2.4 ms, FA: 60°, NSA: 15, TR: 150 ms) of the leg phantom in the birdcage coil. A multislice axial phase-sensitive B_1 scan (Resolution: $5 \times 5 \times 30$ mm^3, TA: 7.8 mins, TE: 2.1 ms, FA: 60°, NSA: 12, TR: 210 ms) was also collected in leg phantom and a human calf and ^{23}Na image, and

the phase-sensitive B_1 maps were then used to correct 3D GRE ^{23}Na images (Resolution: $3 \times 3 \times 30$ mm^3,TA: 5 mins, TR:6 ms, TE:1.57 ms, FA: 32°, NSA: 183).

4.5.3.2 Results

The result can be seen in Fig.[4.28], a line profile has been placed along the centre of the bottle and the percentage of nominal flip angle along this profile can be see in Fig.[4.30].

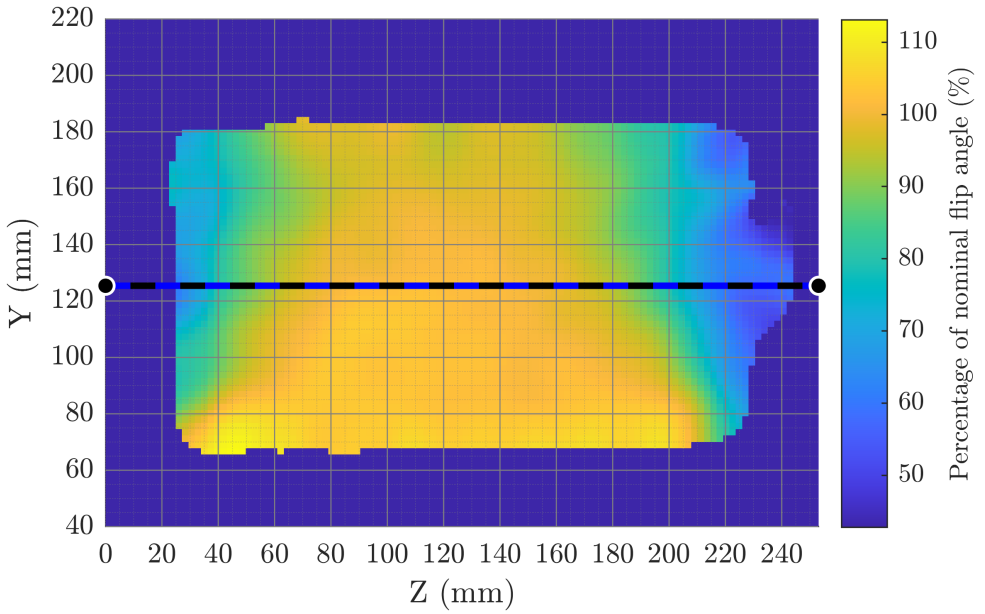

Figure 4.28: B_1 map in the bottle phantom in the PulseTeq leg coil. The profile of the line through the centre of the bottle shown in Fig.[4.30].

A multislice axial phase-sensitive B_1 scan in the leg phantom and a human calf and are shown in Fig.[4.29a]. Fig.[4.29] demonstrates that the phase-sensitive B_1 mapping can be carried out to correct muiltislice acquisitions for the leg phantom and the calf. The multislice axial images demonstrate that the B_1 field in the z-direction is approximately uniform in the central three 30 mm slices, in agreement with the sagittal leg phantom B_1 map which exhibits a region of approximately 80 mm in the z-direction where the B_1 field is uniform (Fig.[4.30]). The change in signal intensity in-plane across the leg bottle phantom in the y-direction is as expected, the bottle phantom does not completely fill the bore of the RF coil therefore the bottle is off centre in the bottom of the coil and signal intensity change close to the rungs is seen. This can be seen to be corrected by applying B_1 mapping correction.

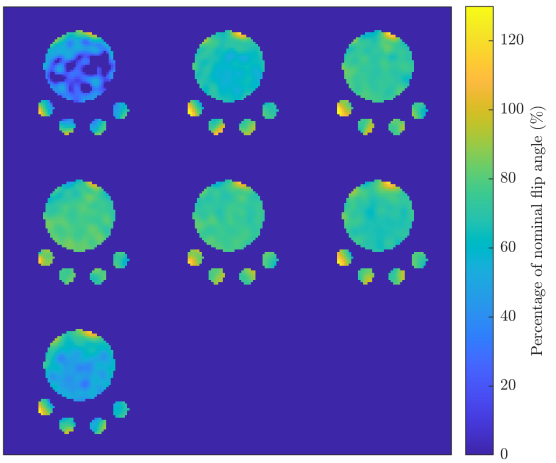

(a) Phase-sensitive B_1 map of the leg phantom.

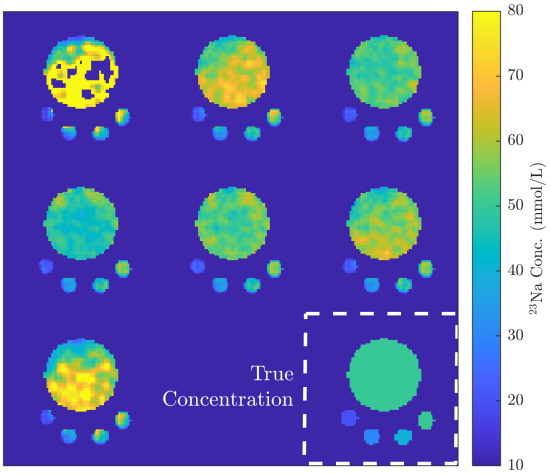

(b) Phase-sensitive B_1 corrected TSC map of the leg phantom.

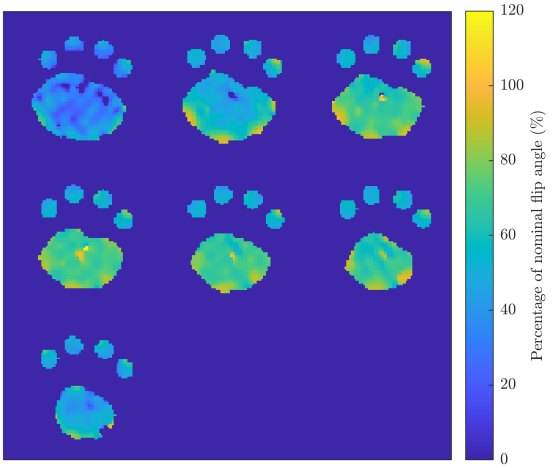

(c) Phase-sensitive B_1 map of the calf.

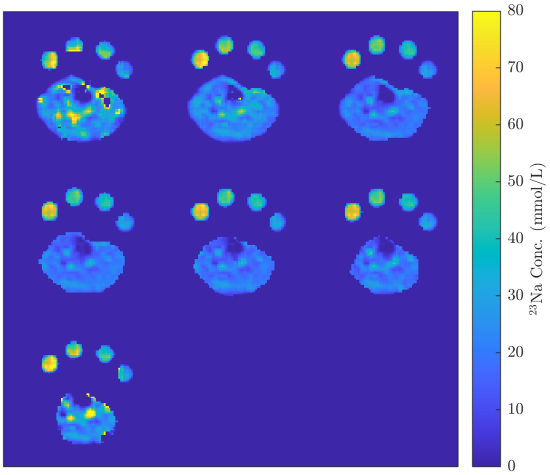

(d) Phase-sensitive B_1 corrected TSC map of the calf.

Figure 4.29: Multislice ^{23}Na maps demonstrating the uniform region in the centre of the PulseTeq ^{23}Na leg coil and the TSC maps after phase-sensitive B_1 correction.

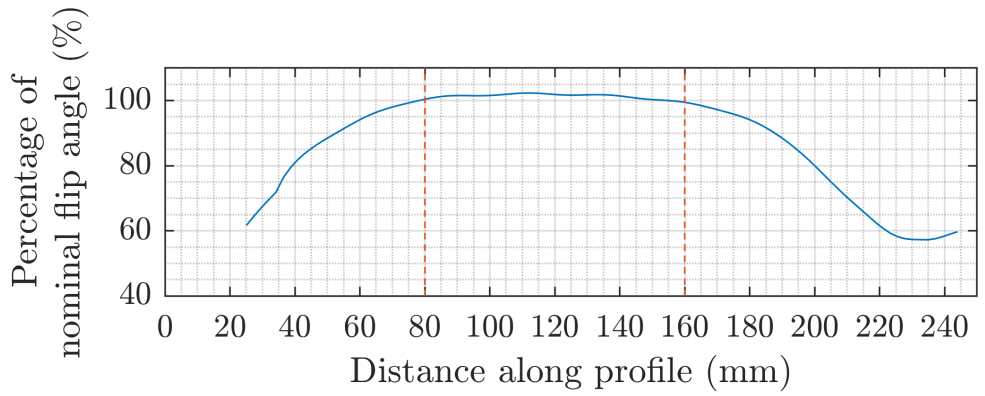

Figure 4.30: The profile of the line in Fig.[4.28], showing the flip angle through the centre of the bottle. The orange dashed lines shows the $\sim$ 80 mm region over which the B_1 field is approximately homogeneous.

4.5.4 Discussion

Here, B_1 correction of ^{23}Na images has been performed to improve the accuracy of the ^{23}Na concentration maps. The B_1 maps show that the B_1 field inside the birdcage leg coil is not completely homogeneous, with increased B_1 field around the rungs of the birdcage. Despite there being a foam mat placed under the leg to keep the leg away from the rungs, this spacing is not large enough to remove the field effects of close to the rungs, a thicker mat could be used but the space inside the coil for the leg and reference bottles is limited. B_1 corrections increased the homogeneity of the ^{23}Na concentration maps across the leg bottle phantom. In agreement with previous work [51,52] the phase-sensitive B_1 mapping method was more accurate than the double angle method, since noise in the B_1 map produced by the double angle method was imposed onto the ^{23}Na concentration maps. The remaining variance across the leg bottle phantom after B_1 correction could be due to a number of reasons [51, 52, 74]. The B_1 correction used here did not take relaxation into account. The fast T_2^* decay of ^{23}Na will cause transverse relaxation during the RF pulses, reducing the produced flip angle. The pulse length of the phase-sensitive method was 3.8 ms, long enough for the ^{23}Na signal with a T_2 of 0.5-3.0 ms to decay. This can be corrected for if the T_2^* is known, and T_2^* mapping is discussed in Section [4.8]. It should be noted that for the phantom work the composition of the reference bottles and the leg bottle phantom are identical (apart from ^{23}Na concentration), therefore it was not necessary for relaxation differences to be taken into account when calibrating the ^{23}Na concentration of the leg phantom, and difference with calf muscle have been ignored here, and will be studied in Section [4.6] and [4.8].

Wen et al. [74] demonstrated that imperfect spoiling can lead to artifacts in the phase-sensitive B_1 mapping. In this work the TR was chosen to be greater than the T_2^* ($TR>5\cdot T_2^*$). The same work showed that this imperfect spoiling can be corrected for if the parameters spoiling method used are known, increasing the efficiency of the spoiling will allow for shorter TRs, speeding up the scan in future.

4.6 Longitudinal Relaxation (T_1) Correction

Section [4.3] demonstrated that to achieve the maximum image SNR per unit time a short TR should be used to collect many averages. However it was shown that using a short TR introduces a T_1 dependency in the ^{23}Na signal intensity. In order to produce accurate ^{23}Na quantification this section looks at correcting the T_1 dependency.
The T_1 weighting of the measured ^{23}Na concentration $[Na]$ is given by

$$[Na]_{tiss} = \frac{S_{Na_{tiss}}}{S_{Na_{ref}}} \cdot [Na]_{ref} \cdot \left(\frac{1 - \exp\left(-\frac{TR}{T_{1ref}}\right)}{1 - \cos\alpha \cdot \exp\left(-\frac{TR}{T_{1tiss}}\right)} \right) \tag{4.7}$$

where $S_{Na_{tiss}}$ is the ^{23}Na signal intensity. If data is collected using a short TR scan the T_1 signal dependency can be corrected for by either measuring T_1 or using the expected ratios between the calf signal and bottle signal as plot in Section [4.3] Fig.[4.10c].

4.6.1 Method

To assess the feasibility of correcting for the T_1 signal dependency ^{23}Na *in vivo* data were collected using the PulseTeq leg coil. $5 \times 5 \times 30$ mm^3 resolution 3D GRE scans were acquired in three healthy subjects (2M:1F, 25-48 years) with a short TR of 13 ms (TE: 1.27 ms, TR: 13 ms, FA: 46°, NSA: 131, TA: 8 min) and a long TR of 100 ms (TE: 1.26 ms, TR: 100 ms, FA: 90°, NSA: 16, TA: 8 min). A phase-sensitive B_1 map (Section [4.5]) was also collected to correct for B_1 field inhomogeneities. The ratio between the calf and bottle signal for TR = 13 ms and TR = 100 ms in Fig.[4.10c] of 1.46 was used to adjust the signal in the leg for the short TR scan to assess the correction of T_1 effects. The ^{23}Na signal from the reference bottles was then used to convert the pixels intensities to ^{23}Na concentration as described in Section [4.4].

4.6.2 Results

Fig.[4.31a] shows example 3D GRE images collected at short and long TR. The average image SNR in the calf muscle across the three subjects for the short TR was 11.4 ± 0.2

and for the long TR it was 9.3 ± 0.6, Whilst improved visualisation of the skin is apparent for the short TR. The linear regression of the reference bottles for Subject 1 can be seen in Fig.[4.31b]. Note the improved fit of the regression line at shorter TR (R^2 = 0.984) compared to long TR due to higher image SNR.

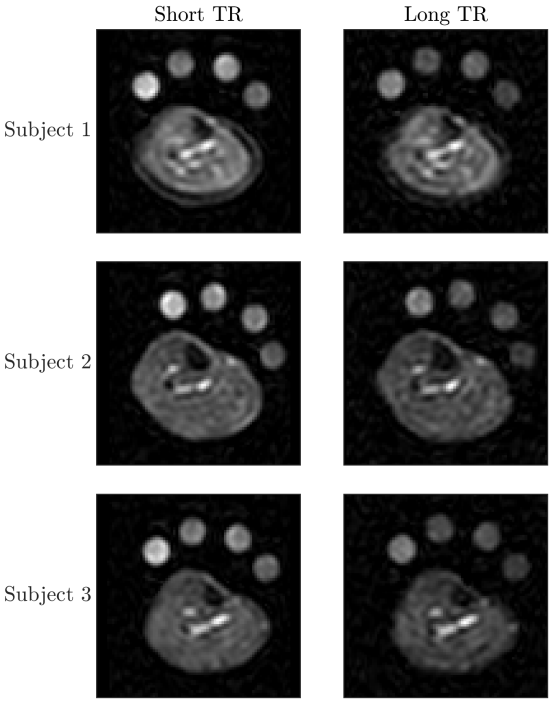

(a) ^{23}Na images acquired at short TR (13 ms) and long TR (100 ms) for the three subjects.

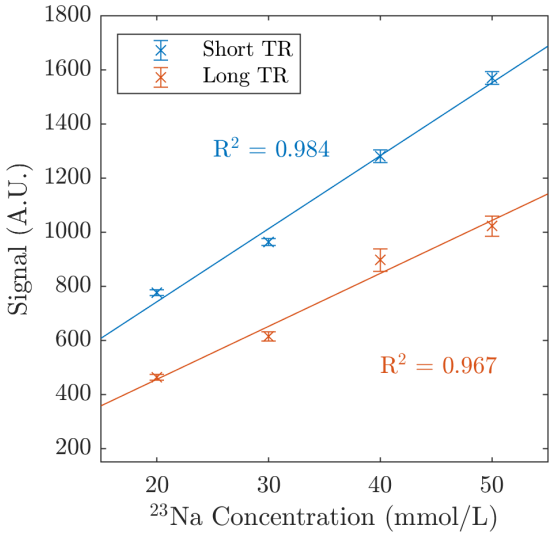

(b) Linear regression of the reference bottles for the short and long TR scans.

Figure 4.31: Example ^{23}Na images collected at short and long TE, and associated regression curves for reference bottles.

An example TSC map acquired using the short TR before and after relaxation weighting correction using the ratio method can be seen in Fig.[4.32] along with a TSC map from a long TR image.

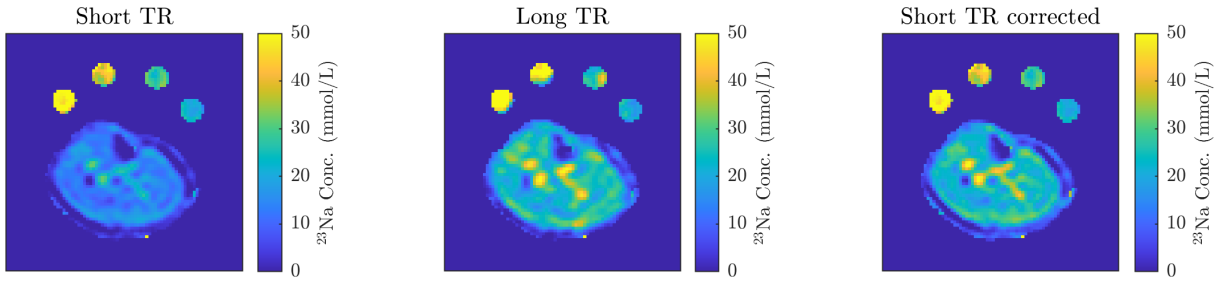

Figure 4.32: Tissue sodium concentration maps collected using a short TR (13 ms) and long TR (100 ms), alongside the short TR map corrected for T_1 effects.

Fig.[4.33] shows the histograms of these three images in Fig.[4.32] quantitatively demonstrating the T_1 correction.

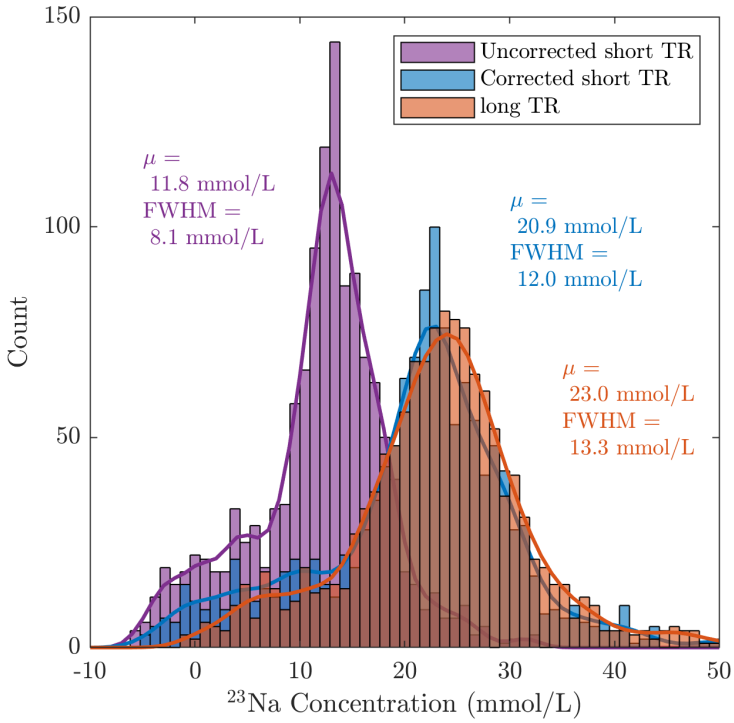

Figure 4.33: Histogram of the ^{23}Na concentrations in calf images shown in Fig.[4.32].

The TSC maps in Fig.[4.32] and histogram in Fig.[4.33] demonstrates the T_1 weighting effects present in the short TR image, with the measured ^{23}Na concentration in the calf muscle being lower for the short TR than long TR 3D GRE image. On applying T_1 correction the calf ^{23}Na concentration in the short TR image can be seen to have a matched distribution of a values to the long TR image.

4.6.3 Discussion

This data demonstrates the viability of correcting the short TR images for T_1 effects using the ratio method, enabling the short TR images with the increased SNR to be used for ^{23}Na quantification. The T_1 correction applied here was implemented globally across the slice and did not take into account the different T_1s of different tissues. To address this in future, a T_1 map could be collected using the variable flip angle (VFA) method, as published recently by Coste et al. [75]. Of note is that the greater number of averages afforded by the short TR reduced the background noise in the images, and in particular

the skin signal can be seen to be easier to identify in the short TR scans compared to the long.

4.7 UTE Imaging

As outlined in Section [2.2.2.2] radial sampling schemes can be used to produce sequences with ultra short echo times (UTE) to capture the fast transverse decay of the ^{23}Na signal. It has been shown that UTE imaging can be more suited to ^{23}Na imaging than cartesian sampling methods [40]. One of the more standard UTE techniques available on the Philips MRI scanners is the stack of stars (SOS) sequence as used in Section [4.2]. It is well suited for scanning the leg because the Cartesian sampling in the z-direction allows for thick slices to be used, appropriate because of the linear geometry of the leg, increasing the signal in the voxel.

4.7.1 Method

To assess the benefits of UTE *in vivo*, the 3D GRE scan with Cartesian sampling (resolution: $3 \times 3 \times 30$ mm^3, TA: 8.1 mins, TE: 2.02 ms, FA: 20°, TR: 9 ms, number of slices: 7) was compared to 3D UTE sampling (resolution: $3 \times 3 \times 30$ mm^3, TA: 8.1 mins, TE: 0.13 ms, FA: 20°, TR: 9 ms, number of slices: 7). Both scans were of the same acquisition time of ~ 8 minutes. Modifying the scan duration for the GRE sequence was performed by increasing the number of averages, while for the UTE sequence this was done by increasing the number of radial spokes. For each image, SNR was assessed along with image characteristics.

In the same scan session a high-resolution ^{1}H mDixon scan was acquired using the Q-Body coil (Resolution: $0.4 \times 0.4 \times 8$ mm^3, TA: 4 mins, TE: 20 ms, FA: 90°, TR: 500 ms, number of slices: 15). The muscles in one slice within the calf were identified using the ^{1}H image. The ^{1}H image was collected in the same space as the ^{23}Na images, therefore the muscle regions could then be applied to the ^{23}Na image.

4.7.2 Results

Resultant example image comparisons of the 3D GRE and 3D UTE scheme are shown in Fig.[4.34].

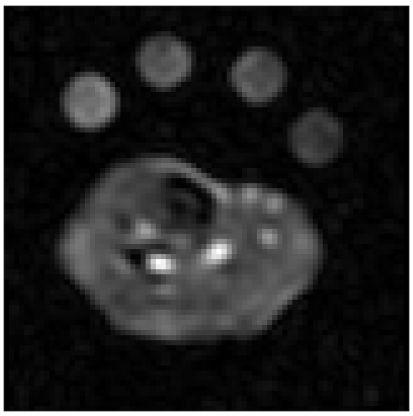

(a) GRE: (i) single slice.

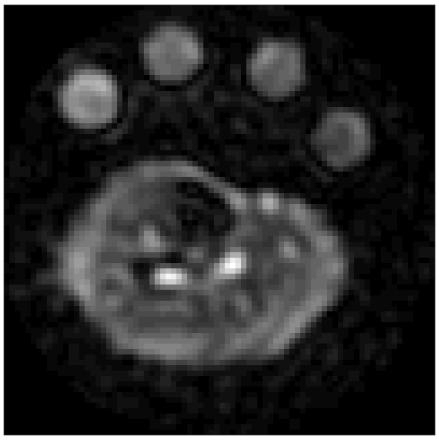

(b) UTE: (i) single slice.

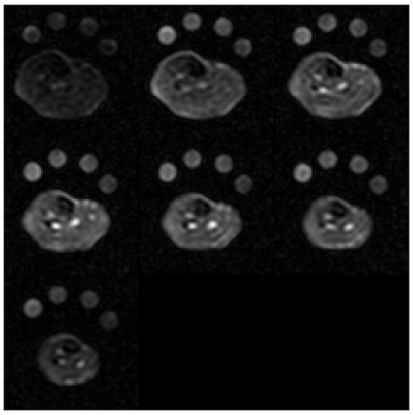

(a) GRE: (ii) 7 slices.

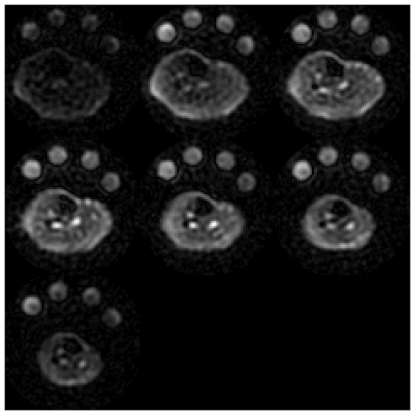

(b) UTE (ii) 7 slice.

Figure 4.34: Comparison between the (a) 3D-GRE and (b) 3D-UTE images for (i) a single slice and (ii) the 7 slices in the multislice dataset. All images are displayed as signal intensities at the same scale.

There are a number of observations that can be made from Fig.[4.34]. The signal is greater in the UTE image, expected due to the shorter TE capturing more of the ^{23}Na before it decays. In the muscle the absolute pixel intensity for the same receiver gain scale is 910 in the GRE image SNR and 1073 in the UTE image. Similar increased signal intensity can be seen in the bottles as shown in Fig.[4.35], where the regression line for ^{23}Na quantification is also shown. A larger ^{23}Na signal can also be seen in the skin in the UTE images signal.

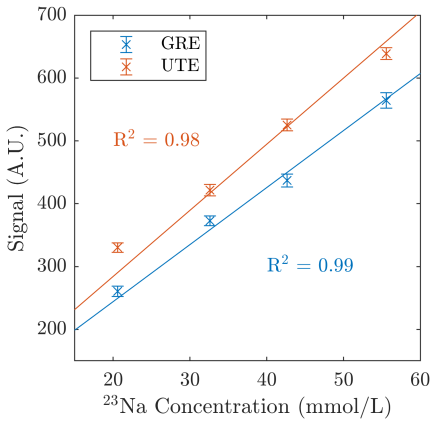

Figure 4.35: The mean pixel intensities in the references bottles used for the linear regression acquired using GRE and UTE. Note higher signal due to shorter TE.

However, it can be seen that the noise is greater in the UTE image and the image does not appear as sharp as the GRE image. Thus, when considering image SNR, for the GRE image in the muscle this was 19 ± 6 and for the UTE image was 11 ± 3. This is as expected as the radial sampling provides non-uniform k-space sampling, over sampling the centre of k-space and under sampling the outer regions, this leads to inhomogeneous distribution of noise in k-space, and can lead to an image SNR loss of 26 % [36], this also effects the bottles which are small and so are blurred.

Using the linear regression of the reference bottles, the ^{23}Na images were converted into TSC maps as shown in Fig.[4.36].

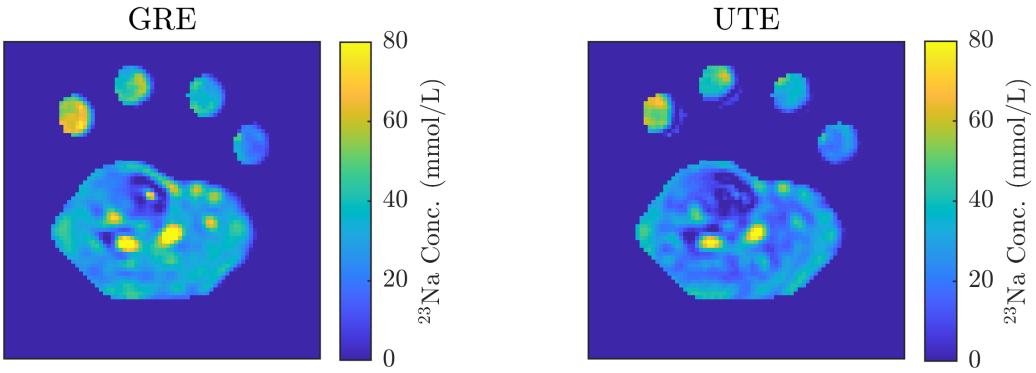

Figure 4.36: TSC in the calf as measured by the GRE and UTE sequences.

Fig.[4.37] shows the ^{1}H mDixon water image. Any visible blood vessels seen in the ^{1}H images were excluded from the muscle regions and an upper threshold concentration of 55 mmol/L was also applied to the ^{23}Na muscle regions. This threshold was used to remove

signal contributions from unidentified vessels or partial volume effects. The threshold level was based on the measured concentration in the identified vessels.

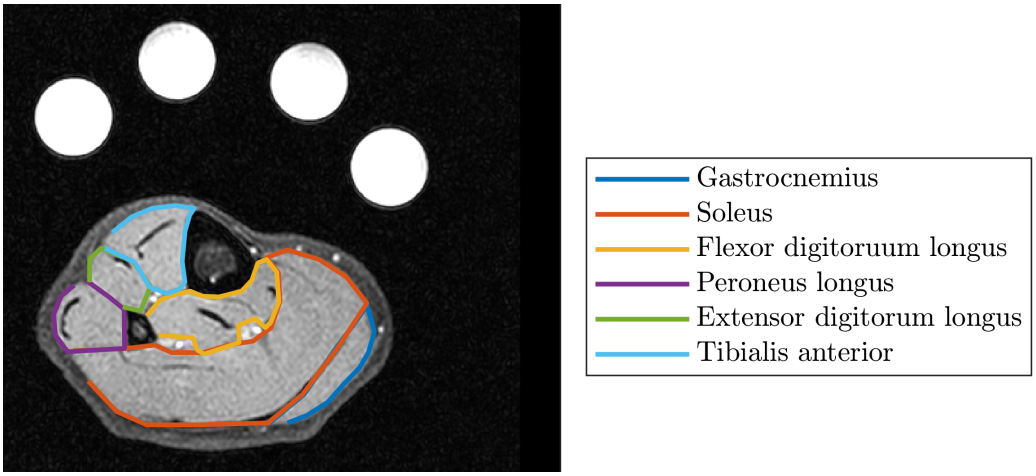

Figure 4.37: ^{1}H mDixon water image used to segment the different muscles in the calf.

Fig.[4.38] shows histograms of the ^{23}Na concentration in all muscles in the calf. The measured mean ^{23}Na concentrations in the reference bottles and muscles of the calf can be seen in Table [4.4].

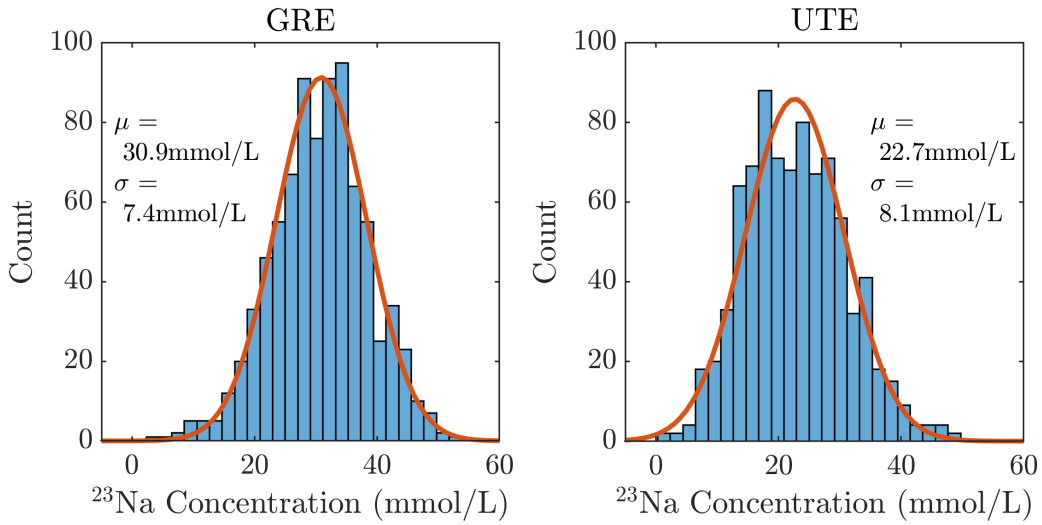

Figure 4.38: TSC in the all the muscle in the leg as measured by GRE and UTE sequences.

	^{23}Na Concentration mean ± SD (mmol/L)		
Region \ Method	GRE	UTE	IPC
20 mmol/L bottle	22±9	22±7	20.6±0.3
30 mmol/L bottle	34±9	33±8	32.6±0.6
40 mmol/L bottle	41±11	43±8	42.6±0.6
50 mmol/L bottle	55±13	54±8	54.3±1.0
Gastrocnemius	35±3	30±4	—
Soleus	31±7	22±7	—
Flexor digitoruum longus	32±10	21±10	—
Peroneus longus	36±6	28±7	—
Extensor digitorum longus	28±7	26±11	—
Tibialis anterior	22±6	14±9	—
All muscle	31±7	23±8	—
Skin	32±9	28±9	—

Table 4.4: ^{23}Na concentrations in the reference bottles and leg as measured by GRE and UTE sequences and as measured by Inductively Coupled Plasma (ICP) Spectroscopy.

Both the TSC maps and the mean concentrations show that there is a systematic difference in the measured ^{23}Na concentration in the calf as measured by the 3D GRE and 3D UTE methods.

4.7.3 Discussion

Here 3D GRE and 3D UTE ^{23}Na images have been compared. A likely cause of the disparity in TSC measured between the two imaging sequences is a difference in the T_2^* relaxation times between the reference bottles and different tissues *in vivo*. GRE overestimates the TSC as bottles are likely to have a shorter T_2^* and this will result in

a lower signal in the GRE image for a given echo time, therefore this is attributed to a higher TSC for GRE. A UTE sequence, with the shorter TE, will limit the impact of these differences. This highlights the need to know the T_2^* of both the tissue and the bottles. Measurement of the T_2^* relaxation time is covered in the following section, Section [4.8]. To overcome the SNR reduction produced by over sampling the centre of k-space for the UTE scheme, there are a number of radial sampling schemes that sample k-space uniformly which could be implemented in the future. The main techniques are twisted projection imaging (TPI) [34], density-adapted 3D projection reconstruction (DA-3DPR) [35] and 3D cones trajectories [36]. These sampling schemes are not currently available on the Philips scanner software, future work will look to implementing one of these techniques to realise the full benefit of UTE imaging.

4.8 Measurement of the ^{23}Na Transverse Relaxation (T_2^*) Time in The Muscle and the Reference Bottles

The ^{23}Na PulseTeq leg coil was used to measure the T_2^* of sodium in the muscles. This was performed using a series of 3D UTE stack of stars multi echo scans (Resolution: $3 \times 3 \times 30\text{mm}^3$, TA: 5.3 mins, TE1: 0.18 ms, FA: 90°, TR: 100 ms, B_1 : 30 μT). The sequence is described in detail in Section [2.2.2].

4.8.1 Methods and Results: Fully Sampled T_2^* Curve

For an initial estimate of the T_2^* decay a set of five scans were carried out on a healthy subject. Each scan was collected with an echo train of eight echoes. The echoes were equally spaced (ΔTE = 4.5 ms) and the first TE in each echo train was selected so that the TEs of all five scans fully sampled the T_2^* decay. Thus in total the scan comprised of 40 data points to fully sample the T_2^* decay curve. The TEs used are outlined in Table [4.5], the scans were all collected with a TR = 100 ms and each scan took 5 min, resulting

in a total time of 25 minutes.

Scan \ Echo	TE (ms) 1	2	3	4	5	6	7	8
1	0.18	4.68	9.18	13.68	18.18	22.68	27.18	31.68
2	0.65	5.15	9.65	14.15	18.65	23.15	27.65	32.15
3	1.20	5.70	10.20	14.70	19.20	23.70	28.20	32.70
4	1.80	6.30	10.80	15.30	19.80	24.30	28.80	33.30
5	3.24	7.74	12.24	16.74	21.24	25.74	30.24	34.74

Table 4.5: Echo times (TEs) used in each of the multi-echo scans.

All the ^{23}Na images collected can be seen in Fig.[4.39a], one ROI was drawn inside the muscle in the calf and another inside the 50mmol/L reference bottles, the positioning of the ROIs are shown in Fig.[4.39b].

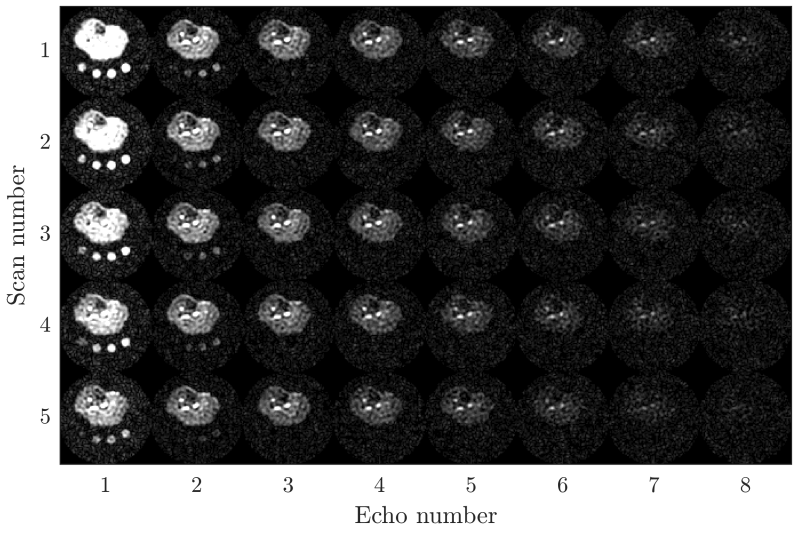

(a) ^{23}Na images collected for T_2^* mapping , the echo times (TEs) are listed in Table [4.5].

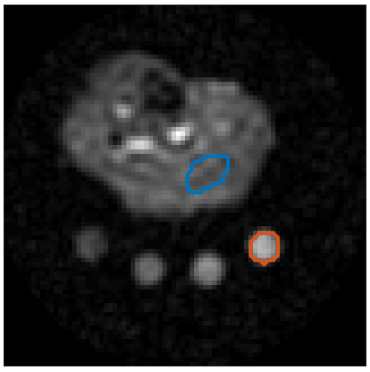

(b) ^{23}Na image (TE = 0.18 ms) showing the ROIs used when measuring the T_2^* decay.

Figure 4.39: Multi-echo ^{23}Na images and associated ROIs interrogated.

The average signal inside an ROI across all images was calculated and the plot of ^{23}Na signal versus TE is shown in Fig.[4.40]. As outlined in Section [2.1.5.3] the signal in the muscle is expected to follow a bi-exponential decay and so was fit to Eq.[2.25], whilst the

signal in the bottle was fit to a mono-exponential decay. All fitting was carried out using the Trust-Region Algorithm, a nonlinear least squares method.

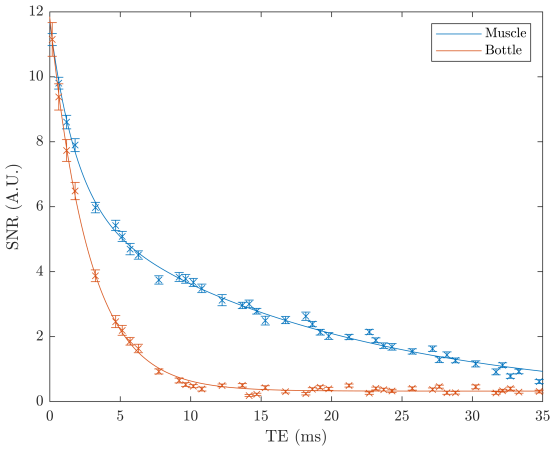

(a) The decays with a bi-exponential fit for the muscle signal and a mono-exponential fit for the 50 mmol/L reference bottle signal.

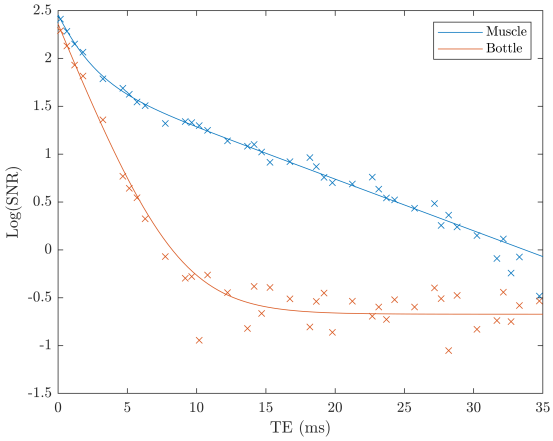

(b) The log of the T_2^* decay in the muscle and reference bottle.

Figure 4.40: T_2^* ^{23}Na decay of the muscle and the 50 mmol/L reference bottle.

For the muscle this resulted in a slow component $T_{2s}^* = 18.5 \pm 1.6$ ms and fast component $T_{2f}^* = 1.9 \pm 0.4$ ms, with the fraction $f_f = 0.53 \pm 0.04$ for the slow component. For the reference bottles the T_2^* was 2.7 ± 0.2 ms.

4.8.2 Methods and Results: Estimating T_2^* Using a Reduced Number of TEs

Since the scans used to obtain the initial fit in Fig.[4.40] took a total acquisition of 25 min, the next aim was to reduce the total scan time by collecting fewer TEs such that a measure could be collected for each participant in future. Therefore, the minimum number of TEs needed to sample the bi-exponential fit and still achieve a good fit was assessed.

Using the data from the fully sampled T_2^* scan each possible combination of five scans were fit to a bi-exponential decay. The Sum of Squares Error (SSE) between each fitted curve and the fully sampled fit was used to assess the accuracy of each fit, Fig.[4.41a].

By assessing the fits produced by the combination of scans with the smallest SSE in each group it can be seen that even just one scan produces a strong agreement.

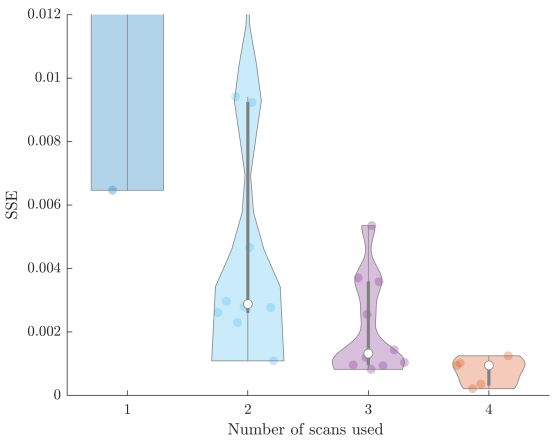

(a) The sum of squares error (SSE) of the fit produced by different combinations of multiecho scans.

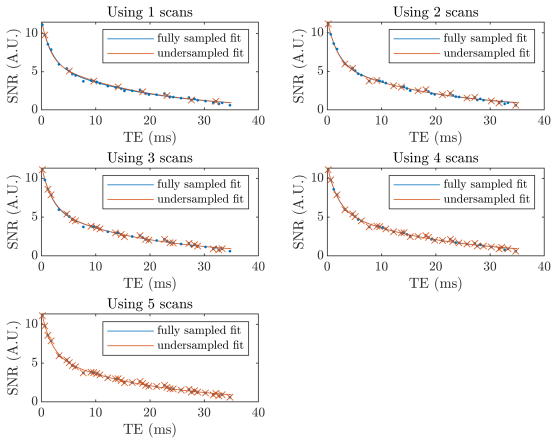

(b) The fits of the combination of scans with the smallest SSE in each group.

Figure 4.41: T_2^* fits to decays measured for different combinations of multiecho scans.

Having evaluated the required scheme, three scans with the sequence parameters described above and using the TEs outlined in Scan 1, 3 and 4 in Table [4.5] were chosen to measure the transverse relaxation (T_2^*) in the calf of four subjects (age:25-31 years, 3M:1F). Again, an ROI was drawn in the muscle and the mean signal was calculated in the muscle ROI. The signal in the calf muscle was normalised to its maximum predicted at TE = 0 ms, the results can be seen in Fig.[4.42a]. Similarly this was performed for the reference bottles, the results of which can be seen in Fig.[4.42b].

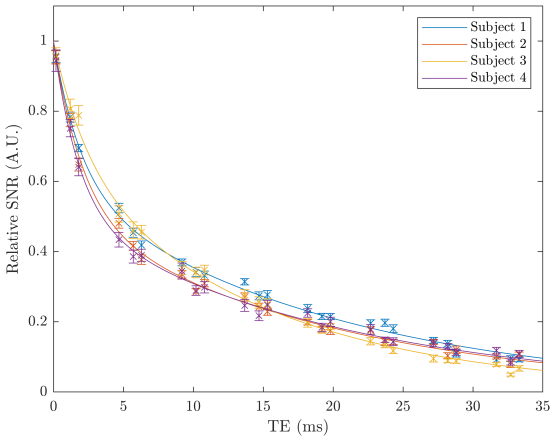

(a) The T_2^* decay with a bi-exponential fit of ^{23}Na signal in the calf muscle in four healthy subjects.

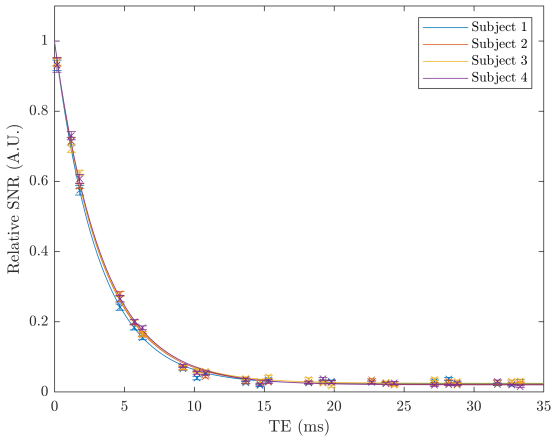

(b) The T_2^* decay with a mono-exponential fit of ^{23}Na signal in the reference bottles.

Figure 4.42: Calf and reference bottle T_2^* decay.

The muscle signal was fitted with a bi-exponential decay and the bottles with a mono-

Bottle	50 mmol/L		40 mmol/L		30 mmol/L		20 mmol/L	
Subject	T_2^* (Mean ±SD ms)	R^2	T_2^* (Mean ±SD ms)	R^2	T_2^* (Mean ±SD ms)	R^2	T_2^* (Mean ±SD ms)	R^2
1	3.2±0.2	0.998	2.8±0.1	0.999	3.1±0.3	0.996	2.2±0.3	0.992
2	3.3±0.2	0.997	2.9±0.2	0.997	3.2±0.2	0.997	2.6±0.3	0.991
3	3.3±0.2	0.998	3.0±0.2	0.997	3.4±0.2	0.997	2.6±0.3	0.994
4	3.4±0.2	0.999	3.2±0.1	0.997	3.5±0.2	0.997	2.5±0.2	0.996
Mean	3.3±0.1		3.0±0.1		3.3±0.2		2.5±0.2	

Table 4.7: The fitting parameters of the mono-exponential T_2^* decay of the ^{23}Na signal in the four references bottles for the four subjects.

exponential decay, the resulting fitting parameters can be seen in Table [4.6] and Table [4.7] .

Subject	Fast Fraction	T_2 slow component (ms)	T_2 fast component (ms)	R^2
1	0.60±0.06	19±2	1.9±0.7	0.996
2	0.52±0.06	19±3	2.1±0.6	0.997
3	0.67±0.10	15±2	2.4±1.3	0.996
4	0.51±0.05	20±2	1.8±0.5	0.996
Mean	0.57±0.04	18±1	2.1±0.1	

Table 4.6: The fitting parameters of the bi-exponential T_2^* decay of the ^{23}Na signal in the muscle.

4.8.3 Discussion

The echo times used provided a good fit in all of the subjects ($R^2 = 0.996$) and in the reference bottles ($R^2 = 0.991$). In a homogeneous environment the fraction of T_{2f} and T_{2s} is 60:40 but by fitting T_2^* curves this allowed for deviations from this ratio. The fitted value of f_f of 0.57 ± 0.08 is in agreement with the literature [76, 77]. The variance in the measured fractions reflects the in-homogeneous environment in the tissue.

For the shortest TEs, the ^{23}Na signal in the muscle decays at a similar rate as the ^{23}Na signal in the bottle. Knowing the transverse relaxation time in both the muscle and reference bottles, will allow in future the ^{23}Na signal at a given TE to be corrected for T_2^* decay [78].

4.9 Full *in vivo* Calf Muscle Protocol

The work in this Chapter has shown how tissue sodium concentration (TSC) in the calf can be estimated by combining measures from a number of different pulse sequences. These measures can be carried out within a 60 minute scan session as outlined below in Table [4.8]

Nucleus	Scan Type	Duration	Example image
^{1}H	Survey	13 s	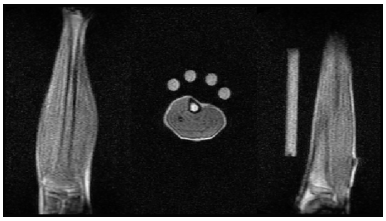
^{1}H	mDixon *Muscle volume* *Fat fraction* *Water fraction*	243 s	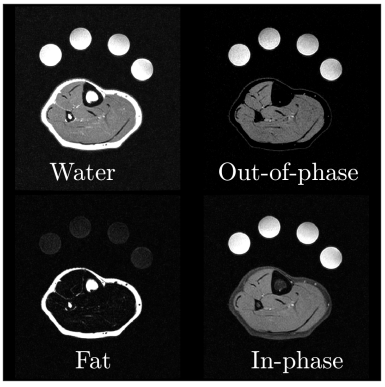
^{23}Na	GRE/UTE scans *TSC*	912 s	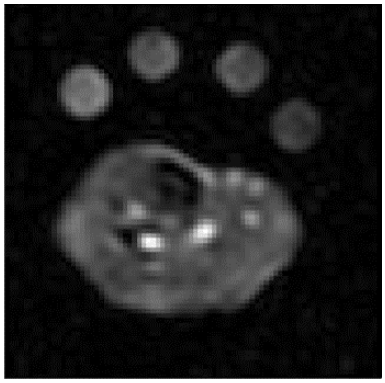

^{23}Na	Phase-sensitive B_1 map *B_1 correction*	467 s	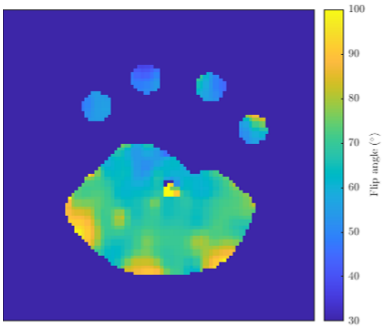
^{1}H	Dual-echo B_0 map *B_0 assessment and correction*	70 s	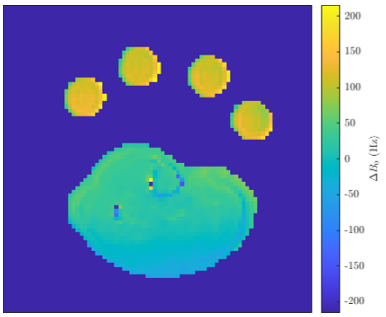
^{23}Na	T_2^* map *Assessment of slow and fast relaxation components*	954 s	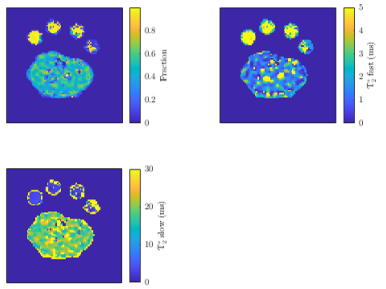

Table 4.8: A 60 minute ^{23}Na scan protocol for assessment of calf muscle.

To date, the complete protocol has been collected in three healthy subjects and the measured ^{23}Na concentrations in the muscle and skin are given in Table [4.9].

Subject	Muscle mean±SD mmol/L	Skin mean±SD mmol/L
1	21 ± 10	8 ± 6
2	19 ± 6	16 ± 8
3	20 ± 5	14 ± 5

Table 4.9: ^{23}Na concentration in the calf measured using the full protocol.

4.10 Discussion and Future Directions

In this chapter, the development of ^{23}Na imaging for assessment of the calf muscle and skin has been outlined. The chapter commenced with an outline of initial work using a single transmit/receive loop surface and a dual UTE scheme to study the response following anaerobic exercise. The surface coil was shown to detect a decline in ^{23}Na intensity as the tissue ^{23}Na signal returned to baseline following exercise. However the surface coil had an inhomogeneous transit field with the receive sensitivity dropping away from the coil, thus the coverage of the calf muscles was limited to the gastrocnemius and partial coverage of the soleus. Further the quantification of the ^{23}Na signal was limited due to the difficulty in placing the reference bottles in a similar coil sensitivity. A recent study by Milani et al. [53] has assessed integrating the reference phantoms within the surface coil loop to overcome this issue to allow the assessment of ^{23}Na quantification of the upper leg, not an area which would be possible to scan with a birdcage leg coil.

The main focus of this chapter was to optimise measurements in the whole calf using a birdcage PulseTeq coil, this included optimising the 3D GRE sequence for image SNR per unit time, B_1 correction methods, assessment of relaxation weighting, comparison with a 3D UTE sequence, ^{23}Na quantification and T_2^* mapping. The ^{23}Na imaging protocol to study the calf muscle was optimised to estimate total ^{23}Na concentration in the muscle and skin and allow the spatial distribution to be mapped and overlaid onto anatomical mDixon ^{1}H images. A phase sensitive B_1 mapping method has been implemented and shown to provide a more accurate B_1 correction than the double angle B_1 mapping. Accurate assessment of TSC was possible over the central three slices of the 3D GRE volume. The 3D GRE scheme was compared to 3D UTE and the 3D UTE sequence was shown to provide higher ^{23}Na signal intensity due to the lower TE, however, image SNR was affected by noise issues. The 3D UTE scheme allowed T_2^* mapping of the calf across a wide range of echo times to estimate the slow and fast relaxation rates and their fractions. In future work the T_1 of ^{23}Na will also be assessed by performing a variable flip angle (VFA) 3D UTE measure as performed by Coste et al. [75]. Here a T_1 relaxation weighting ratio correction has been performed to correct the short TR data acquisitions. In future

work, individual subject T_1 and T_2^* measures in the reference bottles and the calf will be used to correct relaxation weighting in the quantification of TSC following the relaxation equation

$$[Na]_{tiss} = \frac{S_{Na_{tiss}}}{S_{Na_{ref}}} \cdot [Na]_{ref} \cdot \frac{1 - \exp\left(-\frac{TR}{T_{1ref}}\right)}{1 - \cos\alpha \cdot \exp\left(-\frac{TR}{T_{1tiss}}\right)} \cdot \frac{\exp\left(-\frac{TE}{T^{\star}_{2ref}}\right)}{0.6 \cdot \exp\left(-\frac{TE}{T^{\star}_{2tiss}}\right) + 0.4 \cdot \exp\left(-\frac{TE}{T^{\star}_{2tiss}}\right)} \tag{4.8}$$

where $[Na]$ is the ^{23}Na concentration, S_{Na} is the ^{23}Na signal intensity.

The first studies to be performed in future work will be the assessment of repeatability of measures in the same subjects, by scanning ten healthy volunteers five times to thus determine the sensitivity of measures.

The following sections outline future directions to explore using the optimised imaging protocol developed in this chapter.

4.10.1 Assessing Muscle Damage Using ^{23}Na Imaging

The developed protocol will allow a detailed investigation of muscle atrophy in collaboration with the MSK group of the Biomedical Research Centre in Nottingham. Acute atrophy results in muscle fibre volume shrinking that may result in a relative increase of extracellular volume and affect ^{23}Na concentration. In future, studies will be performed to induce muscle force loss and delayed recovery in the calf in healthy volunteers against a control leg with no intervention. Data will be collected using the full protocol (Section [4.9]) to assess TSC along with ^{1}H measures of muscle volume and fat and water fractions from the mDixon scan. A recent study by Gerlach et al. [77], showed that atrophy, induced by unloading in the orthosis leg compared to the control leg, led to relative increases in TSC of between 10 and 18 % across calf muscle groups, whilst the control leg did not significantly change.

4.10.2 Assessing Response to Exercise Using ^{23}Na Imaging

In future studies the methods implemented in this thesis could be used to study ^{23}Na in diabetic patients. Na+/K+-ATPase activity is decreased in patients suffering from dia-

betes. A sufficiently high concentration of the hormone insulin in the blood will directly enhance the Na+/K+ pump activity in the muscle, kidney, liver, amongst other organs. Chang et al. [69] evaluated the signal intensity (SI) of ^{23}Na pre- and post-exercise. The ^{23}Na signal was assessed in patients with diabetes and in healthy subjects, in all three compartments of the calf muscle: tibialis anterior, soleus, and the gastrocnemius muscles it was found that the ^{23}Na signal intensity in the soleus and gastrocnemius immediately increased significantly after exercise for both diabetic patients and healthy subjects. However, the signal intensity return to baseline was slower in diabetics. An explanation for this can be supported by the fact that, in patients with diabetes mellitus, muscle function is reduced and accompanied by impaired functioning of the Na+/K+ pump.

4.10.3 Assessing Clinical Disease Populations using ^{23}Na Imaging

The ^{23}Na calf protocol can be used to investigate a number of diseases. Prior studies have used ^{23}Na imaging of the muscle to study hypertension, with an increase in ^{23}Na content being shown with high blood pressure. Kopp *et al.* [28] showed that patients with hypertension had a 29 % increase in ^{23}Na content compared to healthy subjects. Kannenkeril et al. [70] found that subjects with type-2 diabetes had significantly greater ^{23}Na concentration in the muscle, with diabetics having a TSC of 20.6 $\pm$ 3.5 mmol/L compared to hypertension patients of 16 $\pm$ 2.5 mmol/L, P<0.001. Renal disease can also be investigated with this protocol, including conditions such as CKD and AKI. Schneider et al. [55], found that in patients with CKD have a high skin ^{23}Na content. Hammond et al. [56] observed that in AKI patients scanned before dialysis have a higher calf and skin ^{23}Na concentration than healthy controls.

4.10.4 Assessing Muscle Response of Haemodialysis

The protocol described in Section [4.9] can also be used to assess muscle and skin ^{23}Na storage in patients undergoing hemodialysis with either a “sodium-positive” or a “sodium-negative” profile. The intervention will be the individualization of intradialytic ^{23}Na

flux in either direction (i.e. into or from the patient) using the Electrolyte Balancing Control (EBC) of the dialysis system. ^{23}Na scans will be conducted prior and following haemodialysis sessions. These studies will provide additional information to earlier studies described in Section [4.1.4] as they will be collected with 3D schemes (GRE or UTE with shorter TE) along with B_1 correction and assessment of relaxation time changes. In addition the ^{1}H mDixon scan will be used to assess water content.

4.11 Conclusion

This chapter has developed a ^{23}Na imaging protocol for the assessment of tissue sodium concentration in the human calf muscle. A 3D GRE ^{23}Na imaging scheme was evaluated with the trade-offs of image SNR per unit time and relaxation weighting evaluated, and corrections assessed. B_1 mapping schemes of double angle and phase-sensitive methods were compared to correct ^{23}Na images to compute TSC, with the phase-sensitive method shown to be superior. 3D GRE and 3D UTE schemes are compared and finally the T_2^* of the slow and fast ^{23}Na components evaluated. The chapter concludes with an optimised ^{23}Na imaging protocol of the calf for future studies in clinical populations.

Chapter 5

Development of ^{23}Na Imaging in the Abdomen

This chapter outlines the development of ^{23}Na imaging of the abdomen. It describes the use of the dual loops ^{23}Na coil for the acquisition of healthy volunteer and Chronic Kidney Disease (CKD) data. The optimisation of the gradient recalled echo (GRE) scheme for body imaging under the condition of SAR constraints is then outlined followed by evaluation in healthy volunteers. Next, a comparison is made between the dual loops ^{23}Na coil and the 6-channel ^{23}Na coil. This is followed by work performing receive sensitivity correction for the 6-channel ^{23}Na. The feasibility of carrying out ^{1}H measures using the ^{1}H Q-Body coil (for structural measures and assessment of oxygenation) alongside ^{23}Na imaging using the 6-channel ^{23}Na coil is investigated. This work have been presented as 'Optimisation of Renal Sodium MR' at the 3rd International Conference on Functional Renal Imaging 2019, Nottingham, UK and as 'Comparison Between Single Channel Dual Loops ^{23}Na Coil and 6-Channel Flexible Wraparound ^{23}Na Coil for Renal Sodium Imaging' at the ISMRM & SMRT Virtual Conference & Exhibition, August 2020.

5.1 Introduction to ^{23}Na Renal Imaging Studies

The most important role of the kidney is to maintain the overall fluid balance in the body. Normal renal function is determined by the regulation of extracellular sodium in the kidney, established by a sodium concentration gradient from the cortex to the medulla. This drives the re-absorption of water into the collecting ducts in the medulla. Alterations in the sodium concentration gradient (corticomedullary sodium gradient (CMSG)) may be caused by several different renal diseases, such as nephropathy, acute kidney failure, or irregular kidney function after transplantation. The CMSG is generated by the sodium/potassium adenosine triphosphatase transporter. Efficient function of this transporter depends on renal blood flow to maintain oxygen for ATP production within the mitochondria in the renal cortex. Reduced blood flow is a common occurrence in renal disease as has been shown using MRI by Buchanan et al. [79].

Methods to assess ^{23}Na in the kidney include micropuncture or slice section analysis which have been performed in animal studies but these methods are invasive and not suitable for human studies [17–19, 80]. Sodium MRI provides the unique capability to non-invasively assess the sodium distribution within the kidney. To date, still only a few studies by a small number of research groups have performed ^{23}Na imaging of the kidney, and these are outlined below to illustrate the potential utility and applicability of ^{23}Na MRI to assess renal sodium handling.

^{23}Na MRI of the kidney was first performed in 1988 at 1.5 Telsa [81] using a 25 cm diameter RF coil to yield low resolution ^{23}Na images in a 50 minute scan time. It was not until 2006, as MR hardware and imaging techniques developed, that sodium imaging of the kidney was performed at 3 Tesla by Maril et al. [10]. Maril et al. produced the first maps of sodium distribution in the kidney and a qualitative measure of the CMSG. A 3D GRE sequence was collected at $3 \times 3 \times 15$ mm^3 with a TE/TR of 1.8/30 ms and data collected with 24 averages in a 25 minute acquisition. The TE of 1.8 ms was achieved by using a hard, nonselective excitation RF pulse. From this data Maril et al. showed that the ^{23}Na signal intensity increases linearly from cortex to medulla with a mean slope of 1.6 ± 0.2 A.U. per mm which then decreased towards the renal pelvis. Water deprivation

was found to increase this gradient by 25 %.

Quantitative measurement of the sodium concentration in the kidney was first achieved by Haneder et al. in 2011 [60]. In this study, the effect of water loading on kidney ^{23}Na concentration was measured in healthy volunteers. Subjects abstained from water intake for six hours prior to their first ^{23}Na MRI and subsequently ingested 1 litre of water 30 minutes prior to their second ^{23}Na MRI. Water loading caused a reduction in the sodium concentration within the kidney, with a decrease from 64 ± 9 mmol/L to 49 ± 5 mmol/L in the cortex and 108 ± 11 mmol/L to 82 ± 10 mmol/L in the medulla, but the corticomedullary sodium concentration gradient was not affected. They then advanced these ^{23}Na MRI measures by assessing the corticomedullary gradient [82] using higher spatial resolution isotropic voxels and investigated the use of the cerebrospinal fluid (CSF) ^{23}Na signal as an internal reference. In 2014, Haneder et al. [83] evaluated the feasibility of *in vivo* ^{23}Na MRI of the corticomedullary gradient and measurement of ^{23}Na transverse relaxation times (T_2^*) in human kidneys at ultra-high field (7 Tesla), showing mean corticomedullary ^{23}Na signal-to-noise ratio (SNR) increased from the cortex (32.2 ± 5.6) towards the medullary pyramids (85.7 ± 16.0) and ^{23}Na T_2^* relaxation times differed statistically significantly ($P < 0.001$) between the cortex (17.9 ± 0.8 ms) and the medulla (20.6 ± 1.0 ms). A recent study in 2020 by Grist et. al. [21] performed ^{23}Na imaging of healthy subjects across two sites (n = 6 per site) on a GE system, using a single flexible surface loop coil at Site A and two Helmholtz loop coils placed anteriorly and posteriorly over the kidneys at Site B. They measured ^{23}Na concentrations of 136 ± 7 mmol/L in the medulla and 72 ± 6 mmol/L in the cortex.

This chapter outlines the development of ^{23}Na imaging to study the kidneys. It commences with work using the dual loops coils to measure tissue sodium concentration (TSC). This is followed by the optimisation of the 3D GRE acquisition scheme and a comparison of the dual loops coil with the 6-channel body coil. Work performing receive sensitivity correction for the 6-channel ^{23}Na is then performed and the feasibility of carrying out ^{1}H measures using the ^{1}H Q-Body coil (for structural measures and assessment of oxygenation) alongside^{23}Na imaging using the 6-channel ^{23}Na coil is investigated.

5.2 Initial Measures in Healthy Volunteer and Chronic Kidney Disease Using the Dual loops Coil

^{23}Na MRI is the only imaging technique that can map the sodium distribution in the kidneys [22], and thus provide a marker of preserved tubule and integrated nephron function. Preliminary studies have shown a reduction in the tissue sodium concentration (TSC) and the ^{23}Na CMSG in transplanted versus native kidneys, suggesting these parameters may provide biomarkers for early kidney damage in CKD [23]. Here the dual loops coil is assessed for measurement of ^{23}Na in the kidney.

5.2.1 Methods

Three healthy volunteers (25-27 years, 2M:1F), and three patients (66-71 years, 3M) with CKD were scanned to assess the feasibility of imaging the kidneys using the PulseTeq ^{23}Na dual loops coil. The scans were carried out on the 3T Achieva scanner. An axial free breathing ^{23}Na 3D GRE scan (resolution: $5 \times 5 \times 30$ mm^3, TE: 1.5 ms, TR: 100 ms, FA: 81° (limited by TR), NSA: 12, TA: 8 mins) was acquired in each subject. The dual loops were placed on the subjects, one anteriorly and one posteriorly. Initially, in the healthy subject the loops were placed centrally in the left-right direction. However, subsequently for the CKD subjects, due to the limited FOV of the dual loops coil, they were positioned off-centre in the left-right direction so that they were above and below the right kidney, to guarantee good coverage of one kidney. A double angle B_1 map (resolution: $5 \times 5 \times 30$ mm^3, TE: 2.4 ms, TR: 150 ms, FA: 35/70°, NSA: 12, TA: 10 mins) was also collected to estimate thE ^{23}Na B_1 field transmit and allow for correction of B_1 inhomogeneity in the estimation of TSC. Three ^{23}Na reference bottles (30 mmol/L, 60 mmol/L and 120 mmol/L NaCl) were placed beneath the posterior coil to allow for calibration of the TSC maps, a measurement of the background noise (0 mmol/L NaCl) was also used as an additional reference point for the linear regression. A ^{1}H T_1 weighted (T_1W) bFTE scan was also collected in each patient in a single breathhold (resolution: $1.8 \times 1.8 \times 15$ mm^3,

TE: 1.2 ms, TR: 2 ms, FA: 50°, TA: 10 s) in the same space as the ^{23}Na images.

As for Chapter 4, the 3D GRE ^{23}Na images were corrected using the B_1 map. The reference bottles were then used to create a linear calibration curve which was used to compute the TSC in the kidneys. The kidneys were segmented from the ^{1}H image and the ^{23}Na concentrations within the kidney assessed through histogram analysis.

5.2.2 Results

The double angle B_1 maps collected in the healthy volunteers are shown in Fig.[5.1] with the approximate location of the anterior and posterior loops elements shown by the white boxes.

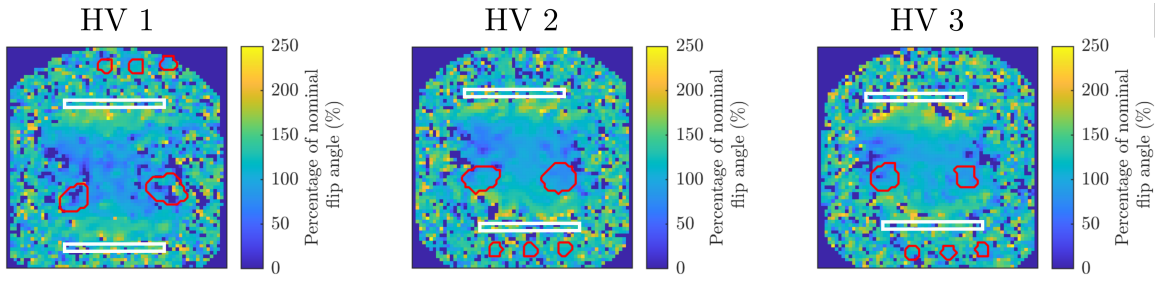

Figure 5.1: Double angle B_1 maps showing the percentage of the nominal flip angle achieved in the three healthy subjects, the position of the kidneys and reference bottles are outlined in red and the approximate location of the coil's loops are outlined in white.

Fig.[5.2] shows the computed TSC maps for the central slice of the 3D GRE acquisition overlaid on the ^{1}H images for the healthy volunteers, along with histograms of the ^{23}Na concentration in the kidneys. Note the axial slices contain a differing distribution of signal from the medulla and cortex. Fig.[5.3] shows an example zoomed ^{23}Na image of the right kidney of HV2 overlaid on a ^{1}H image. The zoomed image illustrates the higher ^{23}Na concentration in the medulla at ∼100 mmol/L compared to that in the cortex at ∼50 mmol/L. For each subject, the ^{23}Na concentrations in the reference bottles and kidney are given in Table [5.1], alongside the reference bottle linear regression's R^2 value. The ^{23}Na concentration in left kidney in HV1 is low (6 ± 15 mmol/L) due to the inaccurate B_1 map for the left kidney of HV1. The B_1 map has a large uncertainty (percentage of nominal flip angle = 80 ± 52 %).

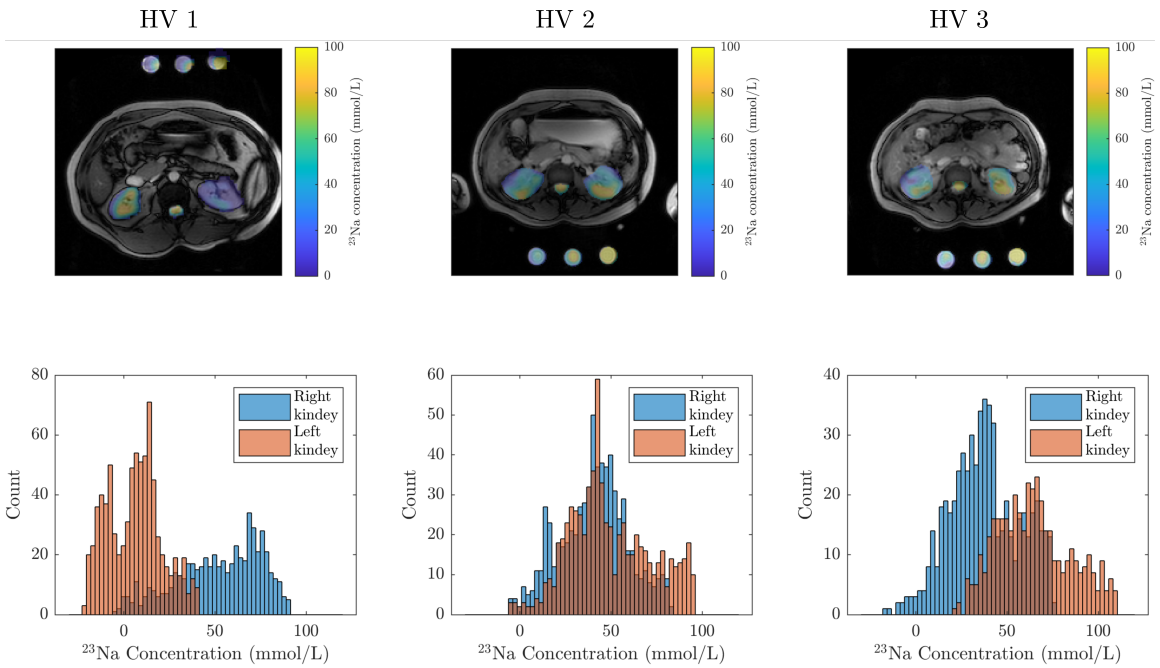

Figure 5.2: Top: ^{23}Na concentration in the kidneys of three healthy volunteers overlaid on their ^{1}H image. Bottom: Histograms of the ^{23}Na concentrations in the left and right kidneys.

	^{23}Na Concentration mean ± SD (mmol/L)					
Subject	HV1	HV2	HV3	CKD1	CKD2	CKD3
30 mmol/L bottle	37±20	33±14	30±24	36±15	25±9	29±21
60 mmol/L bottle	42±26	59±34	61±23	64±23	83±24	61±28
120 mmol/L bottle	127±80	120±41	118±47	117±46	110±41	11±6
Left kidney*	6±15	49±23	65±20	-12±12	-23±23	2±2
Right kidney	52±23	41±19	38±19	64±20	24±9	69±24
	^{23}Na calibration linear regression R^2					
	0.924	0.996	0.999	0.983	0.875	0.996**

Table 5.1: Measured ^{23}Na concentrations in the reference bottles and left kidneys.
* Due to coil positioning, the left kidney of the CKD patients did not have sufficient coil coverage to compute TSC.
** Fit to 30 and 60 mmol/L bottles and background noise signal for linear regression.

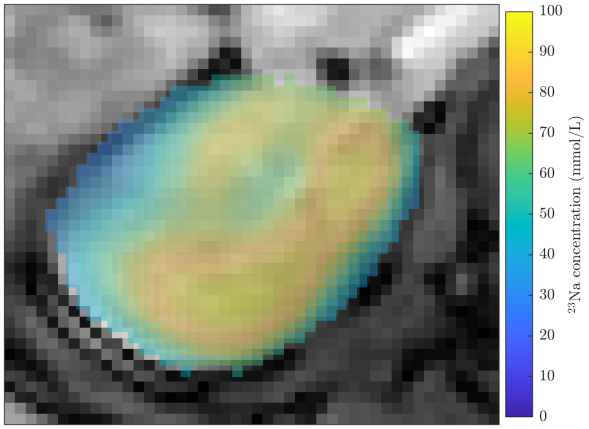

Figure 5.3: Right kidney ^{23}Na concentration of HV2 overlaid on the corresponding ^{1}H image, note the higher ^{23}Na in the centre of the image corresponds to the medulla.

The double angle B_1 maps for the CKD subjects are shown in Fig.[5.4] and illustrate the placement of the loops off centre to cover one kidney and how this effects the B_1 transmit fields.

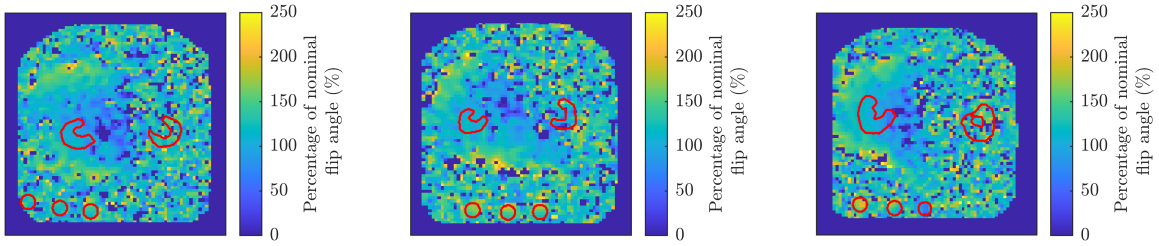

Figure 5.4: Double angle B_1 maps showing the percentage of the nominal flip angle achieved in the three CKD participants, the position of the kidneys and reference bottles defined from the ^{1}H images are outlined in red and the approximate location of the coil loops are outlined in white.

Fig.[5.5] shows the ^{1}H images of the three CKD patients with ^{23}Na concentrations in the kidney and reference bottles overlaid. Note, for the CKD patients the dual loops were positioned over the right kidney (resulting in the percentage of nominal flip angle being 100 ± 10 %) as compared to the left kidney where the confidence in the B_1 was low (116 ± 60 %). Table [5.1] provides the mean ^{23}Na concentrations in the reference bottles and the left kidney, values are also provide for the right kidney but these are expected to be erroneous due to coil positioning. Table [5.1] also provides the R^2 of the linear regression of the bottles, for CKD3 the left most (in subject's reference frame) 120 mmol/L bottle was excluded from the fit as this was positioned outside the FOV of the B_1 map.

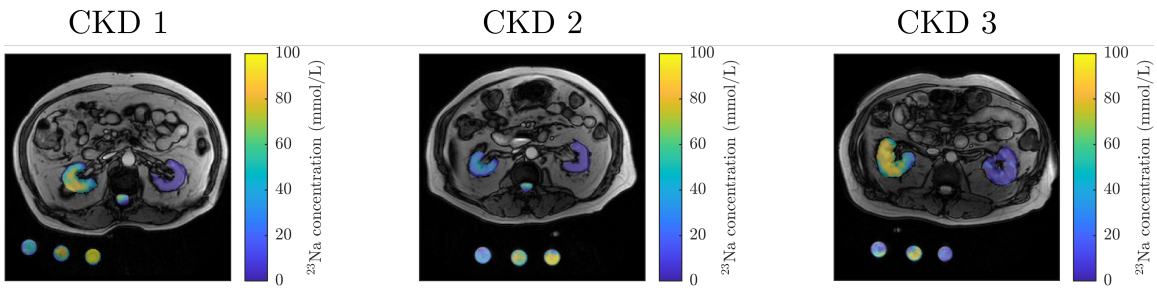

Figure 5.5: ^{1}H images of three CKD patients with the measured ^{23}Na concentration in the kidney and reference bottles overlaid.

5.2.3 Discussion

A number of observations can be made from the scans carried out on the healthy volunteers and CKD patients using the dual loops coil. For the healthy volunteers the loops were placed in the centre of the body (in the left-right direction) but the kidneys are anatomically located at the edge of the coils' sensitivity region. The confidence in the measured B_1 in the left kidney of HV1 was low, suggesting it was outside the coil's sensitivity region. With the kidneys positioned at the edge of the sensitivity region, the image SNR in the kidney will be low which will produce an inaccurate B_1 map and inaccuracy in the corrected ^{23}Na GRE image used for TSC estimation. This results in the measured difference in ^{23}Na concentration between the two kidneys in HV1. Another factor influencing the measured sodium concentration is the proportion of the medulla and cortex within the FOV. In HV1, higher ^{23}Na concentration towards the centre of the kidney is likely attributed to the higher ^{23}Na concentration in the medulla as is illustrated by the zoomed image shown in Fig.[5.3]. The reference bottles in HV1 moved slightly during the scanning session, between the ^{1}H and ^{23}Na scans, the effects can be seen in Fig.[5.2] as the ^{23}Na overlay is offset from the ^{1}H image. In subsequent scans the reference bottles were moved from an anterior to posterior position to reduce movement during the scan session. For the CKD subjects, whilst every care was taken to position the loops above and below the kidney, with the reference bottles directly below the lower loop, the B_1 maps in Fig.[5.4] show that this was not always possible in practice. This can be seen in the B_1 map from the CKD2 data in Fig.[5.4], where the lower coil was placed towards the centre of the body and the top coil is placed on the side of the patient. As the coils

are designed to be positioned opposite each other this placement has reduced the B_1 field produced and resulting in a low image SNR in the right kidney, which, in turn produced an inaccurate B_1 map. This incorrect positioning explains the lower ^{23}Na concentration in the right kidney in CKD2 compared the other two CKD patient's data, 24 ± 9 mmol/L for CKD2 versus 64 ± 20 mmol/L and 69 ± 24 mmol/L for CKD1 and CKD3 respectively. In the data collected for CKD3 the reference bottles were not positioned directly below the loop, the left-most bottle (120 mmol/L NaCl) thus experienced a low B_1 field, therefore producing a low MR signal. Thus for CKD3, the linear regression of the bottles omitted the 120 mmol/L reference bottle. The low MR signal in the 120 mmol/L bottle can be seen to have limited the accuracy of the B_1 map in this bottle (74 ± 28 % of nominal flip angle) and therefore the B_1 correction with a mean measured ^{23}Na concentration of 11 ± 6 compared to the reference solution concentration of 120 mmol/L. In the right kidney of CKD1 and CKD3 there are regions of higher ^{23}Na concentration, these likely correspond to the renal pyramids.

This data has shown the limitations of using the dual loops coil. In regions not between the loops, the B_1 map consists mainly of noise, these regions produce a low MR signal and the double angle B_1 mapping method will have failed to produce accurate B_1 maps (discussed in Chapter 4, Section [4.5.2]) and thus the ^{23}Na concentration is inaccurate. The data in Table [5.1] shows large variances in the measured sodium concentration in the reference bottles, particularly the left most 120 mmol/L reference bottle, which reduced the linear regression's fit. The variance in ^{23}Na concentration in the kidney is partly explained by the difference in ^{23}Na concentration between the renal cortex and medulla but it is also likely to have been affected by imperfect B_1 correction.

The work here has shown that the limited FOV of the dual loops ^{23}Na coil necessitates accurate positioning to measure ^{23}Na concentration reliably in one kidney. A coil with a larger FOV, such as the 6-channel ^{23}Na body coil will allow for TSC to be measured in both kidneys without such dependency on positioning of the subject and coil. In future, implementing a more accurate B_1 mapping method, such as the phase-sensitive method used in the calf (Section [4.5.1]) will also improve the B_1 correction accuracy and in-turn

the TSC.

5.3 Optimisation of the Gradient Recalled Echo (GRE) sequence for abdominal imaging

The previous section has shown ^{23}Na images acquired with a flip angle of 81 °and TR of 100 ms, however ^{23}Na imaging is hampered by low tissue SNR. Chapter 4 Section [4.3] assessed optimisation of the GRE scheme and outlined that the signal (S) in a GRE scheme, assuming a longitudinal steady state has been reached and perfect spoiling, is primarily dependent on flip angle (FA), repetition time (TR) and echo time (TE).

$$S \propto \frac{\sin\alpha \cdot \left(1 - e^{-TR/T_1}\right)}{1 - \cos\alpha \cdot e^{-TR/T_1}} \cdot e^{-TE/T_2{}^\star} \tag{5.1}$$

where α is the flip angle, TR is the repetition time and T_1 is the longitudinal relaxation time. For a given TR and T_1, the maximum signal is obtained at the Ernst angle α_{Ernst} given by

$$\alpha_{Ernst} = \cos^{-1}\left(e^{-TR/T_1}\right). \tag{5.2}$$

The relationship in Equation [5.1] is plot in Fig.[5.6a]. The maximum signal occurs when the TR is long enough to allow the longitudinal magnetisation to fully recover, approximately $5 \times T_1$, and if $TR >> T_1$ then the optimal flip angle is 90°. However, a longer TR increases the total acquisition time (TA) of the scan, alternatively by using a shorter TR, the available time can instead be used to collect a number of averages (NSA) which will increase the SNR by the square root of the number of acquisitions, $\sqrt{N_{acq}}$. However, limitations can dictate the possible values the GRE sequence parameters can take, these are imposed by the scanner and RF coil hardware, such as the maximum average RF power and the maximum B_1 delivered by the RF coil. At higher B_0 field or when imaging the body compared to the periphery, the pulse sequence must take into account the RF deposition, and as a result the RF pulse length, TR and flip angle cannot necessarily be adjusted in isolation from one another. A given flip angle (FA) may require

a longer TR to satisfy the SAR limit

$$SAR \propto \frac{{B_0}^2\alpha^2}{TR\tau_{RF}} \tag{5.3}$$

with the flip angle given by

$$\alpha \propto B_1\tau \tag{5.4}$$

where B_1 is the amplitude of the RF pulse and τ is its duration. Other considerations for ^{23}Na imaging are that due to the short bi-exponential transverse decay of ^{23}Na, the acquisition must be collected as soon as possible after the excitation, whilst the maximum B_1 is limited by the RF coil. Previous work by Stobbe et al. [84] has performed optimisation for signal to noise ratio under SAR constraints. This showed a substantial gain in SNR for ^{23}Na imaging in the brain at 4.7T by using a shorter TR and lower flip angle RF pulses at the Ernst angle compared to 90° pulses at a longer repetition time which was required to remain within the constraints dictated by SAR limits. Stobbe et al. [84] also assessed the longitudinal relaxation weighting of performing a shorter TR for ^{23}Na measures. Some of the prior studies performing ^{23}Na imaging of the abdomen have also collected data at short TR. For example, James et al. [85] performed *in vivo* ^{23}Na imaging of the abdomen at 3T using a short TR (12 ms) and flip angle (50°), whilst a study by Grist et al. [21] used a TR of 50 ms and flip angle of 60° to collect ^{23}Na images of the kidney.

The following section outlines the methods to optimise GRE scan parameters for the dual loops ^{23}Na body coil.

5.3.1 Methods

To ascertain the optimum GRE sequence parameters for abdominal imaging using the dual loops coil, a series of low resolution 3D GRE (10 × 10 × 30 mm^3, FOV: 350 × 350 × 200 mm^3, BW: 490 Hz) scans were carried out on the 10 L 100 mmol/L ^{23}Na body phantom. The series consisted of seven scans. For each scan a given B_1 amplitude was chosen (5 - 40 μT) and the smallest Ernst angle and corresponding TR was calculated (black curve

in Fig.[5.6a]). The position of the scans collected within the plot of theoretical intensity are shown in Fig.[5.6a] alongside the scan's pulse sequence parameters.

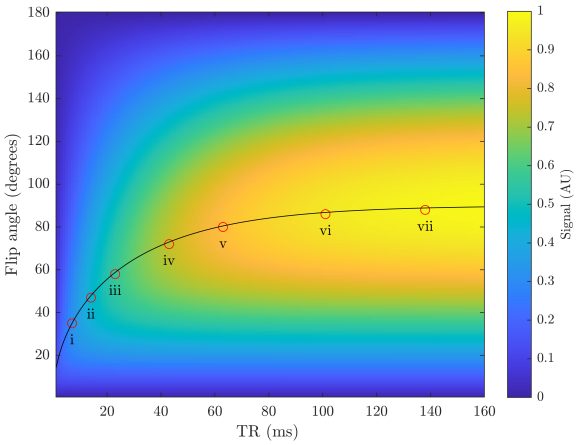

(a) The dependence of signal intensity on TR and flip angle for a T_1 of 35 ms. The positions of the scans are shown by the red circles and the Ernst angle for a given TR is shown by the black line.

Scan	TR (ms)	Flip angle (Deg)	TE (ms)	B_1 (μT)	TA (s)
i	7	35	1.54	5	1.9
ii	14	47	1.45	7.5	3.7
iii	23	58	1.39	10	6.1
iv	42	72	1.27	15	11.2
v	62	80	1.17	20	16.5
vi	100	86	1.03	30	26.6
vii	137	88	0.94	40	36.4

(b) The key sequence parameters of TR, flip angle, TE, maximum B_1 amplitude, and acquisition time (TA) for a single 3D GRE acquisition whilst remaining within SAR limits.

Figure 5.6: The scan parameters for the optimisation of the 3D GRE scan series.

For each image collected at a given TR, an ROI was placed at the centre of the phantom, midway between the two loops, as shown by the blue square in Fig.[5.7a]. The image SNR in the ROI was calculated from the mean signal divided by the variance in background noise. This was then plotted against the TR used for a single image acquisition.

To demonstrate experimentally the benefits of using a shorter TR, a series of scans were performed varying the NSA for a given TR so that each scan was approximately the same total duration of 200s. The scan parameters are listed in Table [5.2]

Finally, the parameters in Table [5.2] were tested *in vivo* using the same 3D GRE $10\times10\times30$ mm^3 scan series as for the phantom for a 200s total acquisition time. The dual loops coil was positioned anterior and posterior to the left kidney.

5.3.2 Results

A set of single acquisitions collected with the dual loops coil on the body phantom can be seen in Fig.[5.7a].

Scan	TR (ms)	Flip angle (Deg)	TE (ms)	B_1 (μT)	NSA	TA (s)
i	7	35	1.54	5	110	200
ii	14	47	1.45	7.5	55	200
iii	23	58	1.39	10	33	197
iv	42	72	1.27	15	18	197
v	62	80	1.17	20	12	194
vi	100	86	1.03	30	8	209
vii	137	88	0.94	40	4	183

Table 5.2: Parameters for the scan series tested *in vivo*. The number of averages were varied so that all the scans had approximately the same total acquisition time (TA).

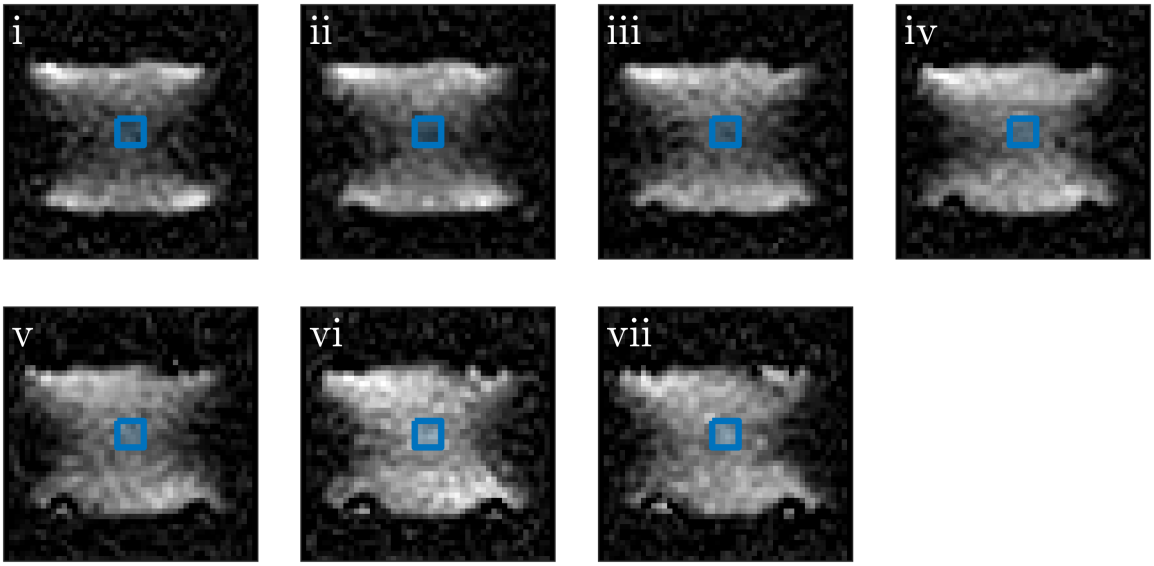

(a) ^{23}Na 3D GRE 10×10×30 mm^3 single acquisition scans collected on the 10 L 100 mmol/L ^{23}Na body phantom. Each image was acquired using the scan parameters given in Fig.[5.6b]. Blue squares show the ROI placed midway between the loops.

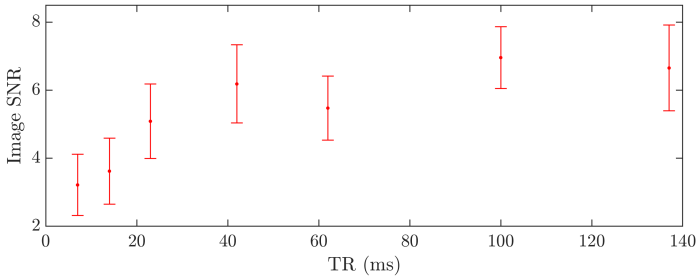

(b) Image SNR in the blue ROIs in Fig.[5.7a] for a single acquisition with the range of scan parameters outlined in Fig.[5.6b].

Figure 5.7: ^{23}Na 3D GRE single acquisition phantom scans.

As expected from Equation [5.1], for a single acquisition the greatest image SNR was

measured at the longest TR, as measured in the ROI and shown in Fig.[5.7b]. However, the longer TR resulted in a longer total scan time (TA). Fig.[5.8a] shows scans acquired across the range of TR values for a given TA of ∼200 s, it can be seen that the greatest image SNR per unit scan time is obtained when using a shorter TR and collecting many averages, Fig.[5.8b].

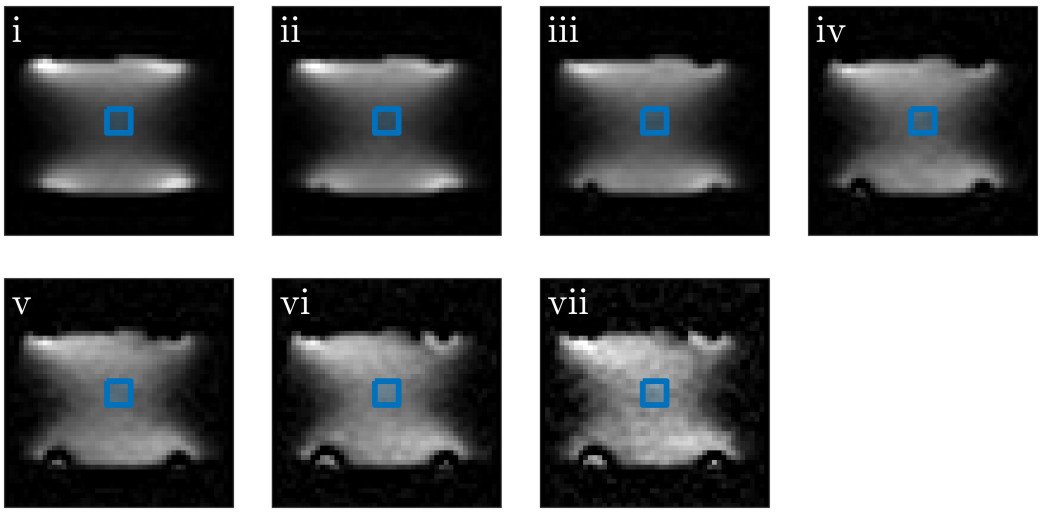

(a) ^{23}Na 3D GRE 10×10×30 mm^3 scans collected on the 10L 100 mmol/L ^{23}Na body phantom, TA of ∼200 s. Each image was acquired using the scan parameters given in Table [5.2].

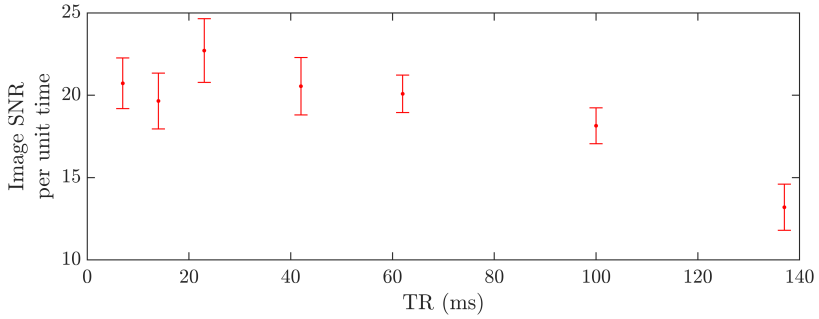

(b) Image SNR per unit scan time in the blue squares in the images in (a).

Figure 5.8: ^{23}Na GRE scans collected at a range of TRs and corresponding Ernst angle with the same total acquisition time of ∼200 s.

The images collected *in vivo* can be seen in Fig.[5.9a], for each of the scans outlined in Table [5.2]. The ^{23}Na concentration was significantly lower in the body than the 10 L body phantom. The image SNR per unit time in the left kidney is plot in Fig.[5.9b], showing the same pattern as for the body phantom.

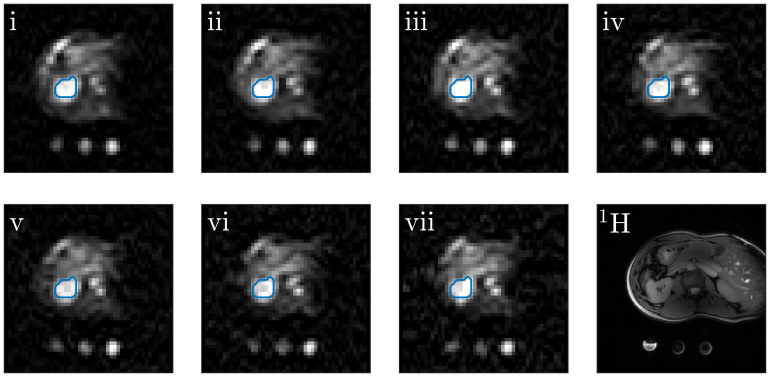

(a) ^{23}Na 3D GRE 10×10×30 mm^3 scans carried out *in vivo*. Each image was acquired using the scan parameters provided in Table [5.2].

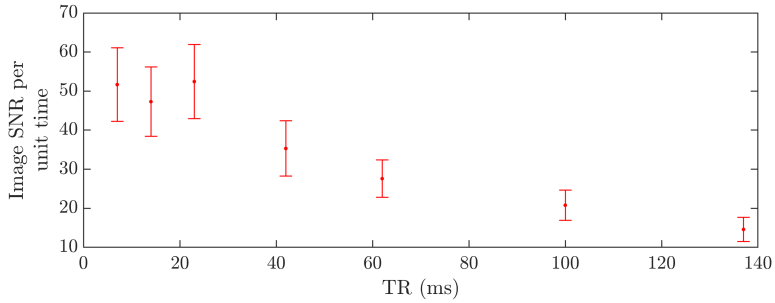

(b) Image SNR per unit time measured from the 3D GRE for the blue ROI in the images in left kidney (a).

Figure 5.9: ^{23}Na scans collected *in vivo* at a range of TRs and corresponding Ernst angle with the same total acquisition time of ∼200 s.

Fig.[5.10] shows the ten slices collected in ^{23}Na 3D GRE scan alongside the corresponding ^{1}H images.

5.3.3 Discussion

These experiments have demonstrated that to achieve the maximum image SNR per unit time, while keeping within the SAR constraints, a short TR should be used. This allows a high number of signal averages whilst keeping the B_1 low to allow the scan to remain under the average power limit, note here that an 88° flip angle was constrained to a shortest TR of 137 ms. Despite improving the image SNR per unit time, the FOV of the dual loops still remains challenging due to the need for placement of the coil over the both kidneys. The next section thus explores the benefits of using a 6-channel ^{23}Na coil to perform ^{23}Na imaging of the abdomen.

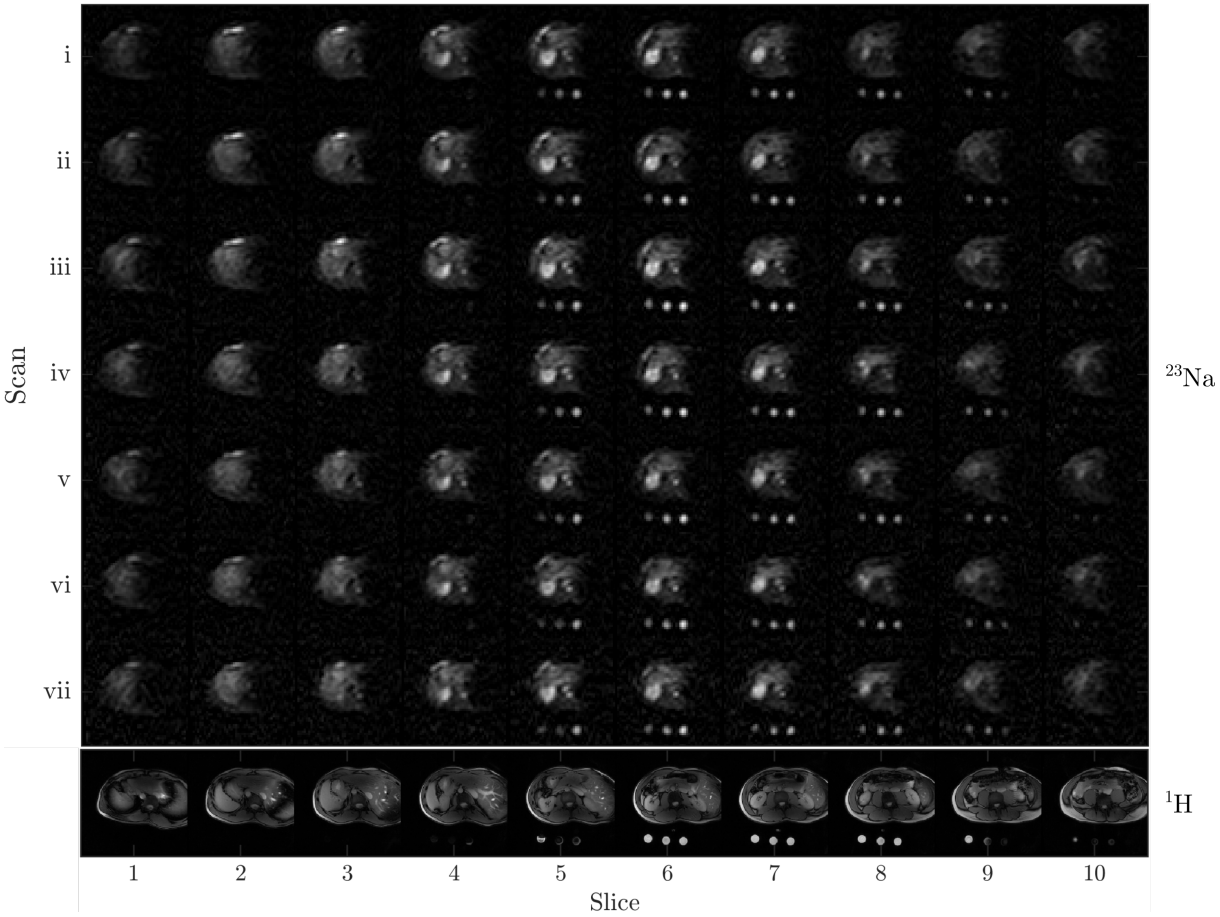

Figure 5.10: The ten slices of the 3D GRE acquisition collected for each of the seven scans in Table [5.2], showing the variation in ^{23}Na signal intensity with TR and Ernst angle across slices, the corresponding ^{1}H images are shown on the bottom row.

5.4 Dual Loops versus 6-Channel Body Coil

In this section, the performance of the ^{23}Na dual loops coil and the 6-channel body coil are compared, with GRE scans collected on the body phantom and in healthy volunteers.

5.4.1 Method

Data was collected using the optimised GRE scan parameters derived above in Section [4.3] on the body phantom and *in vivo* (n = 3 healthy subjects, age 25 - 28 years). The dual loops coil was positioned centrally. The 3D GRE sequence parameters were for the dual loops: TR: 7 ms, TE: 1.54 ms, FA: 35°, resolution: $3 \times 3 \times 20$ mm^3, 8 slices, TA 20 mins, NSA: 406; and for the 6-channel coil: TR: 8 ms, TE: 1.97 ms, FA: 35°, resolution: $5 \times 5 \times 20$ mm^3, 8 slices, TA 20 mins, NSA: 406. The dual loops coil images were reconstructed on

the scanner. The scanner software is unable to combine the six MN channels therefore the individual six receive channel's data was reconstructed by the scanner software, and the six images were then combined offline in Matlab (The MathWorks Inc, USA) using the sum-of-squares method. To measure image SNR differences between the two coils, two circular ROIs were placed inside the phantom where the kidneys would typically be located *in vivo*. In the human scan session a single breathhold ^{1}H T_1W B-FTE scan (resolution: $1.8 \times 1.8 \times 15$ mm^3, TE: 1.2 ms, TR: 2 ms, FA: 50°, TA: 10 s) was collected in order to segment the kidney and generate ROIs. The kidney ROIs were then applied to the ^{23}Na images and the image SNR for the kidneys in the central slice was measured.

5.4.2 Results

Fig.[5.11] compares the 3D GRE images collected on the body phantom using the dual loops coil and the 6-channel coil.

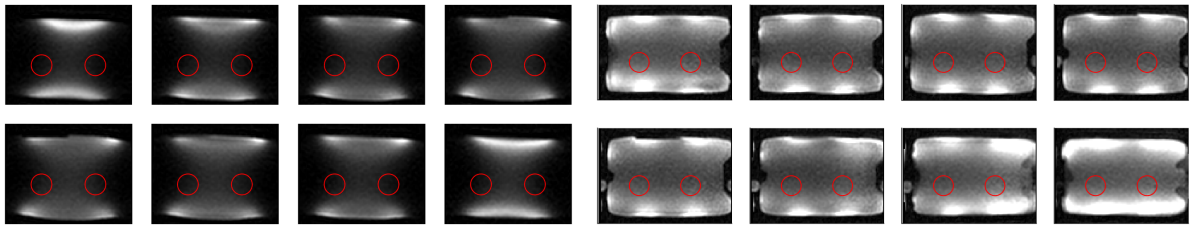

(a) Dual loops coil. (b) 6-channel coil.

Figure 5.11: ^{23}Na images of the body phantom, used to compare the SNR between the two RF coils. Two circular ROIs were placed within the phantoms in a location where the kidney would be located.

For the dual loops, the image SNR was 6 ± 2 and for the 6-channel coil the image SNR was 19 ± 3 on the body phantom, with comparable SNR in both ROIs. The image SNR within the ROIs shown in Fig.[5.12] for the dual loops coil the right kidney was 7 ± 3 and left kidney was 8 ± 2 for the 6-channel this was measured to be 13 ± 3 in the right kidney and 9 ± 2 in the left. The full coverage across the 8 slices of the 3D GRE acquisition is shown in Fig.[5.13]. Fig.[5.12] compares *in vivo* healthy subject data collected with the dual loops and the 6-channel coil.

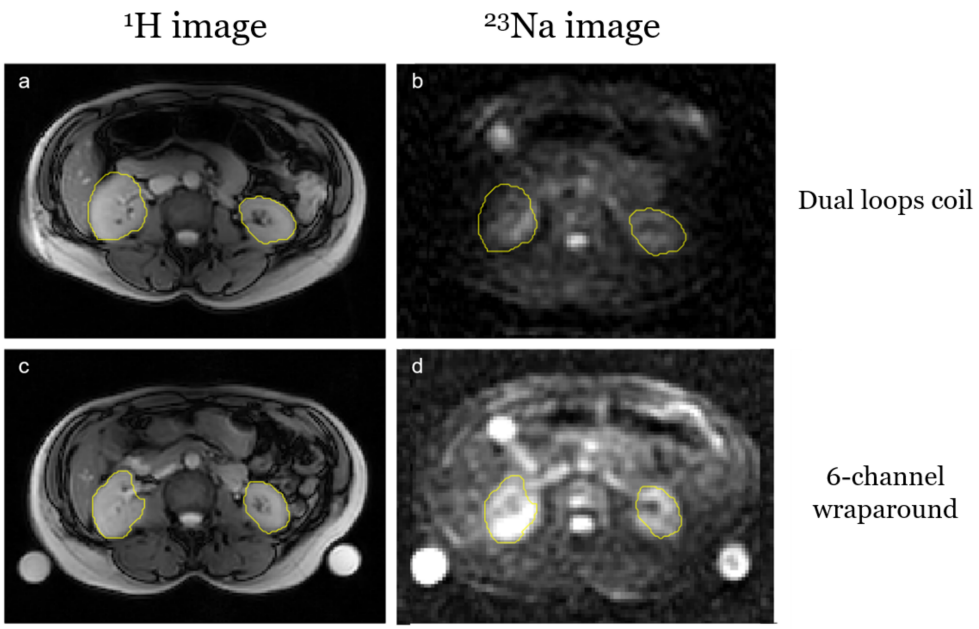

Figure 5.12: ^{1}H and ^{23}Na images of the abdomen for comparison of the image SNR in the kidneys between the dual loops coil and 6-channel QTAR ^{23}Na coil. The yellow boundaries of the kidneys were drawn by hand on the ^{1}H images and overlaid onto the ^{23}Na images. An ROI was also placed in the background signal.

5.4.3 Discussion

These measurements demonstrate that the 6-channel coil provides increased image SNR over the dual loops coil for ^{23}Na imaging and an improved field of view allowing imaging of both kidneys with ease of planning. The dual loops coil does not provide complete coverage of the phantom, with the regions on left and right of the phantom showing very low signal. When the kidneys are imaged with the dual loops they fall right at the edge of the FOV, see Fig.[5.13], so for larger subjects this is restrictive and due to variations in coils positions this could lead to the kidneys being outside of the FOV. This position dependence becomes far less of a concern with the larger FOV covered by the 6-channel coil. Although the reference bottles were present in the 6-channel images, further work is needed to modify the B_1 mapping methods to be usable with the multiple receive channels MN data, to allow the conversion of ^{23}Na signal intensity images into ^{23}Na concentration maps.

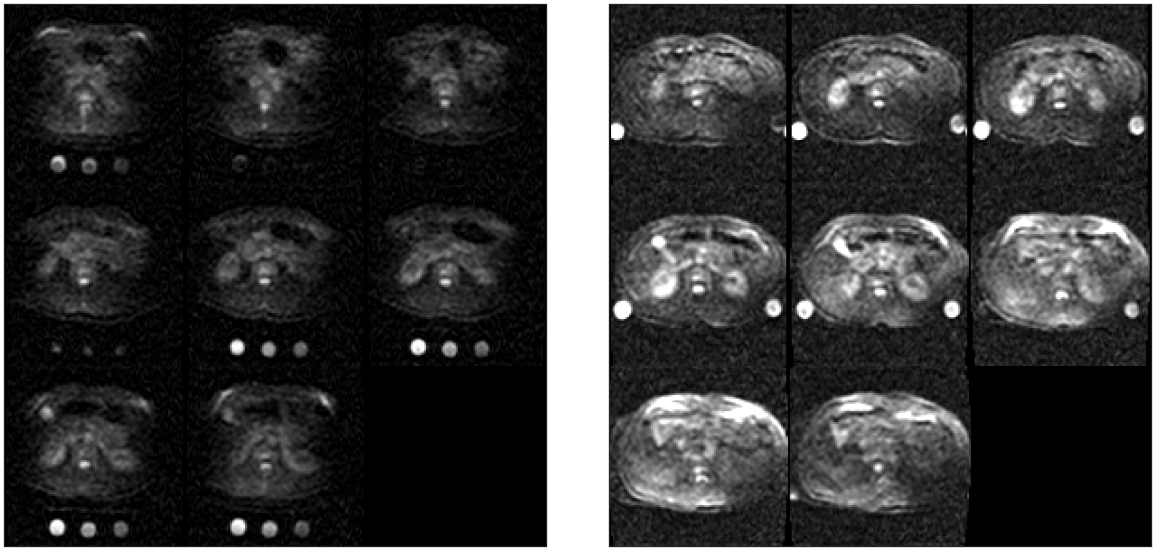

(a) Dual loops coil (b) 6-channel coil

Figure 5.13: 3D GRE ^{23}Na images of the abdomen collected with the dual loops and 6-channel coil, demonstrating the increased homogeneity of coverage of the 6-channel coil compared to the dual loops coil.

5.5 Receive Sensitivity Correction

The 6-channel ^{23}Na body coil is a phased array coil, it has a single transmit element and six receive elements, each of the receive elements measures the RF signal from part of the body. The signals from each receive element are combined to provide a complete image of the whole abdomen. The receive profile of each element is not uniform, the profiles for all six elements will not be identical, and neighbouring profiles will overlap with each other. Therefore, when the signals are combined, and the images are produce the inhomogeneity in these receive profiles will produce artificial variations in signal intensities which if uncorrected will lead to incorrect measures of the ^{23}Na concentration.

The receive sensitivity inhomogeneity can be corrected by measuring a sensitivity profile of the coil, the simplest way this can be done is by collecting two images: The first image is collected using the transmit coil element to both transmit and receive the RF signal, in ^{1}H imaging this is commonly done using the scanners in-build birdcage coil, the receive profile of the transmit coil is expected to be uniform and this image is used as a reference image. A second image is collected using the receive element coils. Dividing the second image by the first image provides an estimate of the receive sensitivity profile. These two images

can be collected as two individual so called scout scans, but this requires extra scan time, and also requires that the RF coil used can optionally transmit and receive on just the transmit element, which is not possible for the 6-channel ^{23}Na body coil. Previous work has investigated whether the need for additional scout images can be removed, with work by Murakami et al. [86] showing that the two scout images can be derived from the phased array image to be corrected. The first transmit element image can be approximated by first thresholding the phased array image and then low-pass filtering the resulting binary image. The second scout image can be approximated by low-pass filtering of the image to be corrected. Work by Lachner et al. [87] showed that this technique was appropriate to use in ^{23}Na imaging in the brain. Here this will be applied to the 6-channel ^{23}Na body coil data.

5.5.1 Theory

The data from the receive elements when combined using sum-of-squares will give a signal $S(x, y)$ that will be a function of the objects magnetisation $M(x, y)$, the receive sensitivity $E(x, y)$ and the noise profile $N(x, y)$,

$$S(x, y) = M(x, y)E(x, y) + N(x, y). \tag{5.5}$$

Assuming $M(x, y)$ is significantly larger then $N(x, y)$ then the objects magnetisation can be reclaimed if $E(x, y)$ is known,

$$M(x, y) = \frac{S(x, y)}{E(x, y)}. \tag{5.6}$$

$E(x, y)$ can be measured by low-pass filtering the phased array image with a gaussian kernel with a standard deviation σ_I, this image $im_{pa,lpf}$ is then divided by a reference image. The reference image traditionally will have been an image collected with the coil's transmit element. However, here an artificial image is generated. First the phased array image is thresholded to create a binary mask known as a support image, with the pixels inside the object set to 1 and those outside set to 0, as was done in previous studies [86].

This mask is then low-pass filtered with a gaussian kernel with standard deviation σ_s to produce the reference image $im_{ref,lpf}$.

$$E(x,y) = \frac{im_{pa,lpf}}{im_{ref,lpf}} \tag{5.7}$$

$E(x,y)$ inside the object was normalised to 1 and the region outside the object was set to 0. The steps carried out to produce the coil's sensitivity profile are illustrated in Fig.[5.14].

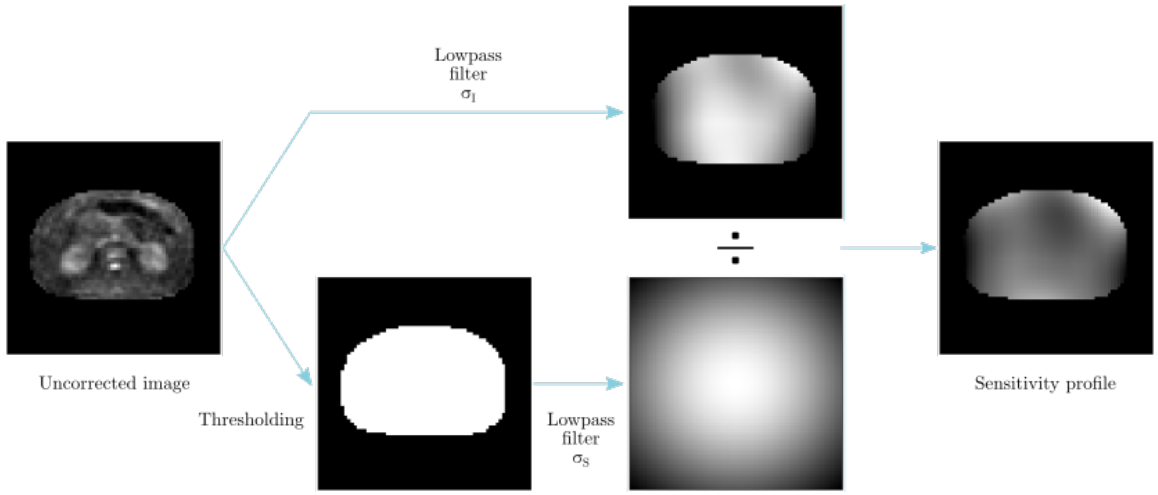

Figure 5.14: The processing steps to produce a RF coil sensitivity profile image from a phased array image.

This sensitivity profile within the object E_{obj} is then applied to the unfiltered phased array image im_{pa}.

$$M(x,y) = \frac{S(x,y)}{E(x,y)} = \frac{im_{pa}}{E_{obj}}. \tag{5.8}$$

The effectiveness of the receive sensitivity correction depends on the correct selection of the low-pass filter parameters applied to the phased array image, σ_I, and to the generated support image, σ_s. With access to a transmit element image these parameters can be selected by comparing the corrected phased array image to the transmit element image [86, 87]. The work by Lachner et al. [87] used a simulated ^{23}Na dataset generated by creating an anatomical model from the ^{1}H images and allocating typical ^{23}Na concentration to the different tissue compartments. This simulated dataset was used as a ground truth to compare the effectiveness of the sensitivity correction and to optimise the filtering

parameters. Their work studied the brain, and the model comprised four compartments whereas the axial slice of the abdomen used here would require more compartments, not all of which have known ^{23}Na concentrations. Further work is needed to investigate creating a ground truth of the abdomen to use as a validation method. Therefore, without access to this validation method a qualitative approach was taken here as follows.

5.5.2 Methods

Data to test the sensitivity correction was collected on the 3T Philips Ingenia using a 3D FFE scan (Resolution: $3 \times 3 \times 20$ mm^3, TA: 20 mins, TE: 1.97 ms, TR: 25 ms, FA: 58°, 8 slices, NSA:120). Data was collected *in vivo* and on the 10 L body ^{23}Na phantom. The ^{23}Na body phantom contains no structure and a homogeneous NaCl concentration throughout. A homogeneous phantom can provide useful insight into the receive sensitivity profile shape, however its lack of structure and its uniformity has limited use in testing the receive sensitivity correction. Thus the same scan was collected *in vivo*. The individual six receive channel's data was reconstructed by the scanner software, and the six images were then combined offline in Matlab (The MathWorks Inc, USA) using the sum-of-squares method. The receive sensitivity correction was then applied to the combined image using a range of σ_I (from 5 to 50 mm) and σ_s (from 3 to 150 mm) values. The effectiveness of the correction was assessed by measuring the standard deviation of the corrected pixel intensities within the phantom.

5.5.3 Results

Fig.[5.15] shows the effect of filtering the phased array image *in vivo*, σ_I must be chosen in order to remove the anatomical structure to show the receive sensitivities. For σ_I = 5-30 mm the kidneys can still be seen, but if too large filters are applied this will remove the receive sensitivity.

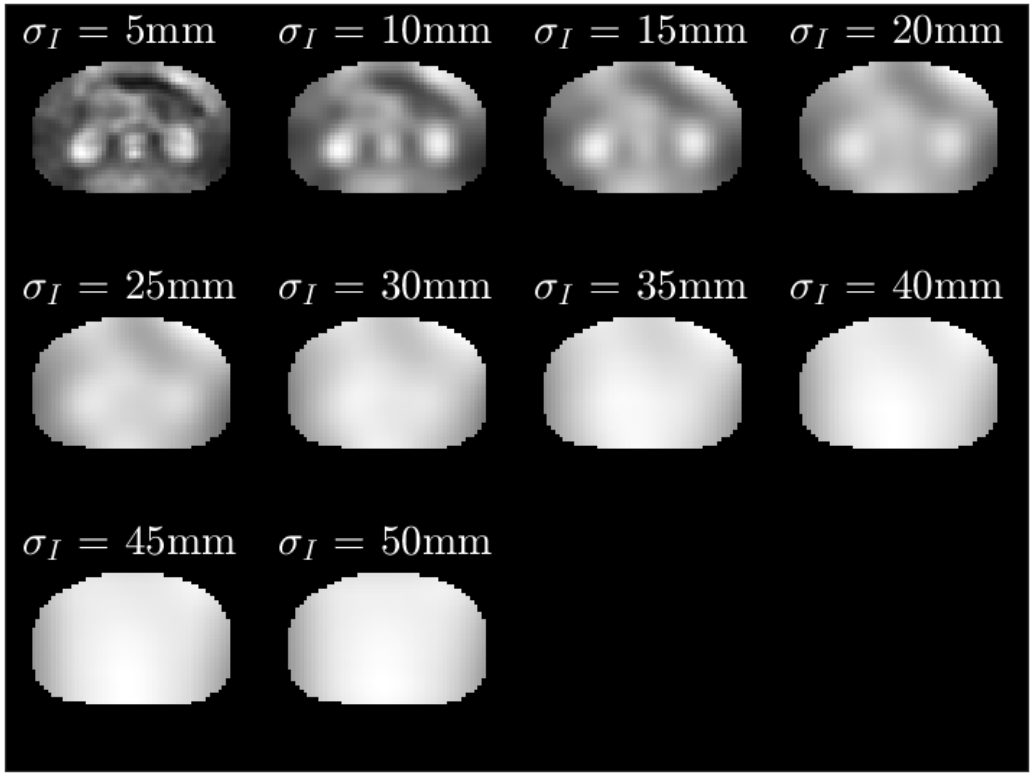

Figure 5.15: The application of the low-pass filter to the phased array ^{23}Na image *in vivo*.

The amount of filtering needed to be applied to the support image is harder to justify. Results of the same scan and correction on a phantom provided some insight into suitable values for σ_s. The standard deviation of the corrected pixel intensities within the phantom can be seen in Fig.[5.16].

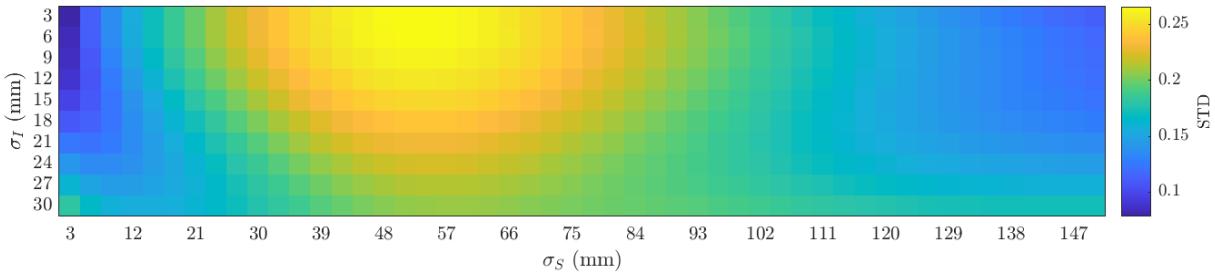

Figure 5.16: Plot showing the dependency of the standard deviation of the corrected phantom image signal intensities on the two filter parameters σ_I and σ_s.

As expected, the minimum standard deviation was achieved when minimum filtering was carried out; in the homogenous phantom the phased array image accurately reflects the sensitivity profile of the coil. As the phased array image is filtered with increasing σ_I the initial effects on the standard deviation is minimal as the filter size is small compared to

the receive sensitivity profile's variations. As the amount of filtering σ_S that the support image undergoes increases, the standard deviation increases caused by the centre of the sensitivity region becoming overestimated, the standard deviation then decreases as the variance across the structure image decreases. For $\sigma_S > 150$ mm the standard deviation in the corrected phantom image plateaus. These phantom measurements were used to inform the best filtering parameters *in vivo*, with the results suggesting that a large value of $\sigma_S \approx 150$ mm is needed. The low-pass filtering of the reference image scan be seen in Fig.[5.17].

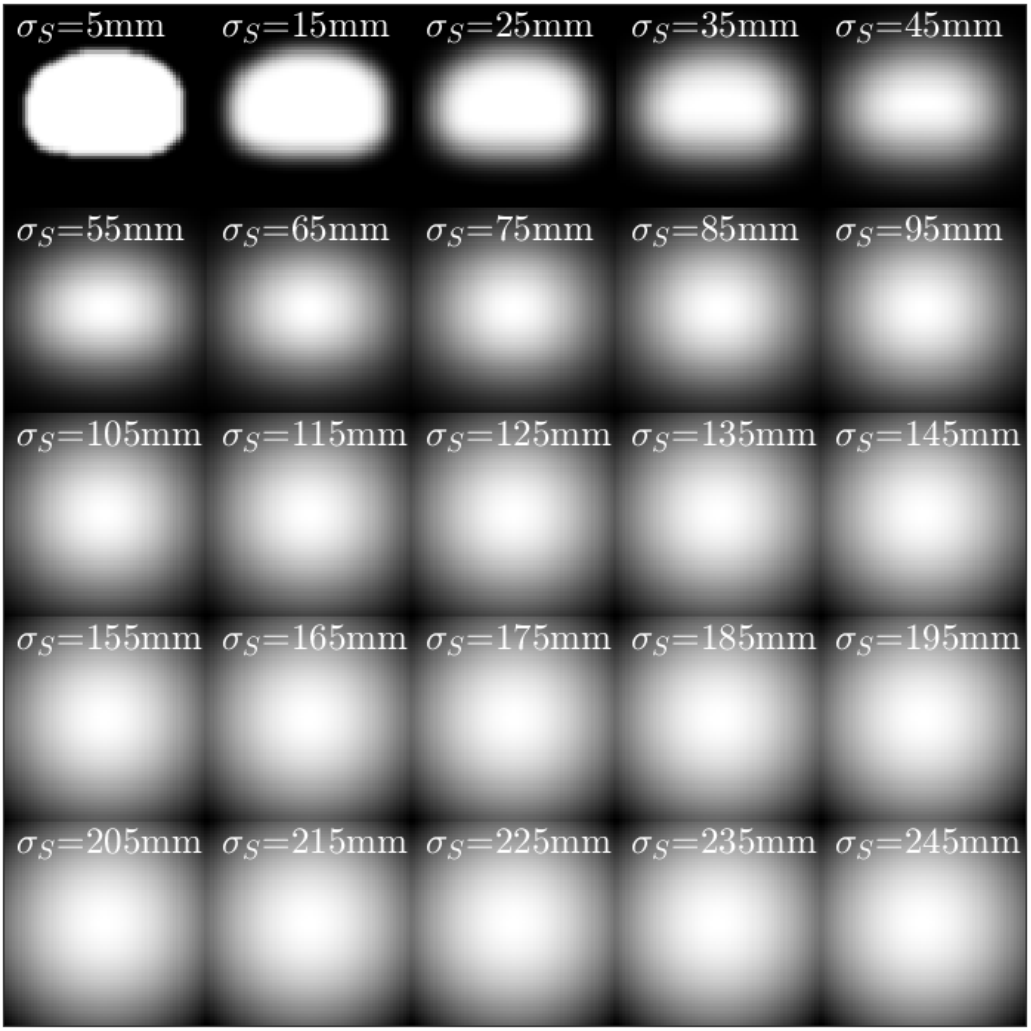

Figure 5.17: The application of the low-pass filter applied to the reference image.

The sensitivity map was applied to the uncorrected phased array image and the results can be seen in Fig.[5.18]. Fig.[5.18a] shows the uncorrected phased array image and Fig.[5.18c] the corrected image using the sensitivity profile shown in Fig.[5.18b]. The phased array

image from the same scan carried out on the body phantom is shown in Fig.[5.18d]. Fig.[5.18e] shows the phased array image of the phantom corrected using a sensitivity profile generated using the same values of σ_I and σ_S used for the *in vivo* correction. The standard deviation of the pixel intensities inside the phantom image reduced from 0.4 in the uncorrected image to 0.13 in the corrected image.

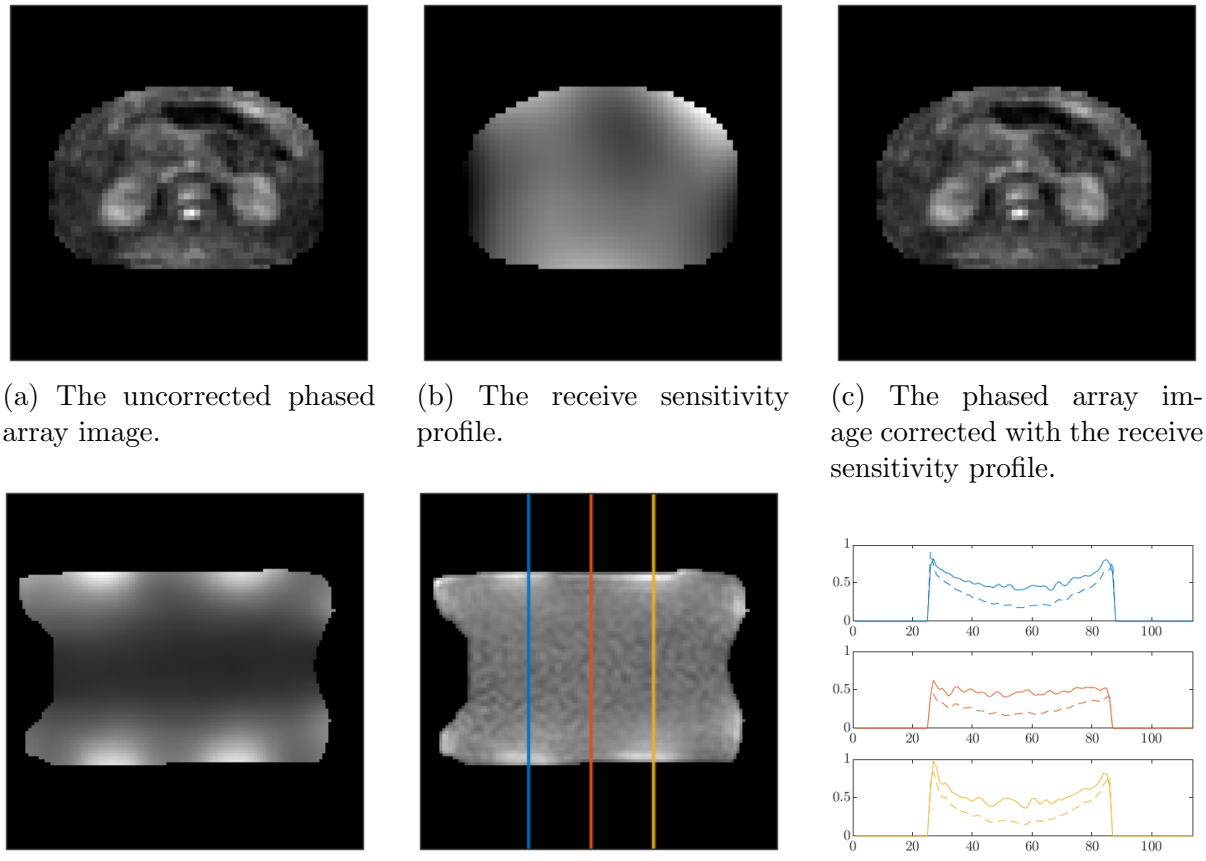

(a) The uncorrected phased array image.

(b) The receive sensitivity profile.

(c) The phased array image corrected with the receive sensitivity profile.

(d) The uncorrected phased array image of the body phantom, demonstrating the receive sensitivity profile.

(e) The phantom image corrected with the receive sensitivity profile generated using the same filtering parameters as used in vivo.

(f) Profiles of the lines shown in (e) for the uncorrected (dashed line) and receive sensitivity corrected (solid line) ^{23}Na image.

Figure 5.18: The application of the receive sensitivity correction *in vivo* and in the ^{23}Na body phantom.

5.5.4 Discussion

Here, a sensitivity map has been generated and applied to the ^{23}Na image in an attempt to correct for the receive inhomogeneity of the 6-channel ^{23}Na body coil. The effects are clearly illustrated in the body phantom. However, *in vivo* the effect of this correction is

subtle. The regions in the corrected image between the kidney and skin on both the right and left of the body have a lower ^{23}Na signal than the rest of the abdomen. Although this may look like an effect of incorrect receive sensitivity correction this is to be expected, as this region mainly comprises of fat, which has very low ^{23}Na concentration. In contrast the centre of the back has a greater ^{23}Na signal due to larger concentration of ^{23}Na in the muscle. These anatomical differences can be seen in the accompanying ^{1}H image seen in Fig.[5.19].

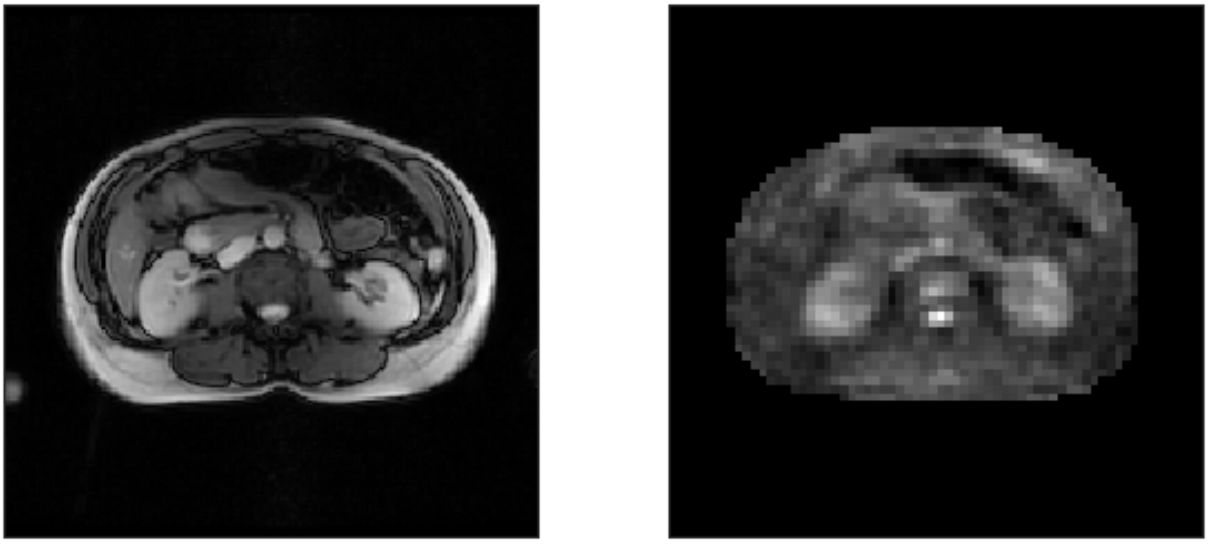

(a) (b)

Figure 5.19: ^{1}H image collected using the in-built Q-body coil shown for in the same slice as the receive sensitivity corrected phased array ^{23}Na image.

Without a ground truth to compare it to, either as a transmit element image or a simulated model, it is not possible to measure the accuracy of this correction method. Previous work by Lachner et al. [87] and the phantom scans shown here suggest it provides an effective method. Lachner et al. [87] produced a ^{23}Na brain model using a proton image to segment the brain into four compartments, white matter, grey matter and CSF both inside and outside the brain. These compartments were allocated a signal intensity based on the known ratio of ^{23}Na signal intensity between the four regions. A similar validation with model signals in the body could be generated, however there are many different tissues present in the abdomen and the ^{23}Na signal is not as well defined for each tissue type. Alternatively, a phantom of the abdomen with more structure present and known ^{23}Na

concentrations could be developed, this would provide further insight into the effectiveness of this receive sensitivity correction method. The earlier work by Murakami et al. [86] presented this method for ^{1}H imaging and highlighted the suitability of using a GRE image to approximate the receive sensitivity profile of the coil due to the low contrast of GRE images, this meant that less filtering was needed to remove the structure from the phased array images. Conversely, the ^{23}Na *in vivo* data shown here had large intensity differences e.g. in the kidney which required a large amount of filtering to remove this structure, it is possible that this amount of filtering will have reduced the accuracy of the sensitivity profile estimation. The low SNR of ^{23}Na imaging could also affect the accuracy of the generated receive sensitivity profile, in regions of low signal the assumption made in Eq.[5.5] that noise is significantly smaller than the signal no longer holds, this could lead to an inaccurate assessment of the coils sensitivity in low signal regions and noise in these regions will be amplified by the correction.

Modification of the coil to allow it to receive on the transmit element would allow for this method to be properly evaluated. Furthermore, it would enable additional imaging techniques to be used with the phased array coil such as shown by Benkhedah et al. [88] who used the transmit reference image when carrying out adaptive combined reconstruction to optimally combine multiple receive coil data. A reference image would also allow for SENSE based methods to be carried out when an accurate sensitivity profile is required. However, such a modification would require a new coil interface at a considerable cost.

5.6 ^{1}H Measurements with the Q-Body Coil

The methods covered in Section [3.5] showed that the 6-channel body coil was compatible with the MRI scanner's in-built ^{1}H coil. Future ^{23}Na studies will benefit from the ability to carryout ^{1}H structural and functional measures collected in multi-parametric renal studies [89] in the same scan session, this includes measures of kidney volume, BOLD T_2^*/R_2^* and T_1 and T_2 mapping. Typically, ^{1}H renal studies have used phased array receive RF coils in conjunction with the Q-Body transmit improving SNR, allowing the use of parallel imaging such as SENSE. In contrast, the ^{1}H scans collected alongside ^{23}Na

scans use the Q-Body coil to transmit and receive. As seen in previous sections, it is useful to be able to collect ^{1}H images to allow for segmentation of the kidney, which then can be applied to the ^{23}Na data. Fig.[5.20] shows an example ^{1}H image collected with the Q-Body RF coil. This is acquired at $1.8 \times 1.8 \times 15\ mm^3$ ^{1}H using a T_1W scheme (TE/TR: 1.2/2 ms, FA: 50°, TA: 10 s).

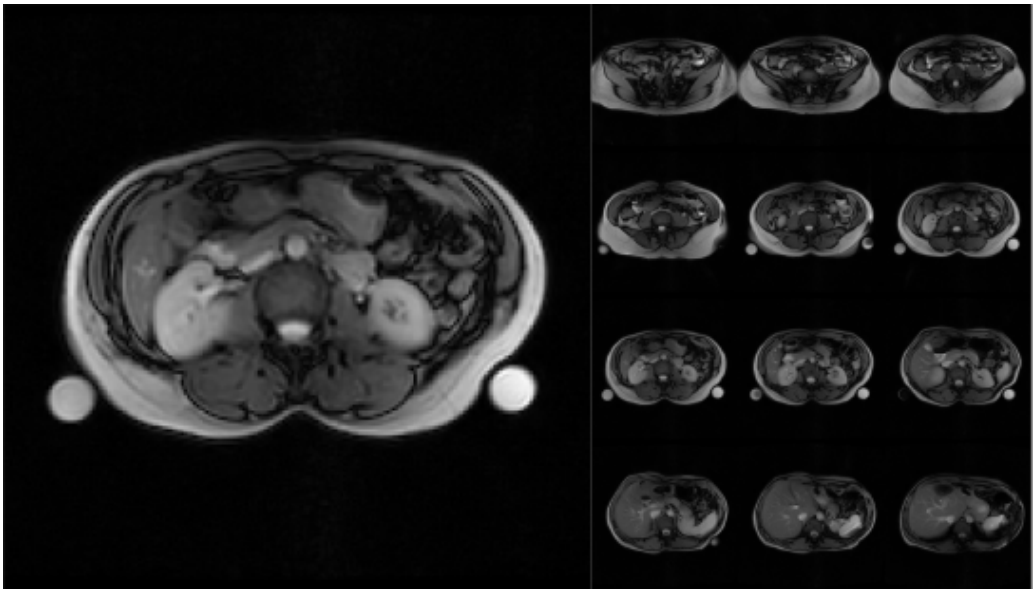

Figure 5.20: ^{1}H image to enable the segmentation of the kidneys.

To assess the feasibility of collecting other ^{1}H functional measures with the Q-Body coil a 12 echo mFFE scan was carried out to measure renal oxygenation using Blood Oxygen Level Dependent (BOLD) T_2^*. BOLD exploits the paramagnetic properties of deoxygenated blood, which acts to shorten T_2^*, this provides an indirect non-invasive assessment of oxygen content in the kidney. The sequence parameters were spatial resolution of $2.5 \times 2.5 \times 10$ mm^3, TE: 5 ms, ΔTE = 3 ms, FA: 25°, TR: 39 ms, TA: 28 s. The calculation of the T_2^* map was carried out using the in-built scanner software and can be seen in Fig.[5.21].

The data shows that there is sufficient SNR to generate a T_2^* map in the kidneys with measures in agreement with previously published values [89].

These ^{1}H measures collected using the Q-Body coil alongside the ^{23}Na 6-channel coil suggest that it will be possible to produce complementary ^{1}H measures in a ^{23}Na scan session.

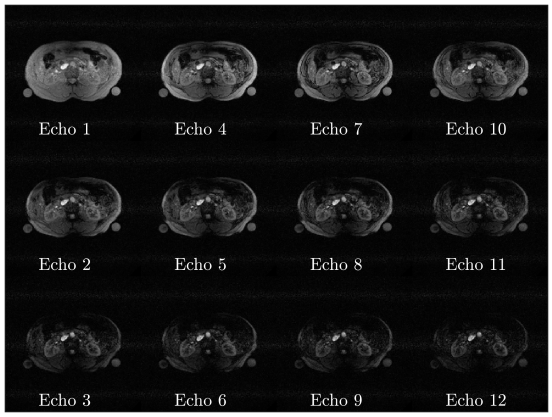

(a) 12 echos (echo 1 = 5ms, ΔTE = 3 ms) used to generate the T_2^* BOLD map.

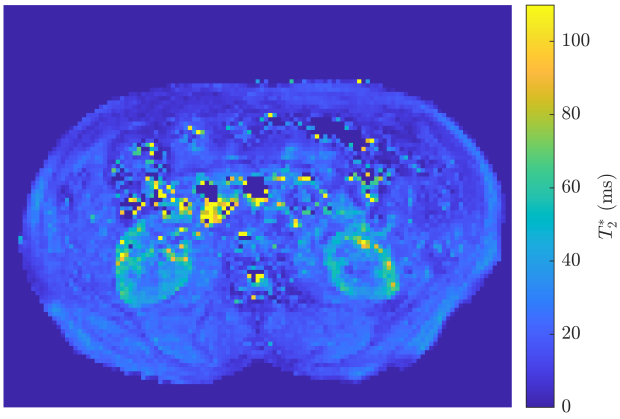

(b) T_2^* BOLD map/

Figure 5.21: ^{1}H BOLD image acquisition.

5.7 Discussion

This chapter has assessed the issues faced when carrying out renal ^{23}Na MRI in the abdomen. Since ^{23}Na has low intrinsic SNR due to the low tissue concentration, an assessment of the scan parameters for optimal image SNR was performed. The use of dual loops were compared with a 6-channel coil. The 6-channel coil was shown to improve the versatility of performing ^{23}Na MRI measures by offering an improved coil profile homogeneity and increased image SNR compared to the dual loops. Having established optimal parameters, evaluated coverage and repeatability, in future studies coronal slices will be collected combined with ^{1}H structural and BOLD measures to assess ^{23}Na and oxygenation measures across the kidney, for this the kidney will be segmented into concentric layers as described by Malani et al. [90]. In future work, these ^{23}Na imaging methods will be used in the assessment of water load as performed by Maril et al. and Haneder et al. [10, 60, 82] to determine reproducibility of assessment of change in sodium concentration. Studies will also be performed to evaluate patients with renal disease against healthy volunteers to determine whether changes in the CMSG can be detected and combined with ^{1}H measures.

Using ^{23}Na MRI with the 6-channel body coil it will also be possible to investigate the effects of different infusions solutions on the ^{23}Na concentration in different organs. Intravenous crystalloids with high chloride content cause a hyperchloraemic metabolic acidosis

and our groups previous work has shown that this results in a decrease in urinary volume and urinary ^{23}Na excretion, and renal blood flow and cortical tissue perfusion as measured by MRI [91–93]. The excretion of ^{23}Na is dependent on chloride concentrations, but little is known of how high and low chloride containing crystalloids alter the distribution of ^{23}Na in the body. In future, non-invasive ^{23}Na imaging with the 6-channel body coil will allow the study of changes in the distribution of ^{23}Na concentration within abdominal organs, muscle and the bladder in response to a randomized, double blinded crossover study of 0.9 % saline (high chloride) and Plasma-Lyte (physiological chloride) infusions. This will be used to test the hypothesis that given the effects of chloride on renal haemodynamics and the Angiotensin 2 receptors [92–94], the total tissue ^{23}Na concentration in the kidneys and bladder will be different from other organs. Such a study will provide information that will help inform perioperative intravenous fluid therapy and will also have implications for other ^{23}Na retention states like congestive cardiac failure, oedema of malnutrition and liver failure.

Chapter 6

Imaging of the Skin

This Chapter outlines work using proton (^{1}H) magnetic resonance imaging (MRI) for the anatomical and physiological study of the skin. Data was collected on the 3T Ingenia scanner using a 47 mm diameter surface coil to collect high resolution (in-plane voxel size of 100 μm) 3D Fast Field Echo (FFE) T_1-weighted images together with multi-echo spin echo (ME-SE) images to generate a T_2 map of the skin layers for assessment of the effect of moisturiser creams on the hydration of the skin. The study was performed on eight healthy volunteers, who were scanned on Day 1 before applying moisturiser cream, 1 hour after applying moisturiser on Day 2, and at Day 8 following twice daily application of moisturiser for a week. The T_1-weighted sequence allowed accurate cross-examination repositioning to ensure the comparability of the measurements. Regions of interest in the epidermis, dermis and hypodermis were generated on the T_2 maps and the thickness of the skin layer measured. It was demonstrated that a surface coil allows high-resolution MRI to study skin hydration from T_2 maps. In future these methods will be used in combination with ^{23}Na imaging to study skin sodium and water content in response to moisturisers, or changes in hydration and sodium following haemodialysis.

6.1 Introduction

This chapter uses proton (^{1}H) magnetic resonance imaging (MRI) to study the morphology and physiology of the skin to assess whether hydration changes of the skin in response to the application of moisturiser creams can be assessed. The assessment of skin properties is important in the cosmetics industry to evaluate the effects skin care products have. Further imaging of the skin could provide for non-invasive *in vivo* skin diagnostic tests, including the assessment of ageing, the effect of treatments such as the effect of haemodialysis on skin hydration, and the localization of skin lesions and tumours. In addition it can be applied to study clinical conditions, for example changes in skin water content in response to haemodialysis.

6.2 Structure of the Skin

The skin is the outermost tissue and largest organ of the human body, it comprises 6% of body weight [95] and makes up the integumentary system, which provides the body with overall protection. Fig.[6.1] illustrates a cross section of the skin. The skin comprises two tissue layers, the outermost tissue layer is the epidermis and the inner tissue layer is the dermis, beneath this lies the third layer of the skin termed the hypodermis.

The epidermis occupies approximately one fifth of the cross section of the tissue layer of the skin at 200 - 500 μm thick dependent on body area. It is made up of four layers of cells comprising the basal layer (stratum basale), the spinous layer (stratum spinosum), the granular cell layer (stratum granulosum), and the stratum corneum which run from deep to superficial. The deepest epidermal layer of the stratum basale attaches the epidermis to the basal lamina, below which lie layers of the dermis. The cells in the stratum basale bond to the dermis via intertwining collagen fibres, referred to as the basement membrane. The stratum basale is a single layer of cells primarily made of basal cells. A basal cell is a cuboidal-shaped stem cell that is a precursor of the keratinocytes, the major cell type, of the epidermis. Keratinocytes are produced from this single layer of cells, which are constantly going through mitosis to produce new cells. As new cells are formed, the

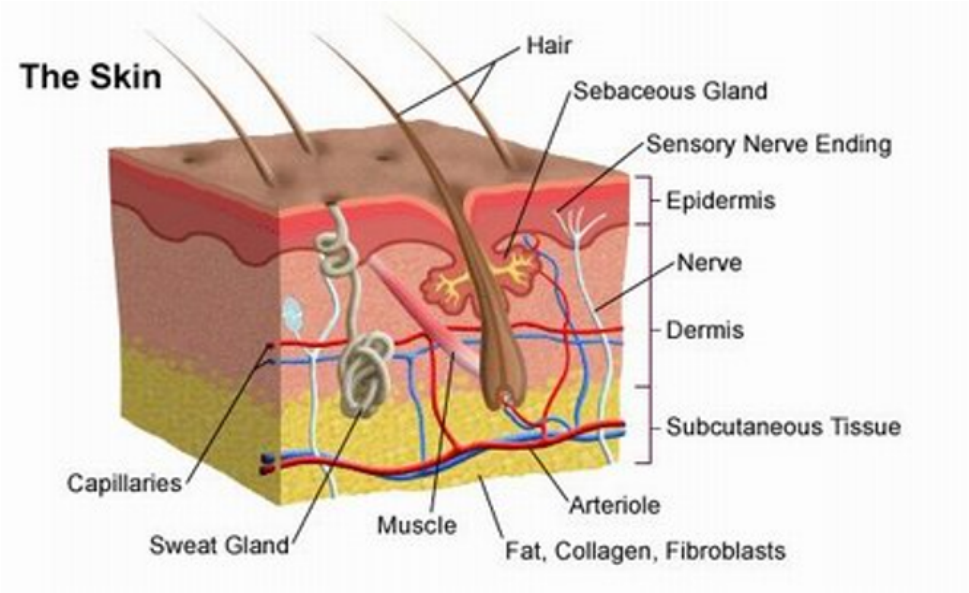

Figure 6.1: Schematic of the skin (Source: https://www.stanfordchildrens.org/en/topic/default?id=anatomy-of-the-skin-85-P01336).

existing cells are pushed superficially away from the stratum basale. Two other cell types are found among the basal cells in the stratum basale, the Merkel cell which functions as a receptor and is responsible for stimulating sensory nerves that the brain perceives as touch, and the melanocyte cell which produces the pigment melanin that gives the skin its colour and also protects the living cells of the epidermis from ultraviolet radiation damage. The spinous layer is composed of eight to 10 layers of keratinocytes, formed as a result of cell division in the stratum basale. Interspersed among the keratinocytes is the Langerhans cell, which functions as a macrophage by engulfing bacteria, foreign particles, and damaged cells that occur in this layer. In the stratum spinosum are keratinocytes which synthesize keratin and release a water-repelling glycolipid that helps prevent water loss from the body, making the skin relatively waterproof. The granular cell layer generates large amounts of the protein keratin which is fibrous, and keratohyalin which accumulates as lamellar granules giving the layer its grainy appearance. The stratum corneum is the most superficial layer and is a dry, dead layer which helps prevent the penetration of microbes and the dehydration of underlying tissues. Cells in this layer are shed periodically and are replaced by cells pushed up from the granular layer. The entire layer is replaced during a period of about two weeks. The epidermis has the highest water content of skin layers, with a large population of bound water and extra-cellular fluid free

water, but does not contain any blood vessels within it.

The dermis occupies approximately four fifths of the cross section of the tissue layer of the skin and is considered the "core" of the integumentary system. The dermis contains cells, dense and irregular connective tissue, blood and lymphatic vessels, nerves, glands, and hair follicles. The dermis is mostly composed of dense irregular connective tissue that is divided into two layers, the papillary dermis and the reticular dermis. The papillary layer is the superficial layer of the dermis and appears finer than the reticular layer. The papillary layer consists of connective tissue with small, densely packed fibres. The reticular layer is much thicker (approximately three times) than the papillary layer and contains connective tissue with larger, thicker fibres. This layer is well vascularized and has a rich sensory and sympathetic nerve supply. The space between the collagen fibres in the dermis is filled with a semi-fluid substance composed primarily of bound water, thus free water content is lower in the dermis compared to the epidermis.

The hypodermis, also termed the subcutaneous layer, is the lowest level of the skin which lies directly below the dermis. It contains loose connective tissue, and a variable amount of subcutaneous fatty tissue containing lipocytes which store fat. The hypodermis serves to connect the skin to the underlying fibrous tissue of the bones and muscles. The hypodermis consists of well-vascularized, loose, areolar connective tissue and adipose tissue, and provides insulation and cushioning.

The skin is a rich source of nitric oxide containing ten times the levels in the blood circulation [96]. Blood flow in the skin is dynamic, ranging from as low as 1% in cold temperatures to as high as 60% when under heat stress. These properties of the skin mean it has the potential to influence systemic blood pressure [97]. Recently, Titze et al. [24] have shown findings to support the idea that the immune and lymphatic systems in the skin work together to regulate blood pressure, and any defects in this regulation are associated with sodium accumulation in the skin. Sodium is stored within the skin bound to proteoglycans, highly glycosylated proteins which are found in the extracellular matrix of connective tissues such as the epidermis and dermis.

6.3 Imaging of the Skin

Non-invasive imaging modalities to study the skin include ultrasound, Optical Coherence Tomography (OCT), confocal microscopy, and MRI.

Ultrasound is low cost and provides a portable method by which to image the skin allowing the assessment of skin thickness as well as deeper subcutaneous structures [98]. Ultrasound probe frequencies used for skin imaging range from 7.5 to 200 MHz, with the higher frequency probes (50–150 MHz) providing a more accurate representation of skin thickness. However, this comes at the expense of reduced penetration depth and hence lower resolution of deeper structures, hence a combination of probe frequencies is often used.

Optical coherence tomography (OCT) is an interferometric imaging technique that has high contrast to differentiate the papillary and reticular dermis. This provides an improvement of the in-depth resolution compared to ultrasound, at $\sim$ 10 μm, and provides a penetration depth of $\sim$ 0.5 mm, so it is well-adapted for the visualization of the epidermis-dermis.

Confocal microscopy has a spatial resolution of $\sim$ 1 μm so provides the method with the most resolving power for *in vivo* studies, but again, penetration depth is limited. Confocal microscopy can be used to study the different layers of the epidermis at a cellular scale [99, 100].

Magnetic resonance profiling is possible with the GARField (Gradient at Right Angles to Field) method [101, 102]. This method provides a map of the ^{1}H density in a sample with an intensity weighted by molecular motion. Experiments have demonstrated that GARField 1D-MRI profiling can differentiate between the stratum corneum and epidermis of the human skin [103]. GARField profiling has been used to study *in vivo* and *in vitro* skin hydration, showing *in vitro* that the signal intensity correlates well with the equilibrium moisture content in the skin, and *in vivo* the effect of a moisturiser cream on water levels in the skin as a function of time. However, the GARField is limited to 1D profiling.

MRI has been shown to provide several advantages for imaging the skin. It provides a

wider field of view than ultrasound, and it can achieve spatial resolution of ∼100 μm to differentiate skin layers, as shown in Fig.[6.2]. It can provide excellent contrast of fat from T_1-weighted images and water from T_2-weighted images. Importantly, in addition to morphological analysis, it can be used to study quantitative measurements of the skin, for example using T_2 mapping [104] to map the water distribution in the skin, and with MRI this is not degraded by the presence of dense tissue as is the case with ultrasound imaging. Calzolari et al. [105] showed that T_2 mapping can provide sensitivity to hydration, and that T_2 mapping provides much greater sensitivity to hydration levels compared to proton density (PD) imaging.

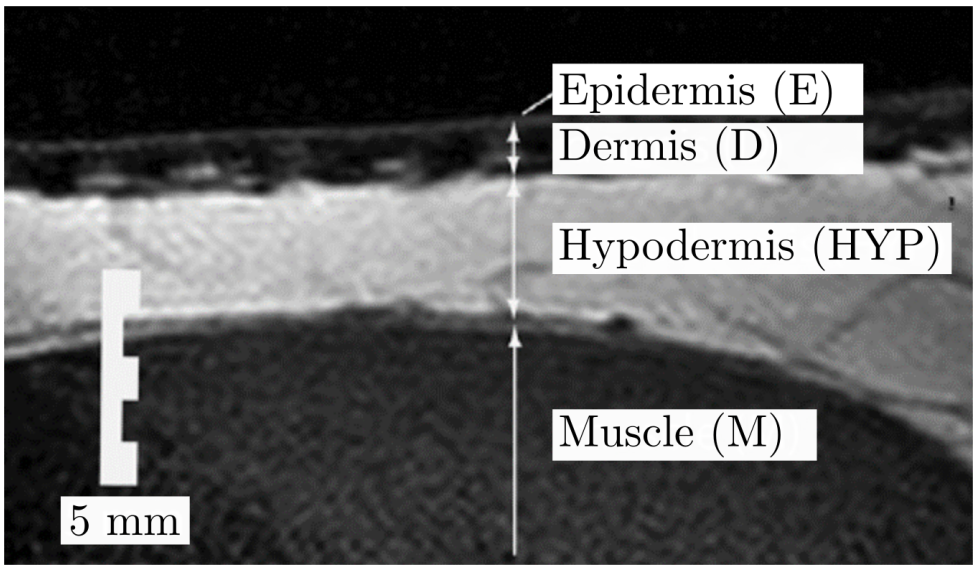

Figure 6.2: MR image of the epidermis, dermis, hypodermis and muscle layers in the arm.

A number of studies have performed MRI of the skin across a range of field strengths from 0.5 T [106], to 1.5 T [107–112], 3 T [112, 113], and 7 T [114]. Studies have assessed the effect of hydration but resolution in the earlier studies was limited due to only lower field strengths being available [108, 115–117]. The key to imaging the skin is to achieve a high signal-to-noise ratio (SNR) due to the narrow thickness of the skin. The SNR depends on the hardware available and the sequence parameters used. Hardware aspects include the strength of the main magnetic field (B_0) and the availability of a small surface coil (such as that outlined in Chapter 3, Section [3.1.2]) for high resolution imaging. This was first demonstrated on a clinical scanner in 1987 but images had low quality and took a considerable time to capture [107]. In 1990, Bittoun et al. [109] collected

high-resolution images of the skin on a whole-body MR system at 1.5 T using a 3.0 cm diameter surface coil to generate images of 70 μm $\times$ 390 μm $\times$ 3 mm allowing different layers of the skin to be delineated in approximately 30 minutes. MRI sequence parameters to optimise for skin imaging include the in-plane spatial resolution, slice thickness, matrix size, bandwidth, and number of signal averages (NSA). The dermis is the most difficult layer of the skin to image since it has a short T_2 and a low proton density, hence a short echo time (TE) is required. A further consideration for skin imaging is artefacts arising from the hypodermis, since this is a fat layer this can lead to chemical shift artefacts. This is especially important if a low readout bandwidth (BW) is used to increase the image SNR. For example, with the fat-water frequency difference at 3 T being 440 Hz, a bandwidth per pixel of 150 Hz/pixel would result in a chemical-shift artifact of $\sim$3 pixels, but using a higher bandwidth of 600 Hz/pixel limits this to 0.73 pixels. One further way to minimise any chemical shift artefact is to choose the readout direction perpendicular to the skin surface and the polarity of the readout gradient such that fat is shifted away from the dermis to avoid signal overlap, also fat suppression can be used.

6.4 Aim

To determine whether high resolution 3T MRI imaging using a commercial microscopy surface coil can detect differences in skin hydration, following the application of two marketed moisturisers. In this study, the skin of the inner forearm arm was chosen as the body site to be imaged with a 47 mm diameter surface coil.

6.5 Methods

This study was funded by Unilever, and underwent ethical review by the University of Nottingham Faculty of Medicine and Health Sciences Ethics Committee (see Appendix B.2). Eight healthy human females aged 20 – 35 years took part in this study. Each subject was asked to self-identify their Fitzpatrick phototype I – IV (see Table [6.1]).
As part of the consent procedure, subjects were shown the INCI (ingredient) list for all

Fitzpatrick phototype	Typical features	Cutaneous response to UV
I	White; very fair; red or blonde hair; blue eyes; freckles	Always burns easily; never tans
II	White; fair; red or blonde hair; blue, hazel, or green eyes	Always burns easily; tans minimally
III	Cream white; fair with any eye or hair color; very common	Burns moderately; tans gradually
IV	Brown; typical Mediterranean white skin	Burns minimally; always tans well
V	Dark brown; mid-eastern skin types, black hair, olive skin	Rarely burns; tans profusely
VI	Black; black hair, black eyes, black skin	Never burns; deeply pigmented

Table 6.1: Fitzpatrick phototype I - VI.

the products to be used, shower gel and both moisturisers (Simple©/Vaseline©) studied, Fig.[6.3].

Figure 6.3: Simple© and Vaseline© moisturiser creams used in the study.

Subjects were asked to confirm that they had a) no known allergies to any of the ingredients in the products, and b) no active skin conditions on their inner forearms, including inner elbow flexor region. Subjects agreed to apply no products to their inner forearms (within at least 3 cm of the test sites) other than those with which they had been provided for the duration of the study. Subjects were asked to use only the shower gel which they were provided and no moisturisers on their inner forearms for 2 weeks prior to the baseline visit (note, stratum corneum turnover time on inner forearm is generally considered to be

2 weeks).

6.6 Study Protocol

The protocol for the study is outlined in Fig.[6.4].

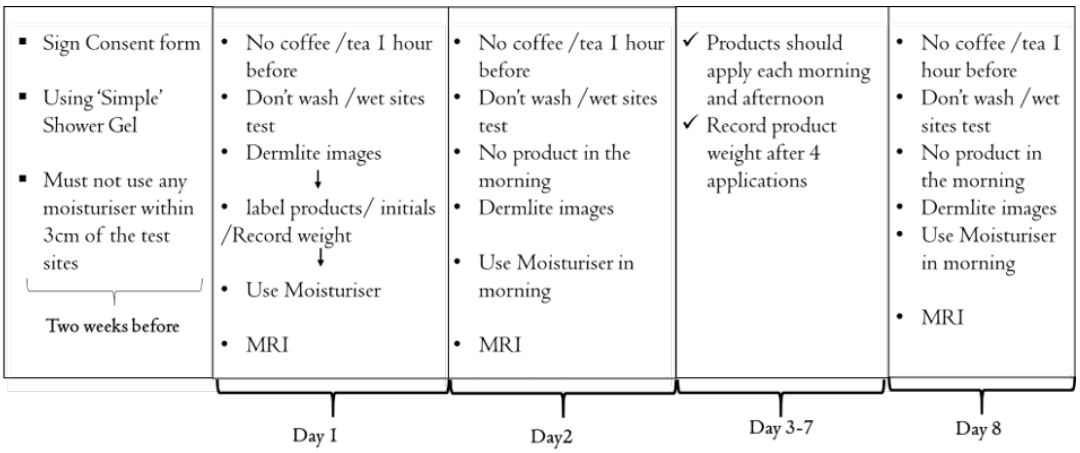

Figure 6.4: Illustration of the study protocol.

This comprised:

Day 1: Baseline MRI scan followed by first application of moisturiser creams

Subjects were asked to follow the restrictions described below before MRI scanning:

- No tea/coffee/caffeinated drinks for approximately 1 hour before each study visit.
- Do not wash/wet test sites for at least 1 hour before each study visit.

Three test sites 3 cm × 3 cm in size, and 3 cm apart were marked on the inner forearm using a surgical marker pen. Areas within 4.5 cm of the wrist and approx. 2 cm of elbow were avoided. The site nearest the wrist was defined as Site 1, the centre site as Site 2 and the site nearest the elbow as Site 3. The positioning of the sites is illustrated in Fig.[6.5]. Test sites were re-marked as needed throughout the study.

First, two replicate DermLite images were collected from each skin site. DermLite images are collected using a dermatoscope (Fig.[6.6]), a high-quality magnifying lens to allow careful examination of the skin structure by taking high-resolution photos. These images were provided to Unilever for analysis.

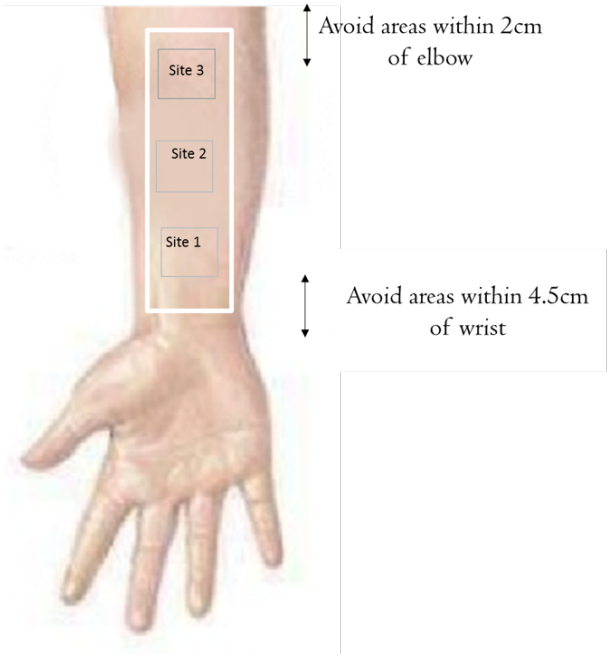

Figure 6.5: The three skin sites in which MRI was assessed. Site 1 and 3 in which moisturiser product applied (Simple©/Vaseline© randomised across subjects), Site 2 was a control site.

This was then followed by a baseline MRI scan of each of the three skin sites (see MRI protocol in Section [6.7] below). On completion of the MRI scan, each subject was given two moisturiser products (Simple© and Vaseline©) which were randomised to the upper or lower test sites (Sites 1 and 3 fixed within an individual to a given moisturiser cream for the entirety of the study). The middle test site (Site 2) on each subject was used as the no-treatment control site.

Following application, the moisturiser product packs were weighed and the weights recorded using a 3 decimal place balance. Subjects were requested to apply 0.02 ± 0.01 g of product to each skin site. When applying the product in the lab on the first visit, the product was placed on the scale and squeezed gently so a very small amount formed at the top of the pack outlet. This was collected using a cotton bud, thus allowing the subject to determine the amount required and make the process of applying the correct dosage more accurate when applying outside of the lab (a new cotton bud was used for each cream). Each cream was applied to the centre of each test skin site and rubbed in using a non-latex glove or finger cots for 30 seconds. It was ensured that each subject was clear on the amount of product to apply and the application procedure at first

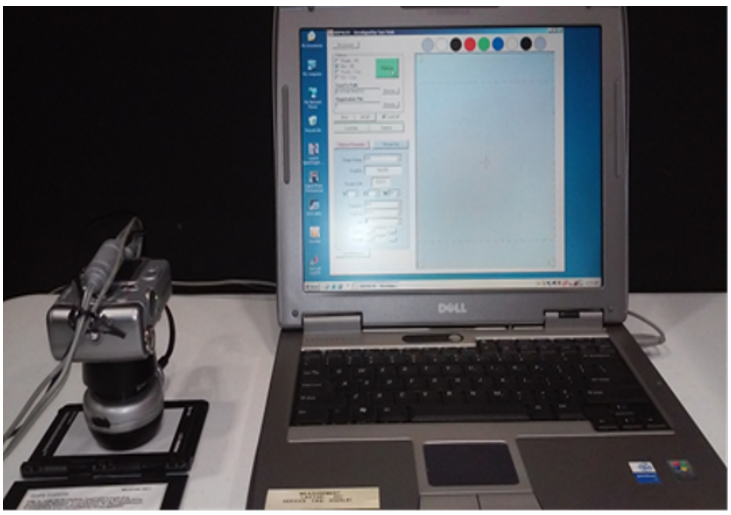

Figure 6.6: Images of the skin collected using the DermLite prior to each MRI scan.

use. After applying the creams, each product was re-weighed, and the amount applied recorded. This procedure was repeated for the second product, using a fresh non-latex glove or finger cot and fresh cotton bud. For each subject a time window during which they should apply products each day was defined (9am ± 1 hour) and (3pm ± 1 hour) and the time the product was applied was recorded using a diary provided to subjects to record both timings and product weight.

Day 2: Second MRI scan followed by third product application

The products were applied 1 hour before the MRI scan session. Again, DermLite images were collected prior to the second MRI scan. Following the scan, subjects applied the products as previously described.

Day 3 – 7: Product applications

Products were applied each morning and afternoon as previously described.

Day 8: Third MRI scan

The products were applied 1 hour before the final third MRI scan session. Again, DermLite images were collected prior to third MRI scan.

6.7 MRI protocol

The MRI protocol was conducted on a 3T Ingenia scanner (Philips Healthcare, Best, The Netherlands) and used a commercial dStream Microscopy coil (Philips Healthcare), with

an internal diameter of 47 mm for high SNR, the coil can be seen in Fig.[6.7]. The imaging protocol was optimised prior to commencing the study.

Figure 6.7: dStream 47 mm internal diameter Microscopy coil (Philips Healthcare).

All participants were placed in the left lateral decubitus position with an extended arm, and the arm was fixed in place with a vacuum bean bag positioner to limit any movement. To image each skin slice, the 47 mm microscopy coil was positioned above each skin site separately (Fig.[6.5]) with the MRI protocol repeated three times within a scan session for each skin site, this procedure was repeated across all three visits (Day 1, Day 2 and Day 8). The following imaging procedure was followed for each skin site. The laser was positioned on the skin site and a survey scan collected (FOV 500 mm × 500 mm × 70 mm, voxel size 1 × 1 × 10 mm^3). This was used to plan a second survey scan which was collected in three perpendicular planes (FOV 250 mm × 250 mm, 3 stacks of 5 slices with voxel size 1 × 1 × 10 mm^3) (Fig.[6.8]).

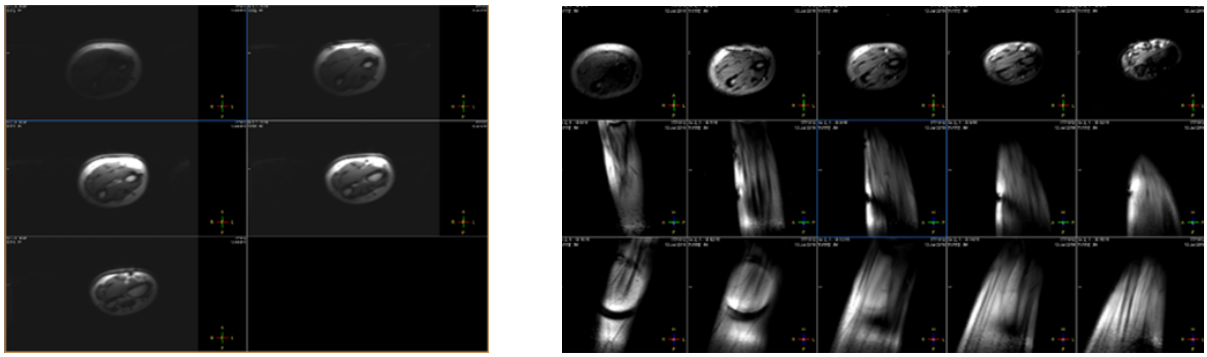

(a) Survey scans. (b) 3 stack survey collected on the ^{1}H surface coil.

Figure 6.8: Survey scans used for planning.

A lower resolution axial fast field echo (FFE) 3D T_1-weighted sequence was then collected

(FOV 100 mm × 100 mm × 26 mm, acquired voxel size 1 × 1 × 2 mm^3, TE/TR = 1.83/58 ms, FA = 30°, BW = 600 Hz, TA = 1 minute 11 s) as shown in Fig.[6.9]. At Visits 2 and 3 this was re-positioned to ensure comparability to the measurements collected at Visit 1.

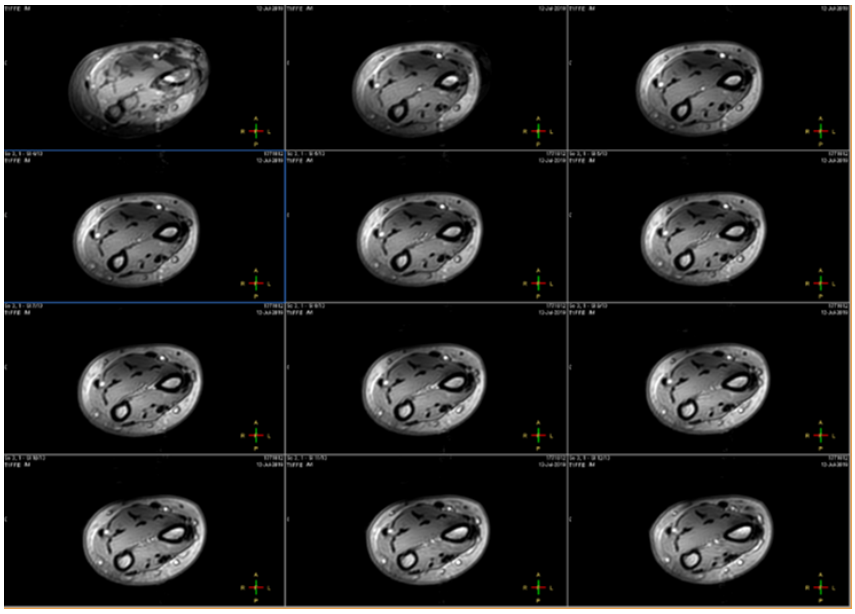

Figure 6.9: Low resolution T_1-weighted scans collected on the ^1H surface coil for planning across scan visits to ensure matched positioning.

From this, a high resolution axial fast field echo (FFE) 3D T_1-weighted sequence was acquired (FOV 28 mm × 28 mm × 26 mm, 13 slices, voxel size 100 μm× 100 μm × 2 mm, TE/TR = 4.4/58 ms, FA = 30°, BW = 600 Hz, acquisition time 8 mins 23 s) (Fig.[6.10]). This was followed by the acquisition of a single slice high resolution multi echo spin-echo (ME-SE) acquisition with 8 echoes from which to generate a T_2 map of skin layers (FOV 28 mm × 26 mm × 2 mm, 1 slice, voxel size 100 μm × 100 μm × 2 mm, TE = 8 ms and ΔTE = 8 ms for 8 echoes (8 – 64 ms), TR = 2000 ms, FA = 90°, BW = 600 Hz, TA = 7 mins 14 s) (Fig.[6.11]).

The ME-SE T_2 mapping sequence was also performed on tubes of the Simple© and Vaseline© moisturiser creams to determine their T_2 values.

All Image analysis was performed with MATLAB to generate a T_2 map from the ME-SE sequence using a mono-exponential regression to:

$$M = M_0 \cdot \exp(-TE/T_2) \tag{6.1}$$

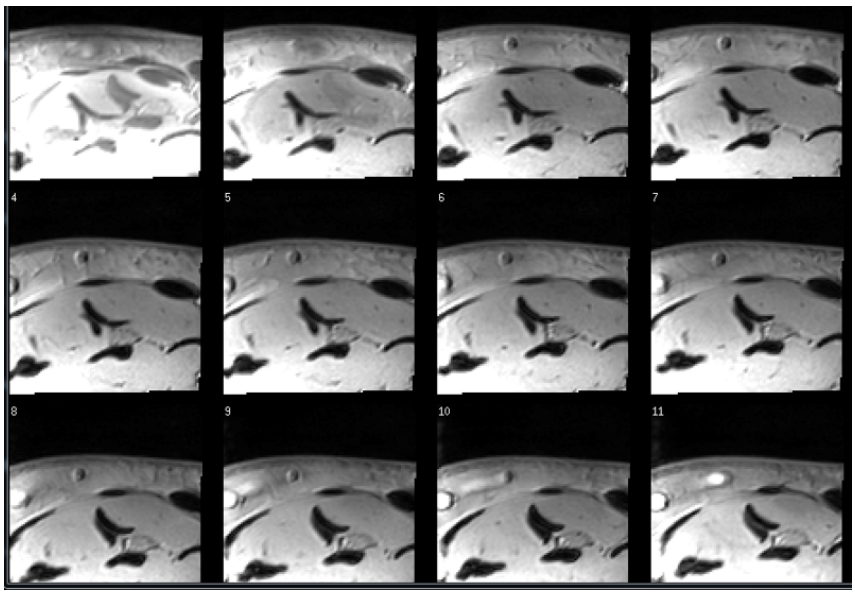

Figure 6.10: Example slices collected in the high resolution T_1-weighted scan.

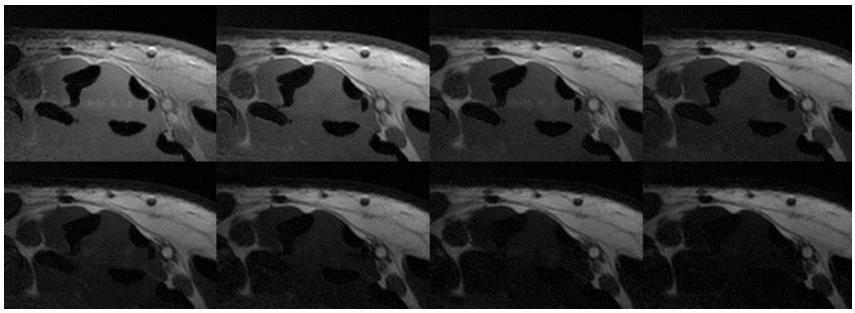

Figure 6.11: Example ME-SE images shown for a single slice for each of the 8 echoes (TE_1 = 8 ms, ΔTE = 8 ms).

where M is the measured signal, M_0 is the equilibrium magnetisation and TE is the echo time (see Chapter 2, Section [2.1.5.2]). Measurements were carried out using quadrangular regions of interest (ROIs) which comprised 100 voxels placed on the T_2 map in the different skin layers of the epidermis, dermis and hypodermis. Measures were assessed from images of the three skin sites collected at each of the three visits (Day 1, Day 2 and Day 8). In addition, the thickness of each skin layer was measured. Statistical analysis was performed using Prism 6 (GraphPad Software, Inc., La Jolla, CA). A Shapiro-Wilk normality test and Kolmogorov-Smirnov test was applied to all T_2 measures. All normal data is expressed as mean $\pm$ standard deviation. Significant differences between scan days for each skin site was assessed using a one-way ANOVA with $P<0.05$ considered statistically significant. For any significant difference, a student test comparing averages between scan days for a

given skin site was performed.

6.8 Results

Eight subjects took part in the pilot study, all completed the study without any issues due to motion artefacts, all subjects had prior experience of taking part in MRI scans. Participants comprised one subject of Fitzpatrick phototype I, three of Fitzpatrick phototype II, and four of Fitzpatrick phototype III. Fig.[6.12] shows an example image of the first echo (8 ms) from the ME-SE scan, rescaled for improved visualisation of the epidermis and dermis layers. Fig.[6.13a] shows the images collected across each of the eight echo times (TE_1 = 8 ms, ΔTE = 8 ms).

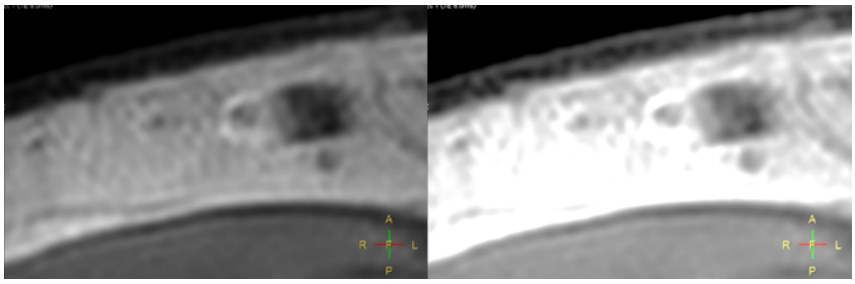

Figure 6.12: Example first echo time (TE = 8 ms) image from the ME-SE dataset, in which the epidermis can be seen as the uppermost thin layer, with the dermis below with shorter T_2, and below this the hypodermis.

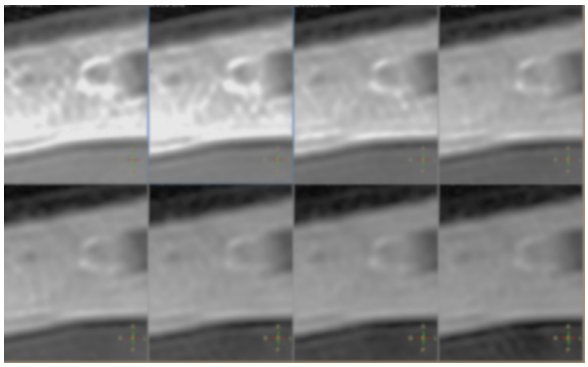

(a) The eight echoes of the ME-SE data set (TE1 = 8 ms, ΔTE = 8 ms), the epidermis can be seen as the uppermost high intensity thin layer with a slower decay and so longer T_2 than the dermis below, below this the hypodermis which has a long T_2.

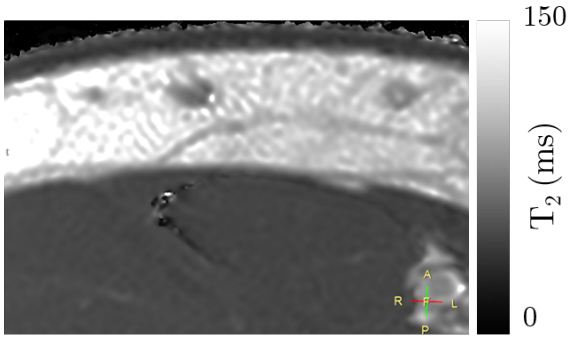

(b) The corresponding T_2 map.

Figure 6.13: Results of the ME-SE T_2 scan.

All T_2 data was normally distributed. The average T_2 relaxation time across the baseline scans for the epidermis and the dermis was 36.7 ± 2.3 ms and 19.1 ± 2.0 ms respectively, whilst the hypodermis had a considerably longer T_2 of 131.4 ± 7.3 ms. Note the larger standard deviation of measures in the hypodermis due to the heterogeneity of its composition. Example T_2 decay curves for each of the skin layers are shown in Fig.[6.14]. The mean epidermis thickness was 0.42 ± 0.13 mm and that of the dermis was 2.36 ± 0.43 mm.

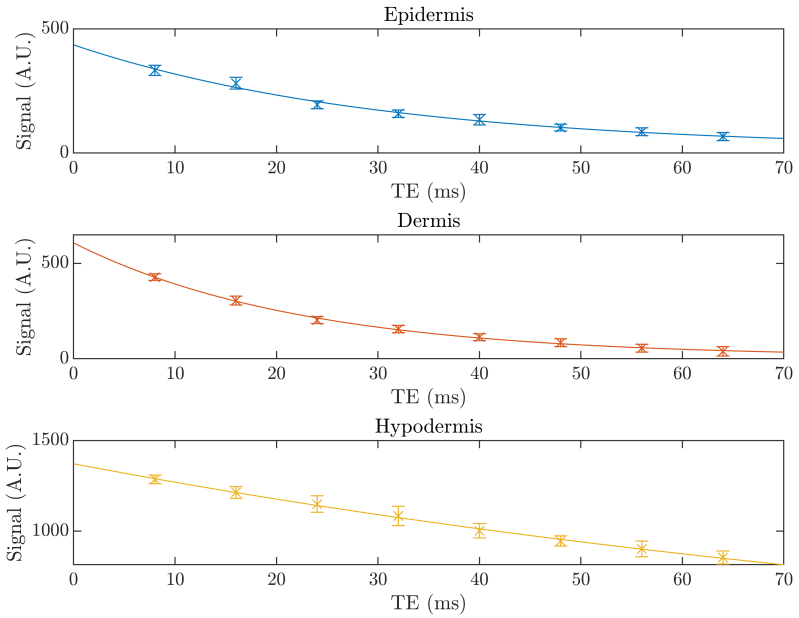

Figure 6.14: The eight echoes of the ME-SE data set (TE_1 = 8 ms, ΔTE = 8 ms) shown for the epidermis, which has a T_2 of 33.8 ms (R^2 = 0.994), the dermis which has a more rapid decay and so shorter T_2 of 23.6 ms (R^2 = 0.998), and the hypodermis which has a long T_2 of 134.3 ms (R^2 = 0.998).

The T_2 values in the epidermis, dermis, and hypodermis after applying Simple© and Vaseline© are shown in Fig.[6.15]. In the epidermis, an ANOVA showed a significant increase in the T_2 of the epidermis at Day 8 compared to Day 1 (P = 0.013), but this difference was not significant between Day 2 compared to Day 1. There was also a weaker significant increase in the T_2 of the epidermis at Day 8 compared to Day 1 (P = 0.041), but not at Day 2 compared to Day 1. ANOVA revealed no significance across visits (Day 1, Day 2 and Day 8) for the control condition for all skin layers (epidermis, dermis and hypodermis). ANOVA also revealed no significant difference across scan days (Day 1, Day 2 and Day 8) for the dermis or hypodermis for either Simple© or Vaseline©. The T_2

relaxation time of Simple© was measured to be 469 ± 21 ms and of Vaseline© was 261 ± 18 ms.

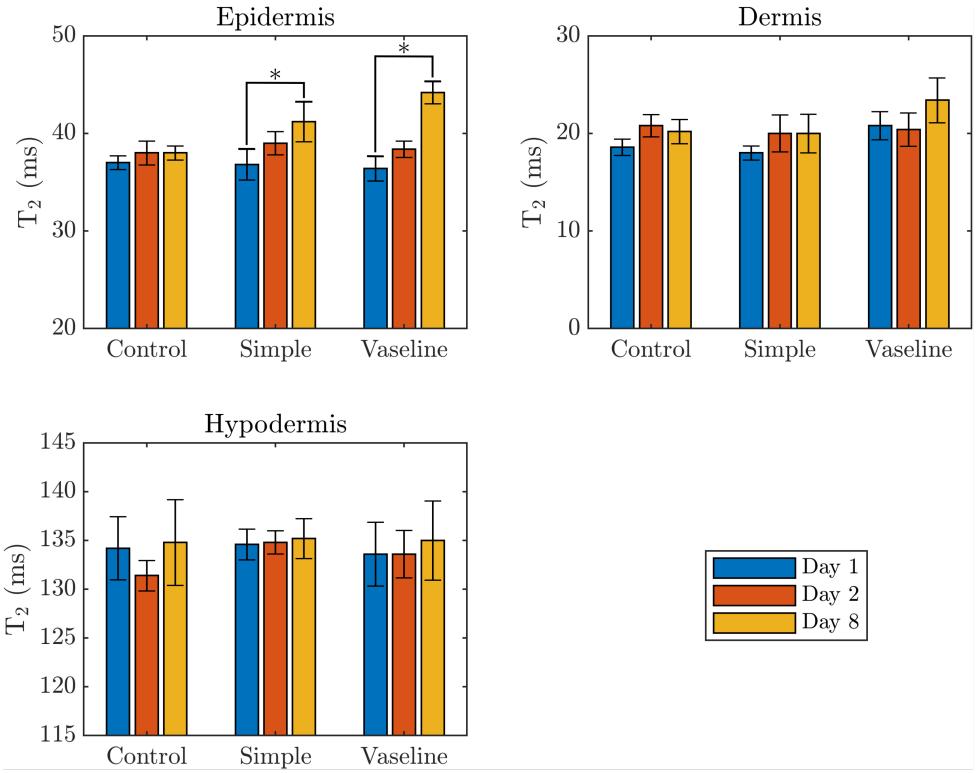

Figure 6.15: The T_2 values in the epidermis, dermis, and hypodermis after applying Simple© and Vaseline© on the three days.

6.9 Discussion

Here, a 47 mm ^{1}H surface coil has been used to collect high resolution T_1-weighted images and a multi-echo spin echo (ME-SE) sequence used to generate T_2 mapping measurements of the skin layers of the forearm. In this work, it has been shown that MRI can be used to investigate skin properties *in vivo* and non-invasively. MRI high-resolution skin images with T_1 and T_2 weighting have been obtained so that the epidermis, dermis, and hypodermis are clearly visible. The acquired T_2 maps of the skin were used to assess changes in hydration across the epidermis, dermis and hypodermis following the application of moisturiser cream (Simple©/Vaseline©) on the skin. This study followed similar procedures to those performed by Mesrar et al. [118] who assessed the effect of hydration in response to Dexeryl© skin cream, Calzolari et al. [105] who used MRI

to evaluate the effect of an amphiphilic cream on the skin, and Gensanne et al. [119] who assessed changes in the hydration of the dermis after hyaluronic acid injection. The baseline measures of T_2 values (epidermis 36.7 ± 2.3 ms, dermis 19.1 ± 2.0 ms, hypodermis 131 ± 7.3 ms) are comparable to those in the literature [105, 118, 119]. After hydration, a significant increase in the T_2 of the epidermis was measured in response to the application of both Simple©, at 4.4 ± 2.4 ms corresponding to a 12 ± 6 % increase ($P = 0.041$), with a greater increase in T_2 in response to the application of Vaseline© at 7.8 ± 1.8 ms corresponding to a 21 ± 7 % increase ($P = 0.013$). This change reflects the osmotic effect of the creams inducing a water movement from deep to superficial layers, as has been previously reported by Ciampi et al [120].

6.10 Future directions

This work has demonstrated the feasibility of generating high quality images of water content in the skin. In future, additional contrast mechanisms will be explored, such as T_1 mapping and magnetization transfer contrast (MTC) to image the skin. MTC of the skin has been performed by Mirrashed et al. [121] who showed that it is possible to visualise the stratum corneum, epidermis and dermis in MTC ratio images which describe the interaction of proton pools, providing unique information about the microscopic chemical environments accessible to mobile water protons.

In this study, young subjects have been imaged and no pathology studied, but in future the direction of study would be to assess changes in the skin layers in ageing skin and pathology where the water concentration, and the macromolecular composition of the tissue may change. An improvement for future studies would also include automated methods to segment the skin layers, as performed recently by Ognard et al. [122].

A further direction for this work is to build on the developments in this thesis in sodium imaging, to collect high resolution proton (^{1}H) MRI and sodium (^{23}Na) images of the skin. This will use the purpose-built dual tuned 50 mm ^{1}H/ 23 mm ^{23}Na RF coils outlined in Chapter 3, which with a matched diameter to the commercial ^{1}H coil used in this chapter, will both maximise depth penetration for high quality proton imaging as well as allow the

assessment of ^{23}Na-MRI measures through MR spectroscopy or imaging of the skin. To perform such studies on the 3T Ingenia the dual tuned skin coil will require a TR switch and preamplifier for use on this scanner. This work will then build on the optimised image quality of ^{1}H described in this chapter to assess the depth penetration and repeatability of combined ^{1}H imaging and ^{23}Na measures.

Sodium (^{23}Na) MRI allows one to assess skin sodium storage and is a valuable tool in studying the effects of tissue sodium accumulation which is thought to change with age and hypertension. Chapter 4 showed the possibility to measure sodium in the skin using a birdcage leg coil but the resolution of ^{23}Na imaging to accurately quantify the skin sodium was limited, since the skin is of only 2 – 3 mm thick. Having developed dedicated high resolution methods for ^{1}H imaging and ^{23}Na imaging and spectroscopy, it will be possible to perform studies of the effects of age and gender on baseline hydration levels, and the impact of short-term hydration status by moisturiser. In addition to understanding skin hydration status and changes with age in healthy populations, this work has clinical implications. It has been proposed that tissue sodium accumulation in the skin/muscle is a key factor in hypertension [26] (as described in Chapter 5). Such high resolution image methods of ^{1}H/^{23}Na in the skin will therefore provide a tool to study the role of tissue sodium accumulation in hypertension and in haemodialysis patients with end-stage kidney disease which is hypothesized to result in changes in tissue sodium. The development of ^{23}Na skin measures would allow for a method to correlate skin sodium content with detailed cardiovascular and functional assessments. Kopp et al. [12] used skin ^{23}Na to show an age-dependant increase but with increased accompanying water content. There was also a significant increase in the ^{23}Na storage in refractory hypertension subjects versus healthy controls, indicating a connection between ^{23}Na storage and cardiovascular morbidity.

6.11 Conclusion

In conclusion, high resolution ^{1}H imaging of the skin has been performed on a clinical scanner using a 47 mm diameter surface coil to generate T_2 maps. It has been possible

to assess changes due to free water in the tissue with a hydration increase of 8 – 21 % in response to moisturising skin creams applied over an eight day period.

Chapter 7

Conclusion

This thesis aimed to develop methods for sodium (^{23}Na) imaging at 3 Tesla, assessing the optimal hardware and pulse sequence schemes to collect ^{23}Na images. The work aimed to ultimately develop methods to measure sodium concentration in the periphery, calf muscle and skin, and sodium distribution within the kidney. Since no work had been performed *in vivo* on sodium imaging on the clinical scanners at the Sir Peter Mansfield Imaging Centre (SPMIC) prior to this thesis, the thesis outlines the hardware development through to the *in vivo* measures.

Chapter 3 overviews the ^{23}Na coils developed and purchased for the assessment of sodium measures in the calf muscle and skin (13 cm loop coil and PulseTeq birdcage coil, home built coils) and abdomen (20 cm dual loops and a 6-channel ^{23}Na QTAR body coil). For each ^{23}Na RF coil, the results of SAR simulations performed to ensure the energy deposition remained within SAR limits are described. A series of tests were performed on each coil prior to use *in vivo* using phantoms including temperature testing, power calibration, proton decoupling and switching time. For this, phantoms were made for power calibration, temperature measurements and to act as reference bottles for the quantification of total sodium concentration. All coils were shown to lead to minimal temperature change. It was ensured that when each of the ^{23}Na RF coils were placed within the ^{1}H Q-body coil minimal coupling between the coils occurred. Power calibration of the ^{23}Na RF coils was performed and transmit/receive switching time of ^{23}Na coils measured, crucial for Ultrashort echo time (UTE) schemes.

Chapter 4 outlines the development of pulse sequences for ^{23}Na imaging of the calf muscle and surrounding skin. Initial work performed on the 3T Achieva system used a 13 cm surface coil and a dual TE 3D UTE acquisition pulse sequence to measure a change in sodium signal intensity in response to exercise, performed whilst lying on the scanner bed by using a Trispect system. Immediately following cessation of exercise, the sodium signal intensity declined, and the return to baseline level was monitored and shown to have a half-life time of $\sim$ 30 mins. However, due to only a single loop coil being employed the coverage of the calf muscles was limited to the medial gastrocnemius muscle and a section of the soleus, also the quantification of total sodium concentration (TSC) was limited due to the positioning of the reference bottles and the limited B_1 mapping. The remainder of Chapter 4 optimised ^{23}Na concentration measures in the calf muscle using a PulseTeq birdcage coil. Prior studies to estimate ^{23}Na in the calf have predominantly implemented single slice 2D GRE schemes with no B_1 correction applied [12, 25, 29, 64–66]. In this chapter a 3D GRE scheme was optimised for image SNR per unit time. It was shown that a shorter TR provided optimal image SNR per unit time compared to a long TR ($\sim$ 100 ms) acquisition. However, the shorter TR led to T_1 relaxation weighting due to the difference in the longitudinal relaxation time between the reference bottles and tissue. Methods to quantify the total sodium concentration using reference bottles were then outlined. The limitation of the use of dual angle B_1 mapping was described and a phase-sensitive method implemented and shown to provide more accurate B_1 mapping, this led to improved TSC estimates as evidenced by a closer fit of the reference bottle signals to the Inductively Coupled Plasma (ICP) spectroscopy measures, and reduced heterogeneity in TSC across the leg phantom and calf muscle. Further it was shown that it was feasible to assess multislice measures of TSC. To correct for the T_1 relaxation weighting of the short TR GRE images, a weighting related to the ratio of the relaxation times of tissue and the reference bottles was applied to the short TR data and validated against long TR measures. A 3D UTE was also implemented and shown to allow a shorter echo time to be sampled, however despite higher signal, the image SNR was found to not be improved due to increased noise in the UTE images. A systematic difference in TSC measured using the

3D GRE and 3D UTE scheme was shown, and this was attributed to the T_2^* relaxation effects. This was assessed from a multi-echo UTE scheme which was used to evaluate the T_2^* in the reference bottles and tissue. This demonstrated the bi-exponential decay of the tissue in the calf muscle wtih T_{2fast}^* of 2.1 ± 0.1 ms and T_{2slow}^* of 18.2 ± 1.2 ms and an estimation of the fast fraction of 0.57 ± 0.08. This work provided an optimised protocol for sodium imaging of the calf muscle which can be collected in a 1 hour scan session. Future work will include the measurement of the T_1 relaxation times using a VFA scan and the assessment of repeatability of measures across healthy volunteers. This protocol will then be applied to the study of changes in TSC in disease, such as in diabetes, and to monitor the changes in muscle and skin sodium in response to haemodialysis.

Chapter 5 outlines methods developed for ^{23}Na imaging of the abdomen, specifically the kidney. Images are compared for dual loops and a 6-channel ^{23}Na QTAR body coil which have been optimised for GRE acquisition parameters taking into account SAR limitations. Images show the higher ^{23}Na signal in the medulla compared to the cortex. However, the dual loops coil was shown to have limited coverage and heterogeneity, and was difficult to position optimally. The 6-channel coil is shown to provide improved heterogeneity and image SNR over the dual loops coil. Methods to correct the receive sensitivity of the 6-channel coil are described. In future the 6-channel body coil will be used for the detailed study of the corticomedullary sodium gradient (CMSG) in healthy volunteer and patients with Chronic Kidney Disease, and higher spatial resolution methods will be implemented along with layer specific analysis of the ^{23}Na images [90]. Further ^{23}Na imaging will be used to study the change in sodium in abdominal organs in response to fluid infusions typically used in surgery.

Chapter 6 describes a study of the skin water content using ^{1}H imaging. A 47 mm surface coil was used to study the epidermis, dermis and hypodermis layers of the skin. Data is collected using high resolution T_1-weighted and T_2 mapping scans. High resolution T_2 mapping is shown to be able to monitor the change in water content in the epidermis due to hydration. Future work will combine high resolution ^{1}H images of the skin with ^{23}Na acquisitions using the dual ^{23}Na/^{1}H coil built. This will provide combined assessment of

salt in the skin layers corrected for water content.

In summary, this thesis has developed both hardware and pulse sequences to enable sodium imaging of the calf muscle and skin, and of the abdomen.

Bibliography

[1] Guillaume Madelin and Ravinder R. Regatte. Biomedical applications of sodium MRI in vivo. *Journal of Magnetic Resonance Imaging*, 38(3):511–529, 9 2013.

[2] Donald W. McRobbie, Elizabeth A. Moore, and Martin J. Graves. *MRI from Picture to Proton.* Cambridge University Press, 2017.

[3] International Electrochemical Commission. Medical electrical equipment: part 2-33. Particular requirements for the safety of magnetic resonance equipment for medical diagnosis, 2010.

[4] Bernard Canaud, Jeroen Kooman, Nicholas M. Selby, Maarten Taal, Susan Francis, Pascal Kopperschmidt, Andreas Maierhofer, Peter Kotanko, and Jens Titze. Sodium and water handling during hemodialysis: new pathophysiologic insights and management approaches for improving outcomes in end-stage kidney disease. *Kidney International*, 95(2):296–309, 2 2019.

[5] William D. Rooney and Charles S. Springer. A comprehensive approach to the analysis and interpretation of the resonances of spins 3/2 from living systems. *NMR in Biomedicine*, 4(5):209–226, 10 1991.

[6] ICRP. Annexes E-H. *Annals of the ICRP*, 39(2):71–118, 4 2009.

[7] A. A. Maudsley and S. K. Hilal. Biological aspects of sodium-23 imaging. *British Medical Bulletin*, 40(2):165–166, 1 1984.

[8] Elizabeth Murphy and David A. Eisner. Regulation of Intracellular and Mitochondrial Sodium in Health and Disease. *Circulation Research*, 104(3), 2009.

[9] Raffi Kalayciyan, Friedrich Wetterling, Sabine Neudecker, Stefan Haneder, Norbert Gretz, and Lothar R. Schad. Bilateral kidney sodium-MRI: Enabling accurate quantification of renal sodium concentration through a two-element phased array system. *Journal of Magnetic Resonance Imaging*, 38(3):564–572, 9 2013.

[10] Nimrod Maril, Yael Rosen, Glenn H. Reynolds, Alex Ivanishev, Long Ngo, and Robert E. Lenkinski. Sodium MRI of the human kidney at 3 tesla. *Magnetic Resonance in Medicine*, 56(6):1229–1234, 12 2006.

[11] Yael Rosen and Robert E. Lenkinski. Sodium MRI of a Human Transplanted Kidney. *Academic Radiology*, 16(7):886–889, 7 2009.

[12] Christoph Kopp, Peter Linz, Anke Dahlmann, Matthias Hammon, Jonathan Jantsch, Dominik N. Müller, Roland E. Schmieder, Alexander Cavallaro, Kai Uwe Eckardt, Michael Uder, Friedrich C. Luft, and Jens Titze. 23Na magnetic resonance imaging-determined tissue sodium in healthy subjects and hypertensive patients. *Hypertension*, 61(3):635–640, 2013.

[13] E.A. Mellon, D.T. Pilkinton, C.M. Clark, M.A. Elliott, W.R. Witschey, A. Borthakur, and R. Reddy. Sodium MR Imaging Detection of Mild Alzheimer Disease: Preliminary Study. *American Journal of Neuroradiology*, 30(5):978–984, 5 2009.

[14] Maria Petracca, Roxana O Vancea, Lazar Fleysher, Laura E Jonkman, Niels Oesingmann, and Matilde Inglese. Brain intra- and extracellular sodium concentration in multiple sclerosis: A 7 T MRI study. *Brain*, 139(3):795–806, 2016.

[15] Friedrich Wetterling, Lindsay Gallagher, Jim Mullin, William M Holmes, Chris McCabe, I Mhairi Macrae, and Andrew J Fagan. Sodium-23 magnetic resonance imaging has potential for improving penumbra detection but not for estimating stroke onset time. *Journal of Cerebral Blood Flow & Metabolism*, 35(1):103–110, 1 2015.

[16] L. J. Appel, E. D. Frohlich, J. E. Hall, T. A. Pearson, R. L. Sacco, D. R. Seals, F. M. Sacks, S. C. Smith, D. K. Vafiadis, and L. V. Van Horn. The Importance of Population-Wide Sodium Reduction as a Means to Prevent Cardiovascular Disease and Stroke: A Call to Action From the American Heart Association. *Circulation*, 123(10):1138–1143, 3 2011.

[17] J. CRABBE and G. NICHOLS. Effects of adrenalectomy, aldosterone and dehydration on electrolyte metabolism of rat renal cortex slices. *The American journal of physiology*, 199:871–875, 11 1960.

[18] G. Nichols and G. Nichols. Effects of Adrenalectomy and Aldosterone on Sodium Concentration in Renal Medulla of Hydropenic Rats. *Proceedings of the Society for Experimental Biology and Medicine*, 101(1):168–171, 11 1959.

[19] K. Hierholzer, M. Wiederholt, H. Holzgreve, G. Giebisch, R. M. Klose, and E. E. Windhager. Micropuncture study of renal transtubular concentration gradients of sodium and potassium in adrenalectomized rats. *Pflügers Archiv für die Gesamte Physiologie des Menschen und der Tiere*, 285(3):193–210, 9 1965.

[20] Nimrod Maril, Raanan Margalit, Joel Mispelter, and Hadassa Degani. Functional sodium magnetic resonance imaging of the intact rat kidney. *Kidney International*, 65(3):927–935, 3 2004.

[21] James T. Grist, Frank Riemer, Esben S.S. Hansen, Rasmus S. Tougaard, Mary A. McLean, Joshua Kaggie, Nikolaj Bøgh, Martin J. Graves, Ferdia A. Gallagher, and Christoffer Laustsen. Visualization of sodium dynamics in the kidney by magnetic resonance imaging in a multi-site study. *Kidney International*, 98(5):1174–1178, 6 2020.

[22] Frank G. Zöllner, Simon Konstandin, Jonathan Lommen, Johannes Budjan, Stefan O. Schoenberg, Lothar R. Schad, and Stefan Haneder. Quantitative sodium MRI of kidney. *NMR in Biomedicine*, 29(2):197–205, 2016.

[23] Chan Hong Moon, Alessandro Furlan, Jung Hwan Kim, Tiejun Zhao, Ron Shapiro, and Kyongtae Ty Bae. Quantitative sodium MR imaging of native versus transplanted kidneys using a dual-tuned proton/sodium (1H/23Na) coil: Initial experience. *European Radiology*, 24(6):1320–1326, 2014.

[24] Jens Titze. Sodium balance is not just a renal affair. *Current Opinion in Nephrology and Hypertension*, 23(2):101–105, 3 2014.

[25] Jens Titze, Natalia Rakova, Christoph Kopp, Anke Dahlmann, Jonathan Jantsch, and Friedrich C. Luft. Balancing wobbles in the body sodium. *Nephrology Dialysis Transplantation*, 31(7):1078–1081, 7 2016.

[26] Jens Titze and Friedrich C. Luft. Speculations on salt and the genesis of arterial hypertension. *Kidney International*, 91(6):1324–1335, 6 2017.

[27] Lucas H. Hofmeister, Stojan Perisic, and Jens Titze. Tissue sodium storage: evidence for kidney-like extrarenal countercurrent systems? *Pflugers Archiv European Journal of Physiology*, 467(3):551–558, 2015.

[28] Christoph Kopp, Peter Linz, Lydia Wachsmuth, Anke Dahlmann, Thomas Horbach, Christof Schöfl, Wolfgang Renz, Davide Santoro, Thoralf Niendorf, Dominik N. Müller, Myriam Neininger, Alexander Cavallaro, Kai Uwe Eckardt, Roland E. Schmieder, Friedrich C. Luft, Michael Uder, and Jens Titze. 23Na magnetic resonance imaging of tissue sodium. *Hypertension*, 59(1):167–172, 2012.

[29] Anke Dahlmann, Kathrin Dörfelt, Florian Eicher, Peter Linz, Christoph Kopp, Irina Mössinger, Stephan Horn, Beatrix Büschges-Seraphin, Peter Wabel, Matthias Hammon, Alexander Cavallaro, Kai-Uwe Eckardt, Peter Kotanko, Nathan W Levin, Bernd Johannes, Michael Uder, Friedrich C Luft, Dominik N Müller, and Jens M Titze. Magnetic resonance-determined sodium removal from tissue stores in hemodialysis patients. *Kidney international*, 87(2):434–41, 2015.

[30] D. A. Feinberg, L. A. Crooks, L. Kaufman, M. Brant-Zawadzki, J. P. Posin, M. Arakawa, J. C. Watts, and J. Hoenninger. Magnetic resonance imaging per-

formance: A comparison of sodium and hydrogen. *Radiology*, 156(1):133–138, 7 1985.

[31] F Bloch. Nuclear induction. *Physica*, 17(3-4):272–281, 1951.

[32] Keith R. Thulborn. Quantitative sodium MR imaging: A review of its evolving role in medicine. *NeuroImage*, 168:250–268, 3 2018.

[33] Donald E. Woessner. NMR relaxation of spin-3/2 nuclei: Effects of structure, order, and dynamics in aqueous heterogeneous systems. *Concepts in Magnetic Resonance*, 13(5):294–325, 1 2001.

[34] Fernando E. Boada, Joseph S. Gillen, Gary X. Shen, Sam Y Chang, and Keith R. Thulborn. Fast three dimensional sodium imaging. *Magnetic Resonance in Medicine*, 37(5):706–715, 5 1997.

[35] Armin M. Nagel, Frederik B. Laun, Marc-AndrÃ© Weber, Christian Matthies, Wolfhard Semmler, and Lothar R. Schad. Sodium MRI using a density-adapted 3D radial acquisition technique. *Magnetic Resonance in Medicine*, 62(6):1565–1573, 12 2009.

[36] Paul T. Gurney, Brian A. Hargreaves, and Dwight G. Nishimura. Design and analysis of a practical 3D cones trajectory. *Magnetic Resonance in Medicine*, 55(3):575–582, 3 2006.

[37] Robert W. Brown, Yu Chung N. Cheng, E. Mark Haacke, Michael R. Thompson, and Ramesh Venkatesan. *Magnetic Resonance Imaging: Physical Principles and Sequence Design: Second Edition*, volume 9780471720. Wiley Blackwell, 6 2014.

[38] Aiming Lu, Ian C. Atkinson, Theodore C. Claiborne, Frederick C. Damen, and Keith R. Thulborn. Quantitative sodium imaging with a flexible twisted projection pulse sequence. *Magnetic Resonance in Medicine*, 63(6):1583–1593, 2010.

[39] Yongxian Qian, Tiejun Zhao, Yik Kiong Hue, Tamer S. Ibrahim, and Fernando E. Boada. High-resolution spiral imaging on a whole-body 7T scanner with minimized image blurring. *Magnetic Resonance in Medicine*, 63(3):543–552, 2010.

[40] Simon Konstandin and Armin M. Nagel. Measurement techniques for magnetic resonance imaging of fast relaxing nuclei, 2 2014.

[41] Dixon WT. Simple proton spectroscopic imaging. *Radiology*, 153(1):189–194, 1984.

[42] Ananda Kumar, William A. Edelstein, and Paul A. Bottomley. Noise figure limits for circular loop MR coils. *Magnetic Resonance in Medicine*, 61(5):1201–1209, 5 2009.

[43] Cecil E. Hayes, William A. Edelstein, John F. Schenck, Otward M. Mueller, and Matthew Eash. An efficient, highly homogeneous radiofrequency coil for whole-body NMR imaging at 1.5 T. *Journal of Magnetic Resonance (1969)*, 63(3):622–628, 7 1985.

[44] Robin A. de Graaf. *In Vivo NMR Spectroscopy: Principles and Techniques: 2nd Edition*. Wiley, Hoboken, UNKNOWN, 2007.

[45] Allen Taflove and Susan C. Hagness. *Computational electrodynamics : the finite-difference time-domain method*. Artech House antennas and propagation library. Artech House, Boston [Mass.] ; London, 3rd ed. edition, 2005.

[46] Kane S. Yee. Numerical Solution of Initial Boundary Value Problems Involving Maxwell's Equations in Isotropic Media, 1966.

[47] E. K. Insko and L. Bolinger. Mapping of the radiofrequency field. *Journal of Magnetic Resonance - Series A*, 103(1):82–85, 6 1993.

[48] Vasily L. Yarnykh. Actual flip-angle imaging in the pulsed steady state: A method for rapid three-dimensional mapping of the transmitted radiofrequency field. *Magnetic Resonance in Medicine*, 57(1):192–200, 2007.

[49] C. H. Oh, S. K. Hilal, Z. H. Cho, and I. K. Mun. Radio frequency field intensity mapping using a composite spin-echo sequence. *Magnetic Resonance Imaging*, 8(1):21–25, 1990.

[50] Glen R. Morrell. A phase-sensitive method of flip angle mapping. *Magnetic Resonance in Medicine*, 60(4):889–894, 10 2008.

[51] Steven P Allen, Glen R Morrell, Brock Peterson, Danny Park, Garry E Gold, Joshua D Kaggie, and Neal K Bangerter. Phase-sensitive sodium B1 mapping. *Magnetic resonance in medicine*, 65(4):1125–30, 4 2011.

[52] Jonathan Lommen, Simon Konstandin, Philipp Krämer, and Lothar R. Schad. Enhancing the quantification of tissue sodium content by MRI: Time-efficient sodium B1 mapping at clinical field strengths. *NMR in Biomedicine*, 29(2):129–136, 2 2016.

[53] Bastien Milani, Jean Delacoste, Michel Burnier, and Menno Pruijm. Exploring a new method for quantitative sodium MRI in the human upper leg with a surface coil and symmetrically arranged reference phantoms. *Quantitative Imaging in Medicine and Surgery*, 9(6):985–999, 2019.

[54] Serpil Muge Deger, Ping Wang, Rachel Fissell, Charles D. Ellis, Cindy Booker, Feng Sha, Jennifer L. Morse, Thomas G. Stewart, John C. Gore, Edward D. Siew, Jens Titze, and Talat Alp Ikizler. Tissue sodium accumulation and peripheral insulin sensitivity in maintenance hemodialysis patients. *Journal of Cachexia, Sarcopenia and Muscle*, 8(3):500–507, 6 2017.

[55] Markus P. Schneider, Ulrike Raff, Christoph Kopp, Johannes B. Scheppach, Sebastian Toncar, Christoph Wanner, Georg Schlieper, Turgay Saritas, Jürgen Floege, Matthias Schmid, Anna Birukov, Anke Dahlmann, Peter Linz, Rolf Janka, Michael Uder, Roland E. Schmieder, Jens M. Titze, and Kai Uwe Eckardt. Skin sodium concentration correlates with left ventricular hypertrophy in CKD. *Journal of the American Society of Nephrology*, 28(6):1867–1876, 2 2017.

[56] Matthias Hammon, Susan Grossmann, Peter Linz, Hannes Seuss, Rebecca Hammon, Daniela Rosenhauer, Rolf Janka, Alexander Cavallaro, Friedrich C. Luft, Jens Titze, Michael Uder, and Anke Dahlmann. 3 Tesla 23Na Magnetic Resonance Imaging During Acute Kidney Injury. *Academic Radiology*, 24(9):1086–1093, 5 2017.

[57] ICRP. Chapters 1-6. *Annals of the ICRP*, 39(2):21–45, 4 2009.

[58] Qi Duan, Jeff H Duyn, Natalia Gudino, Jacco A de Zwart, Peter van Gelderen, Daniel K Sodickson, and Ryan Brown. Characterization of a dielectric phantom for high-field magnetic resonance imaging applications. *Medical physics*, 41(10):102303, 10 2014.

[59] Carlotta Ianniello, Jacco A. de Zwart, Qi Duan, Cem M. Deniz, Leeor Alon, Jae-Seung Lee, Riccardo Lattanzi, and Ryan Brown. Synthesized tissue-equivalent dielectric phantoms using salt and polyvinylpyrrolidone solutions. *Magnetic Resonance in Medicine*, 80(1):413–419, 7 2018.

[60] Stefan Haneder, Simon Konstandin, John N. Morelli, Armin M. Nagel, Frank G. Zoellner, Lothar R. Schad, Stefan O. Schoenberg, and Henrik J. Michaely. Quantitative and Qualitative 23Na MR Imaging of the Human Kidneys at 3 T: Before and after a Water Load. *Radiology*, 260(3):857–865, 9 2011.

[61] ASTM International. Standard Test Method for Measurement of Radio Frequency Induced Heating On or Near Passive Implants During Magnetic Resonance Imaging F2182-19e2, 2020.

[62] National Electrical Manufacturers Association. Characterization of the Specific Absorption Rate for Magnetic Resonance Imaging Systems, 2016.

[63] Csaba P. Kovesdy, Susan L. Furth, and Carmine Zoccali. Obesity and Kidney Disease: Hidden Consequences of the Epidemic, 3 2017.

[64] Matthias Hammon, Susan Grossmann, Peter Linz, Christoph Kopp, Anke Dahlmann, Christoph Garlichs, Rolf Janka, Alexander Cavallaro, Friedrich C. Luft,

Michael Uder, and Jens Titze. 23Na magnetic resonance imaging of the lower leg of acute heart failure patients during diuretic treatment. *PLoS ONE*, 10(10):e0141336, 10 2015.

[65] Matthias Hammon, Susan Grossmann, Peter Linz, Christoph Kopp, Anke Dahlmann, Rolf Janka, Alexander Cavallaro, Michael Uder, and Jens Titze. 3 Tesla 23Na Magnetic Resonance Imaging During Aerobic and Anaerobic Exercise. *Academic Radiology*, 22(9):1181–1190, 9 2015.

[66] Christoph Kopp, Christian Beyer, Peter Linz, Anke Dahlmann, Matthias Hammon, Jonathan Jantsch, Patrick Neubert, Daniela Rosenhauer, Dominik N. Müller, Alexander Cavallaro, Kai Uwe Eckardt, Georg Schett, Friedrich C. Luft, Michael Uder, Jörg H.W. Distler, and Jens Titze. Na+ deposition in the fibrotic skin of systemic sclerosis patients detected by 23Na-magnetic resonance imaging. *Rheumatology (United Kingdom)*, 56(4):556–560, 12 2017.

[67] Navin Bansal, Lidia Szczepaniak, Damian Ternullo, James L Fleckenstein, and Craig R Malloy. Effect of exercise on 23Na MRI relaxation characteristics of the human calf muscle. *Journal of Magnetic Resonance Imaging*, 11(5):532–538, 5 2000.

[68] Chris D. Constantinides, Joseph S. Gillen, Fernando E. Boada, Martin G. Pomper, and Paul A. Bottomley. Human skeletal muscle: Sodium MR imaging and quantification - Potential applications in exercise and disease. *Radiology*, 216(2):559–568, 2000.

[69] Gregory Chang, Ligong Wang, Mark E. Schweitzer, and Ravinder R. Regatte. 3D 23Na MRI of human skeletal muscle at 7 tesla: Initial experience. *European Radiology*, 20(8):2039–2046, 8 2010.

[70] Dennis Kannenkeril, Marina V. Karg, Agnes Bosch, Christian Ott, Peter Linz, Armin M. Nagel, Michael Uder, and Roland E. Schmieder. Tissue sodium content in patients with type 2 diabetes mellitus. *Journal of Diabetes and its Complications*, 33(7):485–489, 7 2019.

[71] Christian Ott, Christoph Kopp, Anke Dahlmann, Axel Schmid, Peter Linz, Alexander Cavallaro, Matthias Hammon, Tilmann Ditting, Roland Veelken, Michael Uder, Jens Titze, and Roland E. Schmieder. Impact of renal denervation on tissue Na+ content in treatment-resistant hypertension. *Clinical Research in Cardiology*, 107(1):42–48, 1 2018.

[72] Rolf Pohmann and Klaus Scheffler. A theoretical and experimental comparison of different techniques for B1 mapping at very high fields. *NMR in Biomedicine*, 26(3):265–275, 3 2013.

[73] Peter Linz, Davide Santoro, Wolfgang Renz, Jan Rieger, Anjuli Ruehle, Jan Ruff, Michael Deimling, Natalia Rakova, Dominik N. Muller, Friedrich C. Luft, Jens Titze, and Thoralf Niendorf. Skin sodium measured with ¡sup¿23¡/sup¿Na MRI at 7.0 T. *NMR in Biomedicine*, 28(1):54–62, 2015.

[74] Jie Wen, Alexander L. Sukstanskii, and Dmitriy A. Yablonskiy. Phase-sensitive B1 mapping: Effects of relaxation and RF spoiling. *Magnetic Resonance in Medicine*, 80(1):101–111, 7 2018.

[75] Arthur Coste, Fawzi Boumezbeur, Alexandre Vignaud, Guillaume Madelin, Kathrin Reetz, Denis Le Bihan, Cécile Rabrait-Lerman, and Sandro Romanzetti. Tissue sodium concentration and sodium T1 mapping of the human brain at 3T using a Variable Flip Angle method. *Magnetic Resonance Imaging*, 58:116–124, 2019.

[76] Guillaume Madelin. Sodium Magnetic Resonance Imaging: Biomedical Applications. 2012.

[77] D. A. Gerlach, K. Schopen, P. Linz, B. Johannes, J. Titze, J. Zange, and J. Rittweger. Atrophy of calf muscles by unloading results in an increase of tissue sodium concentration and fat fraction decrease: a 23Na MRI physiology study. *European Journal of Applied Physiology*, 117(8):1585–1595, 8 2017.

[78] Johanna Lott, Tanja Platt, Sebastian C. Niesporek, Daniel Paech, Nicolas G. R. Behl, Thoralf Niendorf, Peter Bachert, Mark E. Ladd, and Armin M. Nagel.

Corrections of myocardial tissue sodium concentration measurements in human cardiac 23Na MRI at 7 Tesla. *Magnetic Resonance in Medicine*, 2019.

[79] Charlotte E Buchanan, Huda Mahmoud, Eleanor F Cox, Thomas McCulloch, Benjamin L Prestwich, Maarten W Taal, Nicholas M Selby, and Susan T Francis. Quantitative assessment of renal structural and functional changes in chronic kidney disease using multi-parametric magnetic resonance imaging. *Nephrology Dialysis Transplantation*, 35(6):955–964, 6 2020.

[80] Buerkert J, Martin D, Prasad J, and Trigg D. Role of deep nephrons and the terminal collecting duct in a mannitol-induced diuresis. *The American journal of physiology*, 240(5), 1981.

[81] J. B. Ra, S. K. Hilal, C. H. Oh, and I. K. Mun. In vivo magnetic resonance imaging of sodium in the human body. *Magnetic Resonance in Medicine*, 7(1):11–22, 5 1988.

[82] Stefan Haneder, Simon Konstandin, John N. Morelli, Lothar R. Schad, Stefan O. Schoenberg, and Henrik J. Michaely. Assessment of the Renal Corticomedullary 23Na Gradient Using Isotropic Data Sets. *Academic Radiology*, 20(4):407–413, 4 2013.

[83] Stefan Haneder, Vladimir Juras, Henrik J. Michaely, Xeni Deligianni, Oliver Bieri, Stefan O. Schoenberg, Siegfried Trattnig, and Štefan Zbýň. In vivo sodium (23Na) imaging of the human kidneys at 7 T: Preliminary results. *European Radiology*, 24(2):494–501, 2 2014.

[84] Robert Stobbe and Christian Beaulieu. Sodium imaging optimization under specific absorption rate constraint. *Magnetic Resonance in Medicine*, 59(2):345–355, 2008.

[85] Judy R. James, Anshuman Panda, Chen Lin, Ulrike Dydak, Brian M. Dale, and Navin Bansal. In vivo sodium MR imaging of the abdomen at 3T. *Abdominal Imaging*, 40(7):2272–2280, 10 2015.

[86] James W. Murakami, Cecil E. Hayes, and Ed Weinberger. Intensity correction of phased-array surface coil images. *Magnetic Resonance in Medicine*, 35(4):585–590, 4 1996.

[87] Sebastian Lachner, Laurent Ruck, Sebastian C. Niesporek, Matthias Utzschneider, Johanna Lott, Bernhard Hensel, Arnd Dörfler, Michael Uder, and Armin M. Nagel. Comparison of optimized intensity correction methods for 23Na MRI of the human brain using a 32-channel phased array coil at 7 Tesla. *Zeitschrift fur Medizinische Physik*, 30(2):104–115, 5 2020.

[88] Nadia Benkhedah, Stefan H. Hoffmann, Armin Biller, and Armin M. Nagel. Evaluation of adaptive combination of 30-channel head receive coil array data in 23Na MR imaging. *Magnetic Resonance in Medicine*, 75(2):527–536, 2 2016.

[89] Eleanor F. Cox, Charlotte E. Buchanan, Christopher R. Bradley, Benjamin Prestwich, Huda Mahmoud, Maarten Taal, Nicholas M. Selby, and Susan T. Francis. Multiparametric Renal Magnetic Resonance Imaging: Validation, Interventions, and Alterations in Chronic Kidney Disease. *Frontiers in Physiology*, 8(SEP):696, 9 2017.

[90] Bastien Milani, Annalisa Ansaloni, Sofia Sousa-Guimaraes, Nima Vakilzadeh, Maciej Piskunowicz, Bruno Vogt, Matthias Stuber, Michel Burnier, and Menno Pruijm. Reduction of cortical oxygenation in chronic kidney disease: Evidence obtained with a new analysis method of blood oxygenation level-dependent magnetic resonance imaging. *Nephrology Dialysis Transplantation*, 32(12):2097–2105, 12 2017.

[91] Christopher R. Bradley, Damian D. Bragg, Eleanor F. Cox, Ahmed M. El-Sharkawy, Charlotte E. Buchanan, Abeed H. Chowdhury, Ian A. Macdonald, Susan T. Francis, and Dileep N. Lobo. A randomized, controlled, double-blind crossover study on the effects of isoeffective and isovolumetric intravenous crystalloid and gelatin on blood volume, and renal and cardiac hemodynamics. *Clinical Nutrition*, 39(7):2070–2079, 7 2020.

[92] Abeed H. Chowdhury, Eleanor F. Cox, Susan T. Francis, and Dileep N. Lobo. A randomized, controlled, double-blind crossover study on the effects of 1-l infusions of 6% hydroxyethyl starch suspended in 0.9% saline (Voluven) and a balanced solution (Plasma Volume Redibag) on blood volume, renal blood flow velocity, and renal corti. *Annals of Surgery*, 259(5):881–887, 2014.

[93] Abeed H. Chowdhury, Eleanor F. Cox, Susan T. Francis, and Dileep N. Lobo. A randomized, controlled, double-blind crossover study on the effects of 2-L infusions of 0.9% saline and plasma-lyte® 148 on renal blood flow velocity and renal cortical tissue perfusion in healthy volunteers. *Annals of Surgery*, 256(1):18–24, 7 2012.

[94] Dileep N. Lobo and Sherif Awad. Should chloride-rich crystalloids remain the mainstay of fluid resuscitation to prevent 'pre-renal' acute kidney injury?: Con, 1 2014.

[95] Fricke Tobin. Monte Carlo investigation of the Ising model, 2006.

[96] Viknesh Selvarajah, Kathleen Connolly, Carmel McEniery, and Ian Wilkinson. Skin Sodium and Hypertension: a Paradigm Shift? *Current Hypertension Reports*, 20(11):94, 11 2018.

[97] Charkoudian N. Skin blood flow in adult human thermoregulation: how it works, when it does not, and why. *Mayo Clinic proceedings*, 78(5):603–612, 5 2003.

[98] P. A. Payne. High Resolution Medical Ultrasound: Applications in Rheumatology and Dermatology. *Physics and Engineering of Medical Imaging*, pages 378–381, 1987.

[99] Haroon A, Shafi S, and Rao BK. Using Reflectance Confocal Microscopy in Skin Cancer Diagnosis. *Dermatologic clinics*, 35(4):457–464, 10 2017.

[100] Böhling A, Bielfeldt S, Himmelmann A, Keskin M, and Wilhelm KP. Comparison of the stratum corneum thickness measured in vivo with confocal Raman spectroscopy and confocal reflectance microscopy. *Skin research and technology : official journal of International Society for Bioengineering and the Skin (ISBS) [and] International*

Society for Digital Imaging of Skin (ISDIS) [and] International Society for Skin Imaging (ISSI), 20(1):50–57, 2 2014.

[101] McDonald PJ, Akhmerov A, Backhouse LJ, and Pitts S. Magnetic resonance profiling of human skin in vivo using GARField magnets. *Journal of pharmaceutical sciences*, 94(8):1850–1860, 2005.

[102] L. Backhouse, M. Dias, J. P. Gorce, J. Hadgraft, P. J. McDonald, and J. W. Wiechers. GARField magnetic resonance profiling of the ingress of model skin-care product ingredients into human skin in vitro. *Journal of Pharmaceutical Sciences*, 93(9):2274–2283, 9 2004.

[103] M Dias, J Hadgraft, P M Glover, and P J McDonald. Stray field magnetic resonance imaging: a preliminary study of skin hydration. *Journal of Physics D: Applied Physics*, 36(4):364, 1 2003.

[104] Mesrar J, Ognard J, Garetier M, Chechin D, Misery L, and Ben Salem D. In vivo skin moisturizing measurement by high-resolution 3 Tesla magnetic resonance imaging. *Skin research and technology : official journal of International Society for Bioengineering and the Skin (ISBS) [and] International Society for Digital Imaging of Skin (ISDIS) [and] International Society for Skin Imaging (ISSI)*, 23(3):289–294, 8 2017.

[105] Calzolari L, Kastler A, Mac-Mary S, Humbert P, Kastler B, and Aubry S. 3T-MRI analysis of epidermis and dermis moisturizing using the T2-mapping sequence. *Skin research and technology : official journal of International Society for Bioengineering and the Skin (ISBS) [and] International Society for Digital Imaging of Skin (ISDIS) [and] International Society for Skin Imaging (ISSI)*, 19(2):152–154, 5 2013.

[106] Hawnaur JM, Dobson MJ, Zhu XP, and Watson Y. Skin: MR imaging findings at middle field strength. *Radiology*, 201(3):868–872, 1996.

[107] Hyde JS, Jesmanowicz A, and Kneeland JB. Surface coil for MR imaging of the skin. *Magnetic resonance in medicine*, 5(5):456–461, 1987.

[108] Richard S, Querleux B, Bittoun J, Idy-Peretti I, Jolivet O, Cermakova E, and Lévêque JL. In vivo proton relaxation times analysis of the skin layers by magnetic resonance imaging. *The Journal of investigative dermatology*, 97(1):120–125, 1991.

[109] Bittoun J, Saint-Jalmes H, Querleux BG, Darrasse L, Jolivet O, Idy-Peretti I, Wartski M, Richard SB, and Leveque JL. In vivo high-resolution MR imaging of the skin in a whole-body system at 1.5 T. *Radiology*, 176(2):457–460, 1990.

[110] Mäurer J, Requardt H, Sander B, Knollmann FD, Lemke AJ, Vogl TJ, and Felix R. Applications of specialized coils for high-resolution MRI on a whole-body scanner. *Magma (New York, N.Y.)*, 4(1):27–33, 1996.

[111] Jan Weis, Anders Ericsson, Gunnar Åström, Pavol Szomolanyi, and Anders Hemmingsson. High-resolution spectroscopic imaging of the human skin. *Magnetic Resonance Imaging*, 19(2):275–278, 2 2001.

[112] Joëlle K. Barral, Neal K. Bangerter, Bob S. Hu, and Dwight G. Nishimura. In Vivo High-Resolution Magnetic Resonance Skin Imaging at 1.5 T and 3 T. *Magnetic resonance in medicine : official journal of the Society of Magnetic Resonance in Medicine / Society of Magnetic Resonance in Medicine*, 63(3):790, 2010.

[113] Aubry S, Casile C, Humbert P, Jehl J, Vidal C, and Kastler B. Feasibility study of 3-T MR imaging of the skin. *European radiology*, 19(7):1595–1603, 2009.

[114] S Maderwald, S Orzada, A Bitz, O Kraff, I Brote, J Theysohn, M Ladd, S Ladd, and H Quick. A Novel Figure-Eight Coil for Skin Imaging at 7T. In *Proceedings 17th Scientific Meeting, International Society for Magnetic Resonance in Medicine*, volume Honolulu, page 1994, 2009.

[115] Salter DC, Hodgson RJ, Hall LD, Carpenter TA, and Ablett S. Moisturization processes in living human skin studied by magnetic resonance imaging microscopy. *International journal of cosmetic science*, 15(5):219–226, 1993.

[116] Franconi F, Akoka S, Guesnet J, Baret JM, Dersigny D, Breda B, Muller C, and Beau P. Measurement of epidermal moisture content by magnetic resonance imaging: assessment of a hydration cream. *The British journal of dermatology*, 132(6):913–917, 1995.

[117] B. Querleux, S. Richard, J. Bittoun, O. Jolivet, I. Idy-Peretti, R. Bazin, and J.L. Lévêque. In vivo Hydration Profile in Skin Layers by High-Resolution Magnetic Resonance Imaging. *Skin Pharmacology and Physiology*, 7(4):210–216, 1994.

[118] Mesrar J, Ognard J, Garetier M, Chechin D, Misery L, and Ben Salem D. In vivo skin moisturizing measurement by high-resolution 3 Tesla magnetic resonance imaging. *Skin research and technology : official journal of International Society for Bioengineering and the Skin (ISBS) [and] International Society for Digital Imaging of Skin (ISDIS) [and] International Society for Skin Imaging (ISSI)*, 23(3):289–294, 8 2017.

[119] Gensanne D, Josse G, Theunis J, Lagarde JM, and Vincensini D. Quantitative magnetic resonance imaging of subcutaneous adipose tissue. *Skin research and technology : official journal of International Society for Bioengineering and the Skin (ISBS) [and] International Society for Digital Imaging of Skin (ISDIS) [and] International Society for Skin Imaging (ISSI)*, 15(1):45–50, 2009.

[120] Ciampi E, van Ginkel M, McDonald PJ, Pitts S, Bonnist EY, Singleton S, and Williamson AM. Dynamic in vivo mapping of model moisturiser ingress into human skin by GARfield MRI. *NMR in biomedicine*, 24(2):135–144, 2 2011.

[121] Mirrashed F and Sharp JC. In vivo quantitative analysis of the effect of hydration (immersion and Vaseline treatment) in skin layers using high-resolution MRI and magnetisation transfer contrast. *Skin research and technology : official journal of International Society for Bioengineering and the Skin (ISBS) [and] International Society for Digital Imaging of Skin (ISDIS) [and] International Society for Skin Imaging (ISSI)*, 10(1):14–22, 2 2004.

[122] Ognard J, Mesrar J, Benhoumich Y, Misery L, Burdin V, and Ben Salem D. Edge detector-based automatic segmentation of the skin layers and application to moisturization in high-resolution 3 Tesla magnetic resonance imaging. *Skin research and technology : official journal of International Society for Bioengineering and the Skin (ISBS) [and] International Society for Digital Imaging of Skin (ISDIS) [and] International Society for Skin Imaging (ISSI)*, 25(3):339–346, 5 2019.

A.1 6-Channel Coil Element Selection

Before the 6-channel ^{23}Na body RF coil was built, in collaboration with the designers at ClinicalMR Solutions (Brookfield, Wisconsin, USA), the size of the 6 receive elements to form the coil was determined to ensure that the coil had a suitable receive sensitivity to image ^{23}Na in the abdomen. ClinicalMR Solutions provided three proposed loop size options for the receive elements, the elements and the dimensions can be seen in Fig.[1], the coils will be referred to by their width: 8cm, 13cm and 15cm. The final array was made up of 6 identical receive elements but these initial measurements were carried out on a single element. They were supplied with an interface box with the necessary T/R switch and pre-amplifier to enable the individual elements to be used as transmit/receive RF coils. This enabled the sensitivity profiles of each coil to be gauged choose the correct dimensions for the final 6-channel array coil.

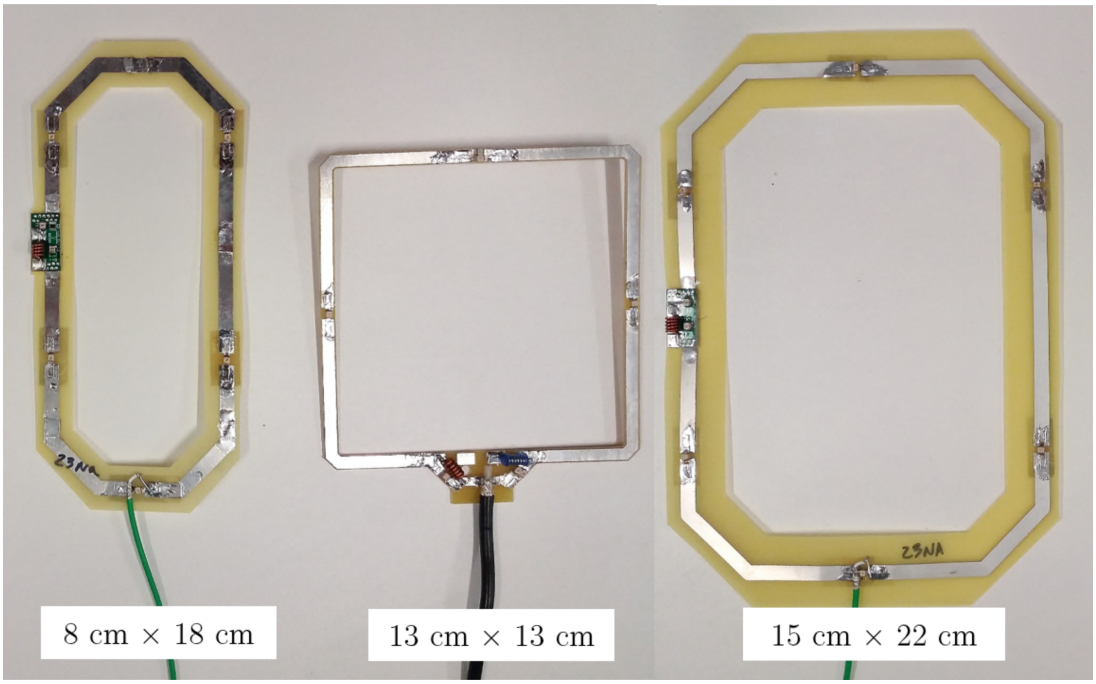

Figure 1: The three options for the receive element sizes for the 6-channel coil.

Firstly, for each coil, the power calibration was carried out (as detailed in Section [3.6]) with the reference solution at a height above the coil equal to the minor radius of each coil element. Using each coil, an axial GRE scan (Resolution:$3 \times 3 \times 30\text{mm}^3$, TA:6 mins, TR:100 ms, TE:2.1 ms, FA: 90°) was carried out on the body phantom containing 50

mmol/L NaCl solution. The images produced by these scans can be seen in Fig.[2].

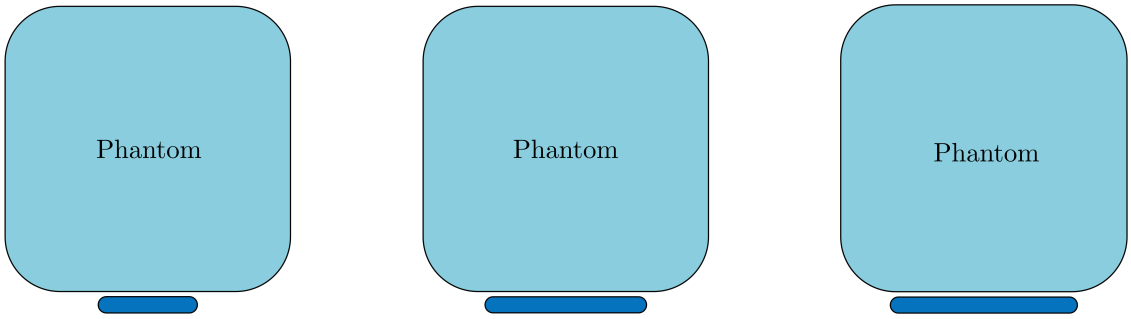

(a) 8cm receive element position.

(b) 13cm receive element position.

(c) 15cm receive element position.

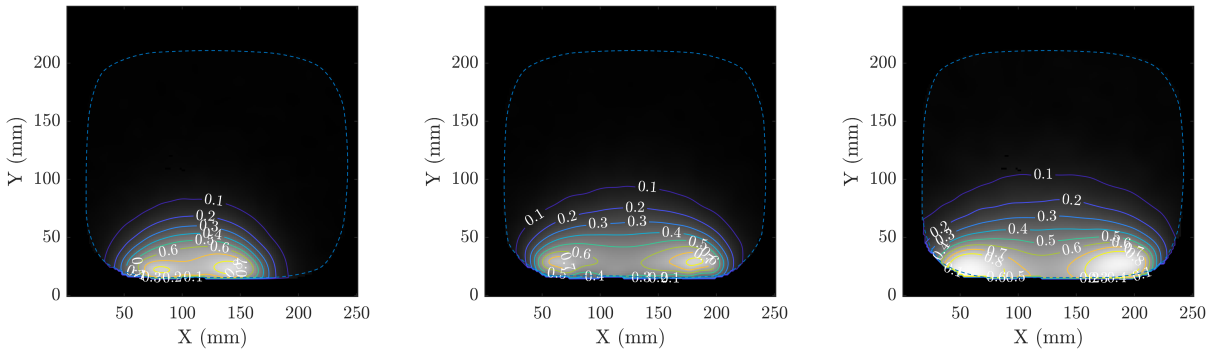

(d) 8cm receive element.

(e) 13cm receive element.

(f) 15cm receive element.

Figure 2: ^{23}Na images acquired with each of the receive elements showing approximate receive profiles of each coil.

The larger the RF coil the greater the depth of the receive sensitivity. The longer coils provided a greater FOV in the z-direction as can be seen in the seven slices in Fig.[3], the signal reduces in the outermost slices, to a lesser extent in the 22cm coil.

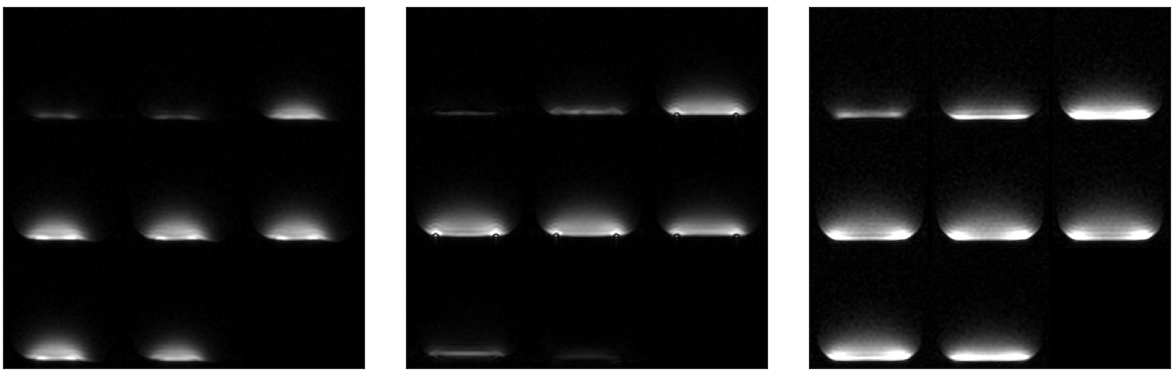

(a) 8cm receive element

(b) 13cm receive element

(c) 15cm receive element

Figure 3: ^{23}Na Images taken with the receive elements showing 7 axial slices to demonstrate the coil's coverage in the z-direction.

For scale, the phantom was 23 cm wide, the outline is shown in Fig.[2]. *In vivo*, the width across the abdomen can be up to 40 cm wide, although the receive element will form part of a receive array, we had to used this data to ensure the complete coverage throughout the abdomen. A diagram showing the suggested phased array sensitivity of the different array elements can be seen in Fig.[4]. The image is approximately to scale, and the ellipse is used to represent a 40 cm wide body.

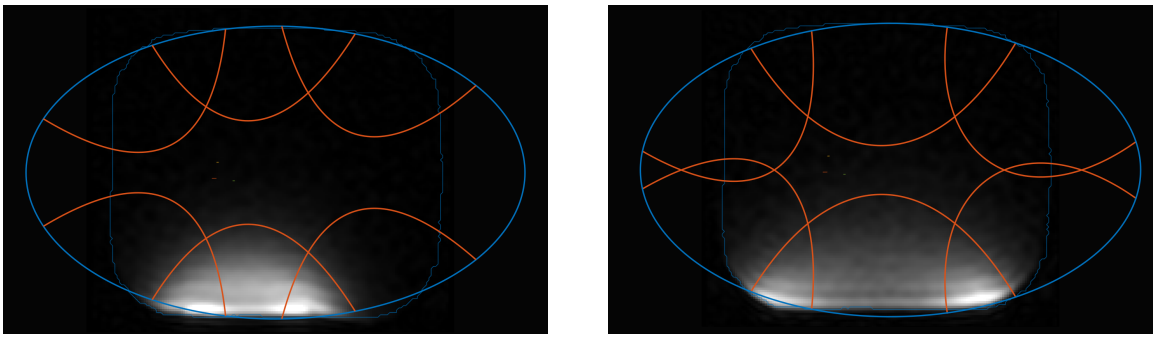

(a) 8cm array element (b) 15cm array element

Figure 4: The suggested receive profiles for the complete receive arrays

These results suggested that an array made up of the six 15 cm×22 cm loops would provide the best coverage in the abdomen, although the kidneys are towards the centre of the body, a coil with complete coverage of the abdomen would allow for imaging of other organs such as the liver.

The measurements here do not show the true receive sensitivity profile of the receive elements as other effects such as the transmit uniformity, dependency on accurate power calibration and the flexing of the coil have been ignored. These tests showed that the 15cm loop was the best option for the receive element size and they were used in the final coil design.

Fig.[5] shows ^{23}Na images from the complete 6-channel coil, a different sized phantom was used but it has a similar width of 29cm. Good coverage is shown throughout the phantom.

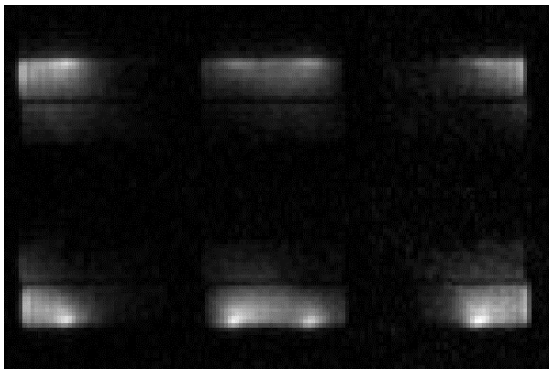

(a) Six separate ^{23}Na images from the receive elements.

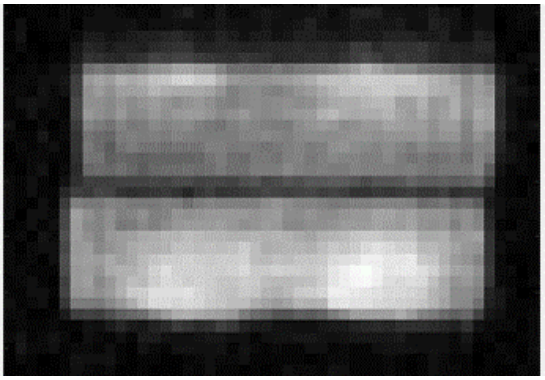

(b) The image produced from the combination of the six channels.

Figure 5: ^{23}Na images from the complete 6-channel coil containing six 15 cm×22 cm loops.

B.2 Scan Ethics

Application of ethical approval to the University of Nottingham Medical School, Ethics Committee

Sodium MRI in the skin, muscle and kidney

Enclosed copies of each of the following:

1. Application of ethical approval to the University of Nottingham Medical School, Ethics Committee.
2. Study Protocol
3. Written Consent Form
4. Volunteer's Information Sheet.
5. Volunteer's Safety Questionnaire
6. Advertisement poster

The University of Nottingham

Application form

UNIVERSITY OF NOTTINGHAM
MEDICAL SCHOOL ETHICS COMMITTEE

In completing this form please refer to the attached Notes of Guidance

Application for approval of all studies involving **Healthy Human Volunteers only**

Please complete in typewritten form application form, consent form (template attached) and subject's information sheet (template attached), in addition please attach a short study protocol and supply 13 copies of each.

1. Title of Project:

Development of Sodium MRI in the skin, muscle and kidney

2. Names, Position, Department and Qualifications of Investigators:

- Prof. Sue Francis (PhD)
  Professor in Physics, Sir Peter Mansfield Imaging Centre (SPMIC), University of Nottingham.

- Dr. Charlotte Buchanan (PhD)
  Research fellow, SPMIC, University of Nottingham

- Mr Benjamin Prestwich
  PhD student Physics, Sir Peter Mansfield Imaging Centre (SPMIC), University of Nottingham.

- Dr Huda Mahmoud
  PhD student medicine, Royal Derby Hospital, University of Nottingham

- Dr Nick Selby
  Associate Professor of Nephrology, Royal Derby Hospital, University of Nottingham

- Dr Maarten Taal
  Professor of Medicine, Royal Derby Hospital, University of Nottingham

-Dr Paul Glover
  Reader in Physics, Sir Peter Mansfield Imaging Centre (SPMIC), University of Nottingham

-Dr Andrew Peters
  Centre Manager, Sir Peter Mansfield Imaging Centre (SPMIC), University of Nottingham

3. Type of Project: (Please tick appropriate box)

a) Classroom procedures:	[ ]	b) Student project	[ ]
c) Development of technique:	[√]	d) Assessment of new drug or formulation:*	[ ]
e) Pilot Study:	[ ]	f) Questionnaire-based study or community survey	[ ]

g) Commercially funded* [ ] h) Other [ ]

4a. <u>Summary of Experimental Protocol</u> - Please give details below (no longer than this side of A4) under the following headings: - 1. Background. 2. Aims (to include hypothesis to be tested), 3. Experimental protocol and methods, 4. Measurable end points/statistical power of the study. 5. Key references. This section must be completed. Even if you are attaching a full protocol a summary should be provided here. Please use 10pt typeface.

1. Background:

Sodium (^{23}Na) MRI has the potential to provide complementary quantitative parameters of tissue health, in a non-invasive manner. Although the clinical use of ^{23}Na MRI was first demonstrated in 1984 (1), it is only with the recent developments in MRI technology that the significant potential of this approach for clinical imaging has started to be explored.

Tissue Sodium Content (TSC) may provide a key quantitative marker for kidney tissue health in kidney disease. Sodium MRI is the only imaging technique that can map the sodium concentration gradient between cortex and medulla, the cortico-medullary gradient (CMSG) (2), and thus provide a marker of preserved tubule and integrated nephron function. By quantifying the flow of sodium through the glomeruli, this could provide a measure of glomerular filtration and thus a spatial map of glomerular sodium flow. This spatial map could allow assessment of regional loss of glomerular function in areas of kidney damage.

Sodium imaging can also be applied in the skin and muscle to assess sodium accumulation. This has been proposed to be a valuable tool in elucidating the role of tissue sodium accumulation in the pathogenesis of salt-sensitive hypertension. Multiple quantum filtered (MQF) will be developed in the kidney and skin and muscle to distinguish between intracellular and extracellular sodium.

2. Aim:

To develop techniques to (1) quantify tissue sodium content (TSC) and the cortico-medullary sodium gradient (CMSG) in the kidney at 3T and 7T and fuse these data with proton images (2) quantify skin and muscle sodium content (3) measure flow of sodium into the kidney via the renal arteries and (4) apply MQF techniques to the kidney, skin and muscle.

3. Experimental protocol and methods:

Studies will be conducted on the 3T and 7T Philips MR scanners at the Sir Peter Mansfield Imaging Centre. Volunteers will also be asked to give a blood sample so that MR results can be correlated with clinical measures. Volunteers will be invited to attend up to 3 scan sessions with each session lasting up to one hour. Scans will be a (1) skin/muscle scan at 3T, (2) kidney scan at 3T and (3) kidney scan at 7T described below:

1) In skin/muscle, we will assess tissue sodium and water content. Tissue sodium content will be measured using spectroscopy of the skin. To measure tissue water content, a fat saturated inversion recovery scan will be used. We will also collect a sodium image of the muscle using a FLASH imaging technique. MQF techniques will also be developed in the skin/muscle.

2) We will develop ^{23}Na MRI strategies for the accurate determination of the TSC and CMSG at 3 T to provide a quantifiable clinical marker. Kidney TSC and CMSG will be assessed using a 2D FLASH sequence. To assess the sensitivity of these measures to change, we will perform a standard water loading and water deprivation modulation in healthy subjects (n = 20) scanning a sub-set of healthy control subjects (n = 10) twice for reproducibility. Subjects will be asked not to consume water for 6 hours prior to scanning and then will be given one litre of water during scanning. Kidney TSC and CMSG will be correlated with established measures of kidney damage including glomerular filtration rate and albuminuria from blood tests and ^{1}H MRI measures of kidney damage (tissue relaxation time, perfusion and diffusion measures). To correlate these measures with structural information, these images will be fused with proton images to allow assessment of the association of structural evidence of tissue damage or fibrosis with functional perturbation of sodium handling resulting in loss of CMSG. Sodium velocimetry methods will be developed to assess the bulk sodium flow into the kidney through the renal artery. We will also create maps of sodium distribution in the microvasculature of the kidney. These images with be combined with proton flow images based on phase contrast MRI of the renal arteries to assess renal blood flow, and arterial spin labelling (ASL) perfusion and diffusion imaging (4-6). The imaging techniques used for sodium diffusion, sodium flow and MQF will have been developed and optimised before application.

3) The measures described in (1) will also be developed and applied at 7T.

Volunteers will be asked to give a blood sample and provide a urine test so that MR results can be correlated with clinical measures. Blood tests will be taken by Dr Huda Mahmoud.

4. Measurable end points/statistical power of the study: 1) TSC quantification and MQF in the skin/muscle at 3T. 2) TSC quantification in kidney and fusion with ^{1}H structural images in n=20 healthy subjects at 3T with

sodium flow mapping. 3) TSC quantification and MQF in kidney and fusion with ^{1}H structural images in 10 healthy subjects at 7T.

5. Key references

(1) Maudsley AA, Hilal SK. Brit Med Bull. 1984;40(2):165-&.(2) Zollner FG, Konstandin S, Lommen J, et al. Nmr Biomed. 2015. (3) Breidthardt T, Cox EF, Squire I, et al. Eur Radiol. 2015;25(6):1684-91. (4) Gardener AG, Francis ST. Magn Reson Med. 2010;63(6):1627-36. (5) Liss P, Cox EF, Eckerbom P, et al. Clinical and Experimental Pharmacology and Physiology. 2013;40(2):158-67.

4b. Lay Summary of project (in lay words)(maximum 200 words) ***Summaries which include language which is too technical for lay members of the Committee will be rejected.***

Sodium MRI has the potential to non-invasively provide information about the kidney that is not currently possible using current imaging techniques. The measurement of sodium content in the kidney could be used to assess changes in diseases such as chronic kidney disease and acute kidney injury. Sodium MRI can also be applied in the skin and muscle to assess the accumulation of salt. This study aims to develop techniques to measure sodium content in the kidney, skin and muscle using MRI. We will also measure sodium flow in and out of the kidney which will then be used as a marker for how well the kidneys are functioning. A final technique (MQF) will be used in the skin, muscle and kidney to distinguish between sodium that is being stored inside cells and outside of cells.

5. Duration of Study: 24 months

6. Location of study: Sir Peter Mansfield Imaging Centre, University of Nottingham.
Proposed starting date: 1st June 2017
Proposed finishing date: 1st June 2019

7. Description and number of volunteers to be studied:

20 healthy adult volunteers with no history of kidney disease will be studied in total (10 subjects scanned twice for reproducibility).

8. Will written consent be obtained from all volunteers? **Yes**

Please give the name, status and relevant qualifications of the person who will give a verbal explanation and obtain consent.

Dr. Charlotte Buchanan, PhD, MR physicist, SPMIC, University of Nottingham
Mr Benjamin Prestwich, PhD student, SPMIC, University of Nottingham

9. Will a disturbance allowance be offered? **Yes**

If Yes, give rate (*delete as appropriate)
£15 per hour

*Per day:
*Per Study:
*Per procedure:
*Give the maximum allowance payable to a volunteer:

10. Will a medical supervisor be present: **No**

11a. Does the study involve the exposure of the patient to radioactive materials? **No**

If your project involves the administration of radioisotopes your attention is drawn to note 10 a) in the attached notes of guidance.

Radiological Practitioner/ARSAC certificate holder
Name Signature* What is the total effective dose

*The Radiological Practitioner/ARSAC certificate holder must sign to accept responsibility for the radiological procedure listed above.

It is the responsibility of the investigator to ensure that the total exposure of a volunteer to ionising radiation will not exceed 5 mSv over any 12 month period.

The Radiation Protection Adviser (RPA) must sign below to confirm that the dose estimate is satisfactory and that the appropriate arrangements are in place for undertaking the procedure.

RPA Name Signature Date

11b. Does the study involve the exposure of the patient to X-rays? No

Type of procedure:

All research involving radiology must be submitted and approved by the Clinical Director for Radiology.

RPA Name Signature* What is the total effective dose

Clinical Director Name Signature Date

12. Will participant's General Practitioners be told about the study? This would be regarded as essential if the study includes consumption of drugs or novel chemical entities or if you are recommending that the volunteer should see their GP as a result of the study.

No

If no please justify

This is a simple MRI experiment which is non-invasive hence we will not need to inform the participants' GPs.

13a 1. If the procedure involves any intervention or treatment (blood sampling, biopsy , i.v injections, manipulation etc) does the practitioner performing this intervention or treatment have personal profession negligence insurance

N/A

2. If the procedure involves new drug, formulation or device, will full insurance cover be provided by the sponsoring drug firm?

N/A

If Yes, **See Guidelines Note 1: Insurance**

Proof of indemnity and a copy of the company's certificate of insurance should be forwarded for consideration at the same time as the application and protocol.

13b. FUNDING

Will there be any material benefits from the study for the Department or individual investigator? (E.g. equipment, research salaries, consumables etc)

No

If yes please specify in general terms what the benefits will be:

13c. <u>Culyer Costing for Trust R&D</u>

Does the study involve any staff who hold a contract with the hospital trust?(This does not include investigators with an honorary contract with the NHS but does include staff whose salary is provided by the NHS eg Nurse, radiographer, physiotherapist)

No

Will the study use any space/facilities belonging to the hospital trust?

No

If you answer yes to either of the above questions please complete and submit the attached QMC Trust R&D form.

14a. <u>Drugs or other substances to be administered (including placebo and comparators</u>)

Drug name:
Generic Name:
Proprietary Name:
Formulation:
Dose:
Frequency:
Route:
Possible complications (append details if necessary)

Please tick where appropriate

CSM status
Product Licence (PL)
Clinical Trials Certificate (CTC)
Clinical Trials Exemption Certificate (CTX)
Doctors & Dentist Exemption Certificate (DDX)

- For drugs with a product licence please append a copy of the relevant data sheet.
- For drugs with a CTC or CTX, please append a statement detailing present knowledge of the drug action, adverse effects, long and short-term safety.
- The number of the PL, CTC, CTX, or DDX <u>MUST</u> be included.

If a new drug formulation is being studied an explicit statement as to the UK licensing status of the product is required. For unlicensed products then information should be given as to its licensing status in other countries and appropriate safety data should be submitted.

Arrangements for the supply, storage and dispensing of trial drugs must be discussed with the Senior Pharmacist at the relevant hospital who must sign below.

14b. <u>Will any drug used be stored in the Pharmacy and dispensed to a prescription written in red?</u>

No

If No, please explain why:

Signature of Pharmacist ……..

Printed Name ……
NB THIS MUST BE OBTAINED

15. Does the project involve painful/dangerous or invasive procedures on volunteers ? No

16. Will blood samples or other specimens be required? Yes

If so, will written informed consent be obtained? **Yes**

What volume will be required and over what duration?*

5ml of blood will be taken per subject during one session.

*Studies involving venepuncture only, where the information generated is of no prognostic significance, will be approved by Chairman's action provided no more than a total of 500mls of blood is taken over a 6 month period and no more than 200mls is taken on a single occasion. Applicants need to submit 1 copy of this form and other documentation with a covering letter to the Chairman.

17. How will the subjects be chosen? Please specify what criteria will be used and which groups you wish to target.

All volunteers will be carefully screened using a Safety Questionnaire (attached) to ensure their safety within the MR scanner. At recruitment all the volunteers will be given an Information Sheet to keep. This describes the nature of MR and an outline of the experimental procedure.

Please include a copy of your proposed poster or advert

18. Describe how possible participants will be approached? Please refer to note 9 in the Guidelines. Please specify whether posters will be used and where they will be placed.

Subjects will be recruited via advertisement by poster on campus, particularly in the Sir Peter Imaging Centre (SPMIC), and in other collaborating schools and organisations. A general advertisement is also placed on the Sir Peter Mansfield Imaging Centre web page.

After the initial contact by advertisement, volunteers will be put in contact with the receptionist at the SPMIC to make further arrangements. By removing direct contact with the investigators for this stage of the arrangements, we will further ensure volunteers feel free to withdraw from the study. One investigator will then be available to explain the study procedures and to answer any question the prospective volunteers may have.

The wording of the web-page advert is:

We often need volunteers for brain and whole body imaging studies. These studies follow protocols that have been approved by the local Ethics Committee. The study will also give an inconvenience allowance, and we will always give you a picture of your insides.

You would have to undergo safety screening before being scanned, and in particular we cannot scan anyone with a pacemaker or any metal implants in their bodies. Please note that you cannot start to participate in a new medical research study within 3 months of finishing a different one on campus.

To register your interest please email Lesley at Lesley.Martin@nottingham.ac.uk

The wording of the advert to be posted about campus is:

Volunteers required for an MRI study of sodium in the body. We are investigating concentration of sodium in kidneys, skin, and muscles and we need volunteers to help us. Participants will be scanned both in 3 and 7 Tesla MRI scanners. The duration of the scans will be limited to 60 minutes and you will get a picture of your scan.

For further details, please email Lesley Martin: Lesley.Martin@nottingham.ac.uk or call 01159514747.

**** If your study is community-based or epidemiological study please answer the following questions (19-21)

19. What sources of information will be included? (tick any that apply) **N/A**

Personal interview	[ ]
Postal questionnaire**	[ ]
Hospital records	[ ]
GP records	[ ]
Occupational records	[ ]
Other, describe	_____

** Please submit a copy of your proposed questionnaire if you are a student please make sure your supervisor has reviewed and approved it.

20. Whose permission will be sought to access this information (eg GP, consultant)?

21. For interview surveys only:

Please indicate who will do interviews (eg Students, research nurses etc)

22. What ethical problems do you foresee in this project?

No major ethical problems are foreseen in this project, however there is a risk that we will notice something unexpected. If we should notice something abnormal on the scan, the principal investigator will arrange for an appropriate medical doctor to contact you to explain the situation and to advise you of any further action that you should take. Usually this will involve contacting your GP.

Any other relevant information? **N/A**

DECLARATION: I will inform the Medical School Ethics Committee as soon as I hear the outcome of any application for funding for the proposed project and/or if there are any significant changes to this proposal. I have read the notes to the investigators and clearly understand my obligations as to the rights, welfare and dignity of the subjects to be studied, particularly with regard to the giving of information and the obtaining of consent.

Signature of Lead Investigator: **Date:**

**Nb If you are student your supervisor must sign this form otherwise it will be rejected

Name and address for correspondence with applicant:

Prof Susan Francis
SPMIC,
University Park
University of Nottingham
Nottingham
NG7 2RD

STUDY PROTOCOL

Sodium MRI of the skin, muscle and kidney

BACKGROUND

Sodium (^{23}Na) MRI has the potential to provide complementary quantitative parameters of tissue health, in a non-invasive manner. Although the clinical use of ^{23}Na MRI was first demonstrated in 1984, it is only with the recent developments in MRI technology that the significant potential of this approach for clinical imaging has started to be explored. The development of sodium imaging can be used to assess the changes to the kidney during chronic kidney disease. Tissue Sodium Content (TSC) could be a key quantitative marker for kidney tissue health in CKD Sodium MRI is the only imaging technique that can map the sodium concentration gradient between cortex and medulla, the cortico-medullary gradient (CMSG), and thus provide a marker of preserved tubule and integrated nephron function. By quantifying the flow of sodium through the glomeruli, this could provide a measure of glomerular filtration and thus a spatial map of glomerular sodium flow could allow assessment of regional loss of glomerular function in areas of kidney damage. Sodium imaging can also be applied in the skin and muscle to assess sodium accumulation. This has been proposed to be a valuable tool in elucidating the role of tissue sodium accumulation in the pathogenesis of salt-sensitive hypertension. Multiple quantum filtered (MQF) will be developed in the kidney and skin and muscle to distinguish between intracellular and extracellular sodium. We have developed and optimised a multi-parametric proton MRI scan of the kidneys and so sodium measures will provide additional information about the health of the kidney.

AIMS

To develop techniques to (1) quantify tissue sodium content (TSC) and the cortico-medullary sodium gradient (CMSG) in the kidney and 3T and 7T and fuse these data with proton images (2) quantify skin and muscle sodium content (3) measure flow of sodium into the kidney via the renal arteries and (4) apply MQF techniques to the kidney, skin and muscle.

METHODS

Studies will be conducted on the 3T and 7T Philips MR scanners at the Sir Peter Mansfield Imaging Centre. Volunteers will also be asked to give a blood sample so that MR results can be correlated with clinical measures. Blood tests will be taken by Dr Huda Mahmoud. Volunteers will be invited to attend up to 3 scan sessions with each session lasting up to one hour. Scans will be a (1) skin/muscle scan at 3T, (2) kidney scan at 3T and (3) kidney scan at 7T described below:

1) In skin/muscle, we will assess tissue sodium and water content. Tissue sodium content will be measured using spectroscopy of the skin. To measure tissue water content, a fat saturated inversion recovery scan will be used. We will also collect a sodium image of the muscle using a FLASH imaging technique. MQF techniques will also be developed in the skin/muscle.

2) We will develop ^{23}Na MRI strategies for the accurate determination of the TSC and CMSG at 3 T to provide a quantifiable clinical marker. Kidney TSC and CMSG will be assessed using a 2D FLASH sequence. To assess the sensitivity of these measures to change, we will perform a standard water loading and water deprivation modulation in healthy subjects (n = 20) scanning a sub-set of healthy control subjects (n = 10) twice for reproducibility. Subjects will be asked not to consume water for 6 hours prior to scanning and then will be given one litre of water during scanning. Kidney TSC and CMSG will be correlated with established measures of kidney damage including glomerular filtration rate and albuminuria from blood tests and ^{1}H MRI measures of kidney damage (tissue relaxation time, perfusion and diffusion measures). To correlate these measures with structural information, these images will be fused with proton images to allow assessment of the association of structural evidence of tissue damage or fibrosis with functional perturbation of sodium handling resulting in loss of CMSG. Sodium velocimetry methods will be developed to assess the bulk sodium flow into the kidney through the renal artery. We will also create maps of sodium distribution in the microvasculature of the kidney. These images with be combined with proton flow images based on phase contrast MRI of the renal arteries to assess renal blood flow, and arterial spin labelling (ASL) perfusion and diffusion imaging (4-6). The imaging techniques used for sodium diffusion, sodium flow and MQF will have been developed and optimised before application.

3) The measures described in (1) will also be developed and applied at 7T.

MRI protocol: MR scanning will be performed on a Philips 7T Achieva scanner and 3T Philips Achieva scanner, using home built coils for skin/muscle assessment and coils manufactured by Clinical MR Solutions, LLC to measure sodium in the skin and muscle and body. These coils will be approved for use by the SPMIC

safety committee which has procedures in place which involves SAR modelling and heating tests. Coils from Clinical MR Solutions will be used to measure sodium in the kidneys, which are approved for human use. Skin and muscle sodium will be assessed using a 2D gradient echo sequence with echo time (TE) of 2 ms and an acquisition time of approximately 13 minutes. Sodium spectroscopy will be used to quantity skin sodium content whilst skin and muscle water content will be measured using a fat saturated inversion recovery technique with spin density contrast. In the kidneys, a gradient echo scheme will be used to measure sodium content and the CMSG. Ultra-short echo time (UTE) schemes will also be assessed and developed for use in sodium imaging in the kidney. Proton images of the kidneys will also be acquired to assess kidney physiology including phase contrast scans of the renal arteries to assess blood flow into the kidneys, arterial spin labelling to measure kidney perfusion and blood oxygen level dependant (BOLD) imaging to assess oxygenation in the kidney.

MEASURABLE END POINTS/STATISTICAL POWER OF THE STUDY

1) TSC quantification in kidney and skin/muscle, and fusion with ^{1}H structural images in n=20 healthy subjects. 2) Sodium flow mapping in n=20 healthy subjects. 3) MQF in 10 healthy subjects. The required number of participants is in line with previous developmental studies (1, 2).

OUTCOMES

This study will develop techniques to quantify tissue sodium content in the skin, muscle and kidney. Sodium flow mapping and MQF will also be developed in the kidneys. These techniques can then be used in further studies of kidney health in kidney disease patients.

WITHDRAWALS

Any volunteer who wishes to withdraw from the study at any time is entitled to do so without giving any reason.

APPROVALS

The University Medical School Ethics Committee approval for the study will be obtained prior to initiation of the study and written informed consent will be obtained from each volunteer prior to their inclusion in the study.

REFERENCES

(1) Breidthardt T, Cox EF, Squire I, et al. Eur Radiol. 2015;25(6):1684-91. (2) Gardener AG, Francis ST. Magn Reson Med. 2010;63(6):1627-36.

Sir Peter Mansfield Imaging Centre
School of Physics and Astronomy

Healthy Volunteer's Consent Form

Sodium MRI of the skin, muscle and kidney
Research Team: Prof Susan Francis, Dr Charlotte Buchanan, Mr Benjamin Prestwich, Dr Huda Mahmoud, Dr Nick Selby, Prof Maarten Taal, Dr Paul Glover, Dr Andrew Peters

Please read this form and sign it once the above named or their designated representative, has explained fully the aims and procedures of the study to you

- I voluntarily agree to take part in this study.
- I confirm that I have been given a full explanation by the above named and that I have read and understand the information sheet given to me which is attached.
- I have been given the opportunity to ask questions and discuss the study with one of the above investigators or their deputies on all aspects of the study and have understood the advice and information given as a result.
- I agree to comply with the reasonable instructions of the supervising investigator and will notify him immediately of any unexpected unusual symptoms or deterioration of health.
- I authorise the investigators to disclose the results of my participation in the study but not my name.
- I understand that information about me recorded during the study will be kept in a secure database. If data is transferred to others it will be made anonymous. Data will be kept for 7 years after the results of this study have been published.
- I authorise the investigators to disclose to me any abnormal test results.
- I understand that I can ask for further instructions or explanations at any time.
- I understand that I am free to withdraw from the study at any time, without having to give a reason for withdrawing.
- I confirm that I have disclosed relevant medical information before the study.
- I understand that my general practitioner may be informed if the scan shows any significant abnormality
- I shall receive a total inconvenience allowance of up to £15 per scan session on completion of the study. If I withdraw from the study for medical reasons not associated with the study I will receive an inconvenience allowance proportional to the length of the period of participation, but if I withdraw for any other reason, the inconvenience allowance to be received, if any, shall be at the discretion of the supervising investigator.
- I have not been a subject in any other research study in the last three months which involved: taking a drug; being paid a disturbance allowance; having an invasive procedure (eg venepuncture >50ml, endoscopy) or exposure to ionising radiation.

Abnormal Findings on a Scan

- I understand that the SPMIC is not a clinical diagnostic facility and so does not routinely inspect images for abnormalities. I understand that my MR scans will NOT routinely be reviewed by a radiologist (or any other medically qualified person) to look for any signs of disease, and it is unlikely that any abnormalities that may be present will be detected.

- One the other hand I understand that if one of the investigators should happen to notice something on my scan which they think is abnormal then they will show my scans to a medically qualified doctor who will contact me if further action is required.

- I understand that if an abnormality were detected on my scan it may affect my ability to get life insurance.

Name: ……

Address: ……..

Telephone number: …….

Signature: ……. **Date:** …….

I confirm that I have fully explained the purpose of the study and what is involved to:

……..

I have given the above named a copy of this form together with the information sheet.

Investigators Signature: …….. **Name:** ……

Study Protocol Number: ……..

MR Centre Number: ……

Sir Peter Mansfield Imaging Centre
School of Physics and Astronomy

The University of Nottingham

Healthy Volunteer's Information Sheet

Sodium MRI of the skin, muscle and kidney
Research Team: Prof Susan Francis, Dr Charlotte Buchanan, Mr Benjamin Prestwich, Dr Huda Mahmoud, Dr Nick Selby, Prof Maarten Taal, Dr Paul Glover, Dr Andrew Peters

You have been invited to take part in a research study. Before you decide whether to take part it is important for you to understand why the research is being done and what it will involve. Please take time to read the following information carefully and discuss it with friends and relatives if you wish to. Ask us if there is anything that is not clear or if you would like more information. Take time to decide whether you wish to take part or not. If you decide to take part you may keep this leaflet. Thank you for reading this.

What is Magnetic Resonance?

Magnetic resonance imaging is a non-invasive, high resolution technique for taking pictures of the inside of the human body. The School of Physics and Astronomy at the University of Nottingham has pioneered the development of MRI and continues to be at the forefront of work in this area. MRI can be used to measure the amount salt (sodium) throughout the body

What are we investigating?

The purpose of this study is to investigate sodium concentrations in the body. We will measure the amount of sodium in three regions; skin, muscle and the kidneys.

What will it involve for you?

You will be asked to complete a brief medical questionnaire and to sign a consent form. You will then be asked to attend the Imaging Centre for less than a total of 3 hours on up to three separate occasions. You can choose how many times you would be happy to attend. You will be scanned on two different MRI scanners either both on the same day, with a break in the middle or on two separate days. We will explain exactly what you will experience while you are in the scanner. We will explain beforehand what will happen and the length of time that you will be scanned.

You will be asked to not consume any liquids for 6 hours before you are due to be scanned. Then during scanning you will be given 1 litre of water to drink during scanning. You will also be asked to complete a blood and urine test, this will be performed by Dr Huda Mahmoud.

The MRI scanner can be quite noisy and so you will wear ear plugs and ear defenders during the scan. The magnet we will be using is very strong, and you may feel slightly dizzy or see flashing lights as you move near to it (but not when you are lying still). For this reason, we will only move you into the magnet very slowly. However if you should feel uncomfortable you will be free to withdraw from the study. Furthermore, because the scanner is built around a large magnet, you will have to remove all metal from your body, including all jewellery. You may prefer to wear loose non-metalllic clothing and/or you may be asked to change into clothing provided.

Are there any risks of taking part?

Magnetic resonance imaging (MRI) uses radio waves similar to those used in radio and TV transmission. These have a much lower energy than X rays and as such are considered biologically safe. Structural MRI using 1.5 T magnets (about 60000 times the earth's magnetic field) and increasingly 3 T magnets is already a routine procedure in medical practice, and not been found to be harmful in any way. We use a stronger magnet (7 T) and use more rapidly changing field gradients but these differences are considered safe. A few people find being in the scanner claustrophobic.

Also some individuals scanned at this high field may experience a feeling of vertigo or (less commonly) flashing lights or a metallic taste as they move around near the scanner We will be following strict national safety guidelines which are designed to prevent the theoretical hazards of MRI which are burns and electric shocks. Such accidents have never occurred in the MR centre and have only very rarely occurred elsewhere. While there is no evidence to suggest that MRI is harmful during pregnancy, the MHRA advises against scanning pregnant women at fields above 2.5T. We have decided not to test for pregnancy as routine but if you think you may be pregnant you should not be scanned.

What will we do if we notice something abnormal on your scan?

Since you are healthy, it is extremely unlikely that your scan will show any abnormality. Even if there were an abnormality it is unlikely that we would notice it since we are taking these scans for scientific research. The SPMIC is not a clinical diagnostic facility and the scans we collect are NOT the same as scans collected by doctors for medical purposes and the pictures will NOT be looked at by a radiologist (a doctor qualified to find abnormalities in scans).

However, there is a possibility that one of the researchers working with your scans might notice something that they consider abnormal. If we should suspect that there was something apparently abnormal on your scan then the scan will be sent to a radiologist who will contact you if they decide that the scan is abnormal and requires further investigation. This could take a few weeks, and once you are notified it could take some time for the problem to be properly investigated.

In the unlikely event that we do notice something abnormal on your scan, giving you this information might have the benefit of allowing you to start treatment earlier than you would have otherwise. But it is also important for you to realise that by providing you with this information there may be implications for your future ability to find employment and obtain insurance.

In 2010 we scanned over 1100 volunteers (most of whom were healthy young people) and happened to notice something that we thought was abnormal on 10 people, of which 3 turned out to be clinical significant problems. However the chances of detecting an abnormality depends on the region of your body we are scanning, the methods we are using to scan you, your age and your health.

What if something goes wrong?

In case you have a complaint (for example on your treatment by a member of staff) you can initially approach the lead investigator (Prof Susan Francis, Sir Peter Mansfield Imaging Centre, School of Physics and Astronomy, University of Nottingham, Nottingham NG7 2RD).
If this achieves no satisfactory outcome (or in case of something serious happened during or following your participation in the study) you can then contact the Chairman of the Ethics Committee (Ethics Committee Secretary, The Dean's Office, Division of Therapeutics and Molecular Medicine, D Floor, South Block, The Medical School, Queen's Medical Centre, Nottingham, NG7 2UH).
In the unlikely event that you suffer injury to yourself or damage to your property as a result in taking part in this research, the University does have an insurance policy to cover harm arising as a result of the defect in the design of the study. In addition, all medical practitioners taking part in the research have personal medical negligence cover.

What if you decide to leave the study?

You are free to leave the study at any time if you chose to do so without giving a reason.

The Data Protection Act

Data about you will be held on computer, but will be treated in the strictest confidence at all times.

Medical Records

We will not contact your GP to inform him/her that you are going to take part in this study. Any information, which is collected about you during the course of the research will be kept strictly confidential. Your name will not be disclosed outside the study centre and any information about

you, which leaves the study centre will have your name (and address) removed so that you cannot be recognised from it.

Publication and Dissemination of the Results

The results of this study may be published in the scientific literature and may also be presented at scientific meetings. All such data will be presented anonymously so that none of the volunteers can be identified.

It is possible that in the future we will realise that we can use the data and images collected in this study in a different way. In that case we will submit another protocol to the Ethics Committee explaining how we will use the data. We are asking you to give us permission now, to use the data collected in unexpected ways in the future, without us contacting you further.

Do you have any further questions?

If you have any questions please ask the person who gave you this sheet or contact Lesley Martin (0115 9514747).

Don't forget, you do not have to be scanned, and you can change your mind, and withdraw from the study, at any time, even whilst being scanned!

The Sir Peter Mansfield Imaging Centre is situated off the Main Visitors car park in grid E4